

UCLA

UCLA Electronic Theses and Dissertations

Title

Influence of Coupling Beam Axial Restraint on Analysis and Design of Reinforced Concrete Coupled Walls

Permalink

<https://escholarship.org/uc/item/7dn6d93f>

Author

Kalbasi Anaraki, Kamiar

Publication Date

2023

Peer reviewed|Thesis/dissertation

UNIVERSITY OF CALIFORNIA

Los Angeles

Influence of Coupling Beam Axial Restraint on
Analysis and Design of Reinforced Concrete Coupled Walls

A dissertation submitted in partial satisfaction of the
requirements for the degree Doctor of Philosophy
in Civil Engineering

by

Kamiar Kalbasi Anaraki

2023

© Copyright by

Kamiar Kalbasi Anaraki

2023

ABSTRACT OF THE DISSERTATION

Influence of Coupling Beam Axial Restraint on Analysis and Design of Reinforced Concrete Coupled Walls

by

Kamiar Kalbasi Anaraki

Doctor of Philosophy in Civil Engineering

University of California, Los Angeles, 2023

Professor John Wright Wallace, Chair

Reinforced concrete coupled shear walls are effective systems for resisting lateral loads, often used in mid to high-rise buildings in earthquake-prone areas. These walls usually feature openings for doors and windows, dividing a solid wall into two separate piers. The strength of these walls comes not just from the sum of two individual piers, but from wall piers cross-section and the framing action between the wall piers through the coupling beams. In an earthquake, coupling beams serve as fuse elements, distributing seismic energy throughout the height of the building. This not only reduces the bending stress at the base of the shear walls but also improves their overall strength, stiffness, and resistance to lateral forces. Properly designed coupling beams, with sufficient longitudinal, diagonal, and confinement reinforcement, can effectively absorb energy while maintaining significant strength and stiffness, even under large deformations. The objective of this study was to develop, calibrate, and validate a new coupling beam model that integrates axial and lateral interactions under cyclic loading conditions. This model aims to

reliably predict the elastic and inelastic responses of diagonally reinforced coupling beam elements. The proposed analytical model incorporates a fiber-based concrete cross-section, and diagonal trusses to account for axial interactions between the nonlinearity in the steel and concrete along the beam's length. This feature allows the model to capture additional axial force developed in the element due to the axial restraint from the wall piers, thereby increasing or decreasing the lateral strength of the beam. Additionally, the model includes the slip-extension behavior between the coupling beam and the supporting wall through zero-length fiber-based elements at both ends of the beam.

Finally, with the development of the new analytical model and recent advancements in understanding the shear strength of RC shear walls, a new coupled/core wall design approach has been introduced to optimize the design of RC core walls. A variety of archetypes have been designed, based on both current design practices and the proposed approach. Detailed analytical models have been developed, and the efficiency of the proposed design has been evaluated through nonlinear static and dynamic analyses. To conduct the dynamic analysis, suites of ground motions were selected using the CMS approach and scaled to the MCE_R level of hazard. It has been demonstrated that the designed archetypes based on proposed procedure provide a more reliable shear responses under seismic loading compared to current design practices.

The dissertation of Kamiar Kalbasi Anaraki is approved.

Henry Burton

Jonathan Paul Stewart

Yousef Bozorgnia

John Wright Wallace, Committee Chair

University of California, Los Angeles

2023

To my Parents

TABLE OF CONTENTS

ABSTRACT OF THE DISSERTATION.....	ii
LIST OF TABLES.....	x
LIST OF FIGURES	xiv
ACKNOWLEDGEMENTS	xxiii
VITA.....	xxiv
1. INTRODUCTION	1
1.1. Background.....	1
1.2. Objectives.....	3
1.3. Organization	4
2. LITERATURE REVIEW.....	6
2.1. Coupled Wall Systems.....	6
2.2. Design Code Provisions and Guidelines	10
2.3. Isolated Coupling Beam Experimental Studies.....	12
2.4. Coupled Wall System Experimental Studies	16
2.5. Axial Restraint of Coupling Beams.....	22
2.6. Existing Coupling Beam Analytical Models	23
2.6.1. Lumped Plasticity Models	23
2.6.2. Distributed Plasticity Models	24
2.6.3. Shortcoming of Current Macroscopic Models.....	25
2.7. Motivation and the Need for Proposed Coupling Beam Analytical Model	26
3. MODEL DESCRIPTION.....	28
3.1. Fiber-Based Concrete Model	29
3.2. Diagonal Reinforcement.....	30

3.3.	Slip/Extension	31
3.4.	Constitutive material models	31
3.4.1.	Steel Reinforcement Constitutive Material Model	32
3.4.2.	Concrete Constitutive Material Model	35
3.4.3.	Slip-Extension Material Model.....	40
4.	EXPERIMENTAL SPECIMEN INVENTORY	47
4.1.	Isolated Coupling Beam Specimens	47
4.1.1.	Specimen CB24F & CB24F-RC	48
4.1.2.	Specimen CB30-H	52
4.1.3.	Specimen CB1 & CB1A	55
4.1.4.	Specimen BRI-1996 BLB & BMB	58
4.2.	System Level Coupled Wall Specimen.....	61
4.2.1.	Specimen BRI-1996.....	62
4.2.2.	Loading and measurements.....	64
5.	ANALYTICAL MODEL VALIDATION	66
5.1.	Isolated Specimens.....	66
5.1.1.	Material Calibration.....	68
5.1.2.	Geometry Calibration	75
5.1.3.	Load Application and Solution Algorithm.....	77
5.1.4.	Comparison of Analytical and Experimental Results	78
5.2.	System-Level Coupled Wall Specimen	89
6.	CORE WALL DESIGN	100
6.1.	Archetypes.....	102

6.2.	Site Specific Design Parameters.....	103
6.3.	Design Process.....	104
6.3.1.	Coupling Beams	105
6.3.2.	Wall Piers Flexural Design.....	105
6.3.3.	Wall Piers Shear Design.....	107
6.4.	ACI 318-19	109
6.5.	ACI 318-25	110
6.6.	Rojas-Wallce Shear Equation (2023).....	111
6.7.	Considering Shear Redistribution in the Design.....	112
6.8.	Design Summary	118
7.	ARCHETYPE CORE WALL ANALYTICAL MODELING.....	137
7.1.	System Modeling	137
7.2.	Damping.....	142
7.2.1.	Modal Analysis.....	143
8.	NONLINEAR ANALYSIS.....	146
8.1.	Failure Assessment	146
8.1.1.	Flexural Failure via Drift Capacity Model.....	146
8.1.2.	Axial Failure.....	149
8.1.3.	Shear Failure	151
8.2.	Nonlinear Static Analysis Results.....	152
8.1.	Ground motion selection	159
8.2.	Analysis Procedure.....	161
8.3.	Nonlinear Dynamic Analysis Results.....	162
8.4.	Summary of Results.....	171

9. SUMMARY AND CONCLUSION	174
9.1. Summary	174
9.2. Conclusions	175
9.3. Future Studies and Possible Model Improvements	177
APPENDIX A - CBeam ELEMENT USER MANUAL	178
APPENDIX B – ARCHETYPES DESIGN (9-Stories).....	179
B.1. 9-Story ACI 318-14	179
B.2. 9-Story ACI 318-19	202
B.3. 9-Story ACI 318-25	218
B.4. 9-Story ACI 318-25 and Rojas and Wallace 2022 Shear Equation	234
B.5. 9-Story ACI 318-25 and Rojas and Wallace 2022 Shear Equation – Considering Shear Distribution	255
APPENDIX C - GROUND MOTION SELECTION	274
C.1. Procedure for Computing CMS	275
C.2. Archetypes Mode Shapes and Modal Periods.....	278
C.3. Selected ground motions	280
REFERENCES	283

LIST OF TABLES

Table 4.1: Materials properties.50

Table 4.2: BRI 1996 coupled wall detailed reinforcement.64

Table 4.3: BRI 1996 coupled wall system material properties.....64

Table 5.1: isolated specimen inventory with its geometry, reinforcing, and materials properties.
.....66

Table 5.2: constitutive concrete material modeling parameters.69

Table 5.3: constitutive material modeling inputs.73

Table 5.4: Bond-Sp01 material input for assigned diagonal steel slip-extension behavior.....74

Table 5.5: Displacement protocols (chord rotation percentage).77

Table 5.6: Assigned shear wall elements properties.93

Table 5.7: BRI-1996 12-story modeling concrete material parameters.94

Table 6.1: Archetypes shear design criteria.103

Table 6.2: Summary of 9-story core-wall design according to ACI 318-14.120

Table 6.3: Summary of 9-story coupling beam design; archetype designed per to ACI 318-14.
.....120

Table 6.4: Summary of 9-story core-wall design according to ACI 318-19.120

Table 6.5: Summary of 9-story coupling beam design; archetype designed per to ACI 318-19.
.....121

Table 6.6: Summary of 9-story core-wall design according to ACI 318-25.121

Table 6.7: Summary of 9-story coupling beam design; archetype designed per to ACI 318-25.
.....121

Table 6.8: Summary of 9-story core-wall design according to ACI 318-25 and the Rojas-Wallace 2022 shear equation.	122
Table 6.9: Summary of 9-story coupling beam design; archetype designed per to ACI 318-25 and the Rojas-Wallace 2022 shear equation.	122
Table 6.10: Summary of 9-story core-wall design according to ACI 318-25 and the Rojas-Wallace 2022 shear equation and redistributed shear demand.	122
Table 6.11: Summary of 9-story coupling beam design; archetype designed per to ACI 318-25 and the Rojas-Wallace 2022 shear equation and redistributed shear demand.	123
Table 6.12: Summary of 12-story core-wall design according to ACI 318-14.	123
Table 6.13: Summary of 12-story coupling beam design; archetype designed per to ACI 318-14.	123
Table 6.14: Summary of 12-story core-wall design according to ACI 318-19.	124
Table 6.15: Summary of 12-story coupling beam design; archetype designed per to ACI 318-19.	124
Table 6.16: Summary of 12-story core-wall design according to ACI 318-25.	124
Table 6.17: Summary of 12-story coupling beam design; archetype designed per to ACI 318-25.	125
Table 6.18: Summary of 12-story core-wall design according to ACI 318-25 and the Rojas-Wallace 2022 shear equation.	125
Table 6.19: Summary of 12-story coupling beam design; archetype designed per to ACI 318-25 and the Rojas-Wallace 2022 shear equation.	125
Table 6.20: Summary of 12-story core-wall design according to ACI 318-25 and the Rojas-Wallace 2022 shear equation and redistributed shear demand.	126
Table 6.21: Summary of 12-story coupling beam design; archetype designed per to ACI 318-25 and the Rojas-Wallace 2022 shear equation and redistributed shear demand.	126
Table 6.22: Summary of 15-story core-wall design according to ACI 318-14.	127

Table 6.23: Summary of 15-story coupling beam design; archetype designed per to ACI 318-14.	127
Table 6.24: Summary of 15-story core-wall design according to ACI 318-19.	128
Table 6.25: Summary of 15-story coupling beam design; archetype designed per to ACI 318-19.	128
Table 6.26: Summary of 15-story core-wall design according to ACI 318-25.	129
Table 6.27: Summary of 15-story coupling beam design; archetype designed per to ACI 318-25.	129
Table 6.28: Summary of 15-story core-wall design according to ACI 318-25 and the Rojas- Wallace 2022 shear equation.	130
Table 6.29: Summary of 15-story coupling beam design; archetype designed per to ACI 318-25 and the Rojas-Wallace 2022 shear equation.	130
Table 6.30: Summary of 15-story core-wall design according to ACI 318-25 and the Rojas- Wallace 2022 shear equation and redistributed shear demand.	131
Table 6.31: Summary of 15-story coupling beam design; archetype designed per to ACI 318-25 and the Rojas-Wallace 2022 shear equation and redistributed shear demand.	131
Table 6.32: Summary of 18-story core-wall design according to ACI 318-14.	132
Table 6.33: Summary of 18-story coupling beam design; archetype designed per to ACI 318-14.	132
Table 6.34: Summary of 18-story core-wall design according to ACI 318-19.	133
Table 6.35: Summary of 18-story coupling beam design; archetype designed per to ACI 318-19.	133
Table 6.36: Summary of 18-story core-wall design according to ACI 318-25.	134
Table 6.37: Summary of 18-story coupling beam design; archetype designed per to ACI 318-25.	134

Table 6.38: Summary of 18-story core-wall design according to ACI 318-25 and the Rojas-Wallace 2022 shear equation.	135
Table 6.39: Summary of 18-story coupling beam design; archetype designed per to ACI 318-25 and the Rojas-Wallace 2022 shear equation.	135
Table 6.40: Summary of 18-story core-wall design according to ACI 318-25 and the Rojas-Wallace 2022 shear equation and redistributed shear demand.	136
Table 6.41: Summary of 18-story coupling beam design; archetype designed per to ACI 318-25 and the Rojas-Wallace 2022 shear equation and redistributed shear demand.	136
Table 8.1: Base shear strength capacity of archetypes.....	153
Table 8.2: Period and spectral accelerations used to condition the suites of ground motions. .	160
Table 8.3. Summary of shear DCR.....	172

LIST OF FIGURES

Figure 1.1: Elevation View of a Typical Coupled Core Wall Building 2

Figure 2.1: Typical floor plan of a structure with core wall and isolated 3-dimensional view of the core wall..... 7

Figure 2.2: Typical reinforcement pattern for conventional and diagonal reinforcement in coupling beams 8

Figure 2.3: Coupled wall deformed shaped; applied axial force from coupling beams on wall piers and expected plastic hinges. 10

Figure 2.4: deformation of RC coupled wall: plastic hinge formation, framing actions, lateral force variations, and diagonally reinforced coupling beam resisting reactions. 11

Figure 2.5: Paulay T. 1971 load-rotation relationship for a conventional coupling beam. 13

Figure 2.6: Paulay T. and Binney J.R. Load-rotation relationship for diagonally reinforced coupling beam (beam 316)..... 14

Figure 2.7: Reinforcement configuration of Santhakumar's (1974) 7-story coupled wall system specimens; left shows Wall A with a conventional reinforced coupling beam, right shows Wall B with a diagonally reinforced coupling beam..... 17

Figure 2.8: Load-deformation of the wall specimen A; Santhakumar (1974)..... 18

Figure 2.9: Load-deformation of the wall specimen B; Santhakumar (1974)..... 18

Figure 2.10: Lumped plasticity models used to simulate coupling beams; left) two rotational hinges at each end to simulate beam nonlinearity and slip-extension, right) shear hinge in the middle of the element to simulate beam nonlinearity and rotational hinges at the ends to simulate slip-extension behavior (Naish et al., 2013)..... 24

Figure 2.11: BTM model used to simulate walls and coupling beams (Lu and Panagiotou, 2016). 25

Figure 3.1: CBeam element constitutive components.....	28
Figure 3.2: reinforced concrete fiber cross-section.....	29
Figure 3.3: uniaxial, tension-compression behavior of ReinforcingSteel material.	33
Figure 3.4: a) buckling behavior at steel material level; b) steel material low-cyclic fatigue behavior.....	34
Figure 3.5: Compression backbone of modified Kent & Park concrete model (1982).	35
Figure 3.6: Yassin, 1994 concrete hysteretic unloading-reloading behavior.....	37
Figure 3.7: Yassine 1994, Parameters illustrating hysteretic behavior in concrete material.	37
Figure 3.8: Illustration of Yassine 1994, representing concrete's hysteretic behavior under tension.....	39
Figure 3.9: Rebar stress-slip backbone curve.	41
Figure 3.10: a) reinforcing bar extended in the support concrete element; b) stress distribution; c) strain distribution; d) bond stress between concrete and steel.	42
Figure 3.11: Ciampi et al. 1981 and Eligehausen et al. 1983 local bond-slip model.....	45
Figure 3.12: a) reinforcing bar slip at the support concrete element; b) stress distribution; c) strain distribution; d) bond stress.....	45
Figure 4.1: Photograph of test specimen construction: a) CB24F beam construction, b) CB24F-RC beam and slab construction (Figure from Naish 2010).	49
Figure 4.2: Naish 2010 test beam geometries ($lnh = 2.4$) with full section confinement: a) CB24F, CB24F-RC elevation; b) CB24F cross section; and c) CB24F-RC cross section (Figure from Naish 2010).	49
Figure 4.3: CB24F and CB24F-RC laboratory test setup (Figure from Naish 2010).	51
Figure 4.4: loading protocol: a) load-control, b) displacement-control (Figure from Naish 2010).	52
Figure 4.5: CB30H test specimen reinforcement configuration (Lim et al., 2016).	53
Figure 4.6: CB30H laboratory test setup (Lim et al., 2016).	54

Figure 4.7: CB30H loading protocol (Lim et al., 2016).	55
Figure 4.8: CB1 and CB1A specimen dimension and reinforcements (Poudel et al., 2018).	56
Figure 4.9: CB1 and CB1A laboratory test setup (Poudel et al., 2018).	57
Figure 4.10: CB1A axial restraint fixture (Poudel et al., 2018).	57
Figure 4.11: CB1 and CB1A loading protocol (Poudel et al., 2018).	58
Figure 4.12: BLB specimen reinforcement configuration and placement of the loadcell within the beam (Sugaya, 2003).	59
Figure 4.13: BLB/BMB laboratory test setup (Sugaya, 2003).	60
Figure 4.14: loading protocol: a) BMB, b) BLB (Sugaya, 2003).	61
Figure 4.15: BRI-1996 target building core wall.	62
Figure 4.16: BRI-1996 specimen reinforcement layout.	63
Figure 4.17: left) BRI-1996 loading configuration; right) cyclic loading protocol. (Sugaya, 2003)	65
Figure 5.1: Specimens detail: a) CB24F; b) CB24F-RC; c) CB30-H; d) CB1; e) CB1A; f) BMB.	67
Figure 5.2: CB24F constitutive concrete material; a) unconfined concrete, b) confined concrete.	69
Figure 5.3: CB24F-RC constitutive concrete material; a) unconfined concrete, b) confined concrete.	70
Figure 5.4: CB30H constitutive concrete material; a) unconfined concrete, b) confined concrete.	70
Figure 5.5: CB1 constitutive concrete material; a) unconfined concrete, b) confined concrete.	71
Figure 5.6: CB1A constitutive concrete material; a) unconfined concrete, b) confined concrete.	71
Figure 5.7: BMB/BLB constitutive concrete material; a) unconfined concrete, b) confined concrete.	72

Figure 5.8: Constitutive steel material; a) CB24F & CB24F-RC, b) CB30F, c) CB1 & CB1A; d) BRI-BMB D16; e) BRI-BMB D13; f) BRI-BMB D10.....	73
Figure 5.9: Slip-extension behavior; a) CB24F & CB24F-RC, b) CB30F, c) CB1 & CB1A; d) BRI-BMB D16; e) BRI-BMB D13; f) BRI-BMB D10.....	75
Figure 5.10: a) cross-section discretization; b) longitudinal discretization and boundary condition.....	76
Figure 5.11: sensitivity of the CBeam model yield strength to the number of segments. a) yield strength sensitivity; b) strength at 2% chord rotation sensitivity; and c) strength at 5% chord rotation sensitivity.....	76
Figure 5.12: Comparison of measured and predicted responses of specimen CB24F: a) lateral load versus chord rotation; b) axial growth under lateral load versus chord rotation.....	79
Figure 5.13: Comparison of measured and predicted responses of specimen CB24F-RC: a) lateral load versus chord rotation; b) axial growth under lateral load versus chord rotation.....	80
Figure 5.14: CB24F vs CB24F-RC global response comparison: a) experimental shear vs chord rotation; b) experimental axial growth vs chord rotation; c) numerical shear vs chord rotation; d) numerical axial growth vs chord rotation.....	81
Figure 5.15: Comparison of measured and predicted responses of specimen CB30-H: a) lateral load versus chord rotation; b) axial growth under lateral load versus chord rotation.....	82
Figure 5.16: Comparison of measured and predicted responses of specimen CB1: a) lateral load versus chord rotation; b) axial growth under lateral load versus chord rotation.....	83
Figure 5.17: Comparison of measured and predicted responses of specimen CB1A: a) lateral load versus chord rotation; b) axial growth under lateral load versus chord rotation.....	84
Figure 5.18: axial restraint force in CB1A specimen.....	85
Figure 5.19: assigned axial restraint behavior.....	85

Figure 5.20: CB1 vs CB1A global response comparison: a) experimental shear versus chord rotation; b) experimental axial growth versus chord rotation; c) numerical shear versus chord rotation; d) numerical axial growth versus chord rotation.....	86
Figure 5.21: BLB versus BMB (Sugaya, 2003).....	88
Figure 5.22: Comparison of measured and predicted responses of specimen BMB.....	89
Figure 5.23: Observed damage of BRI 12-Story Coupled Walls Test (Sugaya, 2003).	91
Figure 5.24: MVLEM-3D in-plane and out-of-plane behavior.....	93
Figure 5.25: BRI-1996 wall pier cross-section and coupling beam discretization.....	93
Figure 5.26: visually represents the BRI-1996 OpenSees analytical model.....	95
Figure 5.27: test versus analytical model BRI-1996 system roof displacement – base shear. ...	96
Figure 5.28: BRI-1996 coupling beams test versus analytical model lateral shear – lateral displacement and axial force – axial growth hysteretic behavior. Floor levels with the same coupling beams are separated with navy boxes; Floor levels connected to actuators are depicted with green boxes.....	98
Figure 6.1: coupled wall internal forces and wall piers P-M diagram.	101
Figure 6.2: typical archetypes floor plan and its isolated core wall 3-dimensional view.....	102
Figure 6.3: ETABS elastic model used to determine the design demands.....	105
Figure 6.4: C-shaped wall centroid to calculate the wall piers demand.....	106
Figure 6.5: Determination of shear demand for walls with $hw/lw \geq 2.0$	110
Figure 6.6: depicts a building with RC wall piers, showing a plastic hinge formation at the base of the walls. This schematic includes plastic framing actions, reactions, and variations in internal and system lateral forces.	113
Figure 6.7: Free body diagram of forces developed due to mobilization of framing plastic mechanism at floor i for the case of framing between two external walls.	114
Figure 6.8: Typical core-wall cross section and its associated P-M diagram in the coupled direction.....	117

Figure 6.9: Design flowchart to minimize the required wall thickness.	118
Figure 6.10: core-wall cross-section detail.	119
Figure 6.11: Coupling beams elevation and cross-section details.....	119
Figure 7.1: Implementation of leaning column in the analytical model. Left) plan view; right) 3-D view.....	138
Figure 7.2: Coupling beam and shear wall elements connection.....	139
Figure 7.3: left) Wall cross-section discretization; right) Coupling beam discretization and its connection to adjacent walls.	140
Figure 7.4: Coupling beam discretization and its connection to adjacent walls.....	142
Figure 7.5: Recommended viscous damping based on building height per PEER TBI, 2017 provision.	143
Figure 7.6: 9-story archetypes mode shapes and their associated modal periods.....	143
Figure 7.7: 12-story archetypes mode shapes and their associated modal periods.....	144
Figure 7.8: 15-story archetypes mode shapes and their associated modal periods.....	144
Figure 7.9: 18-story archetypes mode shapes and their associated modal periods.....	145
Figure 8.1: Histogram of 164 Tests in the Drift capacity model (Abdullah, 2019).	148
Figure 8.2: Comparison of predicted drift capacity with experimental drift capacity (Abdullah, 2019). Left) predicted drift capacity with equation 8.1; right) predicted drift capacity with equation 8.2.....	148
Figure 8.3: Axial load capacity model for a shear wall pier after diagonal cracking.....	150
Figure 8.4: Comparison of predicted drift capacities with experimental drift capacities: a) special walls; and b) ordinary walls.	151
Figure 8.5: Assessment of shear limit exceedance. The red line represents the ACI 318 shear strength, and the black line represents the Rojas-Wallace 2022 shear strength history.....	152
Figure 8.6: 9-story archetypes pushover analysis results (roof drift vs. total base shear).	153

Figure 8.7: 9-story archetypes pushover analysis results (roof drift vs. each base shear in the coupled direction).....	154
Figure 8.8: 9-story archetypes shear distribution ratio between the wall piers.	154
Figure 8.9: 12-story archetypes pushover analysis results (roof drift vs. total base shear).	155
Figure 8.10: 12-story archetypes pushover analysis results (roof drift vs. each base shear in the coupled direction).....	155
Figure 8.11: 12-story archetypes shear distribution ratio between the wall piers.	156
Figure 8.12: 15-story archetypes pushover analysis results (roof drift vs. total base shear). ...	156
Figure 8.13: 15-story archetypes pushover analysis results (roof drift vs. each base shear in the coupled direction).....	157
Figure 8.14: 15-story archetypes shear distribution ratio between the wall piers.	157
Figure 8.15: 18-story archetypes pushover analysis results (roof drift vs. total base shear). ...	158
Figure 8.16: 18-story archetypes pushover analysis results (roof drift vs. each base shear in the coupled direction).....	158
Figure 8.17: 18-story archetypes shear distribution ratio between the wall piers.	159
Figure 8.18: Site specific uniform Hazard Spectrum (UHS).	160
Figure 8.19: Response spectra of selected suites of ground motions conditioned to first and second modes of 9-story archetypes.....	161
Figure 8.20: 9-story archetypes V_e/V_n ratio profile using suites of ground motions conditioned to mode 1; a) ACI 318 shear strength, b) R-W shear strength equation.	162
Figure 8.21: 9-story archetypes V_e/V_n ratio profile using suites of ground motions conditioned to mode 2; a) ACI 318 shear strength, b) R-W shear strength equation.	163
Figure 8.22: comparison between the V_e/V_n (base shear) ratio of 9-story archetypes.....	164
Figure 8.23: comparison between the V_e/V_n (average shear) ratio over the height of 9-story archetypes.	164

Figure 8.24: 12-story archetypes V_eV_n ratio profile using suites of ground motions conditioned to mode 1; a) ACI 318 shear strength, b) R-W shear strength equation.	165
Figure 8.25: 12-story archetypes V_eV_n ratio profile using suites of ground motions conditioned to mode 2; a) ACI 318 shear strength, b) R-W shear strength equation.	165
Figure 8.26: comparison between the V_eV_n (base shear) ratio of 12-story archetypes.....	166
Figure 8.27: comparison between the V_eV_n (average shear) ratio over the height of 12-story archetypes.	167
Figure 8.28: 15-story archetypes V_eV_n ratio profile using suites of ground motions conditioned to mode 1; a) ACI 318 shear strength, b) R-W shear strength equation.	167
Figure 8.29: 15-story archetypes V_eV_n ratio profile using suites of ground motions conditioned to mode 2; a) ACI 318 shear strength, b) R-W shear strength equation.	168
Figure 8.30: comparison between the V_eV_n (base shear) ratio of 15-story archetypes.....	169
Figure 8.31: comparison between the V_eV_n (average shear) ratio over the height of 15-story archetypes.	169
Figure 8.32: 18-story archetypes V_eV_n ratio profile using suites of ground motions conditioned to mode 1; a) ACI 318 shear strength, b) R-W shear strength equation.	169
Figure 8.33: 18-story archetypes V_eV_n ratio profile using suites of ground motions conditioned to mode 2; a) ACI 318 shear strength, b) R-W shear strength equation.	170
Figure 8.34: comparison between the V_eV_n (base shear) ratio of 18-story archetypes.....	171
Figure 8.35: comparison between the V_eV_n (average shear) ratio over the height of 18-story archetypes.	171
Figure 8.36: Comparison between the story height on the based shear V_eV_n ratio.....	172
Figure 8.37: Comparison between the story height on the average of V_eV_n ratio over the height of archetypes.	173

ACKNOWLEDGEMENTS

I would like to express my deepest thanks to Professor John W. Wallace, my academic advisor, for the significant role he has played in my journey through this fascinating research project. His vast knowledge, unwavering support, and encouragement in developing independent thinking have been invaluable throughout my PhD. I also wish to express my gratitude to the members of my Doctoral Committee, Professors Henry Burton, John Stewart, and Yousef Bozorgnia, for their valuable contributions and insights. Special thanks are due to Dr. Farzad Naeim and Dr. Mike Mehraein for their support and guidance, both before and after I started my PhD study at UCLA.

Throughout my PhD, I had the privilege of collaborating with an exceptional team on the FEMA P807-1 project, where I gained insights into wood structures and strategies for mitigating soft-story issues. This project provided the opportunity to work alongside Professor Wallace, David Mar, Kelly Cobeen, Daniel Zepeda, Garrett Hagen, Mike Mahoney, Justin Moresco, and many other distinguished engineers.

I am grateful to all the students I assisted as a Teaching Assistant at UCLA, whose inquiries deepened my understanding of RC structures. The experience was further enriched by the camaraderie and exchange of ideas within our research group.

Lastly, I extend my heartfelt appreciation to my family for their endless love and support. Special thanks to my parents, who have always prioritized the well-being of their children.

VITA

- 2012 B.S., Civil Engineering
K. N. Toosi University of Technology, Tehran, Iran
- 2015 M.S. Earthquake Engineering
K. N. Toosi University of Technology, Tehran, Iran
- 2019 M.S. Structural Engineering
California State University, Fullerton, CA
- 2018-2019 Design Engineer
Degenkolb Engineers, Los Angeles, CA
- 2019-2023 Graduate Student Researcher
Department of Civil and Environmental Engineering
University of California, Los Angeles
- 2019-2023 Teaching Assistant
Department of Civil and Environmental Engineering
University of California, Los Angeles

1. INTRODUCTION

1.1. Background

In regions with high seismic activity, there is a significant risk of structural damage that can lead to human fatalities. The field of structural earthquake engineering focuses extensively on developing methods to construct safe and economical buildings by selecting appropriate levels of stiffness, strength, and deformation capacities to meet prescribed performance objectives for various hazard levels. Use of cantilever (uncoupled) reinforced concrete (RC) shear walls is an effective lateral system in low- to mid-rise buildings; however, use of uncoupled (or weakly coupled) walls may not be suitable for taller buildings. A particularly effective approach for taller buildings in active seismic zones is to combine RC shear walls with coupling beams, where the coupling beams are designed as flexible links to dissipate energy due to the lateral deformations induced by the ground shaking. Coupled walls are often arranged into a central core wall, with space inside the core used to provide space for elevators and stairs, and the coupling beams are provided above openings into the central core (Figure 1.1). The coupling beams are typically provided at each floor level to couple the wall segments and increase the stiffness and strength of the lateral system.

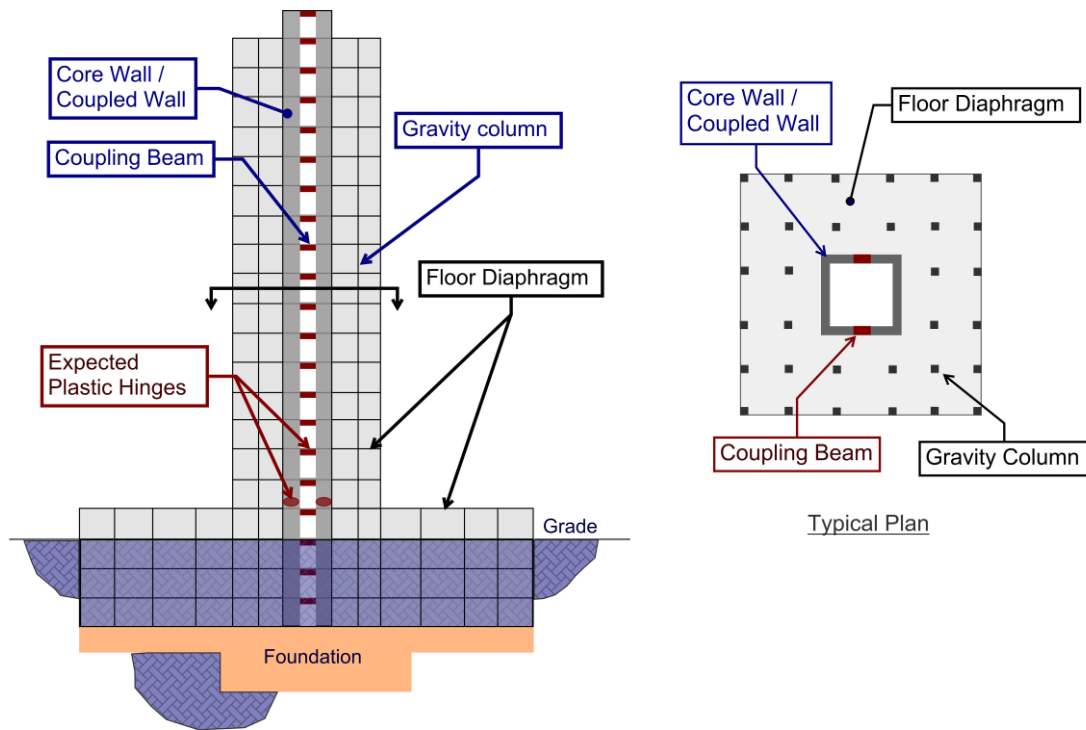


Figure 1.1: Elevation View of a Typical Coupled Core Wall Building.

To design and evaluate the seismic behavior of coupled wall/core wall systems effectively, analytical models must accurately represent the complex behavior of these structures. Computational platforms like OpenSees and Perform-3D, commonly used for nonlinear analysis, employ advanced models, such as the Multiple-Vertical-Line-Element-Model (MVLEM and MVLEM-3D), to simulate the behavior of RC structural walls. However, current models for coupling beams, especially those using a lumped plasticity approach, which are popular due to their simplicity, have limitations that limit their ability to accurately simulate the response of coupling beams. The accuracy of coupling beam models is commonly assessed using test data; however, most test data reported in the literature does not address the influence of axial load (or axial restraint) on beam behavior, resulting in inaccuracies when predicting the behavior of the lateral system and the building. Variation in coupling beam axial load changes the stiffness, strength, and deformation capacity of a beam, which also results in changes to the demands (e.g.,

axial loads and shears) on the wall piers. Following the 2010 and 2011 earthquakes in the Canterbury, New Zealand area, it was observed that coupled walls did not perform as expected, with damage typically observed in wall piers rather than the coupling beams, possibly indicating that the design approach produced unintended results for core wall/coupled wall systems. Improved analytical models are needed to accurately predict the behavior of reinforced concrete coupling beams under varying conditions.

A team from UCLA has created an experimental database for shear walls and has used statistical and machine learning tools to gain insight into the behavior of shear walls. This research has led to proposals to revise the ACI 318-19 provision used to estimate wall shear strength in ACI 318-25, which has remained essentially unchanged for over fifty years. Meanwhile, ACI 318-19 introduced an increase in the shear demand for structural walls by applying an amplification factor of up to 3.0. As a result, with the increased demand and unchanged capacity, the required thickness and web reinforcement for walls have significantly increased. The combination of the proposed shear strength equation and a more realistic analytical model provides an approach that could improve the seismic design and assessment of core walls.

1.2. Objectives

This study focuses on understanding the behavior and response of core wall systems under lateral loading by accurately modeling the strength, stiffness, and deformation capacity of coupling beams and the effect of coupling beam responses on wall piers. The research has eight key objectives:

1. Develop a comprehensive modeling approach to simulate diagonally reinforced coupling beams,
2. Assess the ability of the coupling beam model to simulate coupling beam responses under various boundary conditions and reinforcement designs,

3. Evaluate the ability of the model to simulate the responses of isolated coupling beams and coupled wall systems by comparing responses obtained with the model with response obtained in experiments,
4. Implement the proposed model in OpenSees, an open-source platform, for public use and further development,
5. Use the model to determine the shear demand distribution on the tension and compression piers of a coupled wall and evaluate various approaches used to design coupled wall systems,
6. Design various core wall archetypes with different heights and different wall shear strength estimates, e.g., ACI 318-19 and the proposed model by Rojas-Leon (2022),
7. Propose an improved design method for coupled walls, and
8. Assess the efficiency of the proposed design procedure using nonlinear static and dynamic analysis and compare the efficiency of the design with current design procedures used in practice.

As outlined above, the first phase of the research involves proposing and validating a new numerical model for coupling beams. The next Chapter provides an overview of the nonlinear behavior and expected failure modes of reinforced concrete coupled wall systems using various design standards and approaches.

1.3. Organization

This dissertation is organized into nine chapters. The first chapter provides an introduction, presents background material, outlines study motivations and objectives, and provides an outline of the organization of the dissertation. The second chapter offers a thorough literature review, familiarizing readers with relevant research and identifying research gaps. The third chapter details the proposed analytical model for coupling beams and includes the theoretical basis and

assumptions of the model. The fourth chapter includes a discussion of the experimental programs used to validate the analytical model and includes a discussion of the model calibration process for both isolated coupling beam test specimens and the coupled wall system test specimen. In the fifth chapter, the focus is on bridging theory and practice by comparing results obtained with the analytical model with results obtained in experimental studies to highlight similarities, differences, and key insights.

The sixth chapter includes a discussion of the provisions used to design for various archetypes and introduces and explains the proposed optimized core wall design procedure. Chapter seven delves into the nonlinear modeling of archetypes, with an emphasis on calibrating materials to ensure the accuracy of the model. Chapter eight presents results and includes an interpretation of the results from both nonlinear static and dynamic analyses.

Finally, the ninth chapter summarizes the entire research study, summarizing the main findings, conclusions, and recommendations, especially regarding the nonlinear modeling of core walls and the optimized design methodology. Suggestions for future work to address remaining uncertainties and expand the application scope of the findings are also included.

In addition to these nine core chapters, the dissertation includes four detailed appendices that delve into core wall design specifics, auxiliary calculations such as rebar bond-slip computations, methodologies for site-specific ground motion selection and scaling, and a user manual for the proposed coupling beam model.

2. LITERATURE REVIEW

In this chapter, the behavior, analytical models, and design procedures of coupled/core wall systems subjected to combined gravity and lateral loading as presented in the literature are explored. The discussion begins with an introduction to the components of core wall systems and the anticipated behavior of these components, followed by a presentation of design provisions available in codes and guidelines. Next, a detailed review of experimental studies, with a special focus on diagonally reinforced coupling beams and the influence of axial restraint on lateral responses, is presented. Subsequent sections delve into existing numerical models and highlight advantages and limitations of the various approaches. Based on this review, the need for a new analytical model for coupling beams along with the important features required of a new model are discussed.

2.1. Coupled Wall Systems

Mid- to high-rise buildings commonly utilize reinforced concrete structural walls as a lateral force-resisting system due to their inherent strength and stiffness. By strategically connecting two or more adjacent walls with coupling beams, the stiffness and strength of the lateral system is enhanced. Additionally, during extreme seismic events, coupling beams, if properly designed, act as ductile fuses by undergoing large inelastic rotations without strength degradation. This system is particularly effective in reinforced concrete core walls featuring openings to accommodate doorways and other architectural elements. Figure 2.1 presents a schematic of a typical building plan that utilizes the core wall as the lateral resisting system, along with an isolated three-dimensional view of the core wall.

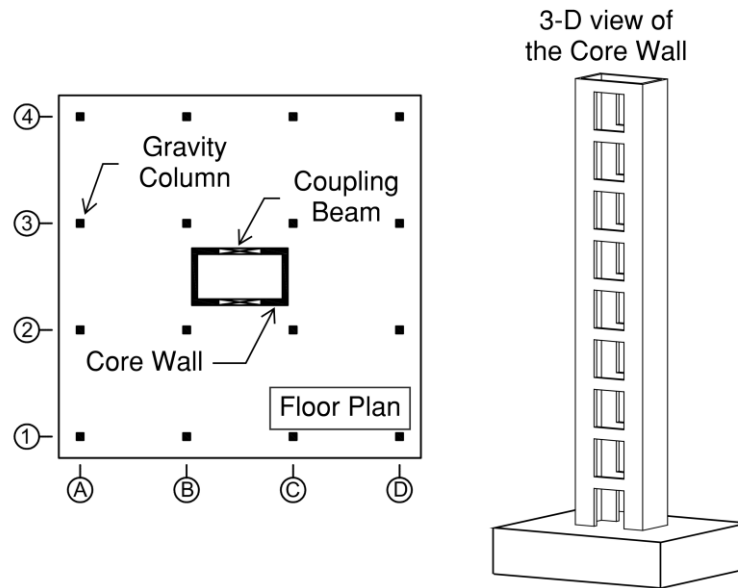


Figure 2.1: Typical floor plan of a structure with core wall and isolated 3-dimensional view of the core wall.

Coupling beams are typically classified as conventionally reinforced coupling beams with flexural strength provided by longitudinal reinforcement or diagonally reinforced coupling beams with diagonal bundles of reinforcement (Figure 2.2). Both beam types incorporate closely spaced shear reinforcement in the form of hoops and cross-ties to provide shear resistance and/or provide confinement. The ACI 318-19 code requires the use of diagonally reinforced beams for beam aspect ratios (clear span l_n to total beam depth h) ≤ 2.0 and if shear stress $\geq 4\sqrt{f'_c}$, whereas longitudinally reinforced beams are used for $l_n/h \geq 4.0$. For l_n/h between 2 and 4, either beam configuration can be used. In core wall buildings, the usual clear span-to-depth ratios fall between 2 and 4 (Naish et al, 2013). An analysis of thirteen coupled wall structures, ranging from 10 to 60 stories high and designed from 1991 to 2007 in the seismically active western regions of the U.S., indicates that a prevalent contemporary beam aspect ratio stands at $l_n/h = 2$, as highlighted in the study by Lehman et al. in 2013.

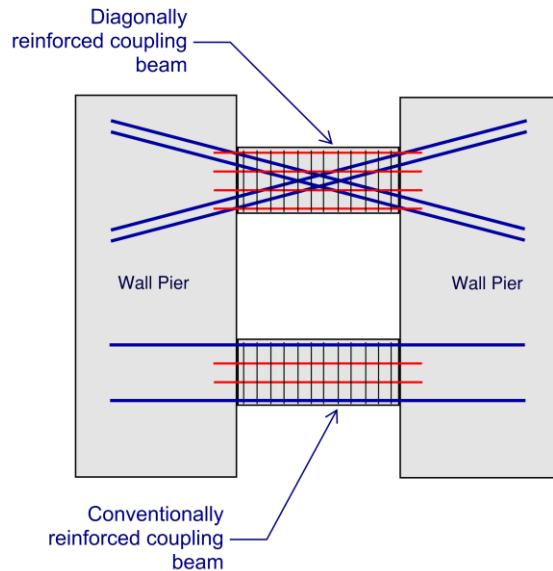


Figure 2.2: Typical reinforcement pattern for conventional and diagonal reinforcement in coupling beams.

Results reported from experimental studies generally indicate that diagonally reinforced coupling beams reach total rotations of 6 to 8% prior to strength loss, whereas conventionally reinforced beams reach total rotations of 3 to 4% prior to strength loss. (Naish et al., 2013, Ji et al., 2017). Results reported by Aktan & Bertero (1984) for conventionally reinforced coupling beams showed that, if beam average shear stress was limited to $3\sqrt{f'_c}$, then the response was primarily governed by flexural behavior. This shear stress limit is usually obtained when a conventionally reinforced beam with aspect ratio of higher than 4; therefore, the current version of the ACI 318 requires using conventionally reinforced coupling beams in this case. On the other hand, beams under intense shear stress can benefit from dual sets of diagonal bundle of bars, which emulate a strut and tie load trajectory. For beams where the ratio of l_n/h is less than 4, this diagonal reinforcement approach not only fosters efficient wall coupling and enhanced deformation capacity but also ensures superior energy dissipation during cyclical loading. Additionally, these diagonal bars counteract shear forces at the beam-wall intersection. To mitigate bar congestion,

Wallace (2007) and Naish (2010) endorsed the use of closely spaced transverse reinforcement along the entire beam span.

In the design of coupled wall/core wall systems, special attention must also be given to the design of the wall piers. In addition to factored gravity load applied to the wall piers, the cumulative shear force exerted on the wall piers by the coupling beams, which act as either upward or downward loads on the wall piers during the lateral deformation as shown in Figure 2.3, must be considered. While the design principles applicable to isolated slender shear walls are also relevant for coupled wall piers, the asymmetrical loading on the coupled wall piers typically necessitates different boundary elements on the interior (the edge of the wall where coupling beams are connected) compared to the exterior boundary elements. Due to the large compression demands at the exterior edge of the coupled walls (where gravity and coupling beam shear demands are additive), the depth of compression is typically large relative to that for isolated walls, and thus, closely spaced transverse reinforcement must be provided over a greater depth. However, at the interior wall edges, a special boundary element may not be required; therefore, less transverse reinforcement may be required relative to an isolated wall with the same gravity stress.

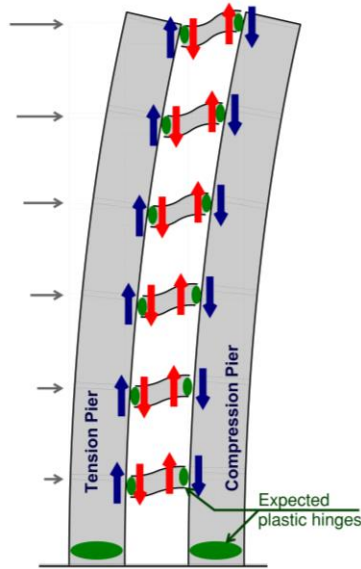


Figure 2.3: Coupled wall deformed shaped; applied axial force from coupling beams on wall piers and expected plastic hinges.

2.2. Design Code Provisions and Guidelines

Similar to isolated cantilevered shear walls, wall piers in a coupled system must be designed for flexural strength, considering the P-M diagram and providing the minimum longitudinal boundary reinforcement. The transverse shear reinforcement in the web shall be designed based on the ASCE 7 loading on the structure amplified by the shear amplification factor recommended in ACI 318-19. At least two layers of web reinforcement, spaced evenly in both horizontal and vertical directions with a minimum ratio of 0.0025 (unless $V_u \leq A_{cv}\lambda\sqrt{f'_c}$) must be provided. To increase the deformation capacity of the system, enhance the compressive stress and strain capacity of the boundary concrete, and minimize the risk of out-of-plane longitudinal bar buckling, ACI requires detailing the boundary elements by providing closely spaced transverse reinforcement in the boundaries.

Diagonally reinforced coupling beams can be conceptualized as a truss with tension and compression diagonals, as illustrated in Figure 2.4. The shear strength of a coupling beam can be ascertained by summing forces in the vertical direction as shown in Figure 2.4, that is: $V_n =$

$2A_{vd}f_y \sin \alpha$. Due to concerns about beam web crushing under elevated shear stresses, ACI 318-19 sets an upper bound on this nominal shear strength at $10A_{cw}\sqrt{f'_c}$. In diagonally reinforced beams, the diagonal truss mechanism simultaneously resists both shear and moment, ensuring equilibrium and meeting the capacity design specifications for shear. The beam nominal moment strength at the wall interface can be deduced by taking moments around the horizontal components of the diagonal bar force, resulting in $M_n = A_{vd}f_yjd \cos \alpha$, where $jd = l_f \tan \alpha$. Hence, shear and moment are related by the following expression: $V_n = M_n/l_f/2$. To prevent diagonal tension (shear) failure, closely spaced transverse reinforcement also is required, but is assumed to not contribute to beam shear strength.

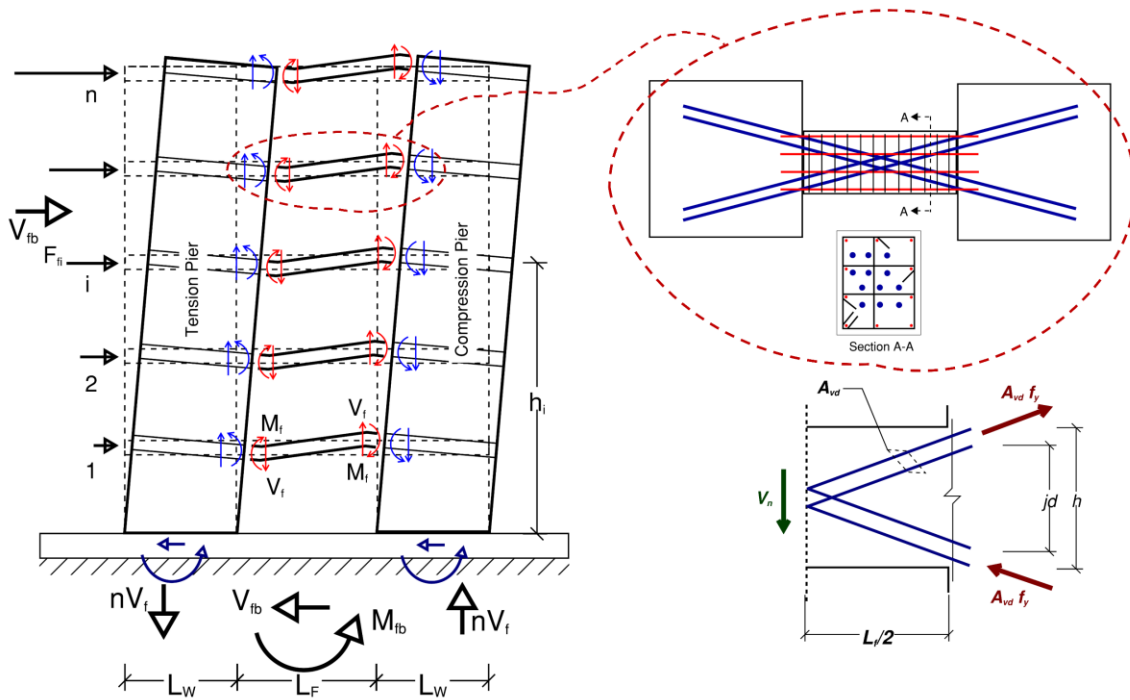


Figure 2.4: deformation of RC coupled wall: plastic hinge formation, framing actions, lateral force variations, and diagonally reinforced coupling beam resisting reactions.

For conventionally reinforced beams, the nominal moment strength (M_n) and the probable moment strength (M_{pr}) is calculated using the same approaches as used for moment frame

beams. Since typical building design is accomplished assuming a rigid in-plane floor diaphragm, it is common practice to ignore any coupling beam axial load on the beam (i.e., assume axial load is zero). This beam shear demand V_e used for design of a conventionally reinforced coupling beam is determined as:

$$V_e = \frac{(M_{pr1} + M_{pr2})}{l_n} + 1.2V_{DL} + 1.0V_{LL} \quad \text{Eq. 2.1}$$

Finally, for modern coupled wall systems design using nonlinear response history analysis, design is usually checked for both a Service Level Earthquake (SLE) and a Maximum Considered Earthquake (MCE) (LATBSDC, 2023). This involves evaluating story drifts, coupling beam rotations, wall shear demands, and checking both the axial compressive strains in shear wall concrete and the axial tensile strains in wall reinforcement against specific acceptance criteria. Different criteria are typically used for yielding regions (well-detailed), where higher strain limits are used, versus at upper levels of core wall (modest or limited detailing), where lower strain or rotation limits are used (LATBSDC, 2023; PEER ATC 72-1, 2010).

The design provisions outlined above have mainly been derived from experimental studies of isolated coupling beams and of coupled walls, as well as analytical studies of prototype buildings. Available research on these topics is summarized in the following sections.

2.3. Isolated Coupling Beam Experimental Studies

Paulay (1991) tested conventionally reinforced coupling beams and noted their limited rotational capacity (refer to Figure 2.5). Later, Paulay and Binney (1974) proposed using diagonal reinforcement in beams with high shear demand to improve their deformation capacity compared to conventionally reinforced beams (refer to Figure 2.6). This method aimed to reduce structural damage by increasing the energy absorbed by coupling beams, as shown by the area within the hysteretic loops. They reported that this new design excelled in several aspects, enhancing ductility, slowing the rate of strength degradation, and significantly reducing shear sliding failures.

However, the design had its drawbacks, with buckling of the compression bars emerging as a primary failure mode. These findings were later verified by researchers like Santhakumar in 1974, who confirmed that diagonal reinforcement significantly increased beam ductility.

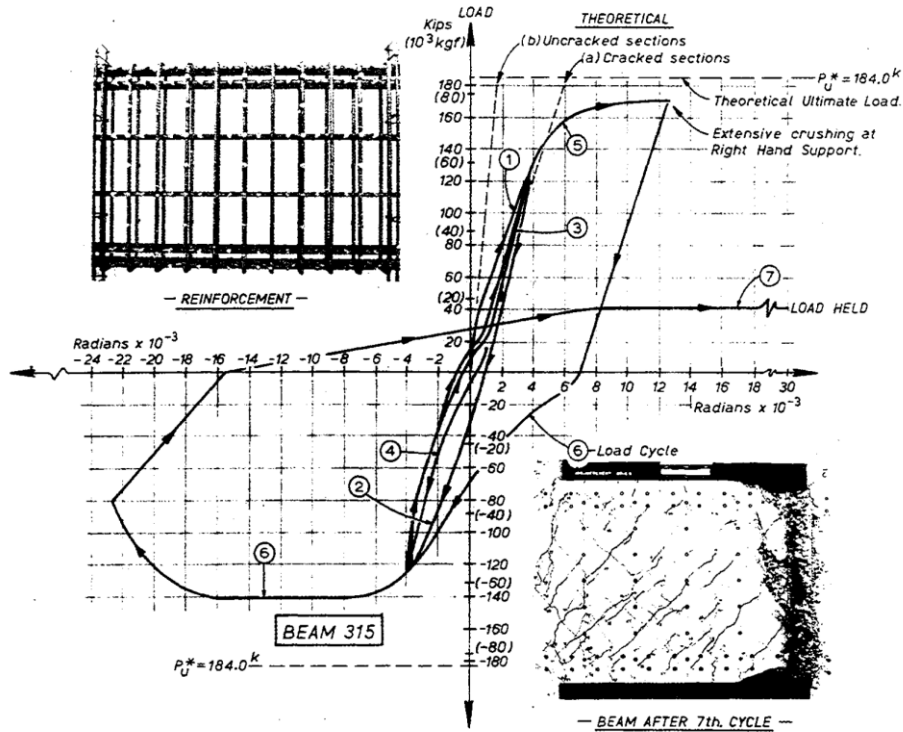


Figure 2.5: Paulay T. 1971 load-rotation relationship for a conventional coupling beam.

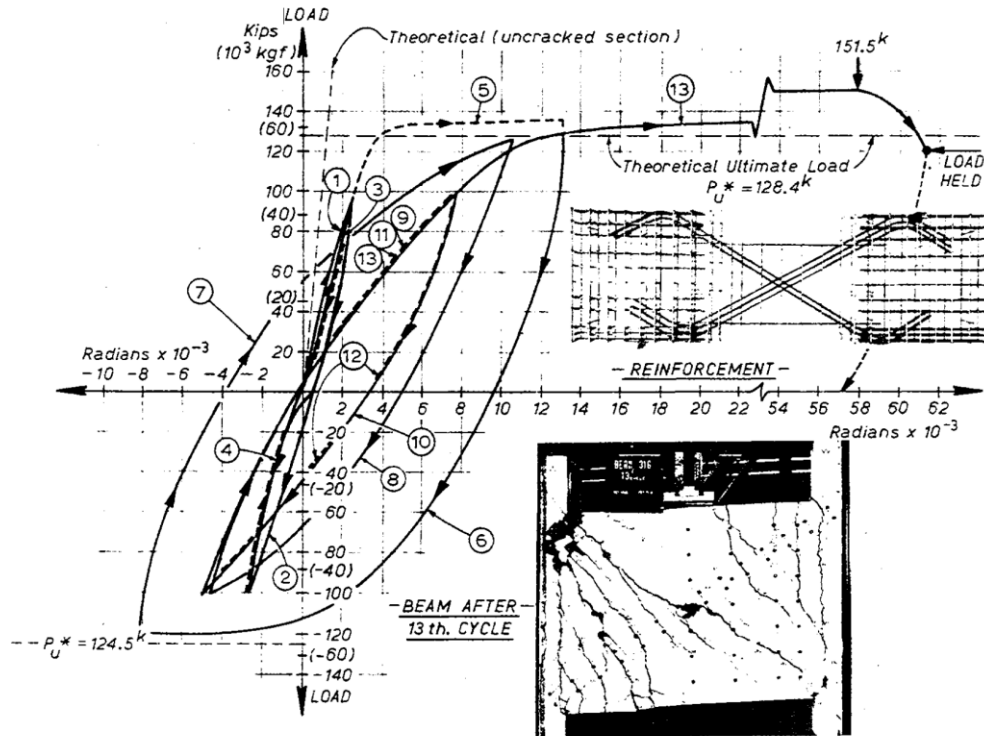


Figure 2.6: Paulay T. and Binney J.R. Load-rotation relationship for diagonally reinforced coupling beam (beam 316).

Since 1974, numerous researchers have explored the concept of using diagonal reinforcement in deep beams with higher shear demands. The goals of these various research programs were diverse, including: conducting detailed experimental programs to investigate beam behavior with various reinforcement patterns, evaluating the different confinement options (confining diagonal bundles versus confining the entire beam section), evaluating the effects of different span-to-depth ratios, and understanding the influence of various concrete strengths and steel properties. The primary focus was to enhance the basic performance and rotational capacity of the beams. Simultaneously, some researchers investigated the use of advanced materials, such as fiber-reinforced concrete, to prevent surface damage under high deformation demands. Results from some of these studies are summarized in the following paragraphs.

Following the studies conducted in the 1970's, researchers such as Barney et al. (1980) and Tassios et al. (1996) tested conventionally reinforced coupling beams with aspect ratios ranging from 2.5 to 5.0 and showed that displacement ductility ranging from 7.8 to 10.0 could be achieved, respectively. Galano and Vignoli (2000) examined 15 different test specimens to assess how shear reinforcement designs affect rotational ductility, with volumetric shear reinforcement ranging from 0.0031 to 0.0039. They found that increasing the confinement reinforcement could increase the displacement ductility of beams, with values ranging from 5.0 to 7.0. Adebar et al. in 2001 studied the complex behavior of axially restrained coupling beams and identified that restraint produced large compression, more than $0.3A_g f'_c$, leading from concrete crushing to reinforcement buckling and reduced the deformation capacity relative to no axial restraint.

Kwan and Zhao (2002) investigated deep coupling beams subjected to cyclic loading. They tested five one-half scale conventionally reinforced coupling beams with aspect ratios between 1.17 to 2.00. Test results demonstrated increasing displacement ductility with increasing aspect ratio (from 4.0 to 6.0, respectively) and with decreasing shear stress (from $9.25\sqrt{f'_c}$ to $6.15\sqrt{f'_c}$, respectively).

In 2008, Fortney et al. explored how the transverse reinforcement ratio, which confines the diagonal bundles, affects coupling beam behavior by significantly preventing the compression bundle from buckling. Although a higher transverse reinforcement ratio improved beam ductility, it complicated construction of the rebar cages and concrete placement. Naish et al., in 2013, demonstrated that beams with full-section confinement performed better or at least as well as those with only diagonal confinement. In 2016, Lim et al. proposed a new design approach, suggesting that existing methods, like those in ACI 318-14, might overestimate the strength of beams.

These studies of isolated coupling beams have produced substantial information that has been used to develop provisions for the design of new buildings (ACI 318-19) and the evaluation and

retrofit of existing buildings (ASCE 41-17). Design requirements for a coupled wall system are more complex and are discussed in the following section.

2.4. Coupled Wall System Experimental Studies

Since the mid-1970s, after introducing diagonal reinforcement in coupling beams, engineers have studied the overall behavior of coupled wall structures. These comprehensive studies have revealed a lot about how these walls deform and collapse under various conditions. Notably, they have found that beams with diagonal reinforcement are more flexible than those with traditional reinforcement. This research has also illuminated how shear forces are transferred between wall piers under tension and compression demands during earthquakes. It has additionally highlighted the potential issues with excessive compression force, particularly when the walls are interconnected by disproportionately stiff coupling beams. To address all these uncertainties associated with coupled wall systems, numerous experimental and analytical studies have been conducted on these systems.

In 1974, Santhakumar tested two reinforced concrete coupled wall systems, each with differently reinforced coupling beams, under reversed cyclic lateral loading. As depicted in Figure 2.7, wall system A used conventionally reinforced concrete beams, while wall system B employed diagonally reinforced beams. Both systems had identical reinforcement in their wall piers.

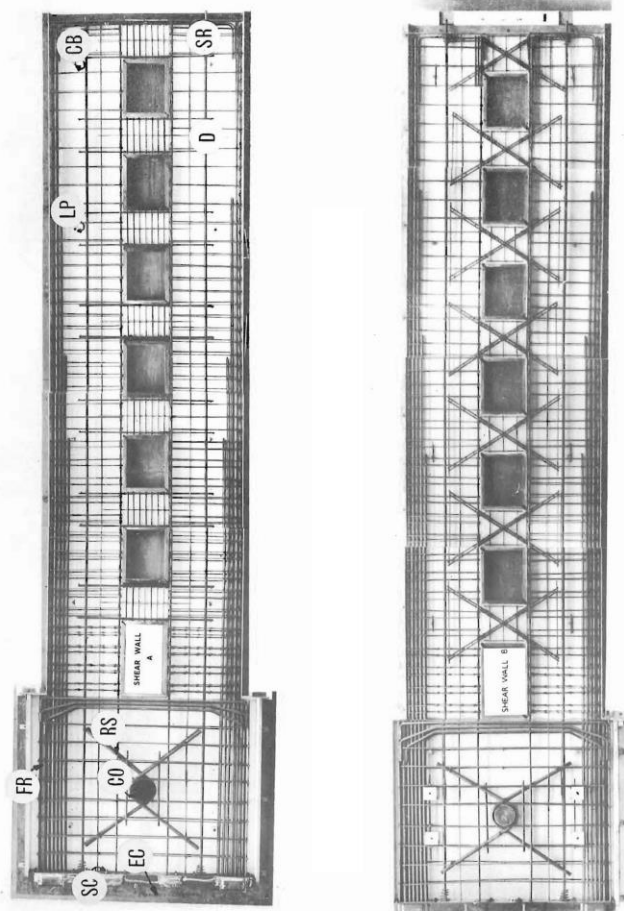


Figure 2.7: Reinforcement configuration of Santhakumar's (1974) 7-story coupled wall system specimens; left shows Wall A with a conventional reinforced coupling beam, right shows Wall B with a diagonally reinforced coupling beam.

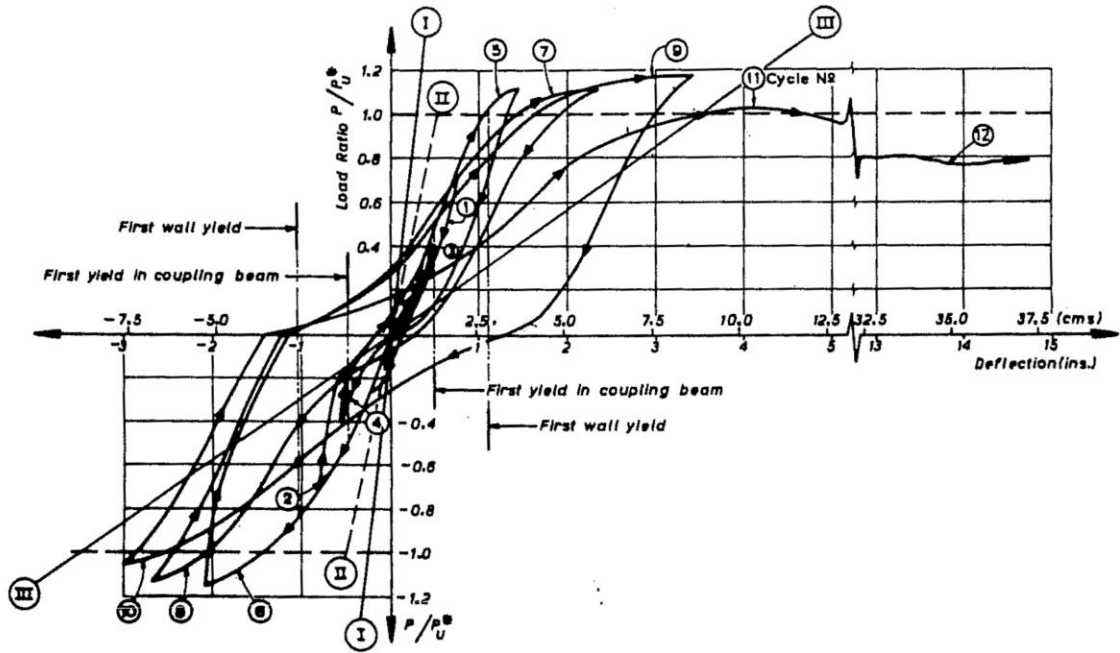


Figure 2.8: Load-deformation of the wall specimen A; Santhakumar (1974).

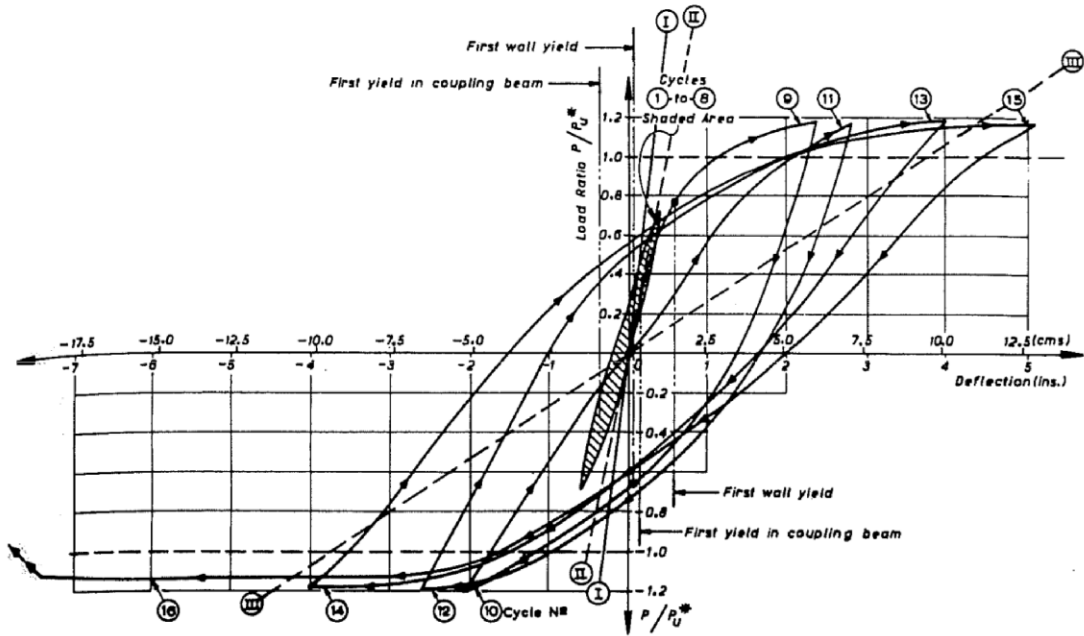


Figure 2.9: Load-deformation of the wall specimen B; Santhakumar (1974).

Santhakumar observed that the shear wall pier carrying axial tension in wall A showed a significant reduction in capacity, evident from the less steep diagonal cracks after reversed cyclic loading. The compression wall pier bore a much larger portion of the total lateral load. System wall B, with diagonally reinforced coupling beams, dissipated much more energy than wall system A. The lateral load versus roof deformation relations, shown in Figures 2.8 and 2.9, indicate that the differing behaviors of the two wall systems are attributed to their beam reinforcement layouts. The pinching seen in the hysteresis loops of wall A stems from the cyclic behavior of the conventionally reinforced coupling beams. In contrast, the diagonal bars in wall B's beams led to an increased capacity for energy dissipation. The hysteresis loops of wall B demonstrate higher ductility without loss of strength compared to wall A.

Subsequent research featured two six-story coupled walls, scaled down by one-third from the prototype building, with a focus on the shear capacity of conventionally reinforced coupling beams (Shiu et al. 1981). A segment of the floor slab was integrated into these tests, primarily to offer a base for exerting cyclic pushover forces onto the samples. Findings by Shiu et al. (1981) indicated that the test specimen response was influenced by the stiffness of the coupling beams. Observations highlighted that, in cases of weaker wall coupling, following formation of plastic hinges in the coupling beams, the walls responded similar to two isolated walls.

In a separate study, two 4-story coupled wall segments representing the first 4 levels of a 15-story benchmark building were tested by Ozselcuk (1990). The objectives of this study were to evaluate shear demands in coupled wall with barbell-shaped cross sections, assess the behavior of boundary columns, and investigate the behavior of the tension and compression piers. Drawing from the experimental data, the study showed that the variation in axial force on the tension and compression piers led to significant variation in pier stiffness and resulted a much larger shear demand in the compression pier relative to the tension pier. Furthermore, a noticeable trend was that amplifying the strength of the coupling beam led to a proportionate increase in damage to the wall piers. Thus, the study's ultimate takeaway was the recommendation to cap the strength of

coupling beams in relation to the strength of the wall pier, ensuring that the compression wall retained appropriate ductility.

Another significant investigation into coupled wall systems was spearheaded by the US-Japan collaborative in 1996. They executed a quasi-static cyclic test on a one-third scale model of a twelve-story reinforced concrete coupled wall system. This monumental test was performed at the Building Research Institute (BRI), and the primary objective was to understand the transfer of shear forces between the tension and compression wall piers of such structural configurations. Notably, this test set itself apart by employing load cells within the coupling beams to track the axial load transfer between the coupling beams and the affiliated wall piers. The specimen was subjected to constant axial loads and incremental quasi-static cyclic lateral loads at various floor levels. One major takeaway was the confirmation that the coupled wall system could achieve large nonlinear deformations prior to reaching the point of failure. The specimen is described in greater detail in Chapters 4 and 5 and is used to validate the numerical models utilized in this study.

Further advancing the field's understanding, in 2005, a unique testing event took place at the LNEC laboratory in Lisbon, Portugal. Researchers closely observed a 5-story reinforced concrete coupled wall system, which featured a 3.15 inches thick slab on each level. When the system was exposed to a series of triaxial ground motions, some crucial observations were made. For instance, after the fourth ground motion, minimal cracking was observed in the wall flanges. However, by the time the system encountered the sixth and most intense ground motion, more severe damage was witnessed. The wall web experienced a distinct diagonal shear failure, leading to a "punching" effect through a portion of the flange. Additionally, multiple horizontal bars in the web fractured, and one edge of the flange suffered vertical crushing. Despite these damages and the high degree of coupling, the coupling beams astonishingly remained intact and exhibited no damage.

Another vital contribution to the knowledge pool came in 2013, when Lehman et al. undertook testing on a three-story coupled wall that represented the first three stories of a ten-story building. Demands from the upper floors were simulated and applied to the top of the third floor. A sudden and unexpected failure was recorded at a drift of 2.27%, where the compression wall pier experienced significant damage. The exact nature of the damage was a combined effect of concrete core disintegration and bar buckling, leading to a marked reduction in strength. A notable observation was the sequence in which different parts of the wall yielded. Initially, the second and third story coupling beams gave way, followed by the wall piers. Lastly, the first story coupling beam buckled under the pressure. Intriguingly, this wasn't the anticipated sequence.

A PEER report was released in 2014 where researchers Lu, Panagiotou, and Koutromanos presented their findings on member forces using a three-dimensional Beam-Truss Model (BTM) designed for RC coupled wall systems. Initially, their calculations determined the shear transferred by a single coupling beam to be 11.7 kips, not factoring in the slab. When considering the slab's strength, they based their calculations on an assumption: the effective flange width was 8 times the slab's thickness, equivalent to 52.8 inches. This assumption yielded a notable increase in shear transfer, rising to 49.2 kips. When the slab's contribution was taken into account, the base shear attributed to the lowest coupling beam was found to be 32.8 kips as opposed to 8.5 kips. Interestingly, even with these variables, the wall's compression pier had its base shear due to coupling surpassing the product of the nominal moment and the effective height. This observation solidified the understanding that the wall piers exhibit a high degree of coupling. This conclusion is in line with earlier research, such as that conducted by Aktan & Bertero (1984), where it was noted that the compression wall pier resists majority of shear force at the building's base.

2.5. Axial Restraint of Coupling Beams

Previous studies on coupling beams/coupled walls have primarily focused on aspects such as reinforcement configuration, aspect ratio, and reinforcement ratio. However, relatively few studies have investigated the effects of axial restraint on the lateral strength, stiffness, and deformation capacities of coupling beams. Like most concrete elements, cyclic deformation causes the rebars to lengthen, leading to axial growth in the element. Additionally, since coupling beams are positioned between two shear walls and often have slabs on top, they experience some level of axial restraint. This restraint increases the axial force on the coupling beam, which increases the moment capacity of the beam, leading to higher shear demands. This axial restraint is significant in terms of the variation in axial force on the wall piers (which comes from coupling beam shear strength) and the subsequent load transferred to the foundation.

Tegos and Penelis (1988) conducted a study on 24 coupling beam specimens, mainly testing them under a constant axial force. Comparing specimens XX1 and XX11 — which were similar except for the axial force applied using oil jacks at the ends — XX1 was subjected to a force of 53.9 kips, while XX11 had no axial load. Their findings indicated that beams under axial force had about a 45% increase in shear strength, but with reduced deformation capacity.

In 2000, Galano and Vignoli tested sixteen coupling beams under complete axial restraint, using two rollers at the beam ends to prevent axial elongation. The degree of axial restraint was the same for all specimens in this study. It was noted that the compressive strength of the concrete had a significant effect on the capacity of the diagonally reinforced specimens, with lower compressive strength specimens suffering compressive strut instability.

Adebar et al., in a 2001 study, examined the effects of axial restraint on a single diagonally reinforced coupling beam. He used two Dywidag rods along the beam's sides for axial restraint. The key finding was that the beam failed due to concrete crushing and reinforcement buckling.

In 2013, Naish et al. tested eight coupling beam specimens to understand their behavior under various conditions. They designed a setup to maintain neutral axial force using two vertical actuators but also investigated the effect of a slab on the beams. This slab could cause axial restraint in the beam. Their analysis showed that the presence of a slab altered the beam's behavior, limiting its axial elongation and increasing its shear strength by an estimated 20%.

In a recent study, Poudel (2018) tested a coupling beam specimen under axial restraint and compared it to a similar beam studied by Ameen in 2017 without axial restraint. Poudel used a high strength threaded rod to connect the top and bottom blocks of the specimen on each side, a method similar to what Adebar et al. used in their 2001 experiment. The results showed that the beam with axial restraint had about a 30% increase in shear strength. However, this beam's ability to deform was reduced by approximately 3%, 10%, or 13%, depending on which definition of deformation capacity Poudel used.

2.6. Existing Coupling Beam Analytical Models

Due to the high costs associated with analyzing, preparing, and processing detailed microscopic models in structural and earthquake engineering, many professionals prefer to use more cost-effective and practical macroscopic models rather than complex and expensive Finite Element Models (FEM). The main two types of macroscopic models are generally divided into two categories: "lumped plasticity" and "distributed plasticity". The next section provides a summary of the common coupling beam models found in academic research.

2.6.1. Lumped Plasticity Models

Lumped plasticity models are effective in clearly representing load-deformation characteristics, as well as reloading/unloading and pinching behaviors, as outlined in standards like ASCE 41 or based on experimental results (e.g., Paulay and Priestley 1992). This modeling approach uses rotational hinges at the ends of elements, and sometimes includes a shear hinge at the midpoint

(refer to Figure 2.10), as shown in study by Naish et al. (2013). These hinges, essentially zero-length springs, represent the nonlinear behavior of the components based on a predefined backbone curve. However, the lateral response of these hinges is separate from the axial movements within the beam. Modern standards attempt to consider the effect of axial forces on lateral behavior by categorizing beam behavior based on axial load assessments, but this approach has two main drawbacks. First, the analyst needs to estimate the average axial force in the coupling beam before the analysis. Second, this model does not account for the axial growth of the component.

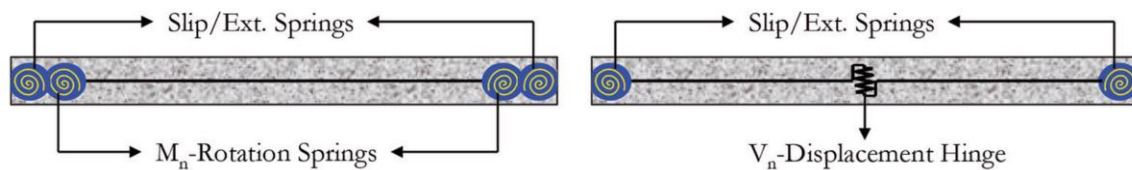


Figure 2.10: Lumped plasticity models used to simulate coupling beams; left) two rotational hinges at each end to simulate beam nonlinearity and slip-extension, right) shear hinge in the middle of the element to simulate beam nonlinearity and rotational hinges at the ends to simulate slip-extension behavior (Naish et al., 2013).

2.6.2. Distributed Plasticity Models

Fiber-based models provide a method to consider how plasticity is distributed both across and along a beam's cross-section. These models are based on traditional displacement-based methods, as shown in research by Hellesland and Scordelis (1981) and Marí (1984), or on newer force-based methods, like those by Spacone et al. (1996) and Neuenhofer and Filippou (1997). A key assumption of fiber-based models is that fibers are aligned straight along the beam's centerline, usually not including diagonal fiber arrangements.

A newer approach in this area is the Beam-Truss Model (BTM), developed by Lu and Panagiotou (see Figure 2.11). The BTM represents reinforced concrete elements using a combination of vertical, horizontal, and diagonal parts. The steel bars and concrete are represented by the

vertical and horizontal components, while the diagonal trusses simulate the diagonal tension/compression in concrete. However, a major challenge with this model is determining the best angle for the diagonal components, as this angle greatly affects the coupling beam's shear capacity. For more information on the impact of diagonal angles and advice on choosing them, one can look at the research of Lu and Panagiotou (2016).

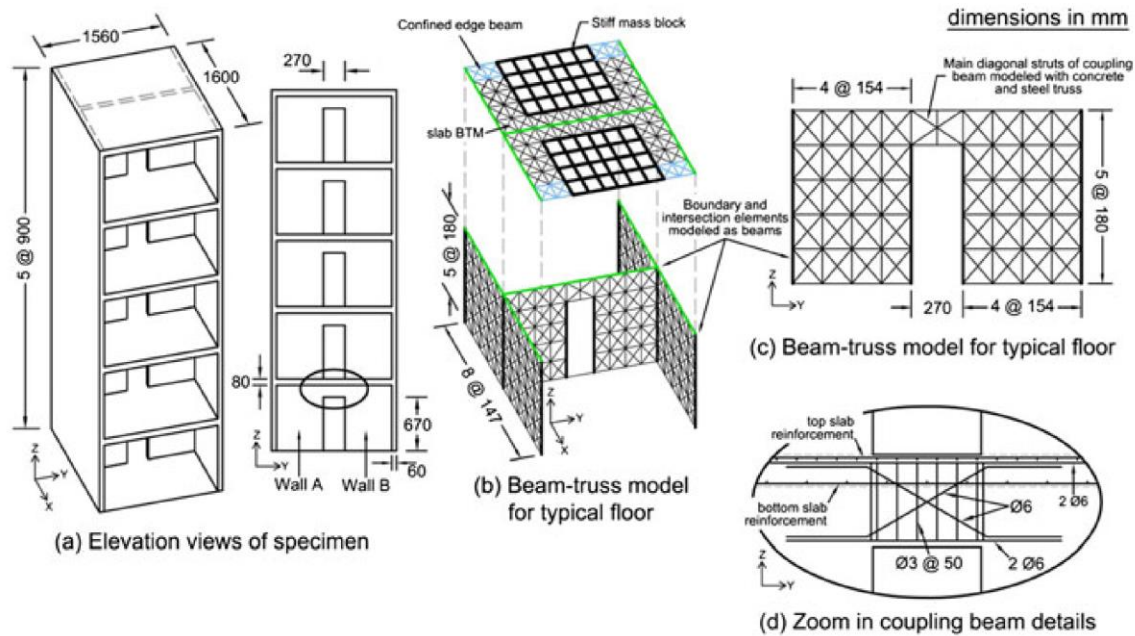


Figure 2.11: BTM model used to simulate walls and coupling beams (Lu and Panagiotou, 2016).

2.6.3. Shortcoming of Current Macroscopic Models

Most macroscopic models for simulating reinforced concrete (RC) coupling beams do not adequately consider the interaction between axial and lateral forces. Fiber-based models, while allowing fiber placement along the centerline of the element, may not be ideal for coupling beams with diagonal reinforcement due to their specific design. The Beam-Truss Model (BTM) was created to better represent these beams, but it faces challenges, including extensive preparatory modeling and related uncertainties, which make it less suitable for regular use. Additionally, research like Naish's study in 2013 has emphasized the significant impact that slip-extension

between wall piers and coupling beams can have on the beams' lateral behavior. This aspect is not effectively addressed by any of the models discussed so far.

2.7. Motivation and the Need for Proposed Coupling Beam Analytical Model

Comprehensive evaluations of earthquake data and experimental results clearly show that axial restraint, mainly from floor slabs and adjacent wall piers, effects coupling beam behavior. It is also clear that wall piers under compression carry much of the load when it comes to shear demand.

In modeling, many macroscopic models designed for reinforced concrete (RC) coupling beams don't fully capture the complex balance between axial and lateral forces. Fiber-based models, which align fibers with the center of the element, may not be ideal for coupling beams with diagonal reinforcement due to their unique implemented features. The Beam-Truss Model (BTM) was introduced to address these types of beams, but it comes with its own difficulties, including intensive initial modeling and related uncertainties, making it less practical for regular use in earthquake-structural engineering. Furthermore, studies like Naish's in 2013 have pointed out the significant role of the interaction between wall piers and coupling beams in the beams' lateral behavior, a factor not fully represented in most current models.

Recent research, like that by Rojas et al. 2023, has introduced new ways to understand the shear strength of RC shear walls. While the traditional ACI formula focused mainly on concrete shape and shear reinforcement for about seventy years, new approaches look beyond these factors. They consider the effects of axial loads, the importance of longitudinal tension reinforcements, and the behavior of the compressed flange.

With these advancements in understanding seismic structural behavior, there's a growing need to update the designs of coupled or core walls. Using these new numerical models allows for more accurate sharing of shear force between wall piers, leading to better-informed designs. The

goal of these modern methods is to help create buildings that use materials efficiently and are more resilient in earthquakes. This chapter shows that, despite significant progress, complexities in RC coupling beam dynamics still exist. The interplay between axial and lateral forces and the relationship between wall piers and coupling beams require further reevaluation. As this chapter ends, upcoming chapters promise to explore innovative modeling techniques aiming to bridge existing gaps and enhance structural resilience in the face of seismic challenges.

3. MODEL DESCRIPTION

The proposed analytical model includes four main components: fiber-based reinforced concrete (RC) sub-elements, diagonal trusses, rigid connectors (handles), and end-sections known as slip-extension zero-length sections (Figure 3.1). The reinforced concrete coupling beam is conceptualized as a series of n segments, placed side-by-side, along the span of the coupling beam. Each segment consists of a concrete element represented by longitudinal fiber elements, and the two bundles of diagonal reinforcement are simulated using truss elements. At the end of each segment, trusses are connected to the concrete section through rigid elements to impose deformation compatibility.

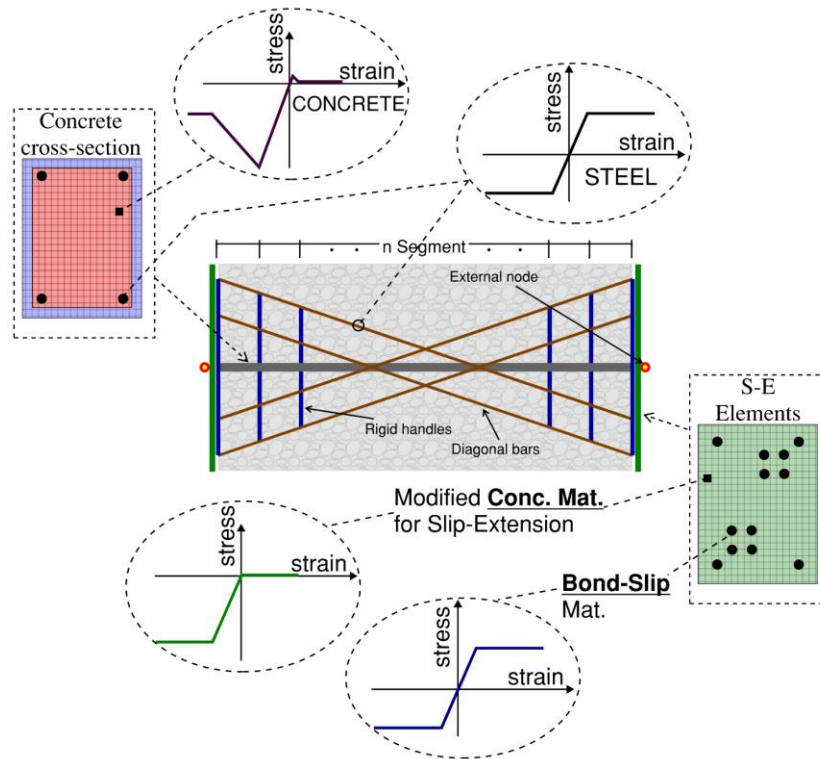


Figure 3.1: CBeam element constitutive components.

The RC sub-elements may include longitudinal reinforcement, but they exclude the diagonal reinforcement. The RC sub-elements are used to capture the geometry of the coupling beam

along the span and to impose deformation compatibility within each element. The number of segments (n) used is a variable; the sensitivity of the model to the number of segments used is assessed in Chapter 5 to develop a recommendation for the number of segments required to achieve reliable results.

Diagonal bundles of reinforcement is modeled separately using diagonal bars at the centroid of the bundle. The area of each truss element represents the total area of the diagonal reinforcement in each bundle (Figure 3.1). The diagonal bars are connected to the RC section using rigid vertical elements. The cyclic behavior of the diagonal bars is under loading and unloading is derived from the constitutive steel material relations.

The remainder of this chapter provides detailed information on the CBeam analytical model, including a thorough discussion of each component of the model and the model parameters, including the recommended material models.

3.1. Fiber-Based Concrete Model

The stiffness matrix of the overall element is assembled from the various components. The stiffness matrix of the fiber cross-section is:

$$K_s = \begin{bmatrix} \sum_{i=1}^n A_i E_i & -\sum_{i=1}^n y_i A_i E_i & \sum_{i=1}^n z_i A_i E_i & \sum_{i=1}^n p_i^2 A_i E_i \\ -\sum_{i=1}^n y_i A_i E_i & \sum_{i=1}^n y_i^2 A_i E_i & -\sum_{i=1}^n y_i z_i A_i E_i & -\sum_{i=1}^n p_i^2 y_i A_i E_i \\ \sum_{i=1}^n z_i A_i E_i & -\sum_{i=1}^n y_i z_i A_i E_i & \sum_{i=1}^n z_i^2 A_i E_i & \sum_{i=1}^n p_i^2 z_i A_i E_i \\ \sum_{i=1}^n p_i^2 A_i E_i & -\sum_{i=1}^n p_i^2 y_i A_i E_i & \sum_{i=1}^n p_i^2 z_i A_i E_i & \sum_{i=1}^n p_i^4 A_i E_i \end{bmatrix} \quad \text{Eq. 3.1}$$

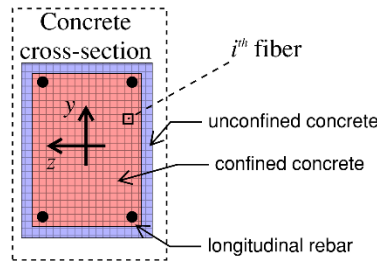


Figure 3.2: reinforced concrete fiber cross-section.

Where n refers to the number of fibers, A_i is the area of the i^{th} fiber, E_i is the Young's modulus associated with the fiber material, and y_i and z_i represent the y and z coordinates of the fibers from a reference point, respectively. The value of p is determined as:

$$p = \sqrt{(y - y_s)^2 + (z - z_s)^2} \quad \text{Eq. 3.2}$$

The stiffness matrix for the cross section is assembled by integrating it over the length of the element using the local element orientation (with the local x -axis assumed along the length of the element). Once the stiffness matrix is assembled, a trivial deformation are applied to obtain the force vector from the internal forces derived from the stress-strain relationship of the constitutive materials assigned to each fiber. The deformations obtained by applying the internal forces from the fibers is then checked to verify that the deformations obtained are equal to, within a tolerance, the trivial deformations initially applied to obtain strains in the fibers (a process known as a convergence test). If convergence is not achieved in each step of loading, it is necessary to go back and update the positions and rotations (trivial deformations) at the nodes, repeating the process until the convergence requirements are met.

For a more comprehensive understanding of these basic concepts and their application, particularly in the context of displacement-based fiber sections, a review of the studies by Taucer et al. (1991) and Du and Hajjar (2021) is recommended.

3.2. Diagonal Reinforcement

In the model, diagonal truss elements are utilized to represent diagonal bars in the coupling beam. The axial stiffness of the truss bars representing the diagonal bundle or bars is decomposed into components along the x and y local axes and combined with the stiffness matrix of the concrete element. Note that, as the diagonal rebars are angled relative to the concrete element, the distance used to obtain the rotational stiffness associated with the diagonal trusses at the beginning and end of each segment are not the same.

3.3. Slip/Extension

Various studies, e.g., Elwood and Eberhard, 2009; Naish et al., 2013, have highlighted that 'slip-extension' behavior at the column-joint and beam-wall interfaces, respectively, can significantly reduce the effective stiffness of reinforced concrete structural elements. For coupling beams, Naish et al. (2013) reported that slip-extension contributed approximately 40 to 50% of the total beam rotation at yield strength. To accurately represent this behavior in the model, two zero-length contact elements are introduced, one at each end (beam-wall interface). The geometry of these zero-length segments are selected to match the coupling beam cross-section (as shown in Figure 3.1); however, different material relations are used to capture the slip-extension behavior.

This modification on the material properties used for the contact element are based on the research conducted by Zhao and Sritharan in 2007. The concrete compressive strength is assigned a value of $0.8f'_{cc}$ of the confined concrete and strength degradation is not considered. For the reinforcement in the contact elements, the "Bond_SP01" stress-strain material model from OpenSees is utilized because it is capable of representing the complex interaction between concrete and the reinforcement material relations. Details of the calibration process for these material relations are provided in the following sections.

3.4. Constitutive material models

The CBeam model is based on a distributed plasticity model; therefore, it directly utilizes material models to predict the behavior of the element. In this regard, understanding the constitutive material behavior and appropriately calibrating the material models to accurately simulate the load versus deformation behavior of coupling beams. Also, since the model is implemented in the OpenSees computational platform, the following sections provide an in-depth assessment of the

material models used for steel, concrete, and bond-slip and the calibration and use of the material models in the CBeam model.

3.4.1. Steel Reinforcement Constitutive Material Model

The behavior of reinforcing steel is described using the stress-strain equation originally developed by Chang and Mander in 1994 and is available in the OpenSees material library as “ReinforcingSteel”. This model accounts for changes in bar area and transitions from engineering stress-strain to a true stress-strain relationship. The model is based on ten key equations and addresses both tension and compression behavior, thus providing the capability to individually control the tension and compression branches of the model.

The model adjusts and resizes the monotonic stress-strain backbone to represent strength degradation during loading and unloading. It uses empirical equations to generate material behavior and was originally calibrated using coefficients based on Panthaki's 1991 study of on the behavior of reinforcement embedded in concrete.

The tension branch of the stress-strain relationship is defined as:

$$f_s = \frac{E_s \varepsilon_{ss}}{\left[1 + \left(\frac{E_s \varepsilon_{ss}}{f_y^+}\right)^{10}\right]^{0.1}} + \frac{\text{sign}(\varepsilon_{ss} - \varepsilon_{sh}^+) + 1}{2} (f_{su}^+ - f_y^+) \left[1 - \left|\frac{\varepsilon_{su}^+ - \varepsilon_{ss}}{\varepsilon_{su}^+ - \varepsilon_{sh}^+}\right|^{p^+}\right] \quad \text{Eq. 3.3}$$

$$E_t = \frac{E_s}{\left[1 + \left(\frac{E_s \varepsilon_{ss}}{f_y^+}\right)^{10}\right]^{1.1}} + \frac{\text{sign}(\varepsilon_{ss} - \varepsilon_{sh}^+) + 1}{2} \text{sign}(\varepsilon_{su}^+ - \varepsilon_{ss}) E_{sh}^+ \left[1 - \left|\frac{f_{su}^+ - f_s}{f_{su}^+ - f_y^+}\right|^{\frac{p^+ - 1}{p^+}}\right] \quad \text{Eq. 3.4}$$

where:

$$\varepsilon_{ss} = \varepsilon_s - \varepsilon_{om}^+ \quad \text{Eq. 3.5}$$

$$p^+ = E_{sh}^+ \frac{\varepsilon_{su}^+ - \varepsilon_{sh}^+}{f_{su}^+ - f_y^+} \quad \text{Eq. 3.6}$$

ε_{om}^+ is strain in which the stress is zero and considered and the relax tension strain in the positive branch, see Figure 3.3.

Similar to the tension branch, the compression branch could be formulated as below:

$$f_s = \frac{E_s \varepsilon_{ss}}{\left[1 + \left(\frac{E_s \varepsilon_{ss}}{f_y}\right)^{10}\right]^{0.1}} + \frac{\text{sign}(\varepsilon_{sh}^- - \varepsilon_{ss}) + 1}{2} (f_{su}^- - f_y^-) \left[1 - \left|\frac{\varepsilon_{su}^- - \varepsilon_{ss}}{\varepsilon_{su}^- - \varepsilon_{sh}^-}\right|^{p^+}\right] \quad \text{Eq. 3.7}$$

$$E_t = \frac{E_s}{\left[1 + \left(\frac{E_s \varepsilon_{ss}}{f_y}\right)^{10}\right]^{1.1}} + \frac{\text{sign}(\varepsilon_{sh}^- - \varepsilon_{ss}) + 1}{2} \text{sign}(\varepsilon_{ss} - \varepsilon_{su}^-) E_{sh}^- \left[1 - \left|\frac{f_{su}^- - f_s}{f_{su}^- - f_y^-}\right|^{\frac{p^- - 1}{p^-}}\right] \quad \text{Eq. 3.8}$$

With these definitions:

$$\varepsilon_{ss} = \varepsilon_s - \varepsilon_{om}^- \quad \text{Eq. 3.9}$$

$$p^- = E_{sh}^- \frac{\varepsilon_{su}^- - \varepsilon_{sh}^-}{f_{su}^- - f_y^-} \quad \text{Eq. 3.10}$$

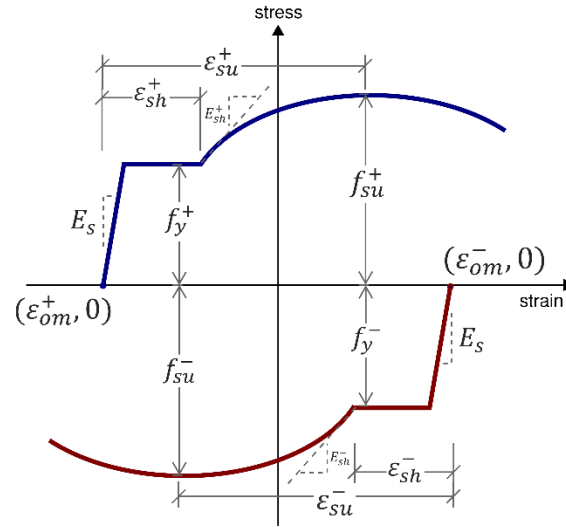


Figure 3.3: uniaxial, tension-compression behavior of ReinforcingSteel material.

The ReinforcingSteel material model also adopts the Gomes and Appleton 1997 approach to incorporate buckling behavior into the compression branch, as shown in Figure 3.4.a. This approach involves internally calculating the buckling stress based on the inputs from the user and then overwriting the compression branch of the Chang and Mander model using a reduced profile. The model also includes the effects of low-cyclic fatigue on top of the basic stress-strain relationship obtained from Chang and Mander, as shown in **Error! Reference source not found..b**. It uses the Coffin-Manson (Uriz and Mahin, 2008) relationship, which establishes a linear

link between the logarithm of the number of repeated cycles until failure (N_f) and the logarithm of the strain experienced in each cycle (ε_i). The low-cyclic fatigue relationship is:

$$\varepsilon_i = \varepsilon_0(N_f)^m \quad \text{Eq. 3.11}$$

where, ε_i is the strain in each cycle, and ε_0 is the strain at which a new material would fail in just one cycle. The variable 'm' captures how the total strain affects the number of cycles until failure. However, this method can be complex, especially in earthquake engineering where the peak values reached in each cycle are typically different and counting the number of cycles is difficult (or complicated). Therefore, the CBeam model uses a modified version of the traditional rainflow cycle counting method to better fit the specific needs of this model. Detailed information on how fatigue is included in the Reinforcing material stress-strain relationship is provided in Uriz and S.A. Mahin, 2008.

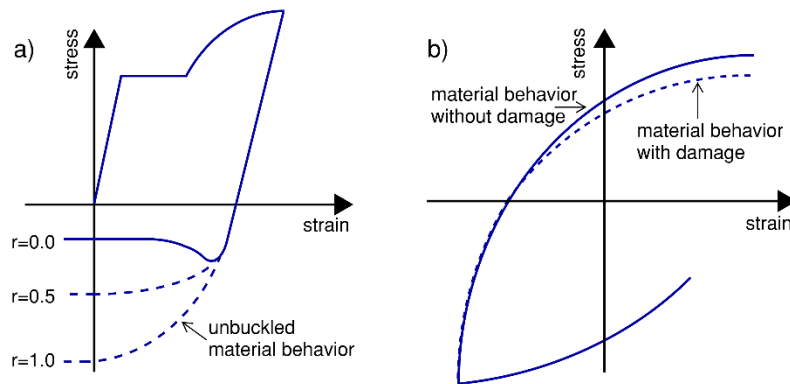


Figure 3.4: a) buckling behavior at steel material level; b) steel material low-cyclic fatigue behavior.

The low-cyclic fatigue formula implemented in OpenSees is the same as explained above but with a different notation: $\varepsilon_a = \beta(2N_f)^a$. In this formula, ε_0 and m from the earlier equation are similar to $\beta \times 2^a$ and a , respectively. Dhakal and Maekawa (2002) developed alternative equations to study low-cyclic fatigue in materials used for reinforcing steel:

$$\begin{cases} \lambda = \frac{L}{D} \sqrt{\frac{f_y}{100}} \\ \beta = \frac{-\lambda}{350} + 0.2 \\ a = -\left(\frac{\lambda}{1200} + 0.441\right) \end{cases} \quad \text{Eq. 3.12}$$

3.4.2. Concrete Constitutive Material Model

The concrete constitutive material model selected for use in the CBeam model is "Concrete02" from the OpenSees material library. Its stress-strain relationship is based on the uniaxial hysteretic model for concrete developed by Yassin in 1994. The monotonic envelope of the model follows the stress-strain relationship from Kent and Park (1971), which was later modified by Scott, Park, and Priestley (1982). Even though more accurate and comprehensive models for concrete stress-strain relationships have been developed, the modified Kent and Park model is widely used in both practical applications and research because it strikes a good balance between simplicity, accuracy, and computational efficiency.

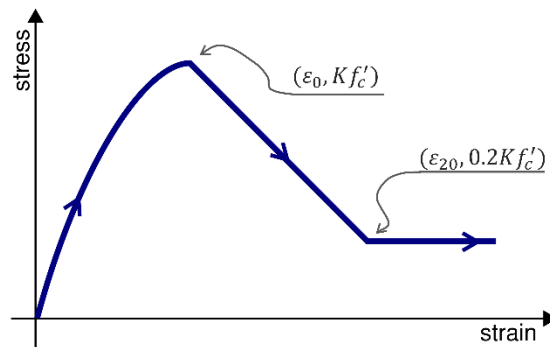


Figure 3.5: Compression backbone of modified Kent & Park concrete model (1982).

In the adapted Kent and Park model (Figure 3.5), the monotonic concrete stress-strain ($\sigma_c - \epsilon_c$) relationship in compression is characterized by three distinct regions. Following the standard where compression is considered positive in concrete, these three regions are identified as:

$$\begin{cases} \varepsilon_c \leq \varepsilon_0 & \sigma_c = Kf'_c \left[2 \left(\frac{\varepsilon_c}{\varepsilon_0} \right) - \left(\frac{\varepsilon_c}{\varepsilon_0} \right)^2 \right] \\ \varepsilon_0 < \varepsilon_c \leq \varepsilon_{20} & \sigma_c = Kf'_c [1 - Z(\varepsilon_c - \varepsilon_0)] \\ \varepsilon_c > \varepsilon_{20} & \sigma_c = 0.2Kf'_c \end{cases} \quad \text{Eq. 3.13}$$

The corresponding tangent moduli (E_t) are expressed by:

$$\begin{cases} \varepsilon_c \leq \varepsilon_0 & E_t = \frac{2Kf'_c}{\varepsilon_0} \left(1 - \frac{\varepsilon_c}{\varepsilon_0} \right) \\ \varepsilon_0 < \varepsilon_c \leq \varepsilon_{20} & E_t = -ZKf'_c \\ \varepsilon_c > \varepsilon_{20} & E_t = 0 \end{cases} \quad \text{Eq. 3.14}$$

here,

$$\begin{aligned} \varepsilon_0 &= 0.002K \\ K &= 1 + \frac{\rho_s f_{yh}}{f'_c} \\ Z &= \frac{0.5}{\frac{3+0.29f'_c}{145f'_c-1000} + 0.75\rho_s \sqrt{\frac{h'}{S_h}} - 0.002K} \end{aligned} \quad \text{Eq. 3.15}$$

Where in the aforementioned equations:

- ε_0 represents the concrete strain at peak compressive stress.
- ε_{20} denotes the concrete strain at 20% of the maximum compressive stress.
- K is a factor reflecting the strength enhancement due to confinement.
- Z denotes the strain softening slope.
- f'_c is the concrete compressive cylinder strength, representing unconfined peak compressive stress in MPa.
- f_{yh} is the yield strength of transverse reinforcement in MPa.
- ρ_s is the ratio of the volume of transverse reinforcement to the volume of the concrete core, measured to the outside of stirrups.
- h' is the width of the concrete core, measured to the outside of stirrups.
- S_h is the spacing, center to center, of stirrups or hoops.

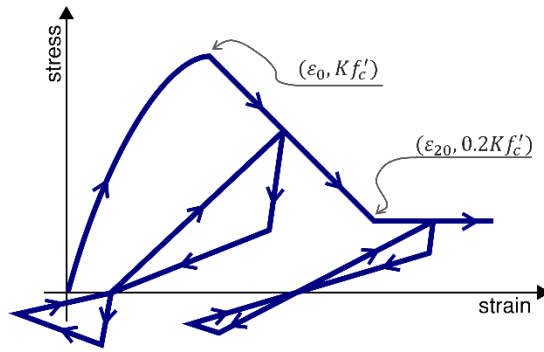


Figure 3.6: Yassin, 1994 concrete hysteretic unloading-reloading behavior.

Yassin (1994) introduced a series of linear stress-strain relationships to represent the hysteretic unloading and reloading rules, as depicted in Figure 3.6. This illustration demonstrates the hysteretic behavior during both compression and tension loading. To maintain clarity, the continuous compression and tension hysteresis loops are considered separately in the model.

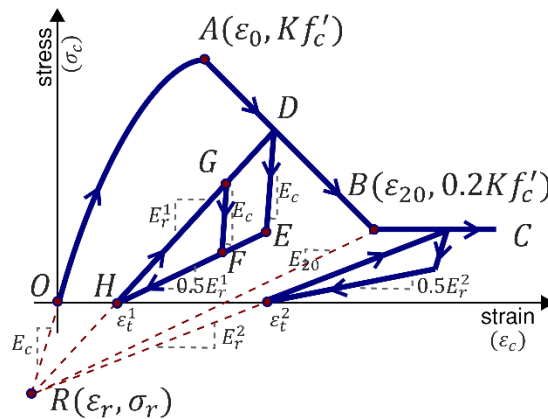


Figure 3.7: Yassine 1994, Parameters illustrating hysteretic behavior in concrete material.

In Figure 3.7, stiffness degradation during unloading and reloading phases in the compression branch are presented for increasing levels of maximum strain. This degradation is characterized by the intersection of the projections of all reloading lines at a singular point, R . This intersection point, R , is identified by the crossing of the tangent to the monotonic envelope curve at the origin

and the extended unloading line from point B , equivalent to residual strength of concrete (i.e., $0.2f'_c$) (Figure 3.7). The expressions for the strain and stress at this intersection point are as follows:

$$\varepsilon_r = \frac{0.2Kf'_c - E_{20}\varepsilon_{20}}{E_c - E_{20}} \quad \text{Eq. 3.16}$$

$$\sigma_r = E_c \varepsilon_r \quad \text{Eq. 3.17}$$

In these expressions, E_c is the origin's tangent modulus of the monotonic envelope curve, and E_{20} is the unloading modulus at point B of the same curve under a compressive stress of $0.2f'_c$. Determination of the value of E_{20} requires experimental methods; Yassin (1994) opted for a value equivalent to 10 percent of E_c .

When unloading from or reloading to a position on the compressive monotonic envelope (marked as point D in Figure 3.7), specifically above the zero-stress axis (indicated as point H in Figure 3.7), the model's response traces two hysteretic branches defined by these two equations:

$$\begin{cases} HD: & \sigma_{max} = \sigma_m + E_r(\varepsilon_c - \varepsilon_m) \\ HE: & \sigma_{min} = 0.5E_r(\varepsilon_c - \varepsilon_t) \end{cases} \quad \text{Eq. 3.18}$$

where,

$$\begin{aligned} E_r &= \frac{\sigma_m - \sigma_r}{\varepsilon_m - \varepsilon_r} \\ \varepsilon_t &= \varepsilon_m - \frac{\sigma_m}{E_r} \end{aligned} \quad \text{Eq. 3.19}$$

here, σ_m and ε_m signify the stress and strain at the unloading point on the compressive monotonic envelope, respectively. Thus, the location of the unloading and reloading loop is contingent on the position of the unloading point. For cycles of partial loading and unloading within these loops, the model pursues a linear trajectory with a slope of E_c .

Trial stress and modulus of elasticity are hypothesized based on linear elastic behavior with a slope of E_c :

$$\sigma_c^T = \sigma_c' + E_c \Delta \varepsilon_c \quad \text{Eq. 3.20}$$

In this equation, σ_c^T represents the newly assumed stress, σ_c' is the preceding stress condition, and $\Delta\varepsilon_c$ is the increment in strain. Subsequently, the actual stress and tangent modulus of the model are ascertained using the ensuing set of rules:

$$\begin{cases} \sigma_{min} \leq \sigma_c^T \leq \sigma_{max} & \rightarrow \sigma_c = \sigma_c^T \text{ \& } E_t = E_c \\ \sigma_c^T < \sigma_{min} & \rightarrow \sigma_c = \sigma_{min} \text{ \& } E_t = 0.5E_r \\ \sigma_c^T > \sigma_{max} & \rightarrow \sigma_c = \sigma_{max} \text{ \& } E_t = E_r \end{cases} \quad \text{Eq. 3.21}$$

The tensile behavior of the model (Figure 3.8) considers degradation of the unloading and reloading stiffness if tensile strain exceeds the strain associated with initial cracking. The maximum tensile strength of concrete is assumed to be equal to $f'_t = 7.5\sqrt{f'_c}$, where f'_t and f'_c are in *psi*.

A depiction of two sequential tensile hysteresis loops can be seen in Figure 3.8, serving as segments of a representative cyclic history, which also incorporates compressive stresses. The model postulates the occurrence of tensile stress at any position along the strain axis, originating either from primary tensile loading or from unloading commencing from a compressive condition. The tensile stress-strain relationship is delineated by three coordinates: $(\varepsilon_t, 0)$, $(\varepsilon_n, 0)$ and $(\varepsilon_u, 0)$, symbolized by points *J*, *K*, and *M*, respectively, in Figure 3.8.

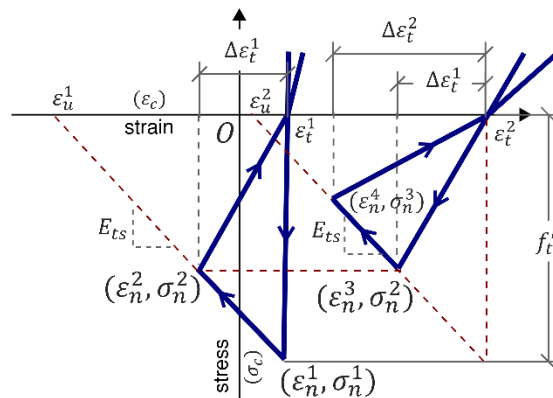


Figure 3.8: Illustration of Yassine 1994, representing concrete's hysteretic behavior under tension.

The parameter ε_t represents the strain at which the unloading line traversing from the compressive stress zone intersects the strain axis, and its value varies with the maximum compressive strain. The parameters ε_n and σ_n denote the strain and stress at the peak of the tensile stress-strain curve, which are articulated by the subsequent equations:

$$\begin{cases} \varepsilon_n = \varepsilon_t + \Delta\varepsilon_t \\ \sigma_n = f'_t \left(1 + \frac{E_{ts}}{E_c}\right) - E_{ts}\Delta\varepsilon_t \end{cases} \quad \text{Eq. 3.22}$$

where $\Delta\varepsilon_t$ is the previous maximum differential between tensile strain and ε_t as shown in Figure 3.8 before initial cracking, $\Delta\varepsilon_t$ is equal to f'_c/E_c . Parameter E_{ts} is the tension stiffening modulus, a value of $0.05E_c$ was used for E_{ts} by Yassin (1994). Parameter ε_u is the strain at the point where the tensile stress is reduced to zero and is given by the expression:

$$\varepsilon_u = \varepsilon_t + f'_t \left(\frac{1}{E_{ts}} + \frac{1}{E_c}\right) \quad \text{Eq. 3.23}$$

With the established control points, the relationship between tensile stress and strain, along with the tangent moduli, are characterized by these equations, given tension is positive:

$$\begin{cases} \varepsilon_t < \varepsilon_c \leq \varepsilon_n & \sigma_c = E_t(\varepsilon_c - \varepsilon_t) & E_t = \frac{\sigma_n}{\varepsilon_n - \varepsilon_t} \\ \varepsilon_n < \varepsilon_c \leq \varepsilon_u & \sigma_c = \sigma_n + E_t(\varepsilon_c - \varepsilon_t) & E_t = -E_{ts} \\ \varepsilon_c > \varepsilon_u & \sigma_c = 0 & E_t = 0 \end{cases} \quad \text{Eq. 3.24}$$

3.4.3. Slip-Extension Material Model

The slip rotation of concrete element from the support comes from two main sources: bond-slip behavior between the rebar and surrounding concrete material and bar longitudinal strains due to the extension of the bar into the support element. As recommended by Alsiwat and Saatcioglu, 1992, the slip component of deformation is either zero or small as compared to bar extension; however, for the sake of completeness, details associated with both conditions is provided below. The bond-slip material's monotonic behavior is represented with an elastic region and a nonlinear section for the post-yield area, depicted in Figure 3.9. The linear portion has a slope represented

as K , while the nonlinear portion delineates the relationship between the stress (σ) and the loaded-end slip (s) as follows:

$$\tilde{\sigma} = \left(\frac{\tilde{S}}{\mu - \tilde{S}} \right) / \left[\left(\frac{1}{\mu \cdot b} \right)^{R_e} + \left(\frac{\tilde{S}}{\mu - \tilde{S}} \right)^{R_e} \right]^{(1/R_e)} \quad \text{Eq. 3.25}$$

In this expression, $\tilde{\sigma}$ represent the normalized bar stress; $\tilde{S} = (S - S_y)/S_y$ is the normalized bar slip; $\mu = (S_u - S_y)/S_y$ represents the ductility coefficient; and b is the factor for stiffness reduction, indicating the ratio of the initial slope of the nonlinear section at the beginning of yielding to the slope in the elastic region (K). Additionally, f_y and f_u denote the yield and ultimate strengths of the steel reinforcing bar respectively, while S_y and S_u represent the loaded-end slips at bar stresses of f_y and f_u , respectively.

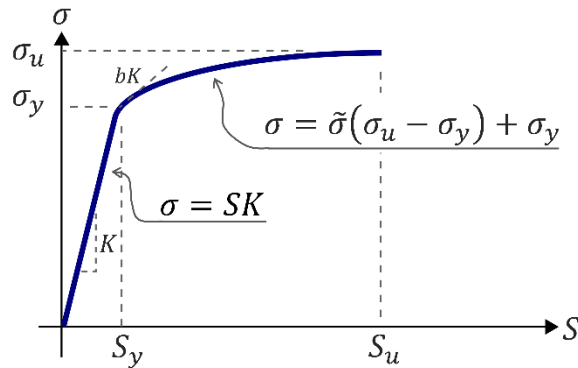


Figure 3.9: Rebar stress-slip backbone curve.

As shown in the Figure 3.9, when the bar stress approaches the yield strength, the slope is (bK). Conversely, as the bar stress nears the ultimate strength, slope of the backbone is almost zero. To uphold a zero-slope close to the bar's ultimate strength, the R_e factor should be just over one; it is assigned a value of 1.01 in the material model implemented in OpenSees, named "Bond_SP01". To construct the envelope for bar stress versus slip response, the required input parameters from the user are S_y , S_u , and b . For comprehensive details on the derivation and the unloading-reloading equation of the material model, refer to Zhao, and Sritharan, 2007.

The values required as input for the Bond_SP01 material model should be obtained from the inherent physics of the structure (extension of the bar in the concrete and slippage of the rebars). The behavior of the reinforcement developed into the supports during extension can be categorized into four subregions, depicted in Figure 3.10. The initial subregion is the elastic region, where the reinforcement exhibits elastic behavior until it reaches its yield strength. The next is the yield plateau, a phase where, once the reinforcement attains its yield strength, it continues to deform without any increment in stress. Subsequently, the strain hardening region is encountered, in which the reinforcement undergoes an increase in stress resulting from strain hardening. Finally, the pullout cone is the last subregion, wherein the reinforcement is extracted from the encompassing concrete and achieves its maximum strength.

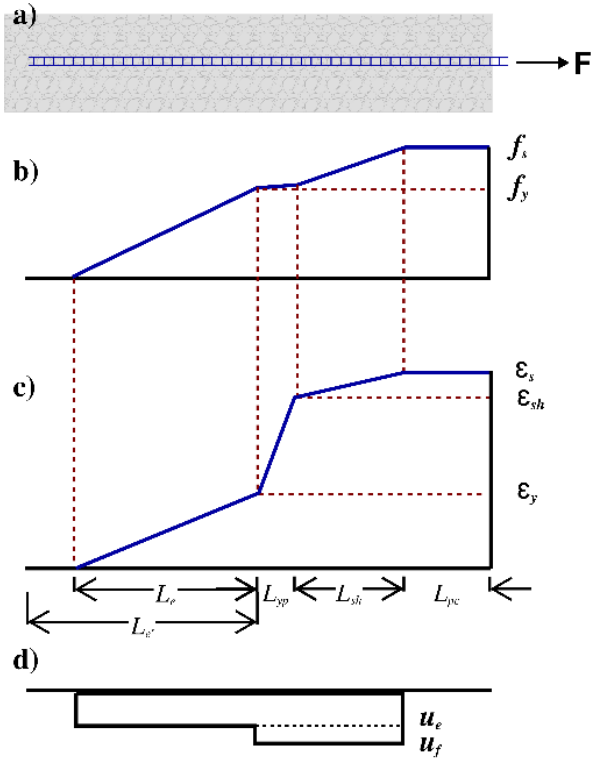


Figure 3.10: a) reinforcing bar extended in the support concrete element; b) stress distribution; c) strain distribution; d) bond stress between concrete and steel.

Each of these four regions is discussed and can be calculated as below.

- Elastic Region: This is the portion of reinforcement over which stress remains elastic. The average bond stress is given by:

$$u_e = u_{ACI} = \frac{f_y d_b}{4l_d} \text{ MPa} \quad \text{Eq. 3.26}$$

$$l_d = \frac{440A_b}{K\sqrt{f'_c}} \frac{f_y}{400} \geq 300 \text{ mm} \quad \text{Eq. 3.27}$$

where u_e is the elastic bond stress (MPa), f'_c is the concrete strength (MPa), f_y is the steel yield strength (MPa), d_b is the bar diameter (mm), l_d is the development length (mm), and A_b is the bar area (mm²). Additionally, a coefficient K is used to reflect the effect of confinement steel, concrete cover, and spacing between bars. It is recommended to use K equal to 3 times the bar diameter ($3d_b$) for practical purposes (Alsiwat and Saatcioglu, 1992).

$$L_e = \frac{f_s d_b}{4u_e} \quad \text{Eq. 3.28}$$

where f_s is the maximum elastic steel stress (MPa). If the obtained L_e is greater than the available elastic length, the bar is stressed to the cutoff point.

- Yield Plateau Region: the approximately constant yield stress of steel occurs in this portion of the reinforcement.

$$L_{yp} = \frac{\Delta f_s d_b}{4u_f} \quad \text{Eq. 3.29}$$

$$u_f = \left(5.5 - 0.07 \frac{S_L}{H_L}\right) \sqrt{\frac{f'_c}{27.6}} \text{ MPa} \quad \text{Eq. 3.30}$$

where, S_L and H_L are the clear spacing and height of lugs on the reinforcing bars. Note that, if the Δf_s between the beginning and end points of the yield plateau is zero, this expression results in zero.

- Strain-Hardening Region: as the same as reinforcing steel material behavior, strain-hardening region occur right after yield plateau region. Because in this region the concrete key between lugs has already been crushed, it is reasonable to use the frictional bond between the concrete and steel.
- Pullout-Cone Region: this portion will form when the end of the embedded reinforcing bar become loose in tension and forming a constant stress strain region. However, per former studies (i.e. Alsiwat and Saatcioglu, 1992) neglecting this portion will not affect the behavior of the bar-extension significantly.

Finally, the total extension of the reinforcing bars (δ_{ext}) can be obtained by integrating the strains along the length of bars as follows:

$$\delta_{ext} = \varepsilon_s L_{pc} + 0.5(\varepsilon_s + \varepsilon_{sh})L_{sh} + 0.5(\varepsilon_{sh} + \varepsilon_y)L_{yp} + 0.5\varepsilon_y L_e \quad \text{Eq. 3.31}$$

In addition to bar-extension, slip may occur at the interface of the rebar and the concrete. Although the development length of the reinforcement is sufficient in all of the test specimens examined in this study—making the effects of bond-slip negligible in comparison to extension—a detailed account of the bond-slip computation and calibration process is provided for thoroughness. Based on the model, which was initially proposed by Ciampi et al. (1981) and Eligehausen et al. (1983), and later modified by Alsiwat and Saatcioglu in 1992, the bond stress at the far end of the bar can be employed to determine the corresponding slip.

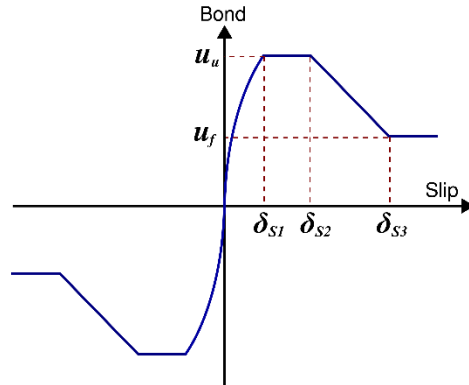


Figure 3.11: Ciampi et al. 1981 and Eligehausen et al. 1983 local bond-slip model.

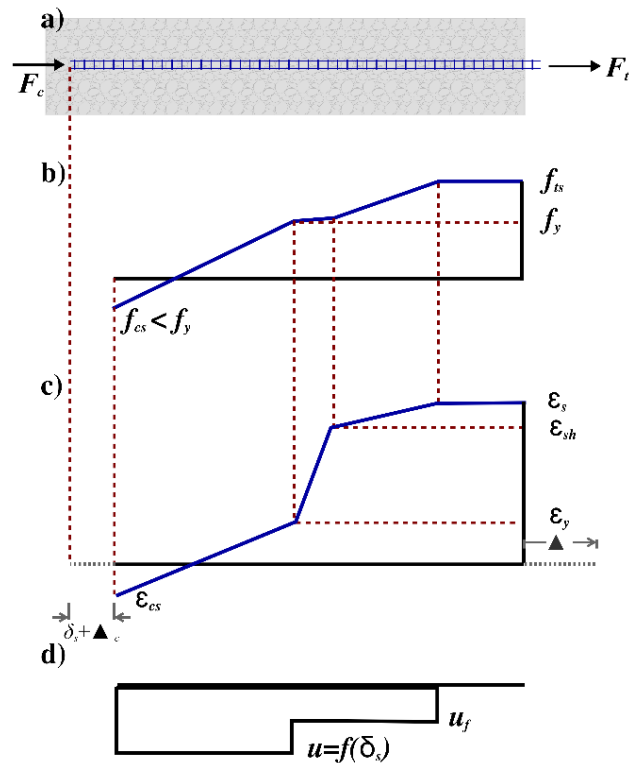


Figure 3.12: a) reinforcing bar slip at the support concrete element; b) stress distribution; c) strain distribution; d) bond stress.

As the same as the bar-extension behavior, the bond-slip behavior of the reinforcements categorized into four subregions, where each region can be formulated as below:

$$u = u_u \left(\frac{\delta_s}{\delta_{s1}} \right)^{0.4} \quad \text{Eq. 3.32}$$

$$u_u = \left(20 - d_b/4 \right) \sqrt{f'_c/30} \quad \text{Eq. 3.33}$$

$$\delta_{s1} = \sqrt{30/f'_c} \quad \text{Eq. 3.34}$$

$$\delta_{s2} = 3.0 \quad \text{Eq. 3.35}$$

$$\delta_{s3} = \text{clear distance between lugs} \quad \text{Eq. 3.36}$$

Finally, the reinforcement slip in the ascending branch can be calculated as follows:

$$\delta_s = \delta_{s1} \left(u'_e / u_u \right)^{2.5} \quad \text{Eq. 3.37}$$

where,

$$\begin{cases} L'_e > L_e & \rightarrow & u'_e = 0 \\ L'_e \leq L_e & \rightarrow & u'_e = f'_s d_b / (4L'_e) \end{cases} \quad \text{Eq. 3.38}$$

in this context, u'_e is indicative of the elastic bond stress at the bar's far end (at the cutoff point); L'_e represents the available elastic length of the bar, calculated by deducting the plastic length from the embedment length; and f'_s signifies the peak elastic steel stress formed in the elastic region. Should the elastic bond stress, u'_e , attain the ultimate bond, u_u , the entire bar undergoes pullout, denoting the failure point. In general, compared to bar extension, the deformation's slip component is either negligible or absent if the rebars are sufficiently developed into the supports. Therefore, in all the following sections and modeling parameters, only the extension behavior is considered.

4. EXPERIMENTAL SPECIMEN INVENTORY

This chapter includes details on the calibration and validation of the analytical macro-model (CBeam) presented in Chapter 3 by utilizing test results from various experimental programs. The tests include a broad spectrum of features and cover a range of reinforcement configurations, aspect ratios, and boundary conditions. An overview of these experimental studies is presented in the subsequent sections, with the first part of the chapter focusing on six tests on isolated coupling beam and the second part of this chapter focusing on tests of coupled wall tests.

4.1. Isolated Coupling Beam Specimens

The selected isolated beam test specimens were subjected to cyclic loading and represent a wide range of parameters to enable a comprehensive validation of the CBeam model. The first two test specimens used to validate the model were selected from an experimental program conducted by Naish and Wallace at UCLA (2010, 2013). Test specimens CB24F and CB24F-RC were identical except CB24F-RC included a 4-inch thick RC slab. Both beams had an aspect ratio of 2.4. These specimens were selected to evaluate the capability of the proposed model to capture the shear force versus rotation behavior of the beam, as well as to capture the effect of the RC slab.

Another test specimen used to validate the model was the CB30H specimen tested by Lim et al., 2016. The test specimen had an aspect ratio of 3.0 and was reinforced with both diagonal and longitudinal reinforcement. This specimen was included to assess the ability of the model to predict the lateral behavior of this hybrid reinforcement configuration.

Additionally, to explicitly study the influence of axial restraint in the proposed model, two identical specimens, CB1 (Ameen et al. 2017) and CB1A (Poudel et al. 2018), both with aspect ratio of 1.9, were selected. These two specimens had identical cross-sections and were subjected to identical

loading protocols, except that the axial growth of specimen CB1A was restrained during the test using two, pretensioned, high-strength steel rods at the centerline of the specimen.

Lastly, the isolated test specimens BLB/BMB from the 1996 BRI study of a 12-story coupled wall was included. Tests on isolated coupling beams were conducted prior to the test of the 12-story coupled wall. One of the tests (BLB) included a load cell embedded at the centerline of the beam to capture the variation of axial load during the test.

Model and test results for each isolated coupling beam test are compared in the following subsections.

4.1.1. Specimen CB24F & CB24F-RC

Specimen Prototypes

These two test specimens represented diagonally reinforced coupling beams in tall residential buildings where an aspect ratio of about 2.4 is common. The prototype beams for these test specimens were 24×30 inches reinforced with two bundles of 8-#11 diagonal bars. Using ACI 318-08 equation 21-9:

$$V_n = 2A_{vd}f_y \sin \alpha \leq 10\sqrt{f'_c}A_{cw} \quad \text{Eq. 4.1}$$

For $\alpha = 15.7^\circ$ (the inclination angle of the diagonal bundles relative to the beam's longitudinal axis) and Grade 60 reinforcement, the nominal shear strengths of the beams is equivalent to $7.3\sqrt{f'_c}A_{vd}$.

The test specimens were carried out on one-half scale beams; therefore, the tested beams had 12x15 inch cross sections with two bundles of 6-#7 diagonal bars (Figures 4.1 and 4.2). One of the specimens (CB24F) excluded the slab, whereas the other (CB24F-RC) included a 4-inch RC slab with #3 bars spaced at 12" on center at the top and bottom of the slab in the transverse direction and at the top of the slab along the beam span.

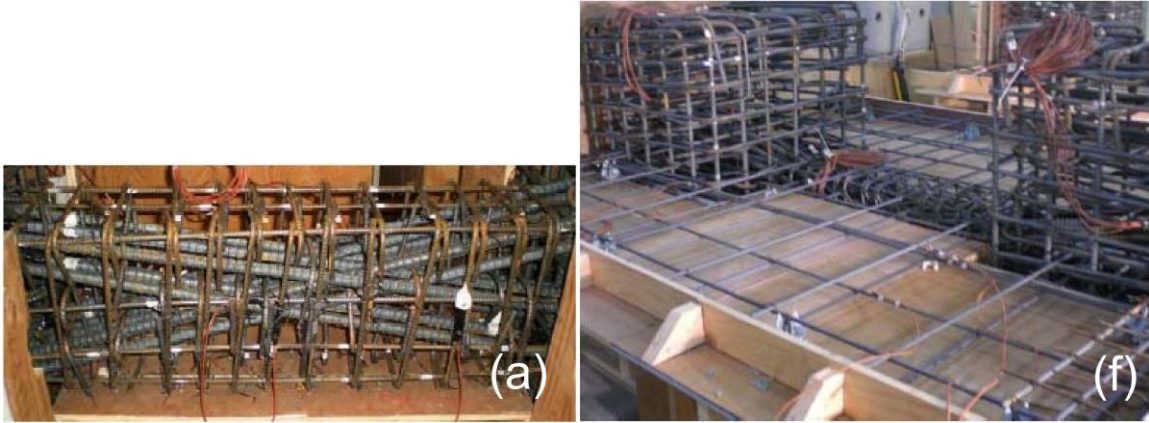


Figure 4.1: Photograph of test specimen construction: a) CB24F beam construction, b) CB24F-RC beam and slab construction (Figure from Naish 2010).

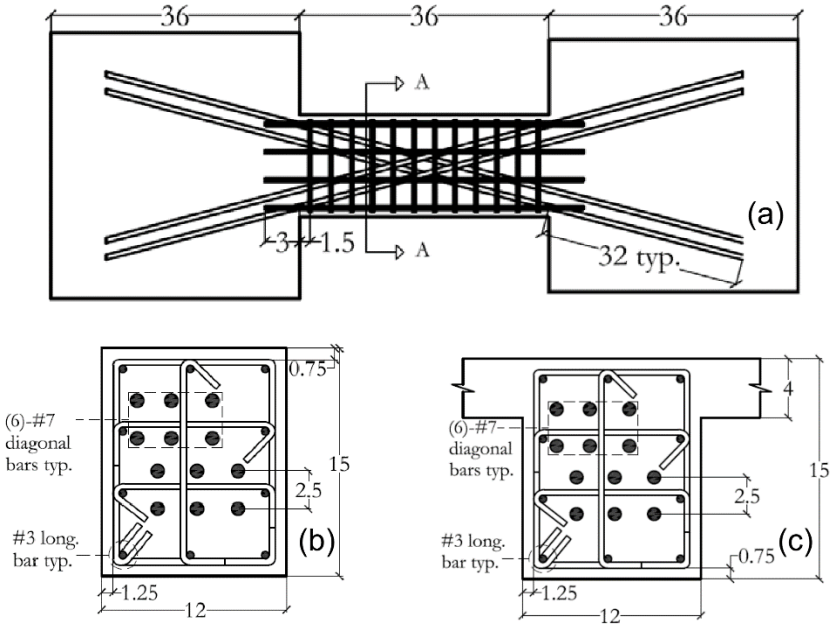


Figure 4.2: Naish 2010 test beam geometries ($\frac{l_n}{h} = 2.4$) with full section confinement: a) CB24F, CB24F-RC elevation; b) CB24F cross section; and c) CB24F-RC cross section (Figure from Naish 2010).

Material Testing

The concrete compressive strength (f'_c), was determined on the test day for each of the test specimens. Concrete material testing was done both at the UCLA material testing lab and Twining

Testing Labs in Long Beach, CA to ensure accuracy and provide redundancy. The yield and ultimate tensile strengths for rebars in the beams were determined using rebar coupons. The rebar in all specimens originated from the same batch for consistency. A summary of these material properties can be found in Table 4.1.

Table 4.1: Materials properties.

Specimen	Steel		Concrete
	f_y (ksi)	f_u (ksi)	f'_c (ksi)
CB24F	70.0	90.0	6.8
CB24F-RC	70.0	90.0	7.3
CB30H	65.3	-	8.4
CB1	62.0	89.0	6.0
CB1A	62.0	89.0	6.4
BLB/BMB	52.9	75.7	6.0

Test Setup

The beams were tested in the UCLA Structural/Earthquake Engineering Research Lab as illustrated in Figure 4.3. Beams were vertically positioned with end blocks that acted as wall boundaries and supports. The top and bottom blocks were grouted and post-tensioned. To prevent rotation at the top of the beam and control the axial force applied to the beam (to zero), two vertical hydraulic actuators were positioned on each side and connected to the steel loading frame. Lateral force was applied through a horizontal actuator to produce zero moment at beam midspan.

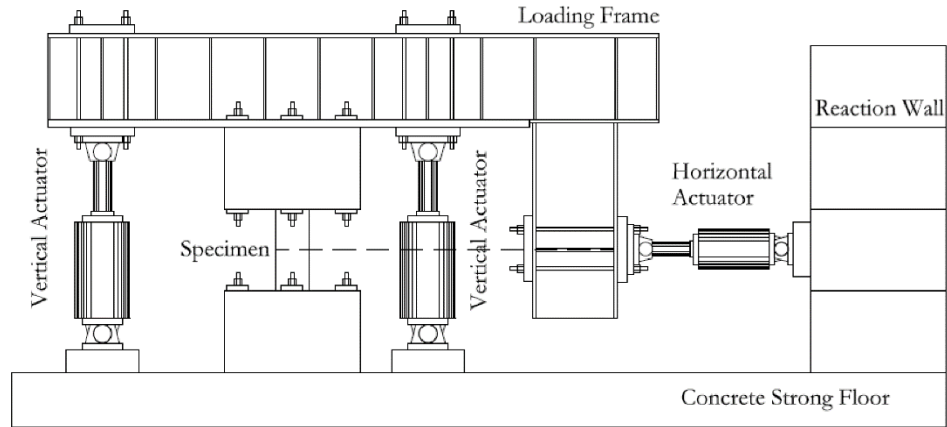


Figure 4.3: CB24F and CB24F-RC laboratory test setup (Figure from Naish 2010).

Test Procedure

The loading protocol included load-controlled and displacement-controlled cycles (Figure 4.4). Prior to reaching the yield point, load controlled cycles were applied at 0.125, 0.25, 0.50, and $0.75V_y$, with $V_y = \frac{2M_y}{l_n}$ with three cycles applied at each increment. Given nominal material properties, V_y was approximated as 120 kips for these two test specimens. Beyond the $0.75V_y$ level of lateral load, the protocol shifted from load-control to displacement-control. During the displacement-controlled portion of the protocol, prior to 3% chord rotation (the ASCE 41-06 collapse prevention limit), three cycles were applied. Beyond this threshold, two cycles were applied at each chord rotation increment.

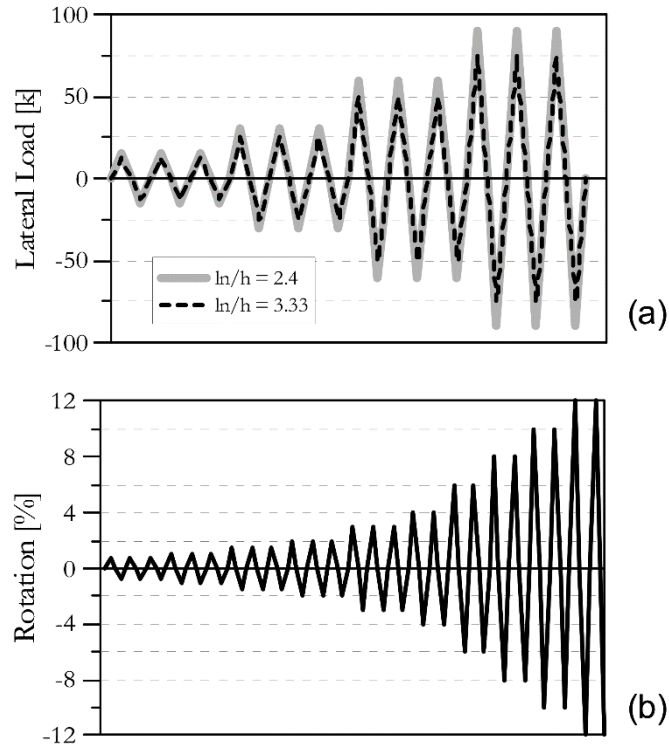


Figure 4.4: loading protocol: a) load-control, b) displacement-control (Figure from Naish 2010).

4.1.2. Specimen CB30-H

Specimen Prototype

The test specimen labeled CB30-H utilizes both diagonal and longitudinal reinforcement layouts, which is referred to as a hybrid reinforcement configuration. This test specimen has a clear span to depth ratio (l_n/h) of 3. Lim et al. 2016 used Eq. 4.2 to definition a η ratio, which represents the contribution of the longitudinal component of diagonal bars to the total tension reinforcement provided (including the longitudinal rebars), adjusted according to their yield strengths:

$$\eta = \frac{A_{vd}f_{yd} \cos \alpha}{A_{vd}f_{yd} \cos \alpha + A_l f_{yl}} \quad \text{Eq. 4.2}$$

where A_{vd} represents the reinforcement area of the diagonal bars, α is the angle between the diagonal bars and the beam longitudinal axis. The yield strengths of diagonal and longitudinal bars are represented by f_{yd} and f_{yl} , respectively.

Specimen CB30-H, illustrated in Figure 4.5, utilizes two D32 (\approx US #10) bars used as diagonal reinforcement. Longitudinal reinforcement consists of one D22 (\approx US #7) and two D25 (\approx US #8) bars on both the top and bottom of the beam (reinforcement ratio (ρ) of 2.7%). This configuration results in an η ratio of 50%. Diagonal bars were bent 50 mm (1.97 in.) from the beam-wall interface and extended into the end block supports. The shear reinforcement consisted of D13 (\approx US #4) @100 mm (3.95 in.) hoops, conforming to the ACI 318-14, chapter 18 section 18.10.7. Plus, four securely anchored D13 (\approx US #4) longitudinal bars were used in conjunction with the crossies as the face rebars.

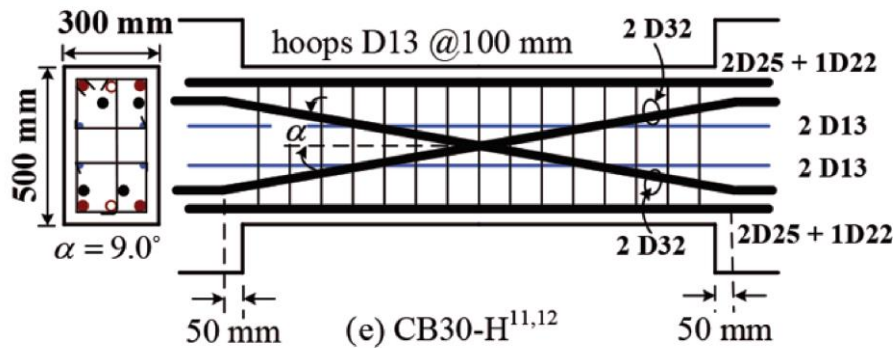


Figure 4.5: CB30H test specimen reinforcement configuration (Lim et al., 2016).

Material Properties

The material properties obtained from material testing for the specimen are outlined in Table 4.1. The concrete strength, f'_c , is based on the mean value from three concrete cylinders tested on the same day as the coupling beam test. Reinforcement yield stress is based on an average of tensile strength coupon tests of three bar samples.

Test Setup

During lab testing, the coupling beam was placed vertically. An L-shaped steel frame was used to transfer loads from actuators to the beam test specimen (Figure 4.6). Two vertical actuators were

used to control the axial load and rotation at top of the beam, and two horizontal actuators affixed to a strong wall were used to apply the lateral load at mid-span of the beam. One of the horizontal actuators was managed by displacement and the other horizontal actuator was controlled by force, ensuring the force acted through the beam mid-height.

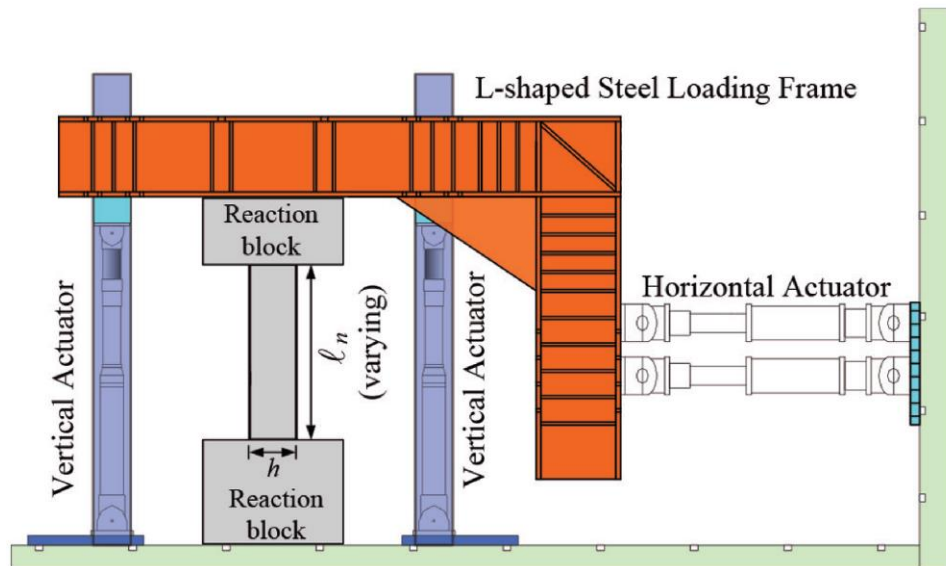


Figure 4.6: CB30H laboratory test setup (Lim et al., 2016).

Test Procedure

Loading protocol used for this test specimen adhering to the ACI 374.1-059 loading guidelines shown in Figure 4.7, applied as a displacement-control.

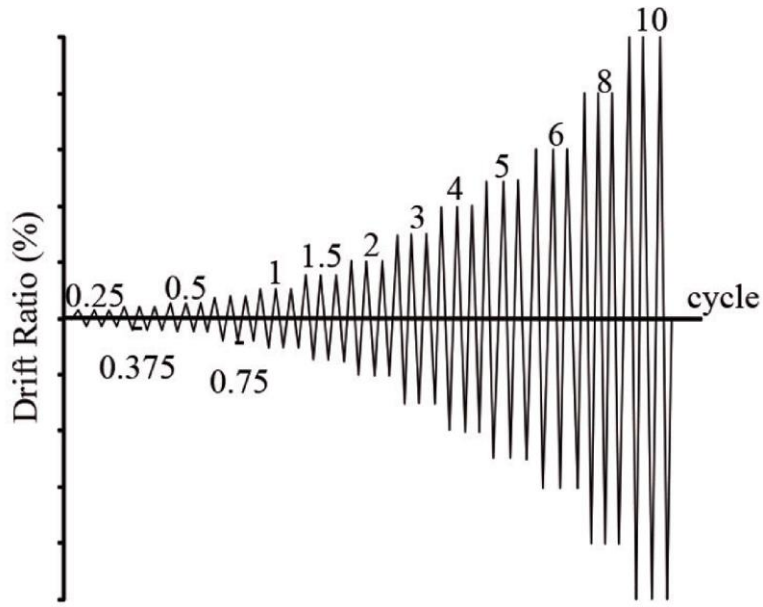


Figure 4.7: CB30H loading protocol (Lim et al., 2016).

4.1.3. Specimen CB1 & CB1A

Specimen Prototype

Two similar coupling beam specimens, CB1 and CB1A selected as one has no axial restraint (CB1), and the other (CB1A) has axial restraint through two 3-inch steel rods (as illustrated in Figure 4.8). Beams had a clear span length of 34 inches; the cross-section is 18 inches by 10 inches, leading to an aspect ratio (l_n/h) of 1.9. These specimens were designed to resist a nominal shear strength of $10\sqrt{f'_c}$ assuming that the two diagonal bundles provide all the shear strength.

The diagonal bundles included 12 #7 bars angled at 18 degrees from the longitudinal axis (see Figure 4.8). Transverse reinforcements were #3 hoops spaced 3 inches apart providing the full-section confinement. 8 #3 longitudinal face bars extended 2 inches into the supports.

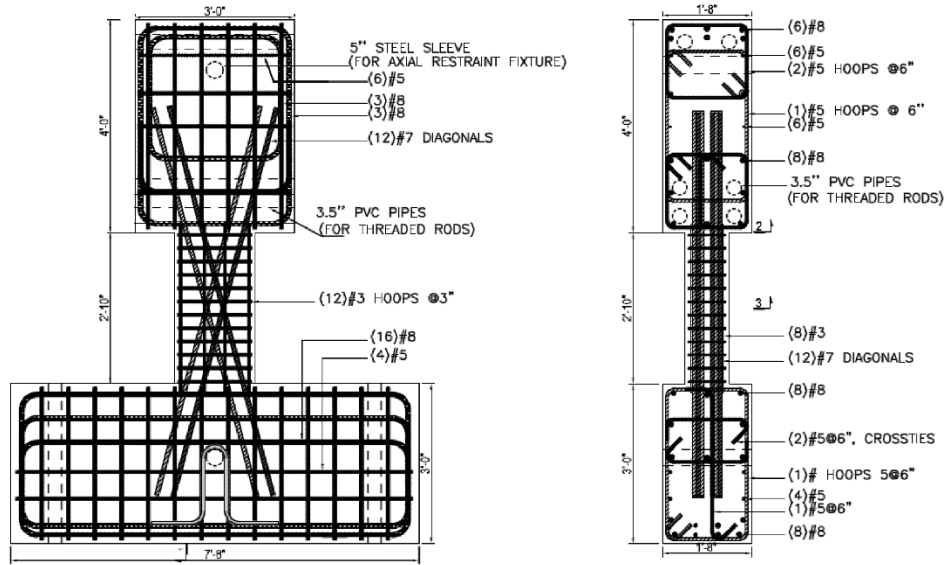


Figure 4.8: CB1 and CB1A specimen dimension and reinforcements (Poudel et al., 2018).

Material Properties

The beams were created using ready-mix concrete targeting a compressive strength of 6000 psi. The concrete's exact strength was verified through ASTM C39 tests on standard 4x8 inch cylinders, with the results listed in Table 4.1. Tensile tests were conducted on diagonal steel rebars used in the specimen and the results are listed in Table 4.1.

Test Setup

The experimental configuration is showcased in Figure 4.9. The bottom block of each specimen was anchored securely to the strong floor via two 2.5-inch rods. Two MTS 201.70 Hydraulic Actuators were placed horizontally and used to apply lateral loads to the specimens. The spacing between the actuators used to control the rotation at top of the beam.

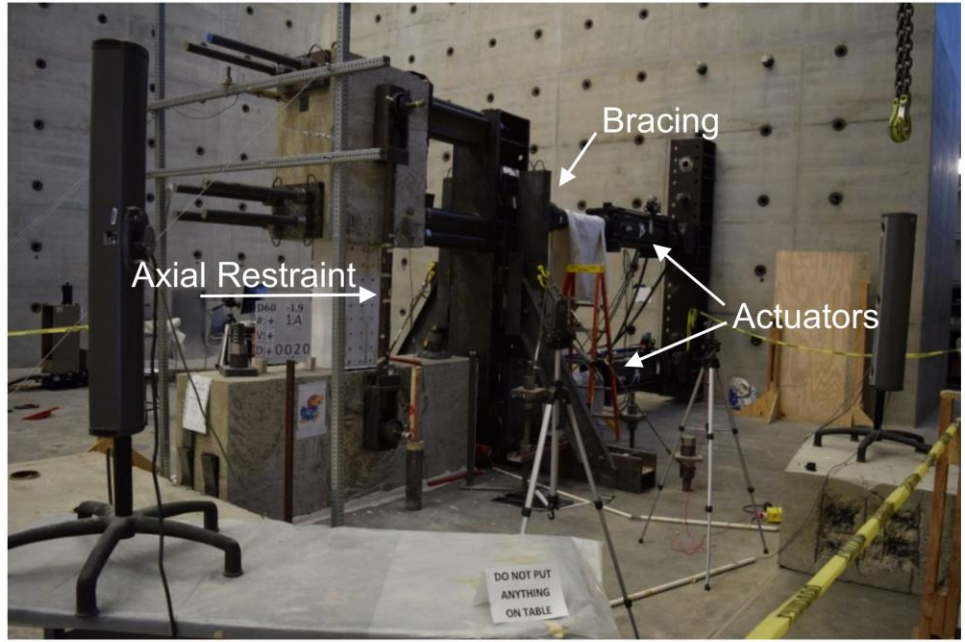


Figure 4.9: CB1 and CB1A laboratory test setup (Poudel et al., 2018).

For CB1A, axial restraint was achieved using 3-inch threaded rods connecting the top and bottom blocks (see Figure 4.10). These rods were then linked to 5-inch diameter steel rods that passed through the blocks, which were prepared with lubrication to ensure smooth rotation of the fixtures during testing.

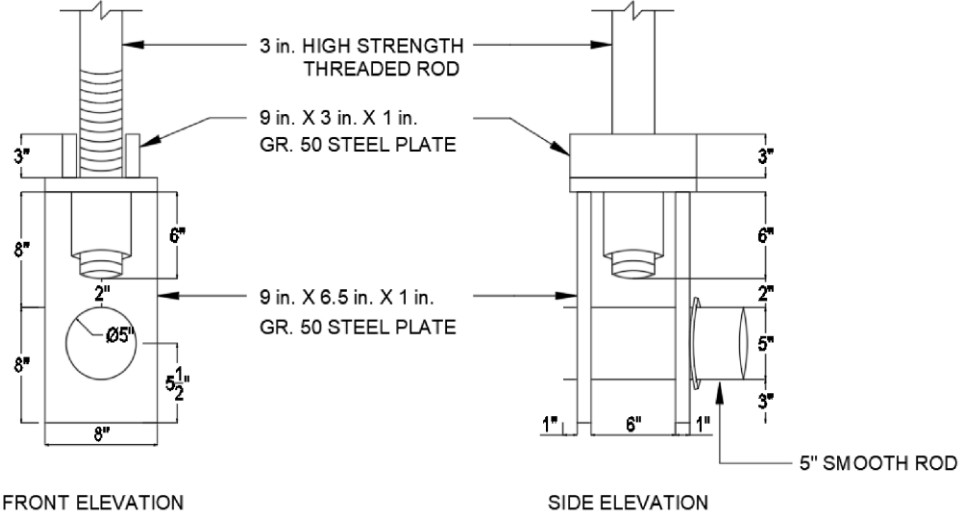


Figure 4.10: CB1A axial restraint fixture (Poudel et al., 2018).

Test Procedure

The beams were subjected to reversed cyclic loading as per the patterns detailed in Figure 4.11, adhering to FEMA 461 (2007) standards. The initial phase of the test was force-controlled, shifting to displacement-control after reaching the diagonal reinforcements to its expected yield stress. During the experiment, force or displacement ratios were carefully adjusted to maintain a zero-moment at midpoint in the beam during the test.

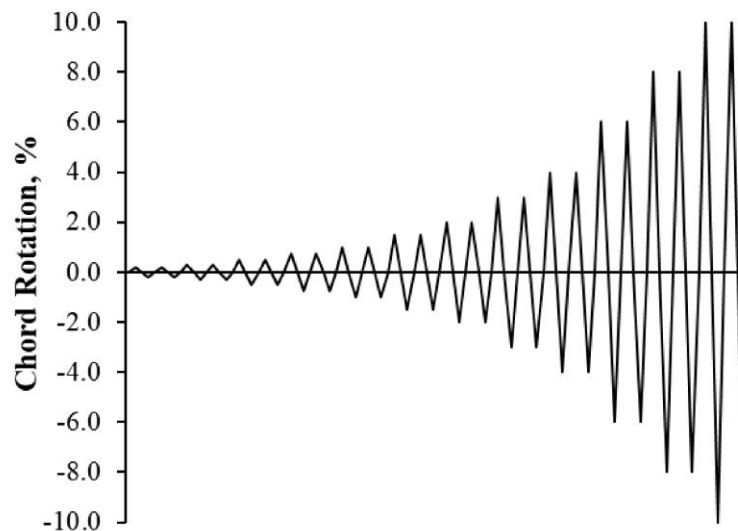


Figure 4.11: CB1 and CB1A loading protocol (Poudel et al., 2018).

4.1.4. Specimen BRI-1996 BLB & BMB

Specimen Prototype

In 1996, as part of a collaborative experimental program between the US and Japan on the coupled wall systems (as referenced by Sugaya et al., 2000), a research team at the Building Research Institute (BRI) conducted testing on two identical isolated coupling beam test specimens. These test specimens represent the second floor coupling beams of a 12-story coupled wall prototype, scaled down to one-third of the original size. The two test specimens we

identical in terms of cross-section and reinforcing; however, in the mid-span of one of the specimens (BLB), a loadcell was placed to capture the variation of axial load in the beam during the test. Configuration of the test specimen is depicted in Figure 4.12.

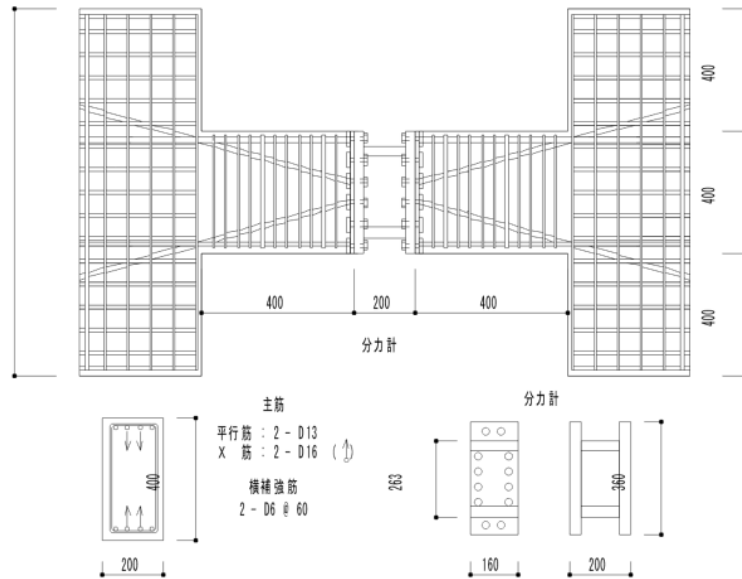


Figure 4.12: BLB specimen reinforcement configuration and placement of the loadcell within the beam (Sugaya, 2003).

Material Properties

The concrete chosen for these test specimens was marked with a design strength of 5.23 ksi. Both specimens, BMB and BLB, included longitudinal rebars of D13, and diagonal reinforcement of D16. Steel rebars are made of SD 295A material (Japanese standard). The results obtained from the material testing on these rebars and concrete material are presented in Table 4.1.

Test Setup

The experimental setup was designed to apply an anti-symmetric moment on the coupling beams. This was achieved through the utilization of a vertically oriented actuator to control the applied

rotation at the end of the specimen and impose the axial load on the specimens. Another actuator placed horizontally at mid-span of the beam to apply the lateral load on the specimens. A visualization of the test setup is shown in Figure 4.13.

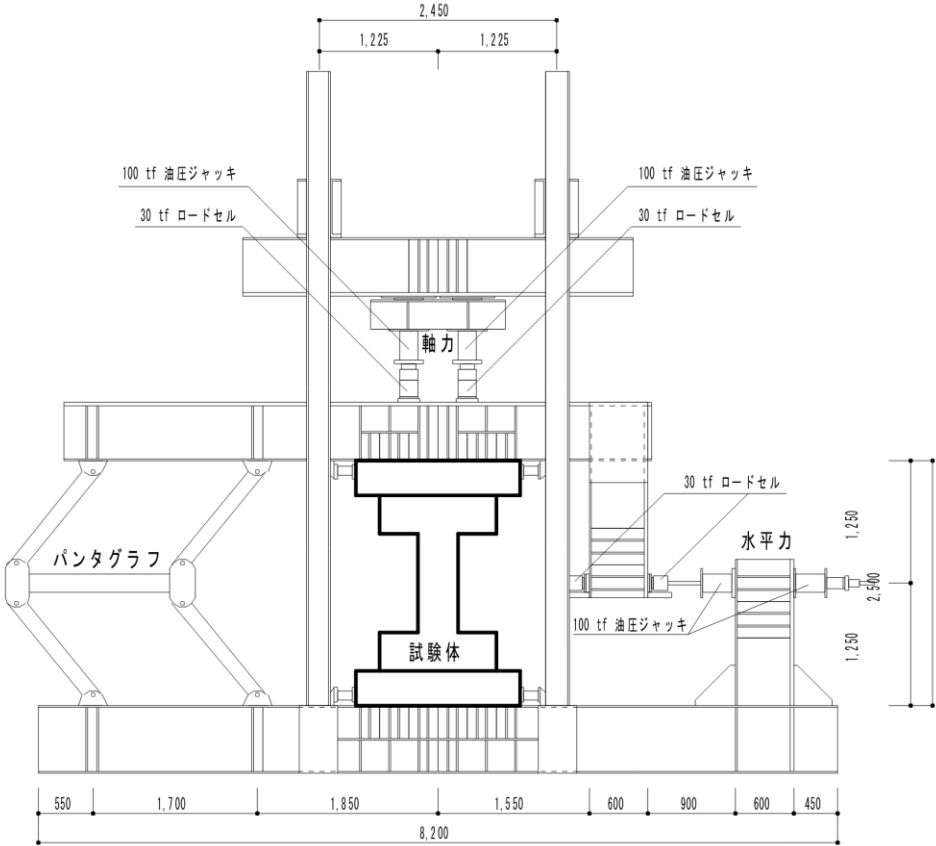


Figure 4.13: BLB/BMB laboratory test setup (Sugaya, 2003).

Test Procedure

During the test, a constant axial load (originating from the self-weight of the specimen itself and the vertical actuators, approximately about 14.17 kips) applied to the BMB specimen prior to application of lateral loading. The specimen then underwent lateral cycles at specific chord angles, increasing in intensity. In contrast, the BLB underwent a similar loading procedure but with incremental adjustments to the axial force to adjust the axial load obtained from the loadcell.

This axial force experienced increments, maxing out at a certain level, and at each distinct axial force level, a shear force was systematically applied. A chronological depiction of these forces is shown in Figure 4.14.

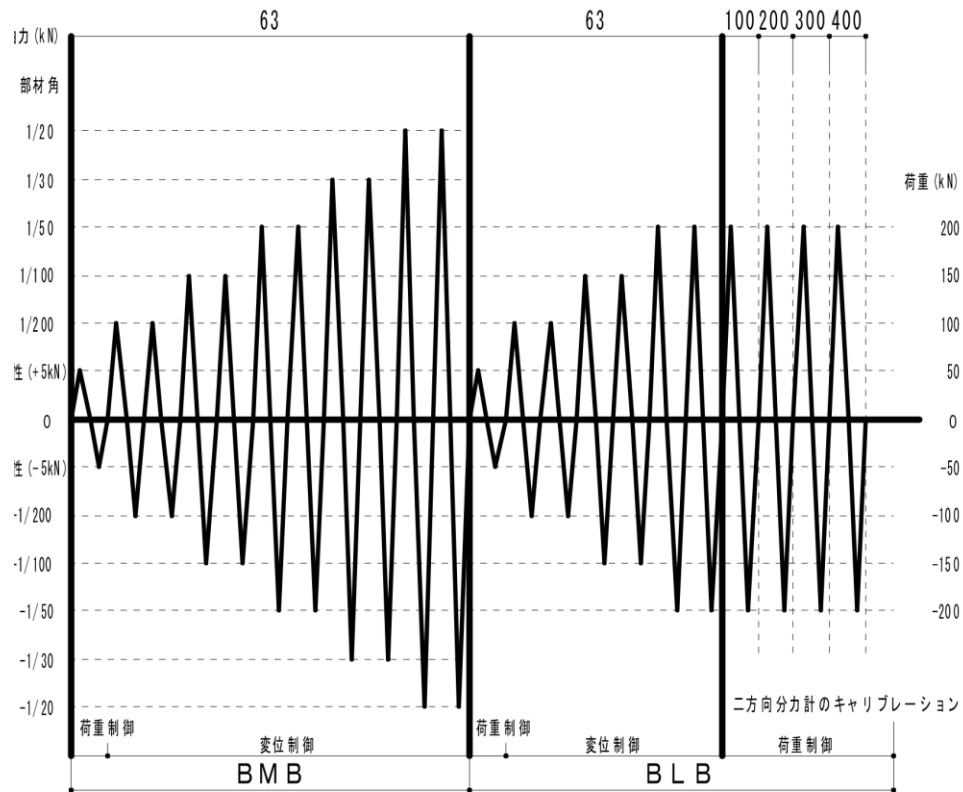


Figure 4.14: loading protocol: a) BMB, b) BLB (Sugaya, 2003).

4.2. System Level Coupled Wall Specimen

To confirm the efficiency of the proposed analytical coupling beam model in conjunction with wall element to create a core wall/coupled wall system, experimentally obtained data from a one-third 12-story coupled wall system test specimen utilized. This test (BRI-1996) was conducted by the US-Japan Collaborative and is documented in Sugaya, 2003. This experiment was conducted at the Building Research Institute (BRI) and aimed to analyze the shear force transition between tension and compression elements of the coupled shear walls. Notably, this experiment

incorporated load cells directly within the coupling beam elements, offering insights into the axial load variation between the coupling beams and the interconnected wall piers. The specimen underwent fixed axial loads and escalating cyclic lateral loads applied at the 12th, 7th, and 4th floors. The system is designed to utilize the coupling beams as fuse hinge along the height and hinged at the base of the shear wall as its targeted failure mechanism. The findings confirmed the coupled wall system's robustness in withstanding lateral loads and its capacity to endure significant nonlinear deformations before total collapse.

4.2.1. Specimen BRI-1996

Figure 4.15 depicts the RC core wall of the target building, which was selected as the basis layout for the 12-story T-shaped BRI-1996 coupled wall test.

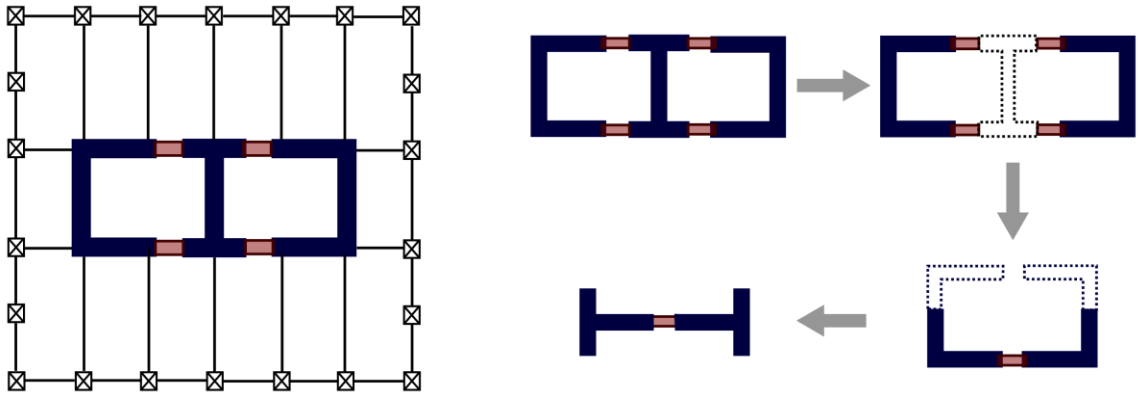


Figure 4.15: BRI-1996 target building core wall.

The specimen was constructed as a one-third scale symmetric T-shaped coupled wall with a total height of 567 inches and a width of 197 inches (total length in the web direction). The typical story height is 47.2 inches with a consistent web and flange thickness of 7.9 inches. Two wall piers are interconnected using 15.7×7.9 inches diagonally reinforced coupling beams that span 39.4 inches across all 12 floor levels.

The typical longitudinal and horizontal web and flange reinforcement ratio (outside of the confined area) is 0.64%. Each of the wall piers comprises two confined areas: one at the web-flange intersection and the other at the inner edge, with an increasing number of rebars down the height. Refer to Table 4.2 for detailed reinforcing information. Coupling beams from the 2nd to 7th floors consist of two D-16 diagonal bars, while those from the 8th floor to the roof are constructed with two D-13 diagonal bars. Additionally, all coupling beams contain two longitudinal D-10 bars; two legs of D-6 hoops spaced at 3.9 inches apart providing the full-section confinement. Figure 4.16 illustrates the location of reinforcements for walls and coupling beams in the BRI-1996 specimen.

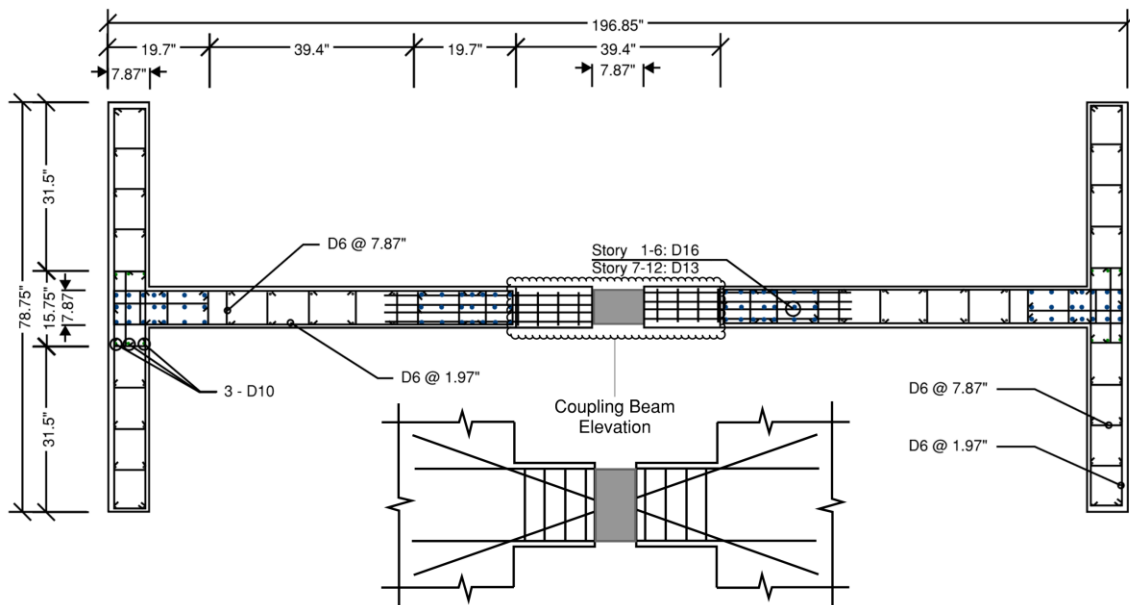


Figure 4.16: BRI-1996 specimen reinforcement layout.

Table 4.2: BRI 1996 coupled wall detailed reinforcement.

Story	Shear Walls		Confined Area		
	Web/Flange		Length	Rebar	Hoops
	Longitudinal	Horizontal			
10th-12th	D6 @ 1.97"	D6 @ 7.87"	11.81"	14-D13	D6 @ 1.97"
7th-9th	D6 @ 1.97"	D6 @ 7.87"	15.75"	17-D13	D6 @ 1.97"
4th-6th	D6 @ 1.97"	D6 @ 7.87"	19.69"	20-D16	D6 @ 1.97"
1st-3rd	D6 @ 1.97"	D6 @ 7.87"	19.69"	20-D16	D6 @ 1.97"
Level	Coupling Beams		Ties	α	
	Longitudinal	Diagonal			
8th-Roof	2-D10	2-D13	D6 @ 3.94"	18.9°	
2nd-7th	2-D10	2-D16	D6 @ 3.94"	19.0°	

Apart from the reinforcement details, material properties also vary throughout the height of the structure. The compressive strength of the concrete (f'_c) is highest at the first story and decreases progressively up the structure, depending on the age of the cured concrete at the time of the cylinder test. The yield stress (f_y) of the structural steel reinforcements ranges from 45.8 to 51.8 ksi. Table 4.3 summarizes the properties of the constitutive materials.

Table 4.3: BRI 1996 coupled wall system material properties.

Concrete			Steel			
Story	E_s (ksi)	f'_c (ksi)	Rebar Size	E_s (ksi)	f_y (ksi)	f_u (ksi)
1 st	3,385	5.71	D16	25,318	50.9	72.1
2-3 rd	3,172	5.90	D13	25,745	49.6	68.8
4-6 th	2,788	4.23	D10	24,891	51.8	71.3
7-9 th	2,845	4.07	D6	27,025	45.9	80.9
10-11 th	2,688	3.86				
12 th	2,745	3.99				

4.2.2. Loading and measurements

The coupled wall specimen was subjected to a hysteretic lateral load at three levels (4th, 7th, and 12th) using hydraulic jacks with ratios of 1.0, 1.97, and 3.73, respectively. Additionally, a constant axial load was applied at four points using PC strands, with two strands on each pier.

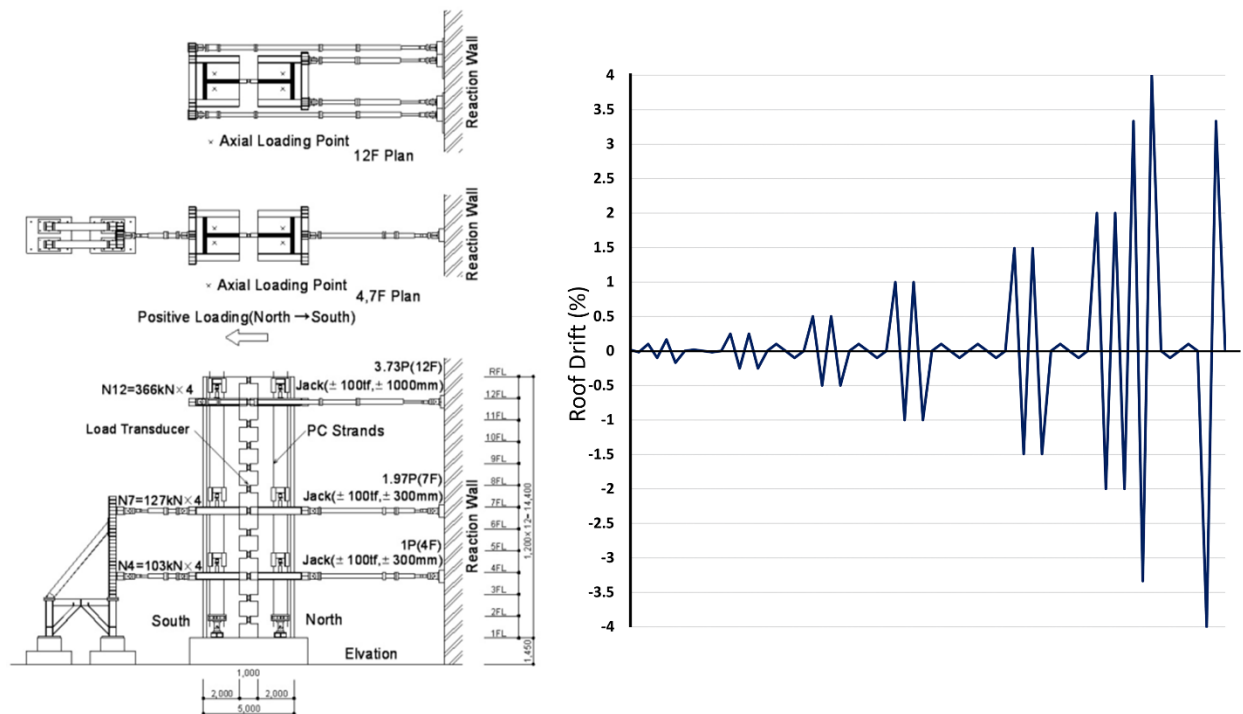


Figure 4.17: left) BRI-1996 loading configuration; right) cyclic loading protocol. (Sugaya, 2003)

During the test, load transducers measured the lateral loads applied to the specimen, registering it as shear force. Measurements were also taken for the coupling beams' shear force, axial force, axial displacement, and rotations.

A unique aspect of the BRI-1996 experiment was the measurement of the axial force and displacement of the coupling beams using load cells positioned at the center of the beams. To study the influence of the load cell placements in the coupling beams, two identical isolated elements were constructed and tested before the 12-story experiment. These were: BMB (coupling beam without a load cell), and BLB (coupling beam with a load cell), which is discussed in detail in the isolated test specimens section.

5. ANALYTICAL MODEL VALIDATION

In Chapter 3, we introduce a new coupling beam model named 'CBeam'. As the coupling beams are one of the key structural elements in the coupled/core wall systems and expected to go under extensive nonlinearity, this chapter assess the model capability to capture different aspects of coupling beams behavior under lateral loading in both isolated and as part of a coupled wall system configuration. The inventory of the experimental programs introduced in chapter 4, is used here as the basis for validation of the model here.

5.1. Isolated Specimens

Geometry and reinforcement details for the beams are summarized in Table 5.1 and Figure 5.1.

Table 5.1: isolated specimen inventory with its geometry, reinforcing, and materials properties.

Specimen	l_n/h	α (degree)	Trans. Reinf.	Long. Reinf.	Diag. Reinf.	f'_c (ksi)	f_y (ksi)	f_u (ksi)
CB24F CB24F- RC	2.4	15.7	#3 @ 3 in.	N/A	12 #7	6.85 7.31	70	90
CB30-H	3.0	9	#4 @ 4 in.	4 #8 + 2 #7	4 #10	8.41	66	90
CB1 CB1A	1.9	18	#3 @ 3 in.	N/A	12 #7	6 6.4	62	90
BMB/BLB	2.5	18.9	#2 @ 2.5"	2 #4	2 #5	6	52.9	75.7

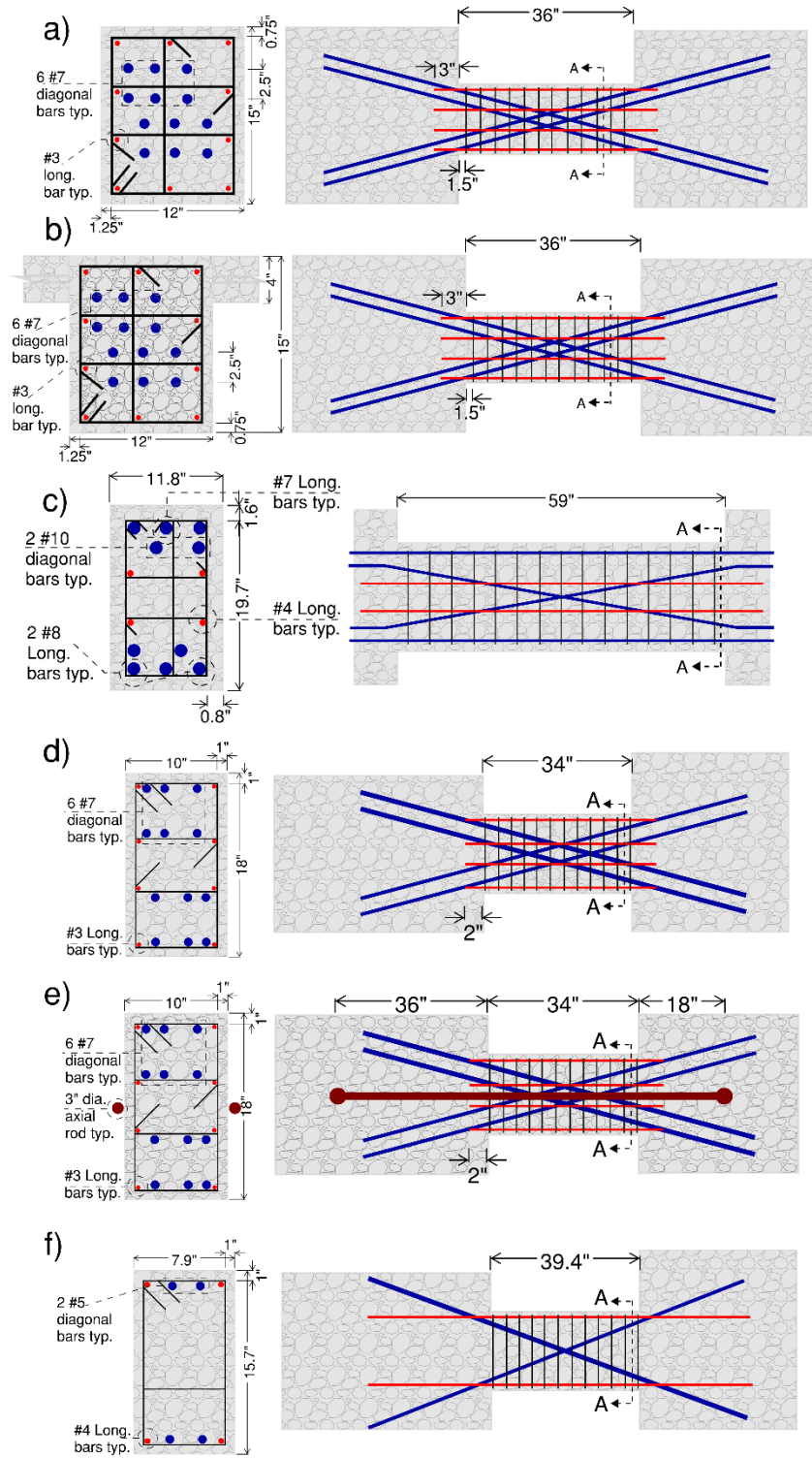


Figure 5.1: Specimens detail: a) CB24F; b) CB24F-RC; c) CB30-H; d) CB1; e) CB1A; f) BMB.

5.1.1. Material Calibration

5.1.1.1. Constitutive Concrete Material

As discussed in chapter 3, Concrete02 used to simulate the constitutive concrete material in the CBeam model. A key feature of this model is its flexibility, allowing for accurate adjustment of parameters such as peak stress (f'_c), strain at peak stress (ϵ_0), concrete crushing strength ($f'_{c,U}$), and strain at crushing strength (ϵ_U). Additionally, the λ parameter, defines the shape of the curve by setting the ratio between the unloading slope at ϵ_U and the initial slope, increases the model's adaptability for simulating concrete behavior.

In the analytical model, especially for concrete under compression (as shown in Figure 3.7), establishing value for these parameters requires calibration. The calibration process is used to adjust the model to match actual concrete behavior, using stress-strain data from monotonic compression tests that were carried out alongside the experiments reported in the literature. Model behavior under tension is controlled using two main parameters, concrete tensile strength f_t and modulus during tension softening E_{ts} .

As the monotonic experimental results reported in the literature are based on the unconfined concrete materials, it is required to adopt a model to adjust the unconfined material parameters to represent a confined concrete material. For this study, the confined concrete envelope is based on empirical relationships established by Mander et al. (1988). These relationships provide essential information about the peak compressive stress (f'_{cc}) and the strain at peak stress (ϵ_{0c}). The confined concrete relation accounts for factors such as the area, layout, spacing, and yield stress of the transverse reinforcement in the confined areas of each test specimen.

Figures 5.2 to 5.7 present visual depictions of the compressive behavior of calibrated model for the unconfined concrete and the resulting model for confined concrete. Furthermore, Table 5.2 contains a detailed list of input parameters for each material.

Table 5.2: constitutive concrete material modeling parameters.

Specimen		f_{pc}	ϵ_{c0}	f_{pcu}	ϵ_U	λ	f_t	E_{ts}
CB24F	Unconfined	6.8	0.002	0.07	0.013	0.01	0.07	450
	Confined	8.0	0.0037	0.4	0.07		0.40	4.5
CB24F-RC	Unconfined	7.3	0.002	0.07	0.013		0.07	460
	Confined	8.6	0.0037	0.43	0.07		0.43	4.6
CB30H	Unconfined	8.4	0.002	0.08	0.015		0.08	490
	Confined	9.9	0.0043	0.5	0.081		0.50	4.9
CB1	Unconfined	6.0	0.002	0.06	0.013		0.06	420
	Confined	7.1	0.0033	0.36	0.53		0.35	4.2
CB1A	Unconfined	6.4	0.002	0.06	0.013		0.06	430
	Confined	7.3	0.0034	0.37	0.54		0.37	4.3
BMB/BLB	Unconfined	6.0	0.002	0.06	0.013		0.06	430
	Confined	7.4	0.0034	0.37	0.54		0.37	4.3

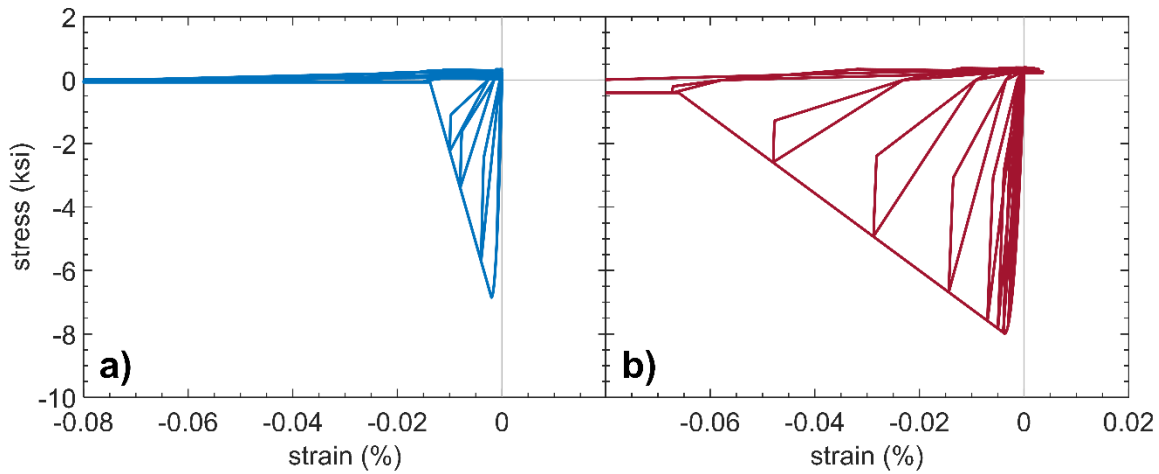


Figure 5.2: CB24F constitutive concrete material; a) unconfined concrete, b) confined concrete.

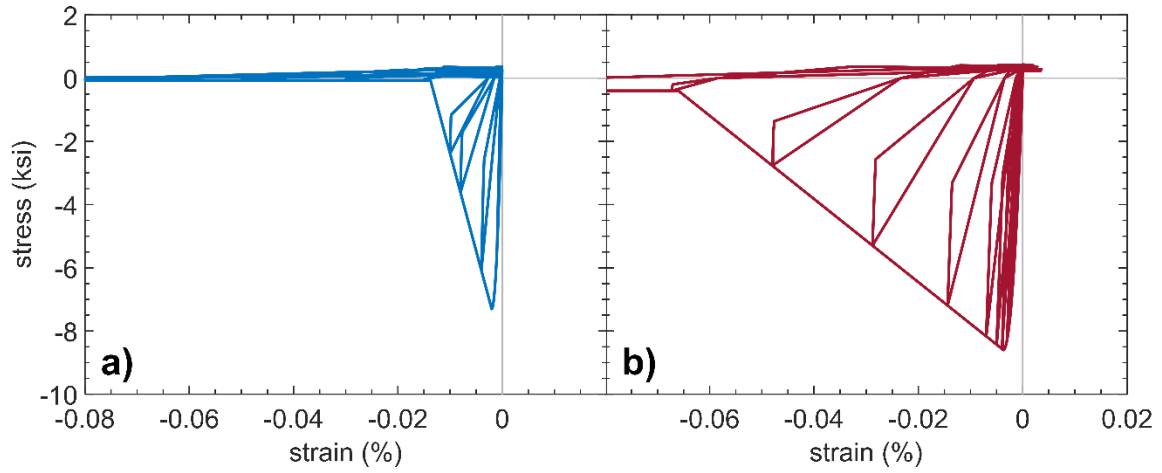


Figure 5.3: CB24F-RC constitutive concrete material; a) unconfined concrete, b) confined concrete.

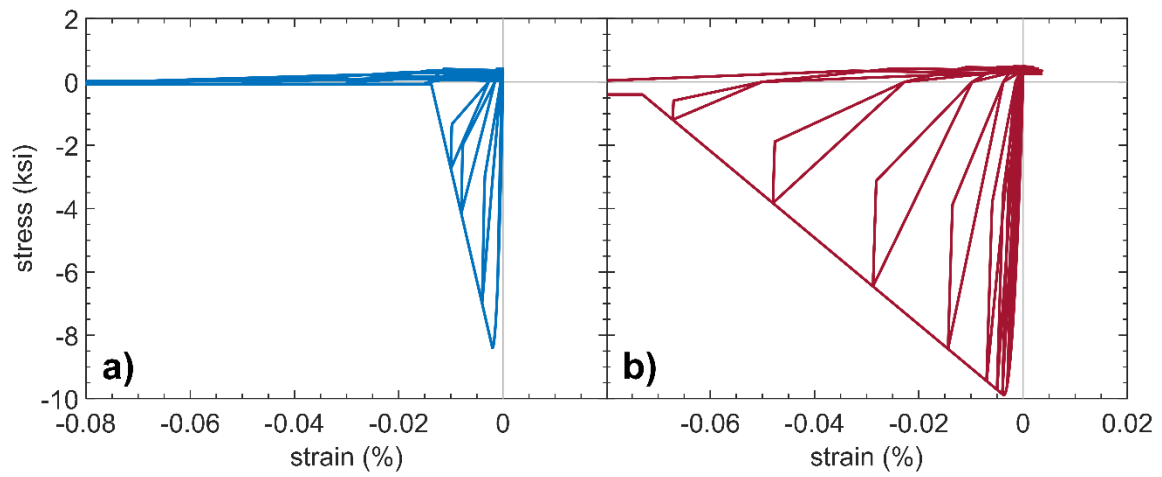


Figure 5.4: CB30H constitutive concrete material; a) unconfined concrete, b) confined concrete.

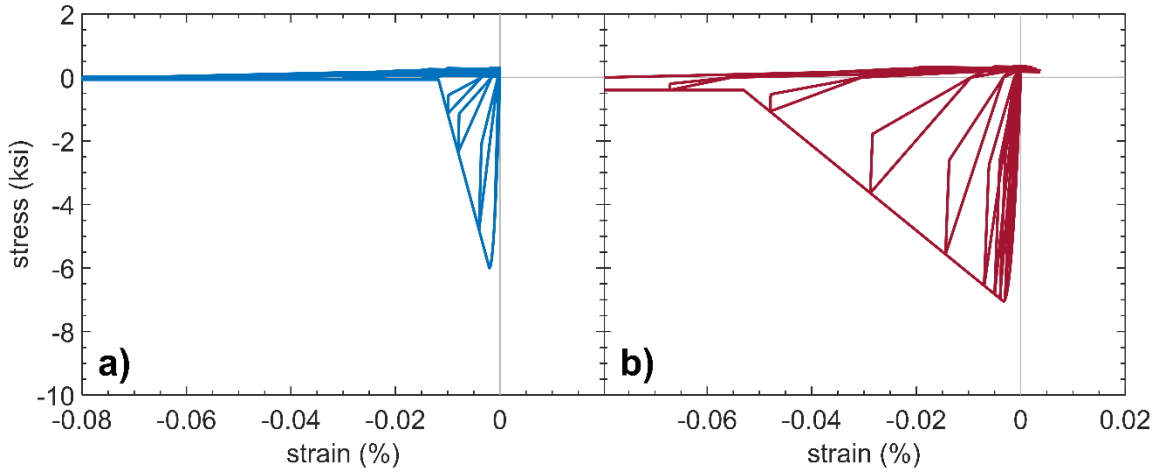


Figure 5.5: CB1 constitutive concrete material; a) unconfined concrete, b) confined concrete.

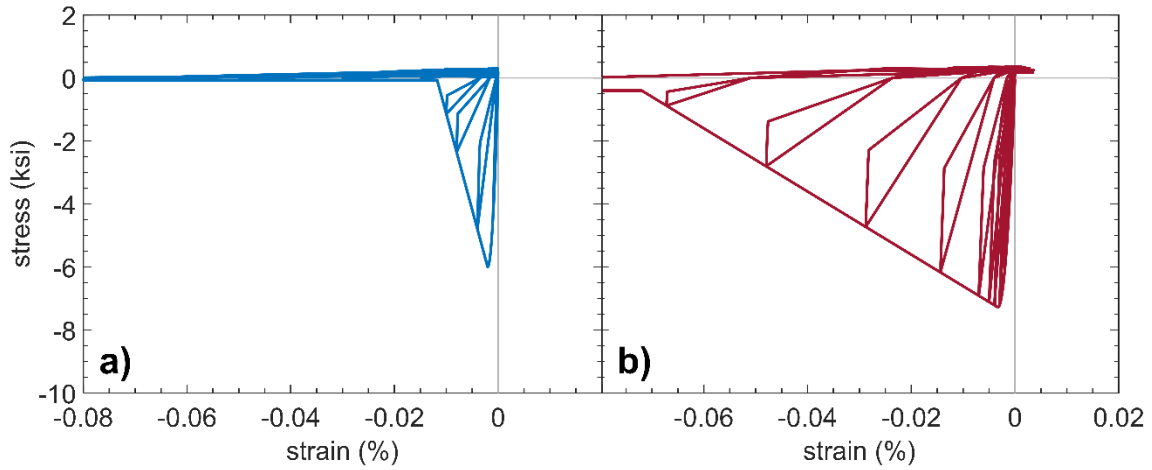


Figure 5.6: CB1A constitutive concrete material; a) unconfined concrete, b) confined concrete.

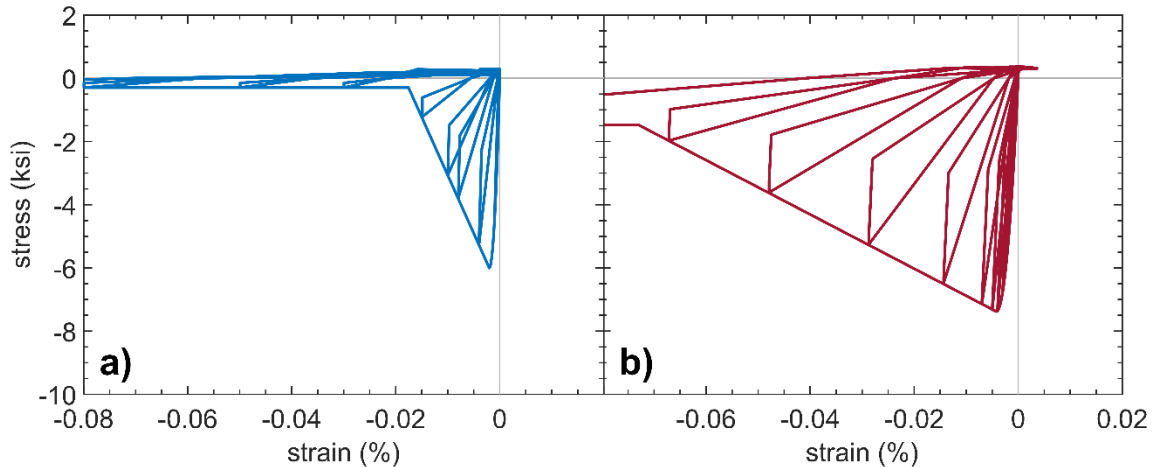


Figure 5.7: BMB/BLB constitutive concrete material; a) unconfined concrete, b) confined concrete.

5.1.1.2. Constitutive Steel Material

To simulate the behavior of reinforcing steel, the Chang and Mander (1994) formulation is adopted. This model is available in the OpenSees material library as “ReinforcingSteel” (detailed information of this material model is provided in chapter 3). The standard stress-strain relationship shown in Figure 3.3 offers a basic understanding of how this material model works under different loading conditions.

A key aspect of this stress-strain relationship is its adaptability, allowing for calibration of various parameters. These parameters include the yield stress (f_y), ultimate stress (f_u), initial strain hardening tangent (E_{sh}), strain at initial strain hardening (ϵ_{sh}), and strain at peak stress (ϵ_{su}). The model also accommodates the inclusion of buckling behavior, using parameters such as the rebar slenderness ratio (l_{sr}), the amplification factor for the buckled stress-strain curve (β), the buckling reduction factor (r), and the buckling constant (γ). Besides these static properties, the material model also considers the dynamic properties of steel by incorporating fatigue-related parameters, which include C_f for the Coffin-Manson constant 'C', α for the Coffin-Manson constant 'a', and C_d for the cyclic strength reduction constant.

Table 5.3 lists the modeling parameters used for each test specimen, and Figure 5.8 shows the resulting uniaxial hysteretic behavior of each steel material with these modeling parameters are applied.

Table 5.3: constitutive material modeling inputs.

Specimen	f_y	f_u	E_s	E_{sh}	ϵ_{sh}	ϵ_{ult}	l_{sr}	β	r	C_f	α	C_d
CB24F & CB24F-RC	70	90					4.5					
CB30H	66	90	29000	870	0.012	0.11	3.2					
CB1 & CB1A	62	89					3.4	1.1	0.8	0.26	0.45	0.4
BRI-BMB D16	52.9	75.7	31006	620			4.8					
BRI-BMB D13	62.6	78.5	25745	530	0.019	0.1	6.0					
BRI-BMB D10	51.8	70.3	24891	520			8.0					

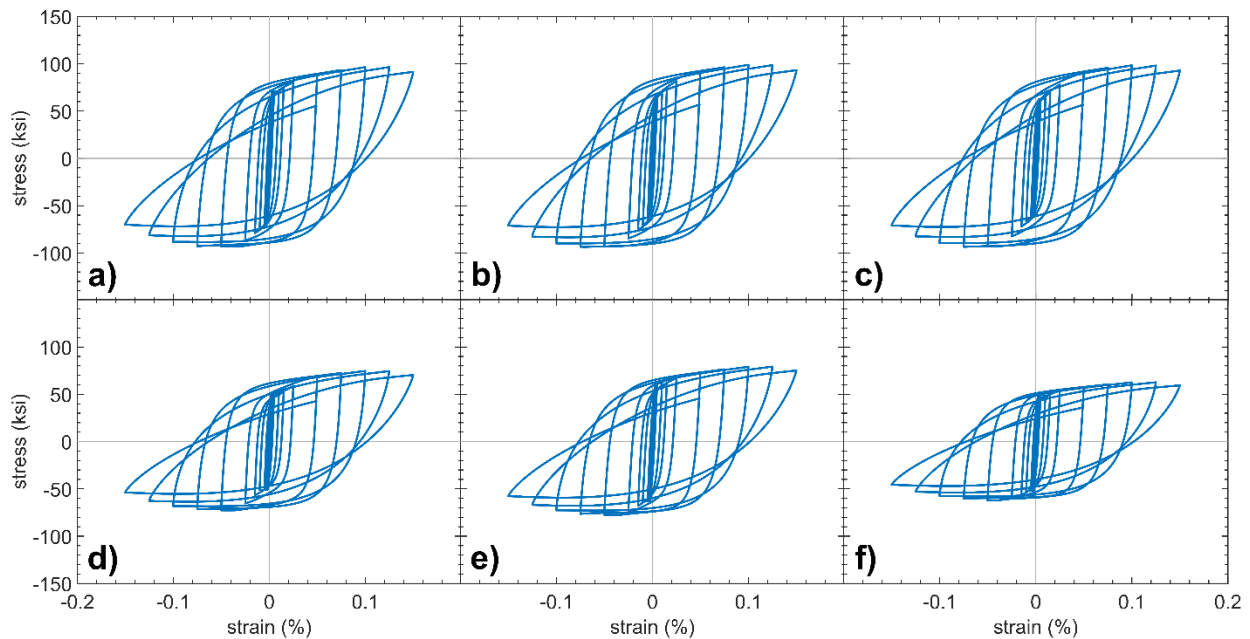


Figure 5.8: Constitutive steel material; a) CB24F & CB24F-RC, b) CB30F, c) CB1 & CB1A; d) BRI-BMB D16; e) BRI-BMB D13; f) BRI-BMB D10.

5.1.1.3. Slip-extension Relationship

To properly simulate the anchorage conditions of reinforcing bars in walls or support blocks, zero-length contact elements are implemented in the model. These elements are specifically designed

to replicate the interaction of rebars with the supports. The material properties of these contact elements follow the slip-extension material model described in section 3.4.3.

The “Bond-SP01” material model in OpenSees provides a versatile set of parameters for accurately defining the slip-extension behavior of reinforcing steel embedded into concrete. These parameters include the yield strength of the reinforcement steel (F_y), the slip at the member interface under yield stress (S_y) measured in inches (not strain), the ultimate strength of the reinforcement steel (F_u), the slip at the loaded end at the point of bar fracture (S_u), the initial hardening ratio in the monotonic slip versus bar stress response (b), and a pinching factor affecting the cyclic slip versus bar response (R). The resulting relations are summarized in Figure 5.9 and Table 5.4 for each specimen.

Table 5.4: Bond-Sp01 material input for assigned diagonal steel slip-extension behavior.

Specimen	F_y	S_y	F_u	S_u	b	R
CB24F & CB24F-RC	70	0.020	90	0.198		
CB30H	66	0.031	90	0.307		
CB1 & CB1A	62	0.018	90	0.183	0.5	0.6
BRI-BMB D16	51	0.015	70	0.154		
BRI-BMB D13	63	0.014	75	0.143		
BRI-BMB D10	52	0.013	60	0.134		

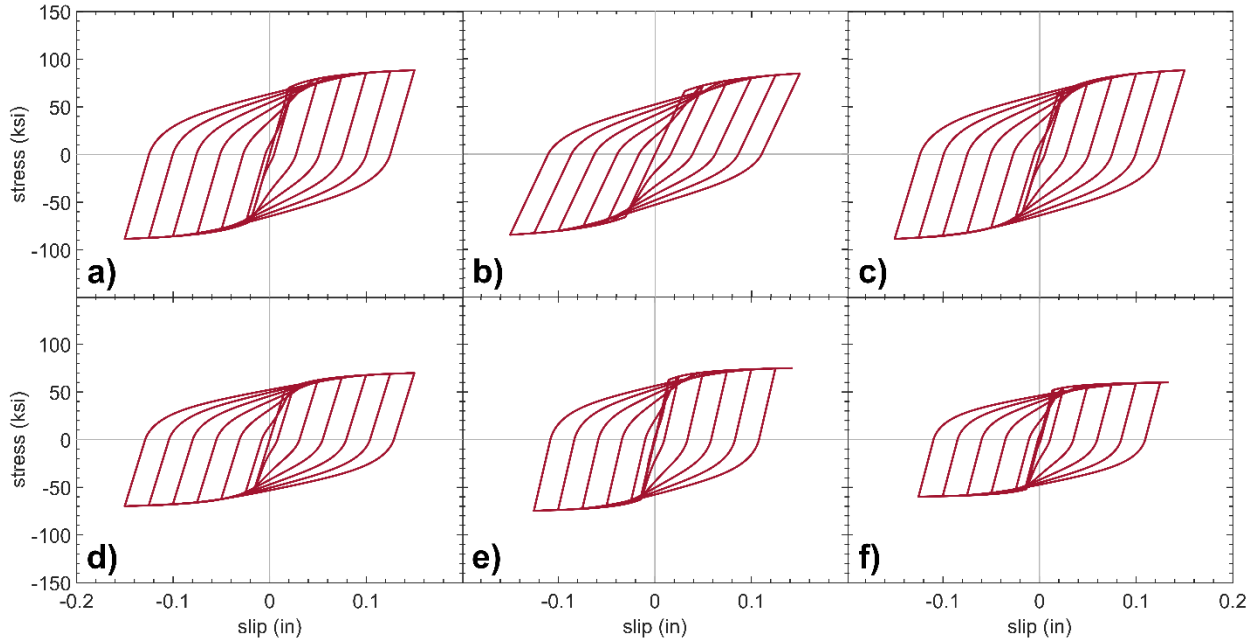


Figure 5.9: Slip-extension behavior; a) CB24F & CB24F-RC, b) CB30F, c) CB1 & CB1A; d) BRI-BMB D16; e) BRI-BMB D13; f) BRI-BMB D10.

5.1.2. Geometry Calibration

The process of geometrically discretizing isolated coupling beam specimens consists of two primary steps. First, the cross-section of the specimen, without diagonal bundles of rebar, is defined using a displacement-based, fiber-based approach. Each cross-section is modeled using fibers of approximately 0.5 inches by 0.5 inches to represent both confined and unconfined concrete areas (Fig. 5.10.a). Next, the diagonal bars are modeled based on the number of layers in each bundle, along the span of the beam (Fig. 5.10.b).

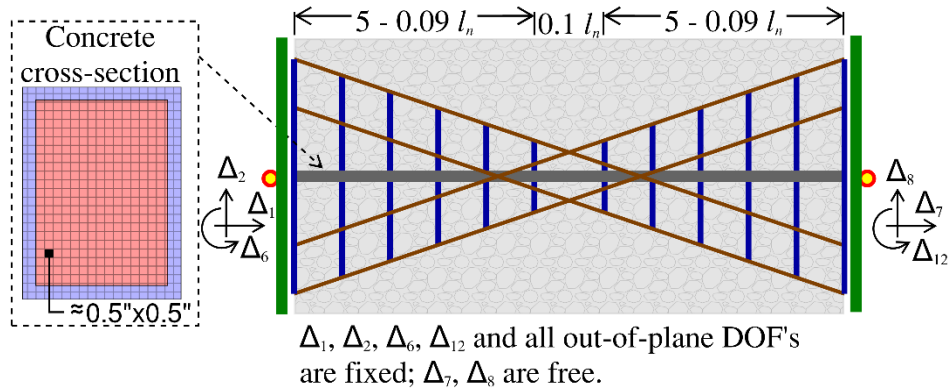


Figure 5.10: a) cross-section discretization; b) longitudinal discretization and boundary condition.

Chapter 3 includes a description of the analytical model of a coupling beam consisting of 'n' segments along its length. A sensitivity study was carried out to determine the ideal number of segments to accurately simulate the measured response of the coupling beam test specimens. This study involved varying the number of segments from one to thirteen and examining the results obtained using the model, e.g., yield strength and strengths at 2% and 5% chord rotations. The findings, shown in Figure 5.11, indicate that there is minimal change in both yield strength and strengths at 2% and 5% chord rotations if more than nine segments are used. Based on this study, a uniform approach of using eleven segments for all specimens was adopted (Figure 5.10.b).

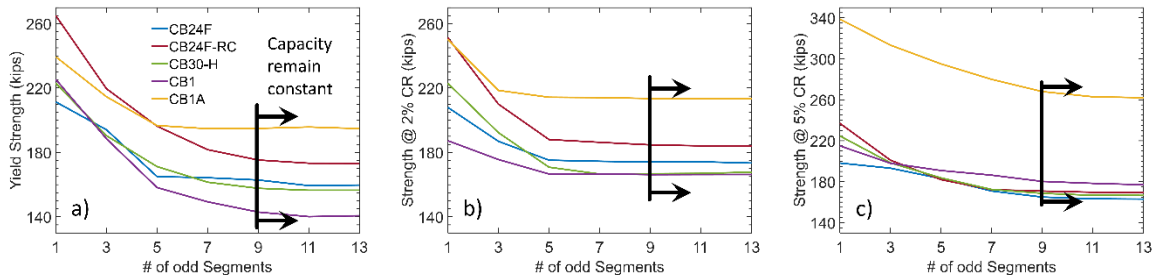


Figure 5.11: sensitivity of the CBeam model yield strength to the number of segments. a) yield strength sensitivity; b) strength at 2% chord rotation sensitivity; and c) strength at 5% chord rotation sensitivity.

5.1.3. Load Application and Solution Algorithm

Before applying lateral forces to the models of the isolated coupling beam test specimens, a constant axial load was applied to the end node of the element with translation in the axial direction (DOF 7) unrestrained (see Figure 5.10 for DOF numbering). This step is necessary to account for the axial load conditions for each of the experimental tests. Subsequently, a displacement-controlled analysis was conducted, involving the application of a cyclic lateral displacement protocol at the free end of the element along DOF 8. The specifics of these displacement protocols, described as chord rotation percentages (representing the tip lateral displacement over the clear length of the element), are detailed in Table 5.5.

Table 5.5: Displacement protocols (chord rotation percentage).

Step	1	2	3	4	5	6	7	8	9	10	11	12
CB24F CB24F-RC	0.5 ^a	1.0 ^a	1.5 ^a	2.0 ^a	3.0 ^a	4.0 ^b	6.0 ^b	8.0 ^b	10.0 ^b	12.0 ^b	-	-
CB30-H	0.25 ^a	0.375 ^a	0.5 ^a	0.75 ^a	1.0 ^a	1.5 ^a	2.0 ^a	3.0 ^a	4.0 ^a	5.0 ^a	6.0 ^a	8.0 ^a
CB1 CB1A	0.2 ^b	0.3 ^b	0.5 ^b	0.75 ^b	1.0 ^b	1.5 ^b	2.0 ^b	3.0 ^b	4.0 ^b	6.0 ^b	8.0 ^b	10.0 ^b
BMB/BLB	0.25	0.5 ^b	1.0 ^b	2.0 ^b	3.3 ^b	-	-	-	-	-	-	-

^a Three cycles per step; ^b Two cycles per step.

The displacement-controlled analysis involved applying a unit point load in line with the applied displacement (DOF 8) representing the load pattern. The analysis included an initial displacement increment of 0.0001 chord rotation. In case of convergence difficulties, a strategy of progressively reducing the displacement increment by half was used, up to a maximum of 10 iterations. If convergence issues continued beyond this point, the analysis was stopped due to divergence errors; however, no divergence errors observed for any of the models used.

The numerical model used the Krylov-Newton solution algorithm, an effective method for solving complex structural problems implemented in OpenSees platform (Scott and Fennes, 2010). To ensure precise and reliable results, a strict convergence tolerance of $1.0e - 6$ was used. This

tolerance was used to monitor the normalized energy increment at each solution step, using the OpenSees command 'test EnergyIncr'.

5.1.4. Comparison of Analytical and Experimental Results

In this section, the analytical results obtained from the numerical simulations are compared with the experimentally measured responses to evaluate the accuracy of the model.

5.1.4.1. Specimens CB24F and CB24F-RC

Specimens CB24F and CB24F-RC are identical except for a 4-inch-thick slab on top of the coupling beam in CB24F-RC. Figures 5.12 and 5.13 offer a comparative analysis of the model predictions (laterally and axially) relative to the experimentally obtained lateral force and axial elongation versus chord rotation. The results for shear versus chord rotation show that the numerical model accurately predicts the initial and cyclic unloading/reloading lateral stiffness, yield and post-yield strength, and pinching characteristics.

However, there is a discrepancy in axial elongation, particularly after about 2% chord rotation (yield rotation), where the model underestimates the axial growth by around 30%. This discrepancy is due to two main reasons. First, as discussed by Naish et al. (2013), when the model starts to crack, the influence of slip-extension becomes more significant, introducing more uncertainties from the calibration of the slip-extension analytical model. Second, the tension behavior of the concrete affects axial growth by impacting the balance between residual stress in the diagonal steel and concrete. The model assumes the tension behavior of confined concrete to be 10% of its compression strength, with a post-yield slope equivalent to 1% of the elastic tangent, due to the lack of experimental results in the literature. Using a smaller concrete tensile strength increases the predicted axial growth; however, to provide a consistent basis for comparison between the models for all tests, the reported results are based on using $0.1f'_{cc}$.

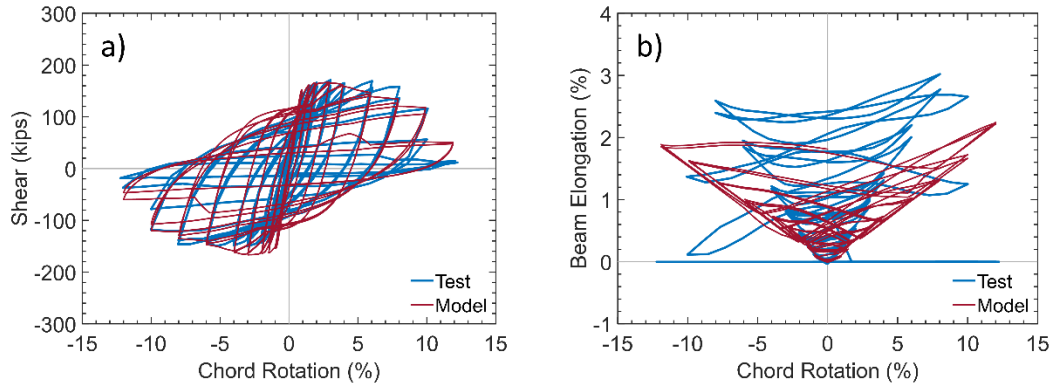


Figure 5.12: Comparison of measured and predicted responses of specimen CB24F: a) lateral load versus chord rotation; b) axial growth under lateral load versus chord rotation.

Focusing on the specimen with the RC slab (CB24F-RC), the analytical model accurately predicts the initial and cyclic unloading-reloading stiffness, and the pinching characteristics of the obtained lateral load-displacement response (Figure 5.13.a). However, similar to the results for CB24F, Figure 5.13.b shows that the model tends to overestimate the axial stiffness of the beam by about 30%. Besides the reasons already discussed for the discrepancy in axial growth between the test obtained values and the analytical model for CB24F, an additional factor is relevant for CB24F-RC. The analytical model is based on the plane-sections assumption, leading to a uniform stress distribution in the RC slab. As a result, the entire T-shaped concrete section contributes to axial stiffness. Whereas, in reality, the stress distribution across the RC slab's cross-section is not uniform (following a 1:1 stress distribution), resulting in less stiffness compare to the analytical model.

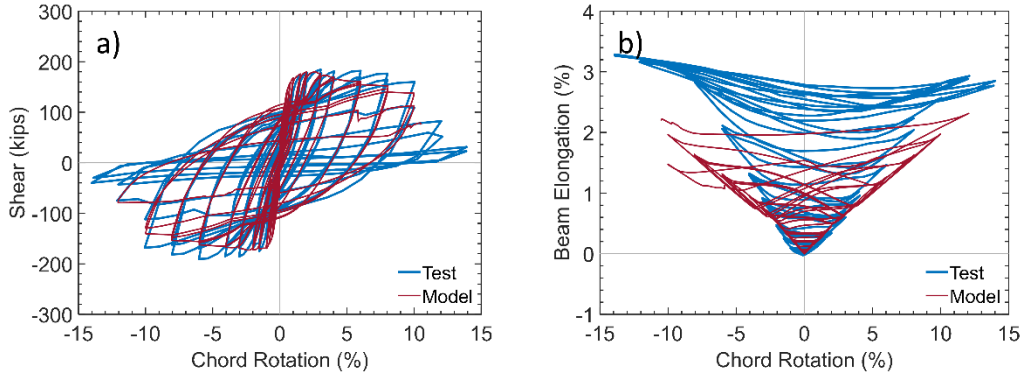


Figure 5.13: Comparison of measured and predicted responses of specimen CB24F-RC: a) lateral load versus chord rotation; b) axial growth under lateral load versus chord rotation.

Comparing the lateral load-deformation behavior of specimens CB24F and CB24F-RC (Figure 5.14), it is noted that the RC slab increases the lateral strength of the specimen by about 17%. However, the moment-curvature analysis suggests (conducted by Naish et al., 2010) that this enhancement in lateral strength is due to the slab itself, rather than the axial restraint provided by the RC slab. It is important to highlight that the comparison of axial growth in both specimens shows that the presence of an RC slab in an isolated test setup does not significantly contribute to axial restraint (Figure 5.14.b). This observation aligns with the predictions of the proposed model (Figure 5.14.d).

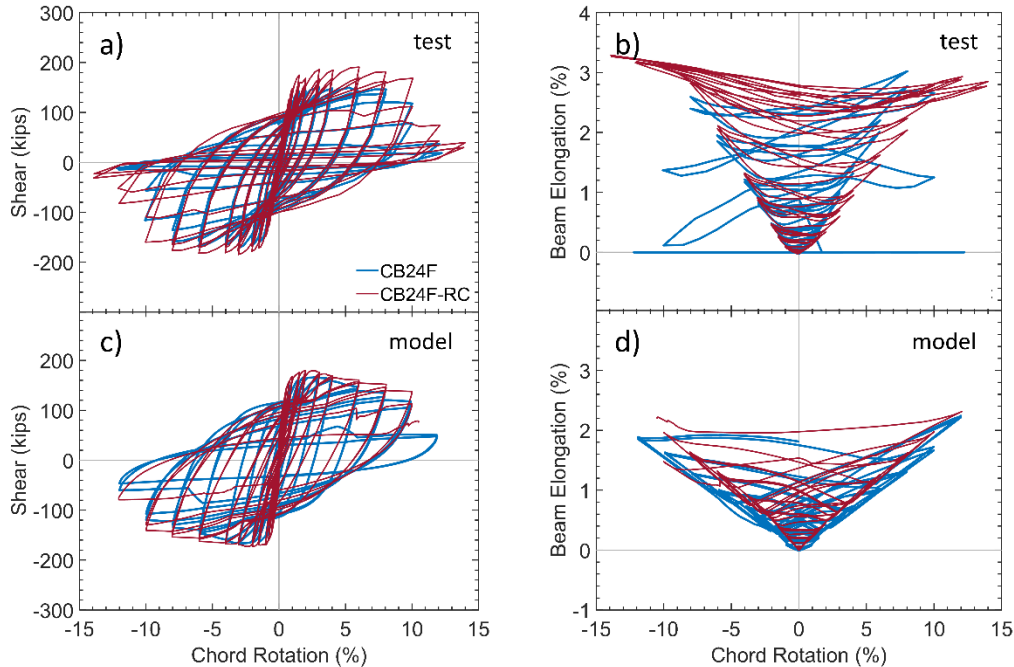


Figure 5.14: CB24F vs CB24F-RC global response comparison: a) experimental shear vs chord rotation; b) experimental axial growth vs chord rotation; c) numerical shear vs chord rotation; d) numerical axial growth vs chord rotation.

5.1.4.2. Specimen CB30-H

Figure 5.15 shows the results for the hybrid reinforced test specimen, CB30-H. The model accurately predicts the lateral strength and stiffness of the specimen. It is observed that, in the test specimen, strength degradation starts at about 4% of the chord rotation, whereas in the model, significant strength degradation initiates at approximately 5.5% chord rotation. The model accurately predicts the specimen's residual strength, with a deviation from the test results of less than 3% in the positive direction and about 10% in the negative direction. The estimated axial growth of the specimen closely matches the experimental obtained values up to around 4% chord rotation. However, it is important to note that the experimental results show axial shortening after lateral strength degradation begins (4.5% chord rotation), which the model is not capable of replicating. This difference could be due to inaccuracies in the material models used, especially parameters related to the concrete material in tension and the assigned slip-extension behavior.

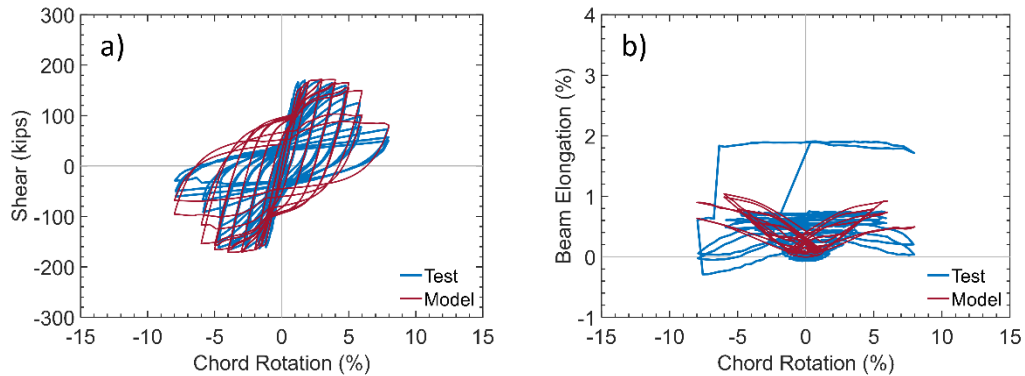


Figure 5.15: Comparison of measured and predicted responses of specimen CB30-H: a) lateral load versus chord rotation; b) axial growth under lateral load versus chord rotation.

5.1.4.3. Specimens CB1 and CB1A

Figure 5.16.a shows a comparison between numerical predictions and experimentally obtained lateral load-chord rotation responses for specimen CB1 (no axial restraint applied to this test specimen). The model accurately predicts the yield strength, ultimate strength, and strength degradation, with less than a 3% discrepancy from the test results. Additionally, the proposed analytical model successfully captures the hysteretic behavior, including unloading/reloading stiffness and the pinching effect. The estimation of axial growth from the model is also reasonably matched the experimentally obtained values. However, similar to previous specimens (CB30-H), the specimen during the experiment exhibits shortening at high chord rotations (after 5.5% chord rotation), a detail that the model does not replicate due to the limitation of the constitutive material models stress-strain relationships.

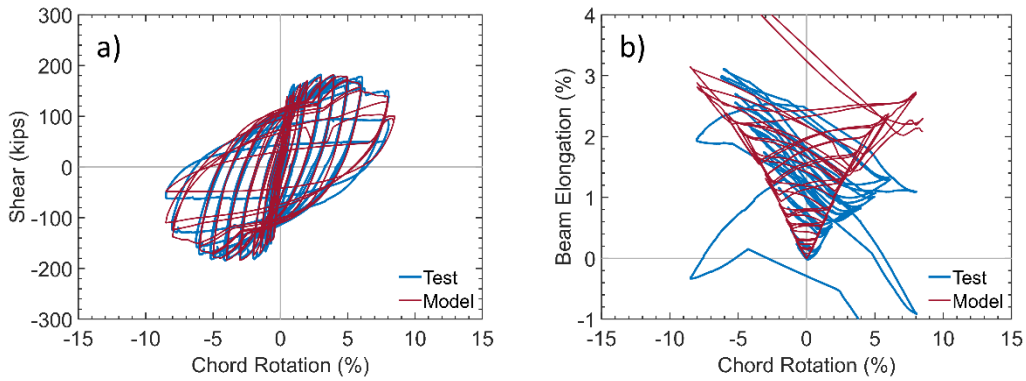


Figure 5.16: Comparison of measured and predicted responses of specimen CB1: a) lateral load versus chord rotation; b) axial growth under lateral load versus chord rotation.

The results depicted in Figure 5.17 illustrate that the axial restraint imposed by high-strength steel rods leads to an increase in the lateral strength of the coupling beam. The CBeam model effectively captures this behavior. The hysteretic behavior of the specimen before strength degradation aligns well with the experimental results. As shown in Figure 5.17.b, the predicted axial growth of the specimen aligns well with the experimentally obtained values.

The results shown in Figure 5.17 indicate that the axial restraint provided by high-strength steel rods results in higher lateral strength for coupling beam CB1A relative to CB1. The CBeam model successfully represents these changes in the lateral and axial strengths. The hysteretic behavior of the test specimen prior to strength degradation is consistent with that measured in the experimental and Figure 5.17.b shows that the model prediction of axial growth closely matches that of the experiment.

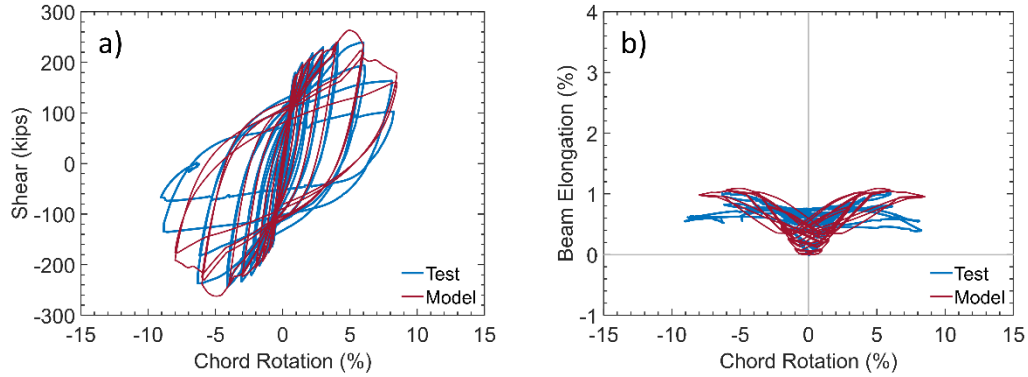


Figure 5.17: Comparison of measured and predicted responses of specimen CB1A: a) lateral load versus chord rotation; b) axial growth under lateral load versus chord rotation.

Comparison of CB1 and CB1A Specimens

The axial and lateral responses of two identical specimens, one with axial restraint and the other without, are compared under the same lateral loading protocol. Figure 5.1 shows the cross-sections of CB1 and CB1A, with axial restraint applied to CB1A using two 3-inch diameter rods on both sides of the specimen. Figure 5.18.b displays the total axial force developed in the rods versus chord rotation during the test. A closer examination of the axial force plot (Figure 5.18.a) indicates a difference in the axial stiffness of the rods prior to and after 1.3% chord rotation (almost 0.4% axial strain, as shown in Figure 5.17.b). Poudel A. et al., 2018 also noted that, due to concrete crushing at the points where the axial restraint fixture connected to the top and bottom blocks, the initial stiffness of the axial restraint system should be adjusted. Figure 5.19 illustrates the axial restraint behavior used in the analytical model to match the observed axial stiffness of the rods. Figure 5.18.b shows that the model predicted a maximum axial force of 215 kips, compared to 220 kips observed in the test, which is about 20% of $A_g f'_c$.

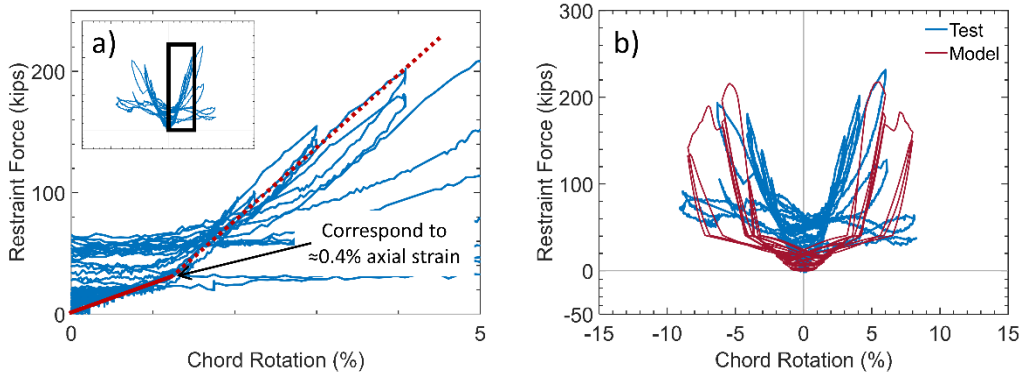


Figure 5.18: axial restraint force in CB1A specimen.

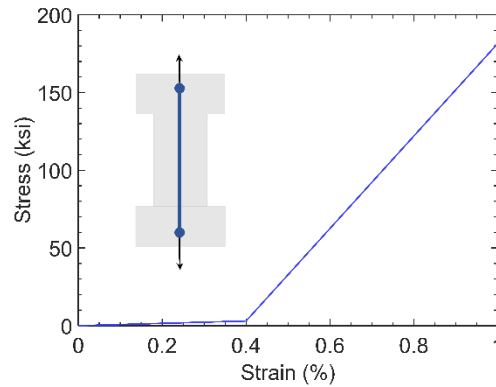


Figure 5.19: assigned axial restraint behavior.

The differences in behavior between specimens CB1 and CB1A, and the ability of the model to capture them, are summarized as follows:

1. **Axial Restraint in CB1A Specimen:** The axial restraint in specimen CB1A significantly reduced the axial elongation of the coupling beam. The model predicted this reduction accurately, with an overestimation of about 5%. The predicted restraint force was slightly less than the obtained value during the experiment.
2. **Increased Lateral Strength Due to Axial restraint:** The axial force from the axial restraint increased the lateral strength of the coupling beam by about 30%. The model

accurately predicted this increase in lateral strength with less than a 3% discrepancy at peak values.

3. **Reduction in Displacement Capacity:** The axial restraint reduced the lateral deformation capacity of the specimen by approximately 10%, which the model effectively captured.
4. **Elongation and Shortening Behavior:** Specimen CB1 elongated up to 2.5% at about 5.5% chord rotation during the experiment and then started to experience shortening in length. The model could not simulate this shortening due to limitations in the hysteretic behavior of the materials (both steel and concrete). In contrast, specimen CB1A exhibited much less elongation during the test, with negligible shortening at high chord rotations. The numerical model satisfactorily captured the experimental behavior even after 5.5% chord rotation.

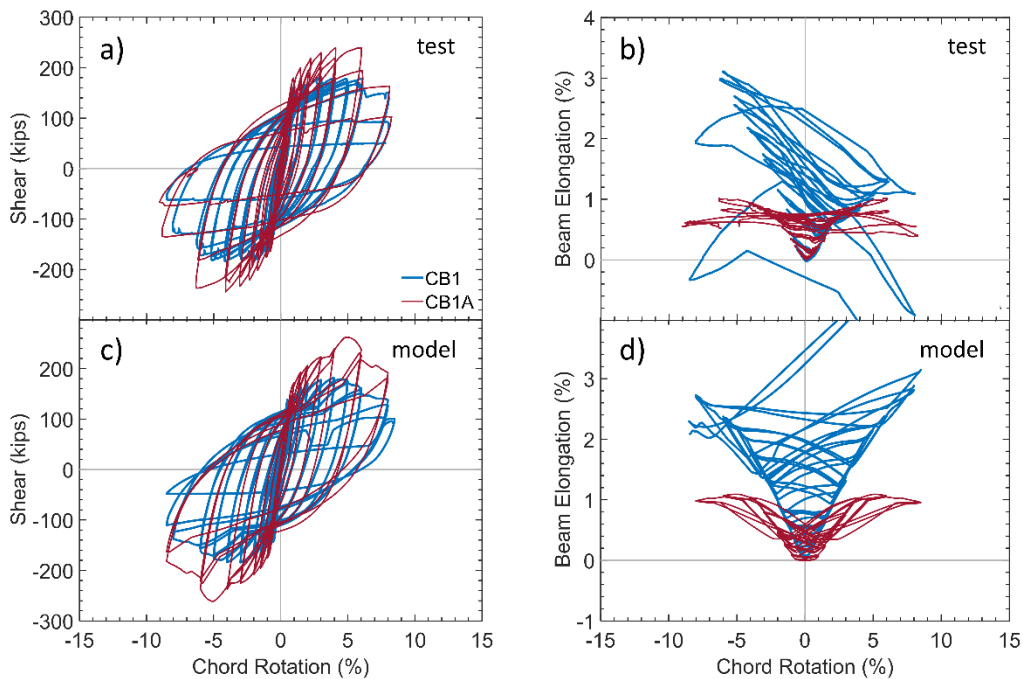


Figure 5.20: CB1 vs CB1A global response comparison: a) experimental shear versus chord rotation; b) experimental axial growth versus chord rotation; c) numerical shear versus chord rotation; d) numerical axial growth versus chord rotation.

5.1.4.4. Specimens BMB/BLB (BRI-1996)

In the 1996-BRI coupled wall experiment program, two identical coupling beam specimens were tested: one without a load cell within the beam (BMB) and the other with a load cell inside the beam (BLB), as shown in Figure 5.21. The purpose of these tests was to assess whether including the load cell affected the behavior of coupling beams, since the load cells were to be used in the coupling beams for the 12-story coupled wall test. According to Figure 5.22, both specimens BMB and BLB showed similar results in terms of lateral strength, rotation capacity, and cracking patterns near the support ends (Figure 5.21). The numerical simulation accurately replicated the strength and stiffness of these specimens. Figure 5.22 compares the experimentally obtained data with the numerically predicted lateral load-deformation response. The yield strength recorded in analytical study was 36 kips, compared to 39 kips obtained from the test. There was also a slight overestimation, around 5%, in initial stiffness, and a modest underestimation, about 5%, in the lateral peak strength of the coupling beam.

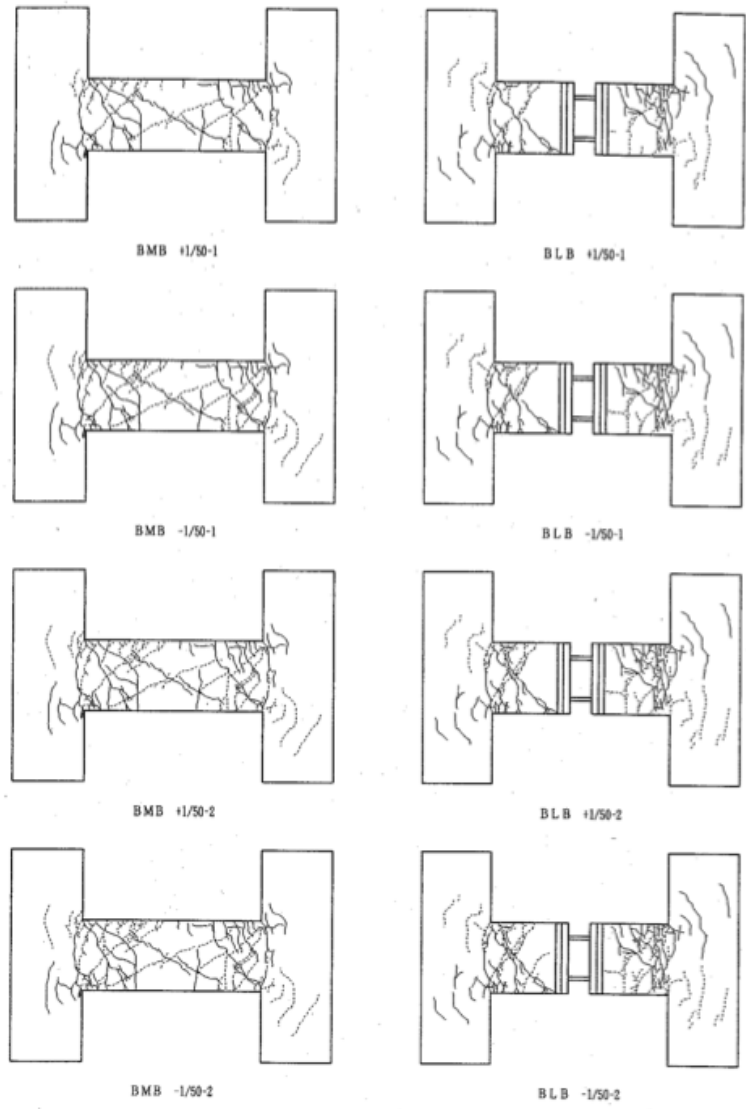


図4-6 (3) 試験体ひび割れ図

Figure 5.21: BLB versus BMB (Sugaya, 2003).

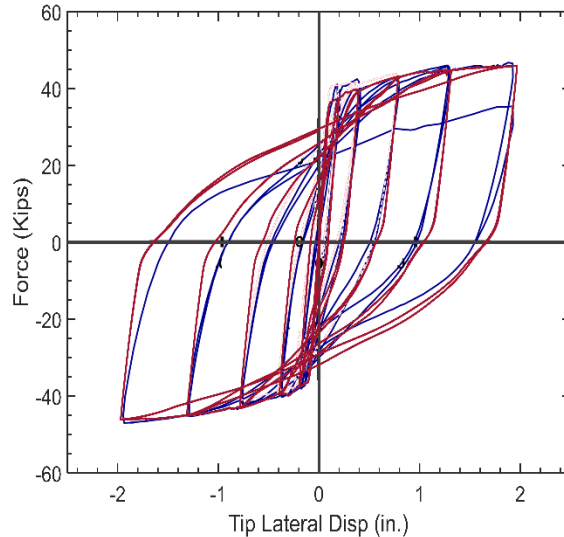


Figure 5.22: Comparison of measured and predicted responses of specimen BMB.

5.2. System-Level Coupled Wall Specimen

5.2.1. Behavior of the Test Specimen

The BRI-1996 T-shaped coupled wall test was subjected to a top (roof) level lateral drift of approximately 4%, leading to a significant decrease in lateral strength. Flexural cracks in the coupling beams started to appear at approximately 0.02% lateral top drift. For the web of the compression wall (what type of cracks, diagonal, horizontal, vertical?) and the flange of the tension wall (horizontal cracks), first cracks were observed around 0.1% top drift. The maximum base shear of 324 kips occurred at roughly 1.5% drift, with approximately 90% of this base shear resisted by the compression wall. At this shear force, the coupling beams reached their maximum shear strength, followed by significant shear strength degradation, causing the wall piers to act more independently (reduced coupling). At around 2% lateral drift, longitudinal (or was it diagonal, or both) reinforcement in the coupling beam buckled and concrete spalling was observed. Accumulated plastic deformations caused the coupling beams to elongate, and which was resisted by the wall piers, resulting in axial compression load within the beams. As top-level drift was increased further, damage (rebar buckling) was observed at base of the wall piers. At about

3.3% lateral top drift, reinforcement at the wall base buckled and fractured, and concrete crushing was evident (Sugaya et al, 2000).

In the early stages of lateral loading, prior to significant yielding (primarily elastic behavior), the shear force distribution in the tension and compression wall piers was approximately equal at all levels over the height of test specimen. However, as drift increased, a shift in shear force ratio between compression and tension walls became noticeable, especially at the 1st and 2nd stories, where the ratio peaked at 9:1 at 1.5% roof drift (Sugaya et al, 2000). This variation in shear force distribution, more pronounced in lower floors, suggested a stronger axial force in the coupling beams at these levels compared to higher floors.

The combined axial forces of the coupling beams over the height of the wall were around 140 kips, correlating to the shear distribution between the wall piers base shear (Sugaya et al, 2000).



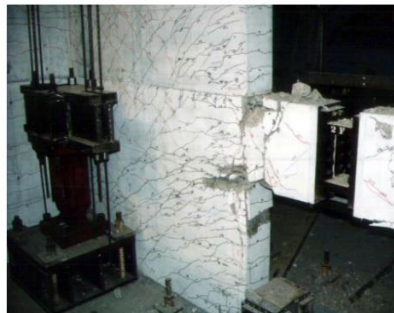
a. Elevation View of Deformed Coupled Wall



b. 8th Floor coupling beam (3.33% drift)



c. 8th Floor coupling beam (3.85% drift)



d. Damage at wall base (2.5%)



e. Damage at wall base (end of test)

Figure 5.23: Observed damage of BRI 12-Story Coupled Walls Test (Sugaya, 2003).

After the tests, Japanese researchers (ref) developed a multi-spring model using fiber elements to simulate the test results and to compare the analytical results obtained from test data. Since the test specimen did not include a slab (so that beam axial loads could be measured with load cells), the role of the floor slab was investigated based on an analytical study. Results of this study indicated that the slab would have a negligible influence on the behavior of the coupling beams;

these results is consistent with the finding from this study based on the test and model results obtained for specimens CB24F and CB24F-RC.

5.2.2. Model Development

This section details the development of a nonlinear OpenSees model for the twelve-story coupled T-walls experiment. The focus is on examining the behavior of the wall piers and coupling beams including the relationship between the axial growth and axial forces of coupling beams. The structural material properties for the test specimen follow the descriptions in section 5.1.

The analytical model replicates the loading sequence applied to the test specimen. Specific weights, including member self-weight, are applied to each floor level; lateral loads applied to 4th, 7th, and 12th levels. The model ensures equal horizontal displacement for nodes on both the left and right wall piers. The base of the model is fixed, preventing both translation and rotation. The model includes features to capture geometric nonlinearity and P-delta effects.

The RC shear walls were simulated using the MVLEM-3D element, an extension of the MVLEM element developed by Kolozvari (2013) and Kolozvari et al. (2015). This model was further developed and implemented in the OpenSees platform by Kalbasi (2019). The model employs vertical fibers, operating under the assumption that plane sections remain plain. This design allows it to simulate the axial and flexural behavior of the wall element. In addition, a shear spring is positioned horizontally within the element to capture wall shear behavior. The out-of-plane behavior is analytically replicated using an elastic Kirchhoff plate formulation. Figure 5.24 showcases the numerical model of the wall elements. The element has been validated against a range of experimental results under various loading conditions (see Kalbasi, 2019). The modeling properties of wall piers are summarized in Table 5.6, with an elastic shear strength of $0.5G =$

$$\frac{0.5E}{2(1-\nu)}$$

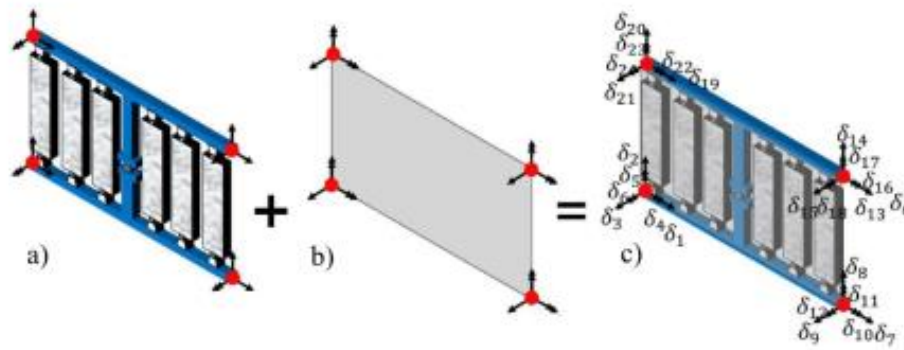


Figure 5.24: MVLEM-3D in-plane and out-of-plane behavior.

Table 5.6: Assigned shear wall elements properties.

Story	t_w (in.)	B.E. Length (in.)	$\rho_{v, BE}$ (%)	$\rho_{v, web}$ (%)	$\rho_{horiz.}$ (%)
12 th		11.81	3.097		
10-11 th					
7-9 th	7.87	15.75	2.821	0.639	0.16
4-6 th					
2-3 rd		19.69	2.655		
1 st					

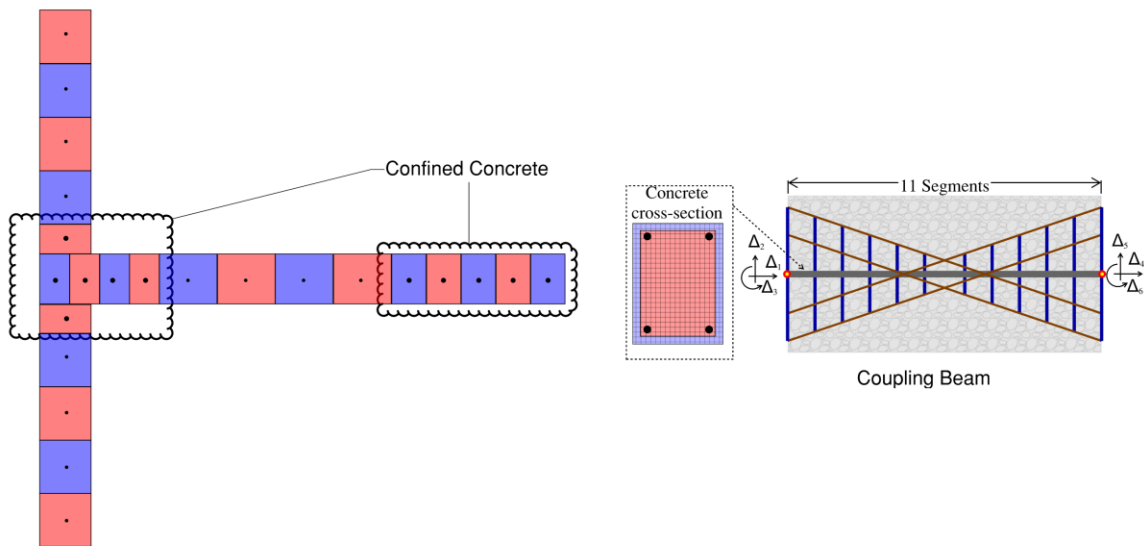


Figure 5.25: BRI-1996 wall pier cross-section and coupling beam discretization.

Steel reinforcement properties are detailed for each distinct rebar types within the OpenSees ReinforcingSteel model, as showcased in Table 5.3. Similarly, the properties of the concrete material are extracted from pre-test concrete cylinder tests. Modeling parameters for concrete compression and tension strengths, both for confined and unconfined concrete materials, are presented in Table 5.7.

Table 5.7: BRI-1996 12-story modeling concrete material parameters.

Story		f_{pc}	ϵ_{c0}	f_{pcu}	ϵ_U	λ	f_t	E_{ts}
12 th	Unconfined	4.0	0.002	0.07	0.013	0.01	0.04	400
	Confined	5.1	0.0035	0.4	0.06		1.0	4.0
10-11 th	Unconfined	3.9	0.002	0.07	0.013		0.04	400
	Confined	5.0	0.0035	0.43	0.06		1.0	4.0
7-9 th	Unconfined	4.1	0.002	0.08	0.015		0.04	400
	Confined	5.2	0.0036	0.5	0.06		1.0	4.0
4-6 th	Unconfined	4.2	0.002	0.06	0.013		0.04	400
	Confined	5.4	0.0037	0.36	0.05		1.1	4.0
2-3 rd	Unconfined	5.9	0.002	0.06	0.013		0.06	600
	Confined	7.3	0.0049	0.37	0.05		1.4	6.0
1 st	Unconfined	5.7	0.002	0.06	0.013		0.06	600
	Confined	7.1	0.0048	0.37	0.05		1.4	6.0

Coupling beams were analytically modeled using the proposed CBeam model, with Figure 5.26 illustrating an analytical representation of the entire structure. The entire coupled wall system model is subjected to specified gravity loads, subsequently followed by a series of nonlinear static pushover analyses (hysteretic analysis). These analyses mimic the displacement history applied to the test specimen. Lateral load patterns are designated to gradually intensify in both positive and negative directions at specific levels, with the specified distribution of forces along the height of the structure (1.0, 1.97, and 3.73 correspond to 4th, 7th, and 12th floor levels).

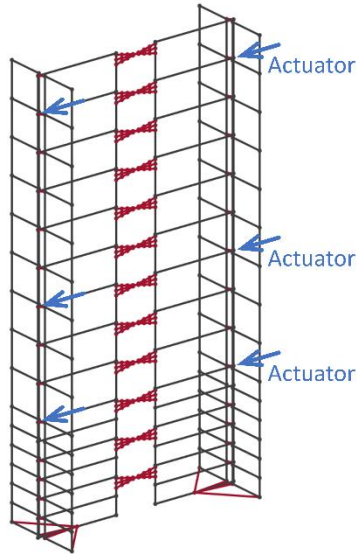


Figure 5.26: visually represents the BRI-1996 OpenSees analytical model.

5.2.3. Predicted Behavior

The hysteretic analysis conducted on the analytical model and completed with less than 12 minutes of runtime using a computer machine running on a 64-bit Windows 11 operating system that was equipped with an Intel(R) Core(TM) i9-10885H CPU @ 2.40GHz processor and 64.0 GB of RAM memory. As depicted in Figures 5.27 and 5.28, a good match is achieved between the observed and predicted base shear versus roof drift responses for the test specimen. The model closely captures the initial stiffness observed in the tests and the estimated yield force for the model is about 5% less than that obtained value in the experiment. Stiffness predictions for higher drift cycles (lateral roof displacements higher than 8 inches) for loading and unloading phases are about 15% higher than obtained values. Two primary factors contribute to these variances:

- The wall model formulation is based on the assumption that a plane-section remains plan, which results in an over-estimation of the contribution of the effective flange width to lateral stiffness. This topic is addressed in more detail in studies such as Kalbasi (2019) and Kolozvari et al. (2021).

- The empirical equations used for slip-extension model calibration (Zhao and Sritharan, 2007) - S_y is based on limited amount of test data. This could result in discrepancies of up to 25% between the predicted slip-extension behavior and obtained S_y values during the tests. The empirical equations used for slip-extension model calibration (Zhao and Sritharan, 2007) - S_y is based on limited amount of test data. This could result in discrepancies of up to 25% between the predicted slip-extension behavior and obtained S_y values during the tests.

Regardless of these potential sources of discrepancies, the model was able to well capture the highly pinched cyclic responses associated with the roof drift versus base shear relationship.

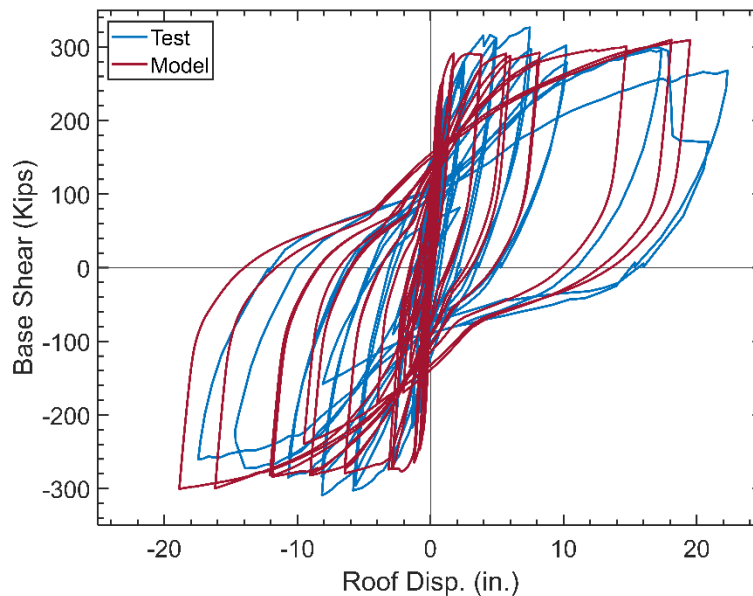


Figure 5.27: test versus analytical model BRI-1996 system roof displacement – base shear.

To assess the efficacy of the numerical model in predicting the behavior of coupling beams over the height of the test specimen, model predictions were compared to experimental results. Figure 5.28.a provides a comparison between shear forces and lateral displacements for all coupling beams over the height of the coupled wall test. Notably, both the initial and unloading-reloading

stiffnesses of all beams are reasonably accurately replicated; however, the pinching behavior, while accurately captured for the 2nd floor beam and all beams above the 7th floor, is slightly underestimated for coupling beams between floors 3 and 7. The yield strengths of coupling beams are generally overestimated from 5% to 15%. Figure 5.28.b reveals that the model reasonably captures the axial growth and force across all coupling beams, although the axial forces developed in the beams, especially for the 2nd-floor beam, are underestimated. This discrepancy is likely a result of the interaction between the nonlinear responses of the wall piers and the coupling beam (jacking behavior as also reported by Malcolm, 2015). Overall, when combined with the “MVLEM-3D” model, the CBeam model reasonably accurately captures the responses obtained in the test of the BRI-1996 structure, providing a balance between model complexity and the simulation of important behavior not captured using modelling approaches currently used for design.

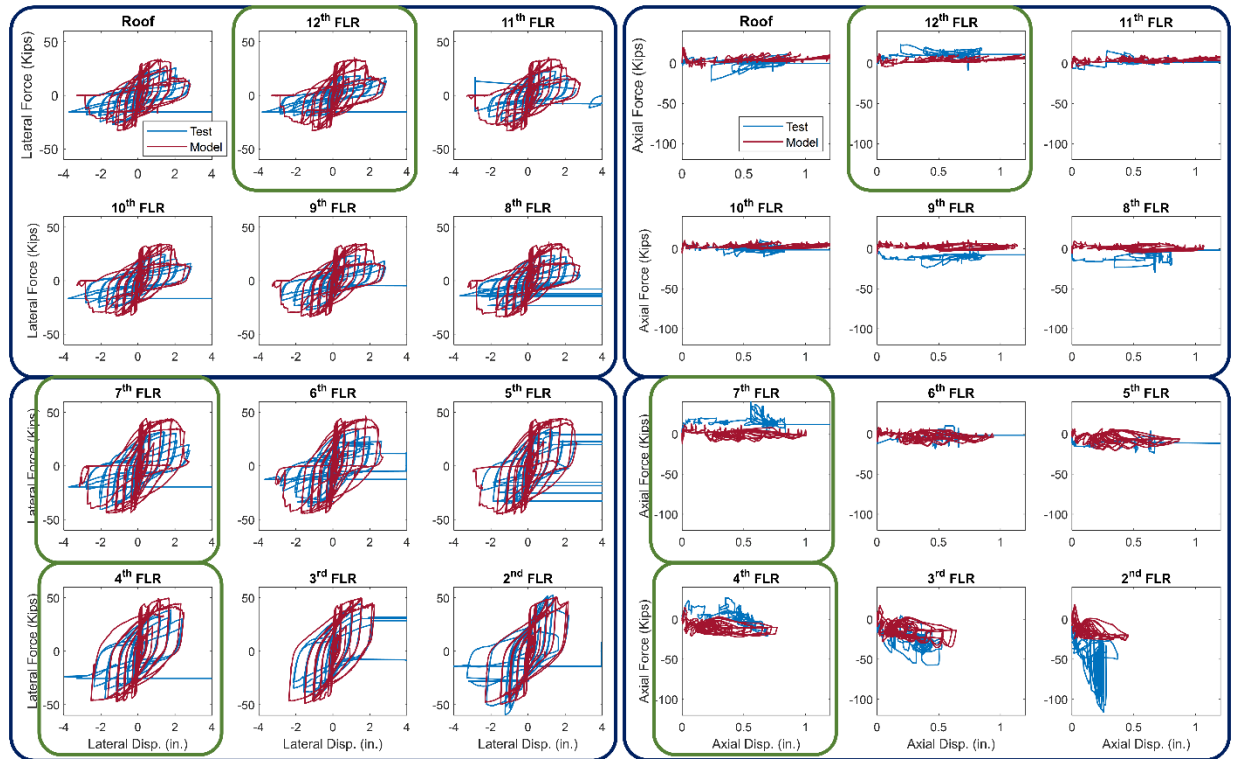


Figure 5.28: BRI-1996 coupling beams test versus analytical model lateral shear – lateral displacement and axial force – axial growth hysteretic behavior. Floor levels with the same coupling beams are separated with navy boxes; Floor levels connected to actuators are depicted with green boxes.

5.2.4. Summary of Analytical Results

The proposed coupling beam model (CBeam) is validated through various isolated test specimens and a 12-story coupled wall system specimen. The analytical study revealed the followings:

1. The model is both computationally efficient (in terms of runtime) and stable (in terms of convergence stability).
2. The lateral strength and stiffness of isolated coupling beam tests under various boundary conditions were accurately captured.
3. Axial growth and axial force in the isolated coupling beams were reasonable well captured in all specimens except the CB24F and CB24F-RC with a maximum discrepancy of 30% from the experimentally obtained values.

4. The model is computationally efficient: the analysis duration for the investigated coupled wall specimen was approximately 12 minutes, with convergence achieved using the Krylov-Newton method, leveraging the current tangent stiffness during the analysis.
5. In conjunction with the MVLEM-3D wall element models, the CBeam model predicts the overall load-displacement behavior of the coupled wall specimen subjected to unidirectional loading with a reasonable degree of accuracy (typically in the range of 0 to 15% for initial and unloading/reloading stiffness). The estimated lateral yield strength of the walls falls within 5% of the experimentally determined values for loading cycles applied in the direction of the coupled wall.
6. Due to the limitations of the plane-sections-remain-plane assumption incorporated within the MVLEM-3D element, effective widths associated with wall flanges are overestimated and the unloading/reloading lateral stiffness of the coupled wall system was overestimated by 15%.
7. The proposed analytical model can predict, with significant precision, the observed lateral strength of coupling beam elements during the experiment. However, determining the axial strength of the coupling beams is more challenging due to various factors, such as the sensitivity of results to slip-extension behavior between rebars and concrete, concrete material tension behavior, the behavior of adjacent wall piers, i.e., their nonlinear strength and stiffness.

6. CORE WALL DESIGN

Linear analysis is commonly used in code-based design to determine the design actions. However, this method doesn't account for the redistribution of internal forces that happens when a structure undergoes nonlinear behavior, a phenomenon confirmed by many experimental studies, such as BRI-1996 as discussed in chapter 5. This redistribution is particularly significant in coupled wall systems, where the interaction between wall piers is heavily influenced by their relative stiffness and strength. Applying nonlinear analysis could potentially allow for improved understanding of the redistribution that occurs, provided the model is capable of modeling the force redistribution. Additionally, considering force redistribution might enable the development of more efficient designs for coupled walls compared to those based solely on conventional linear analysis.

To better understand force redistribution in coupled wall systems, imagine a symmetric planar coupled wall system under lateral forces, without the influence of vertical acceleration or gravity forces, as depicted in Figure 6.1. In linear analysis, identical wall piers are assumed to have the same flexural, shear, and axial stiffness. Under these conditions, analysis would show that both tension and compression wall piers experience the same shears and moments over the wall height. However, the compression wall pier, due to its higher axial compressive force (as can be seen in the P-M diagram of the wall pier), will provide higher moment and shear strength and stiffness than the tension wall pier. Therefore, the shears and moments in the compression wall pier are expected to be greater than those in the tension wall pier.

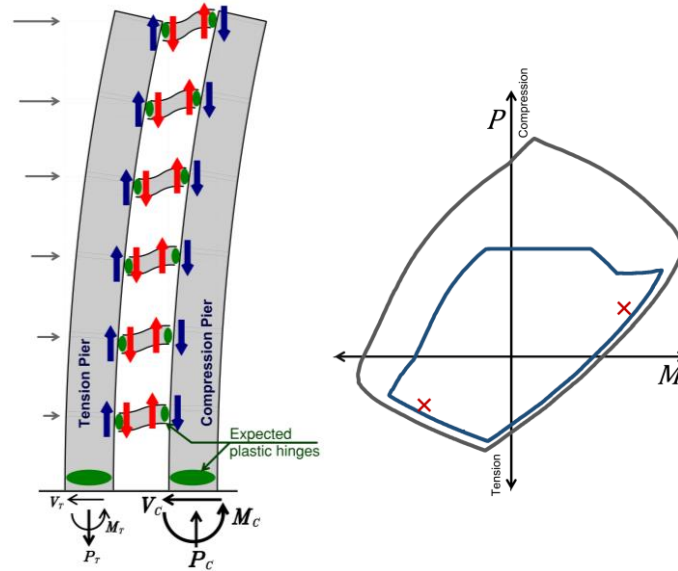


Figure 6.1: coupled wall internal forces and wall piers P-M diagram.

As outlined in the Introduction, this study presents a novel distributed fiber-based diagonally reinforced coupling beam model designed to capture the influence of axial restraint on the lateral strength and stiffness of the coupling beams. The model was validated against a variety of test data under diverse loading and boundary conditions. The results show reasonable accuracy in predicting the data from the tests. With this tool in hand, analytical core wall system models can more effectively represent the redistribution of shear force demands and the variation of axial force demand on between adjacent wall piers.

According to ACI 318-19, the shear demand on walls determined using ASCE 7-16 lateral loads is amplified by a shear amplification factor of up to 3; however, the nominal shear strength of walls is unchanged from prior versions of ACI 318. This increase in demand, along with no change in the capacity, mandates designers to increase wall shear reinforcement and wall thickness to resist the higher demand. Conversely, recent advancements in computational hardware and machine learning algorithms have enable the development of improved expressions for wall shear strength, including equations that account for the influence of axial force, longitudinal reinforcement, and flanges on wall shear strength (Rojas-Leon, 2022).

This chapter introduces a design procedure aimed at accurately capturing the redistribution of shear forces between adjacent wall piers and also considering the influence of axial force, horizontal and longitudinal reinforcement, and wall flanges on wall pier shear strength. The results obtained with the proposed approach are compared to results obtained with the current design practices through various archetypes designs to assess the efficiency of the proposed design approach. Finally, the designs are evaluated using nonlinear static and dynamic analyses in Chapters 7 and 8, respectively, to evaluate the expected performance of the various designs.

6.1. Archetypes

A basic rectangular building floor plan is used as the starting point for verifying the proposed design procedure. The goal is to achieve maximum wall piers axial load ratio of around $0.3A_g f'_c$ under the load combination $1.2D+1.6L$, get as close as possible to the drift limit of 2% per ASCE 7-16, and achieve a $\phi V_n / V_u$ close to 1.0. A typical story height of 13 ft is used. An 8-inch post-tensioned slab is used on all levels, with a 6 ft cantilevered overhang, as depicted in Figure 6.2.

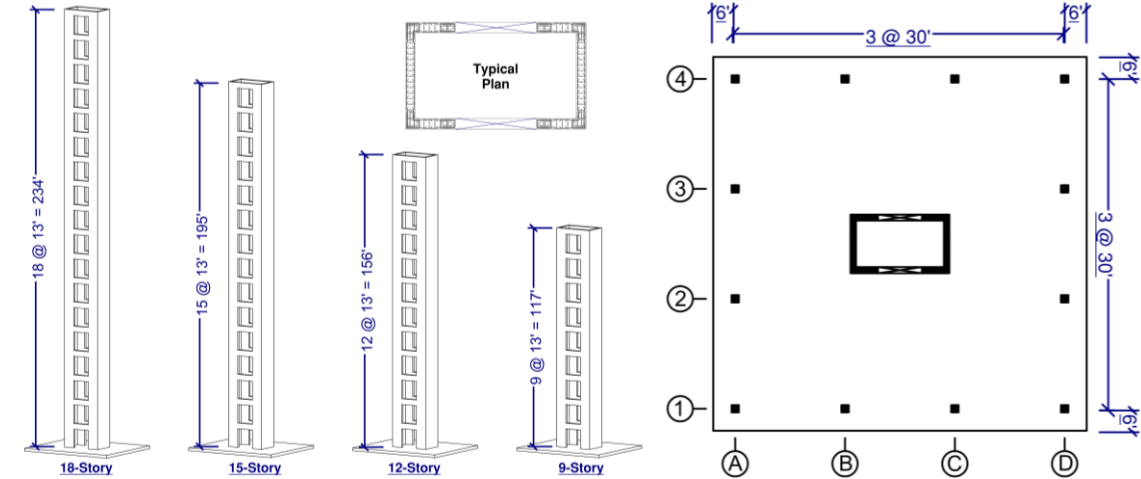


Figure 6.2: typical archetypes floor plan and its isolated core wall 3-dimensional view.

The design includes gravity loads of 100 pounds per square foot (psf) for the weight of the slab, plus an additional 25 psf for superimposed dead loads. The live loads are 50 psf for the floors and 20 psf for the roof. Inside the core of the building, which includes the slab and stairs, the dead load is 100 psf. A live load of 100 psf is also used within the core wall area.

Five different shear design provisions were used for each of the 9, 12, 15, and 18 story archetypes considered. These design criteria are summarized in Table 6.1. Diagonally reinforced coupling beams with an aspect ratio of 3.0 are used throughout all the archetypes. This leads to a total of 20 core wall models, which are divided into different groups for this study.

Table 6.1: Archetypes shear design criteria.

Code	Shear Amplification			Shear Strength	Shear Distribution	R, C _d , Ω ₀
	Ω _v	ω _v	Max.			
ACI 318-14	-	-	-	$(2\sqrt{f'_c} + \rho_{wh}f_y)A_{CV}$	50%-50%	6, 5, 2.5
ACI 318-19	$\frac{M_{pr}}{M_u}$	$1.3 + \frac{n_s}{30} \leq 1.8$ or $1.0 + 0.09h_n^{1/3}$	3.0	$(2\sqrt{f'_c} + \rho_{wh}f_y)A_{CV}$	50%-50%	8, 8, 2.5
ACI 318-25	$\frac{M_{pr}}{M_u} \leq 1.5$	$0.8 + 0.09h_n^{1/3}$	Ω ₀ = 2.5	$(2\sqrt{f'_c} + \rho_{wh}f_y)A_{CV}$	50%-50%	8, 8, 2.5
R-W ¹	$\frac{M_{pr}}{M_u} \leq 1.5$	$0.8 + 0.09h_n^{1/3}$	Ω ₀ = 2.5	$(\alpha_{cp}f'_c + \alpha_{sp}(\rho_{sb} + \rho_{wh})f_y)A_{CV}$	50%-50%	8, 8, 2.5
R-W ²	$\frac{M_{pr}}{M_u} \leq 1.5$	$0.8 + 0.09h_n^{1/3}$	Ω ₀ = 2.5	$(\alpha_{cp}f'_c + \alpha_{sp}(\rho_{sb} + \rho_{wh})f_y)A_{CV}$	Varies	8, 8, 2.5

¹Rojas-Wallace proposed shear strength equation with equal distribution of the shear demand between wall piers.

²Rojas-Wallace proposed shear strength equation with redistribution of the shear demand between wall piers.

6.2. Site Specific Design Parameters

All archetypes are designed for the same location near the intersection of I-405 and Ventura Avenue (Sherman Oaks), in Los Angeles, CA. Site specific design values obtained from the ATC seismic hazard tool (<https://hazards.atcouncil.org>) as below:

$$S_S = 1.961, S_1 = 0.699$$

$$S_{MS} = 2.354, S_{M1} = 0.979$$

$$S_{DS} = 1.569, S_{D1} = 0.653$$

6.3. Design Process

To determine the design actions, the Response Spectrum Analysis (RSA) method from ASCE 7-16 section 12.9.1 for ACI 318-14 archetypes and ASCE 7-22 for the rest of archetypes is used. The base shear force is adjusted to match 100% of the Equivalent Lateral Force (ELF) base shear from ASCE 7 section 12.8, based on a period $T = C_u T_a$. The Complete Quadratic Combination (CQC) technique is used to combine the effects of different vibration modes.

Risk Category I or II is assumed for all archetypes, with an importance factor I_e of 1.0. The soil is assumed to be of Site Class D, and the redundancy factor (ρ) is set at 1.3. The building's story drift is checked to make sure it stays within a limit of two percent during the design procedure.

The demands on the archetypes are obtained using a linear elastic model created using CSI ETABS software. The base of the building is considered fixed, so effects from the interaction between the superstructure and the soil are not included. Each floor diaphragm is assumed to be rigid in-plane.

The flexural stiffness modifiers for in-plane and out-of-plane behavior are set at $0.5I_g$ and $0.25I_g$, respectively. Shear stiffness values for walls and coupling beams are set equal to $0.4G_c A_g$, where $G_c = 0.5E_c$, which represents the stiffness of the entire section against shear force. Figure 6.3 showcases the elastic model used to determine the design demands.

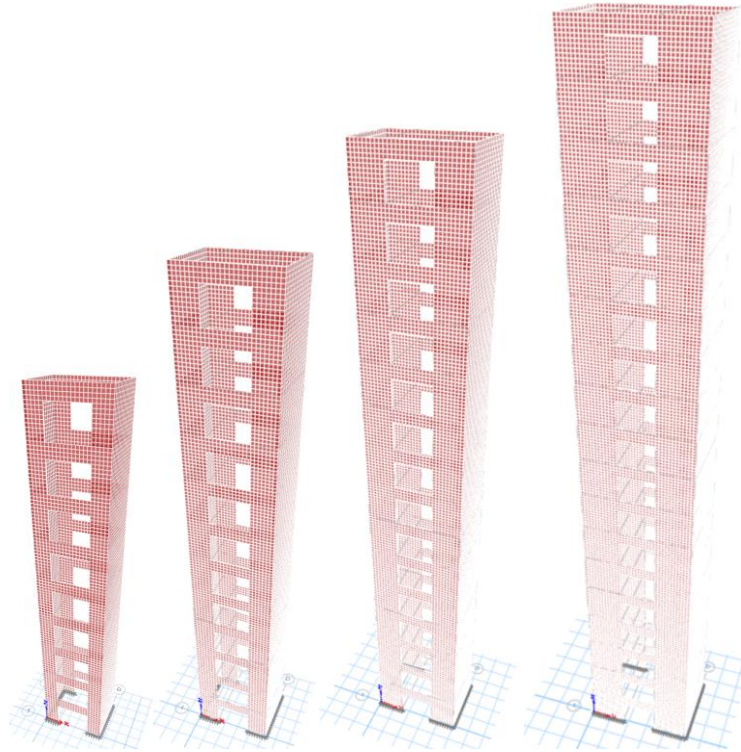


Figure 6.3: ETABS elastic model used to determine the design demands.

6.3.1. Coupling Beams

Diagonally reinforced coupling beams are designed in compliance with ACI 318-14 and 318-19 section 18.10.7 to ensure that the shear demand (V_u) doesn't surpass the designated design strength (ϕV_n). Factors influencing the beam shear strength include the area of the diagonal bars A_{vd} , the reinforcement yield stress f_y , and the inclination angle α of the diagonal reinforcement.

Beam nominal strength is not allowed to exceed $10bd\sqrt{f'_c}$.

6.3.2. Wall Piers Flexural Design

The demands at the centroid of the C-shaped wall piers are determined and include the influence of bi-directional loading. This is achieved by combining 100% of the force from one direction with 30% from the perpendicular direction, as depicted in Figure 6.4 and mandated by ASCE 7-16

Section 12.5.3.1. A 5% shift in the mass center is also considered in the model to account for accidental torsion in the floor plan.

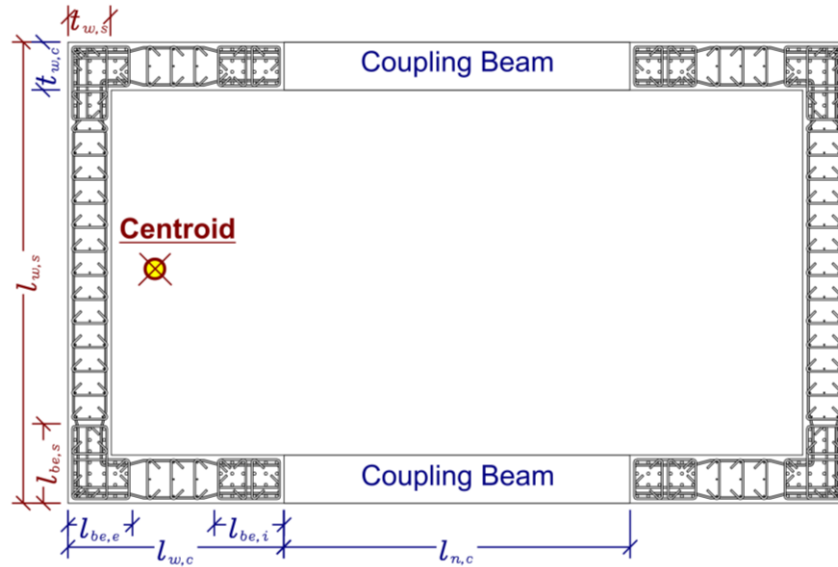


Figure 6.4: C-shaped wall centroid to calculate the wall piers demand.

Wall pier strength is based on ACI 318-14/19 requirements for special structural walls (section 18.10.5). This ensures that $P_u - M_u$ demands at every load combination stay within the bounds of the reduced axial and moment capacities, $(\phi P_n - \phi M_n)$. This consideration is particularly significant for the 6th and 7th load cases as per Section 2 of ASCE 7-16. As demands diminish over the height of the wall, the amount of boundary longitudinal and shear reinforcement is typically reduced to produce an efficient design.

To assess if special boundary elements (SBE) are needed in the wall piers, the displacement-based approach from section 18.10.6.2 is utilized. This approach is chosen because it's less strict than the stress-based approach (section 18.10.6.3). The criterion from section 18.10.6.2 states that, if a wall maximum neutral axis depth (c) is equal to or exceeds a specified limit given by Equation (6.1), then a special boundary element is required.

$$c \geq \frac{l_w}{600(1.5\delta_u/h_w)} \quad \text{Eq. 6.1}$$

Wall transverse reinforcement for a special boundary element is based on ACI 318-19 Sections 18.10.6.2, 18.10.6.4, and 18.10.6.5. The quantity of wall longitudinal reinforcement over the wall height is based on ACI 318-19 Section 18.10.2.3.

A lateral drift capacity check is also required by a new provision in ACI 318-19 section 18.10.6.2. This check, based on research reported by Abdullah and Wallace (2019), is implemented in archetype designs to minimize the risk of strength degradation due to flexural failures. This check provides for a low probability that the estimated drift demand for design earthquake (DE) level shaking does not exceed the wall drift capability. The equations associated with this check are:

$$\frac{1.5\delta_u}{h_w} \leq \frac{\delta_c}{l_w} \quad \text{Eq. 6.2}$$

$$\frac{\delta_c}{h_w} (\%) = 4.0 - \frac{cL_w}{50b^2} - \frac{v_{u,max}}{10\sqrt{f'_c}} \quad \text{Eq. 6.3}$$

6.3.3. Wall Piers Shear Design

In this study, five different wall shear design approaches are considered, and the performance of the structures designed using these approaches is evaluated. For a benchmark in shear design, a series of archetypes have been designed based on ACI 318-14. Notably, in 2019, ACI 318 opted to amplify the shear demand on walls by a factor of up to 3.0. This decision resulted in a notable increase in the required thickness of shear walls and a greater amount of shear reinforcement when compared to the preceding code cycle (ACI 318-14). Furthermore, the upcoming code revision (ACI 318-25) has sanctioned a reduction in the shear amplification demand from 3.0 down to a maximum of $\Omega_0 = 2.5$ (overstrength factor of the system per ASCE 7). Nonetheless, in all these iterations, the shear strength of the walls has been kept consistent ($V_n = V_c + V_s$).

$$V_n = A_{cv}(2\sqrt{f'_c} + \rho_t f_{yt}) \quad \text{Eq. 6.4}$$

With the recent advancements in computational capacities and the adoption of Machine Learning (ML) techniques in the field, various proposals regarding the wall shear strength walls have emerged. These new proposals are based on considerably larger test database than used previously, such as the relation proposed by Rojas-Leon and Wallace (2022). This equation is more complicated than previous expressions, but also is less conservative than the ACI 318 equation and has a much lower coefficient of variation.

In summary, this study considers various design options, with the primary objective to ascertain if a more efficient design approach is possible if shear force redistribution between the tension and compression wall piers is considered and a more comprehensive wall shear strength equation is used that considers, for example, the influence of axial load on wall shear strength. Detailed on the five approaches considered are provided in the following subsections.

6.3.3.1. ACI 318-14

The required wall shear reinforcement in the archetype walls is based on the ACI 318-14 provisions, specifically those outlined in section 18.10. The shear force demands are typically calculated using linear analysis based on the Design Earthquake hazard and specified load combinations. The wall shear demand, denoted as V_w , must be less than the wall shear strength given by Equation 18.10.4.1 (with capacity reduction factor):

$$\phi V_n = \phi V_c + \phi V_s = \phi A_{cv}(\alpha_c \lambda \sqrt{f'_c} + \rho_t f_y) \quad \text{Eq. 6.5}$$

In this equation, the value of α_c is dependent on the ratio of the wall height (h_w) to length (l_w), with a value of 3.0 for ratios up to 1.5, at 2.0 for ratios of 2.0 or higher, and linear variation in between these limits. A minimum of 0.25% horizontal reinforcement is required. Additionally, for any set of vertical wall segments that resists the same lateral force, the shear strength should not be greater than $8A_{cv}\sqrt{f'_c}$, with A_{cv} representing the total concrete area within the boundaries of the web thickness and the wall length. If considering a single segment of a vertical wall, its shear

capacity should not exceed $10A_{cw}\sqrt{f'_c}$, where A_{cw} refers to the concrete area of that particular wall segment.

6.4. ACI 318-19

In ACI 318-19, the prescribed wall shear strength remains consistent with previous versions of the code. However, the design procedure now requires accounting for an increased shear demand, referred to as V_e . This amplified shear demand is derived from two main factors: 1. the potential for greater flexural strength than what's necessary (flexural overstrength) and 2. the effects of higher modes on the structure. These factors and their effects are illustrated in Figure 6.5. The required shear strength, ϕV_n , must then be greater than or equal to V_e . ACI 318-19 calculates the actual shear demand on the wall as:

$$V_e = \omega_v \Omega_v V_u \leq 3.0V_u \quad \text{Eq.6.6}$$

Here, ω_v represents the amplification due to higher mode effects, and Ω_v represents the increase in shear due to flexural overstrength.

Flexural overstrength contributes to a greater shear demand along the wall height, due to the expected (or probable) wall moment capacity at the base being larger than the required moment capacity M_u , because of the strength reduction factor (ϕ) and because the provided steel area ($A_{s,prov}$) is likely greater than the required steel area ($A_{s,req}$). This overstrength is quantified by the expression:

$$M_{pr} = \left(\frac{M_u}{\phi}\right) \left(\frac{f_s}{f_y}\right) \left(\frac{A_{s,prov}}{A_{s,req}}\right) \quad \text{Eq.6.7}$$

If ϕ is estimated as 0.9, the ratio of $\left(\frac{f_s}{f_y}\right)$ is approximated to be at least 1.25, and $\left(\frac{A_{s,prov}}{A_{s,req}}\right) = 1.05$, then $M_{pr} = \left(\frac{M_u}{0.9}\right)(1.25)(1.05) \geq 1.45M_u$. ACI 318-19 requires that $M_{pr} \geq 1.5M_u$, and requires that the actual overstrength be calculated (but puts a limit on the maximum shear amplification of 3.0).

The influence of higher modes leads to an increase in shear demand and affects the effective height of the resulting shear force, which is necessary to determine the probable moment strength $M_{pr,CS}$ at the critical section of the wall, often at the base. As shown in Figure 6.5.d, the shear force distribution over the height of the wall, depicted in Figure 6.5.c, also increases. The code approximates this amplification effect based on the building height, typically related to the number of stories as below:

$$\begin{cases} \frac{h_w}{l_w} \geq 2.0 \rightarrow \begin{cases} \omega_v = 0.9 + \frac{n_s}{10} \leq 1.5 & \text{for } n_s \leq 6 \\ \omega_v = 1.3 + \frac{n_s}{30} \leq 1.8 & \text{for } n_s > 6 \end{cases} \\ \frac{h_w}{l_w} < 2.0 \rightarrow \omega_v = 1.0 \end{cases} \quad \text{Eq.6.8}$$

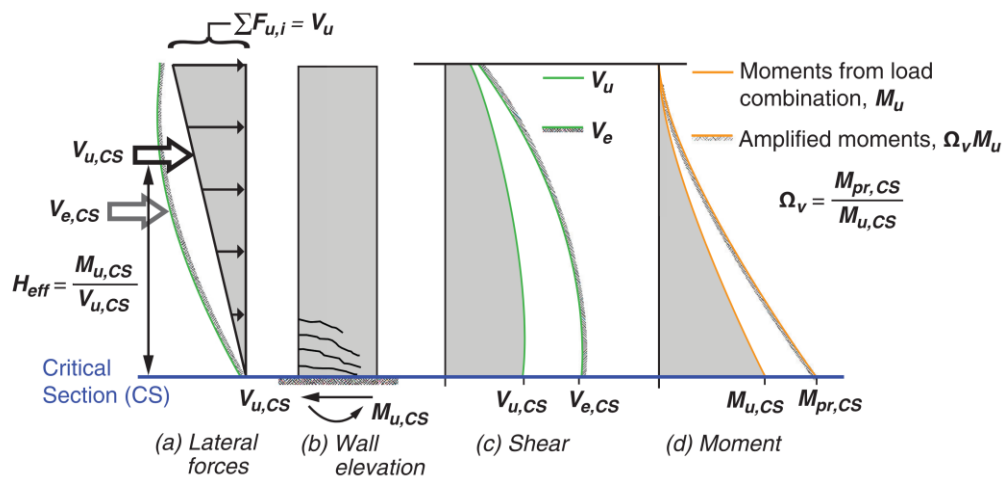


Figure 6.5: Determination of shear demand for walls with $h_w/l_w \geq 2.0$.

6.5. ACI 318-25

In the ACI 318-25 standard, the provisions for wall shear strength and the approach to shear demand amplification is similar to ACI 318-19, except for a modification in the shear amplification factor calculation. This update replaces the previous cap of 3.0, as found in ACI 318-19, with the factor Ω_0 as specified in ASCE 7 as overstrength factors for structural systems in Table 12.2-1. In

situations where strength is constrained by amplified forces using Ω_0 , ASCE 7 allows the redundancy factor, ρ , to be considered as 1.0. Additionally, ACI 318-25 limits the value of Ω_v to 1.5 (no calculation is required). However, in instances where the probable moment strength is directly calculated by the engineer, higher shear amplification may occur, subject to the upper limit of Ω_0 .

Furthermore, ACI 318-25 modifies the equation used to calculate ω_v as:

$$\omega_v = 0.8 + 0.09h_n^{1/3} \quad \text{Eq. 6.9}$$

where (h_n) represents the height above the base in feet.

6.6. Rojas-Wallace Shear Equation (2023)

The provisions for wall shear strength as outlined in ACI 318 do not account for the influence of axial load except for consideration of net tension discussed in Chapter 11. Additionally, factors that one might anticipate affecting wall shear strength, such as the vertical reinforcement of the wall and the cross-sectional configuration, are not included accounted for in ACI 318-19.

Considering recent developments in computational capabilities and the integration of Machine Learning (ML) techniques, several new methodologies for calculating the shear strength of shear walls have been proposed. These methodologies utilize a more extensive database of tests to derive their predictive equations. The shear strength equation assessed in this research has been recently introduced by Rojas and Wallace (2022). This equation deviates from conventional approaches by incorporating a broader range of parameters than considered in ACI 318-19. As a result, it offers a more accurate prediction of wall shear strength.

The equation in question considers the concrete compressive strength, the cross-sectional area, and the quantity and yield strength of both longitudinal reinforcement at the edge of the wall in tension and the horizontal and vertical web reinforcement. It also factors in the axial load ratio on the wall piers and the shear-span ratio.

The nominal shear strength (V_n) is calculated as follows:

$$V_n = \alpha_c A'_g f'_c + \alpha_s (\rho_{sb} f_{ysb} + \rho_{wh} f_{ywh}) A_{cv} \quad \text{Eq. 6.10}$$

where α_c and α_s are coefficients derived from the equations:

$$\begin{cases} \alpha_c = 0.01 \left(9 \frac{(1 + \frac{P_u}{A'_g f'_c})^3}{(\frac{M_u}{V_u l_w})^{1/3}} - 6 \right) \geq 0.01 \\ \alpha_s = \frac{2}{5(\frac{M_u}{V_u l_w})^{1/3}} \geq 0.3 \end{cases} \quad \text{Eq. 6.11}$$

In these equations, P_u , V_u , and M_u represent the factored vertical axial force, shear force, and moment demand on the wall, respectively. A'_g signifies the cross-sectional area of the wall considering the effective flange length under compression. The variables ρ_{sb} and f_{ysb} denote the ratio and yield stress of longitudinal boundary reinforcement under tension, while ρ_{wh} and f_{ywh} correspond to the ratio and yield stress of the wall's horizontal web reinforcement.

Furthermore, the upper limit of wall shear strength has been revised to include the compressive flange's contribution as follows:

$$V_n = \alpha_{shape} A_{cv} 10\lambda \sqrt{f'_c} \quad \text{Eq. 6.12}$$

where α_{shape} is the shape coefficient given by:

$$\alpha_{shape} = 0.7 \left(1 + \frac{b_f t_f}{A_{cv}} \right)^2 \quad \text{Eq. 6.13}$$

Here, b_f and t_f represent the compressive flange length and thickness, respectively.

6.7. Considering Shear Redistribution in the Design

To effectively leverage the enhanced shear strength of walls under compression and to mitigate the reduced shear strength of the tension wall pier in a coupled wall, it is imperative to redistribute the overall shear demand. Based on use of a P-M interaction diagram for the wall piers, the presence of tensile forces (or a reduction in compression force) results in a reduction in moment strength of the tension wall pier. Conversely, the moment strength of the compression wall pier

increases (if below the balanced point). This disparity in stiffness and moment strength between the compression and tension wall piers results in a migration of shear forces from the tension to the compression wall. Moehle (2014) suggests utilizing the ratio of the moment capacities of the wall piers as a basis for the redistribution of shear force demands. However, a more comprehensive approach for this redistribution, along with an algorithm for effective shear design of wall piers, is outlined below. This algorithm could be adjusted to incorporate any shear strength equation that considered wall axial force and other variables on wall shear strength. In this study, the equation proposed by Rojas-Wallace (2022) is used.

To redistribute the base shear demand among the wall piers, a two-dimensional structural system is conceptualized, grounded in the principles of structural mechanics and nonlinear analysis. The system comprises two RC shear wall piers interconnected through beams (alternatively, this could involve slabs, coupling beams, etc.), as illustrated in Figure 6.6.

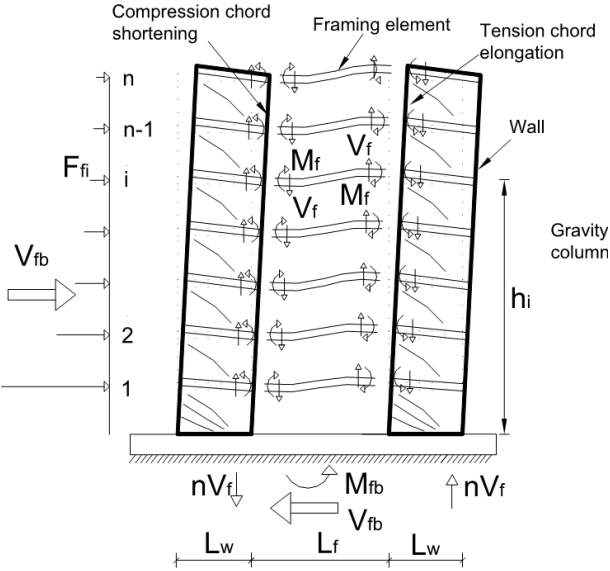


Figure 6.6: depicts a building with RC wall piers, showing a plastic hinge formation at the base of the walls. This schematic includes plastic framing actions, reactions, and variations in internal and system lateral forces.

Assuming the walls are in a nonlinear state with plastic hinges at their bases, a majority of wall deformation originates from either elongation in tensile chords or shortening in compression chords. According to the deformation compatibility theorem, the beams must conform to these imposed deformations, resulting in the formation of plastic hinges at their ends. It is assumed that the framing elements possess sufficient shear capacity to develop their full plastic moment at these ends.

Considering framing element length (L_f), wall length (L_w), and story height (h_i) at each floor level (refer to Figure 6.7), the free body diagram in Figure 6.7 demonstrates the forces developed due to the activation of the framing plastic mechanism at floor i .

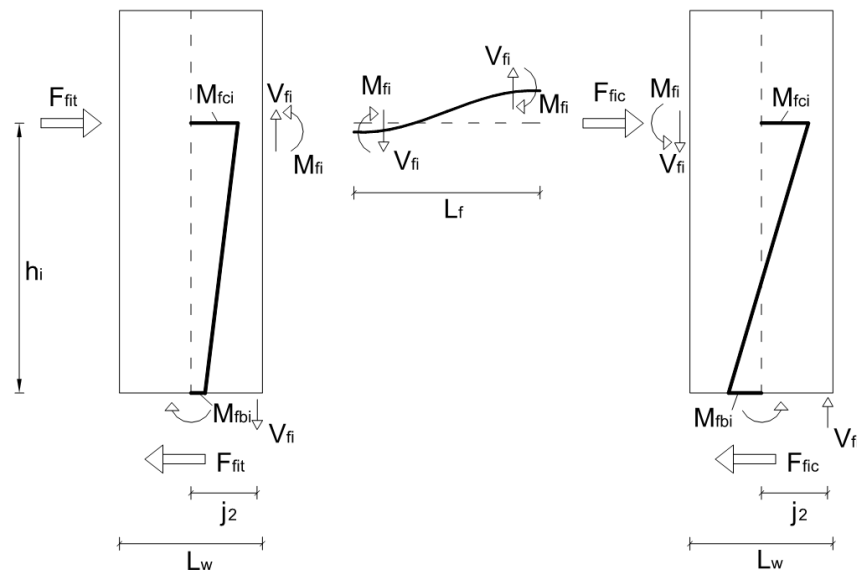


Figure 6.7: Free body diagram of forces developed due to mobilization of framing plastic mechanism at floor i for the case of framing between two external walls.

Calculations for shear forces (V_{fi}) and equivalent moments at each wall pier center (M_{fci}) are derived through the following equations:

$$V_{fi} = \frac{2M_{fi}}{L_f} \quad \text{Eq. 6.14}$$

$$M_{fci} = V_{fi} \frac{L_w}{2} + M_{fi} = M_{fi} \left(\frac{L_w}{L_f} + 1 \right) \quad \text{Eq. 6.15}$$

For wall nonlinear behavior, additional axial forces (V_{fi}) alter the internal compressive forces resisted by the concrete. This results in a modified wall base moment capacity (M_{fbi}), calculated as:

$$M_{fbi} = V_{fi} \frac{L_w}{2} = M_{fi} \frac{L_w}{L_f} \quad \text{Eq. 6.16}$$

The wall pier experiencing an increase in axial force due to framing action will see an increase in its base moment capacity, whereas in the opposite scenario, the moment capacity decreases by M_{fbi} . Lateral forces (F_{fit} and F_{fic}) on each wall pier and the total lateral force can be estimated as follows:

$$F_{fit} = \frac{M_{fci} - M_{fbi}}{h_i} = \frac{M_{fi}}{h_i} \quad \text{Eq. 6.17}$$

$$F_{fic} = \frac{(M_{fci} - M_{fbi})}{h_i} = M_{fi} \frac{\left(1 + 2 \frac{L_w}{L_f}\right)}{h_i} \quad \text{Eq. 6.18}$$

$$F_{fi} = F_{fit} + F_{fic} = \frac{2M_{fi} \left(1 + \frac{L_w}{L_f}\right)}{h_i} \quad \text{Eq. 6.19}$$

In these equations, the lateral force (F_{fi}) is inversely proportional to height, indicating that lower-level hinge formation generates larger lateral forces in the system. For a building with a fully developed nonlinear mechanism across its height, the resultant lateral force profile deviates significantly from the fundamental mode of vibration, exhibiting an increase at higher floor levels. To estimate the developed base forces in a fully activated mechanism, the formula is adjusted as follows:

$$M_{fbt} = M_{fbc} = \frac{L_w}{L_f} \sum_{i=1}^n M_{fi} = n \frac{L_w}{L_f} M_f \quad \text{Eq. 6.20}$$

$$V_{fbt} = \sum_{i=1}^n F_{fit} = \frac{M_f}{h} \sum_{i=1}^n \frac{1}{i} \quad \text{Eq. 6.21}$$

$$V_{fbc} = \sum_{i=1}^n F_{fic} = \frac{M_f}{h} \left(1 + 2 \frac{L_w}{L_f}\right) \sum_{i=1}^n \frac{1}{i} \quad \text{Eq. 6.22}$$

$$V_{fb} = \sum_{i=1}^n F_{fi} = \frac{2M_f \left(1 + \frac{L_w}{L_f}\right)}{h} \sum_{i=1}^n \frac{1}{i} \quad \text{Eq. 6.23}$$

The design of wall piers, once the shear demand is appropriately allocated among them, should adhere to the following procedural steps:

1. Demand Assessment on Coupled Wall: Initially, determine the coupled wall demands, encompassing axial force (P_g), base shear (V_b), and base moment (M_b).
2. Design of Coupled Wall in Solid Direction: In this phase, the coupled wall's solid direction should be designed considering an R-factor of 6, as per standard practice. It is noteworthy that according to ASCE 7-22, the R-factor for a Ductile Coupled Wall is designated as 8. This discrepancy implies that the total required longitudinal boundary reinforcement in the solid direction is anticipated to exceed that in the coupled direction.
3. Selection of Degree of Coupling (DoC): Select a suitable Degree of Coupling, which quantifies the ratio of the total base moment to the moment resisted by the wall piers framing action via the coupling beam. Commonly, a DoC ranging from 0.5 to 0.6 is adopted.
4. Calculation of Shear Demand on Coupling Beams: The total shear demand on the coupling beams can be computed using the formula $DoC \times M_b / l_w$, while the base moment resisted by the wall piers is calculated as $(1 - DoC)M_b / 2$.
5. Correlation of Wall Pier Shear Capacity and Axial Force: This involves relating the wall piers shear capacity to the axial force using the shear strength equation. Here, Rojas and Wallace 2022, equation adopted.
6. Determination of Minimum Longitudinal Reinforcement in Coupled Direction: Irrespective of the designed longitudinal reinforcement in the solid direction, it is essential to ascertain the minimum required longitudinal reinforcement in the coupled direction at each boundary ($A_{s,l}^{min}$, $A_{s,e}^{min}$).

7. Distribution of Surplus Longitudinal Reinforcement: As indicated in the second step, the total A_s calculated exceeds the sum of $A_{s,i}^{min}$ and $A_{s,e}^{min}$. Consequently, the additional required longitudinal reinforcement should be distributed between the boundaries in accordance with the shear distribution ratio.
8. Establishment of Minimum Required Thickness for Coupled Wall: Determine the minimum necessary thickness for the coupled wall.

The process for optimizing core-wall design is elucidated in Figure 6.8 and the accompanying flowchart. This figure presents a typical core-wall cross-section and its associated P-M diagram in the coupled direction, serving as a visual aid to understand the process thoroughly.

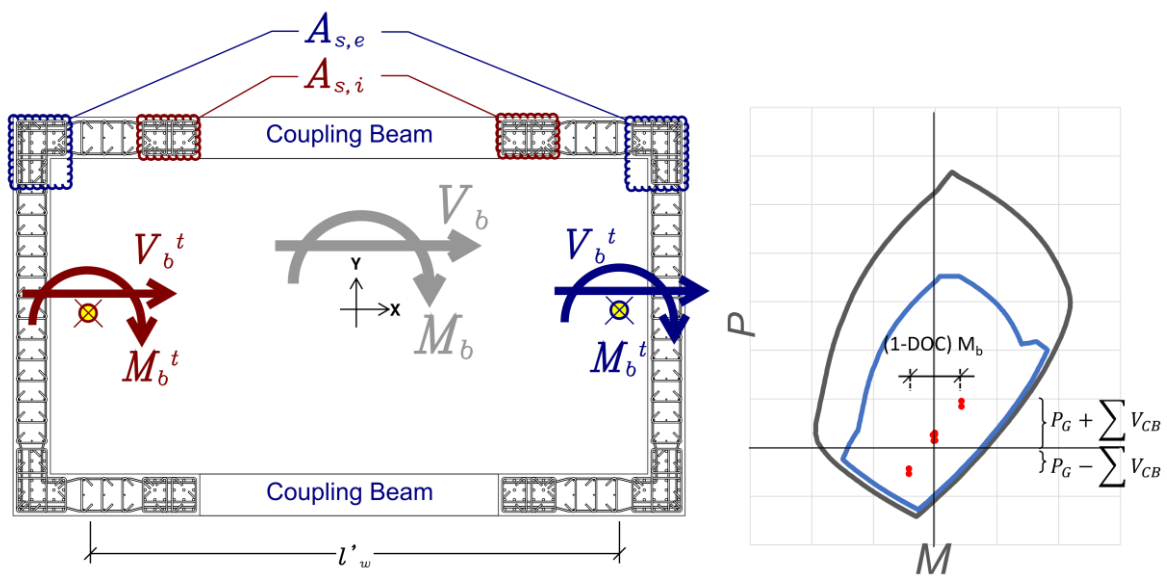


Figure 6.8: Typical core-wall cross section and its associated P-M diagram in the coupled direction.

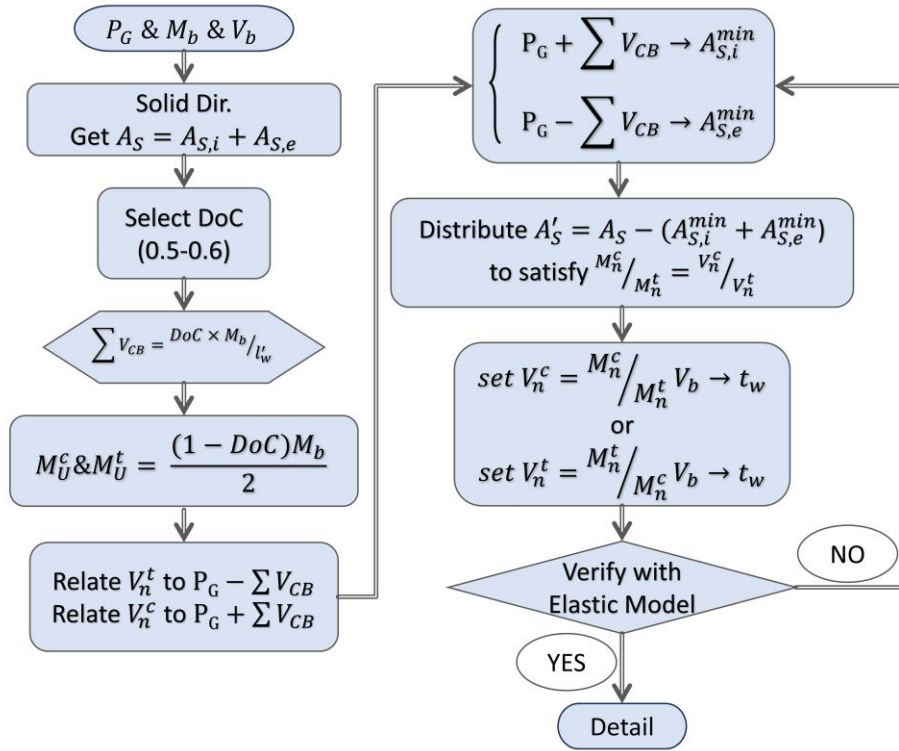


Figure 6.9: Design flowchart to minimize the required wall thickness.

6.8. Design Summary

A succinct summary of the design for each archetype is presented. Figures 6.9 and 6.10 depict the standard detailing of the core wall cross-section and the coupling beams, respectively. For comprehensive calculations pertinent to each archetype, refer to Appendix C, where detailed computational analysis is provided.

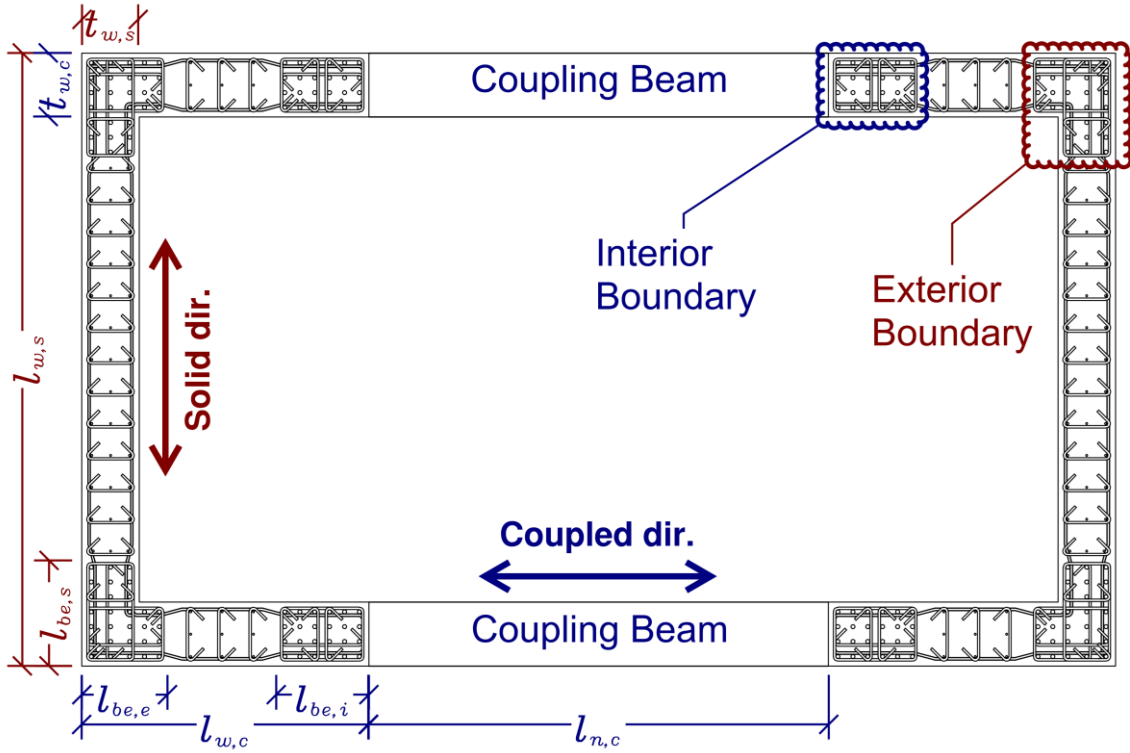


Figure 6.10: core-wall cross-section detail.

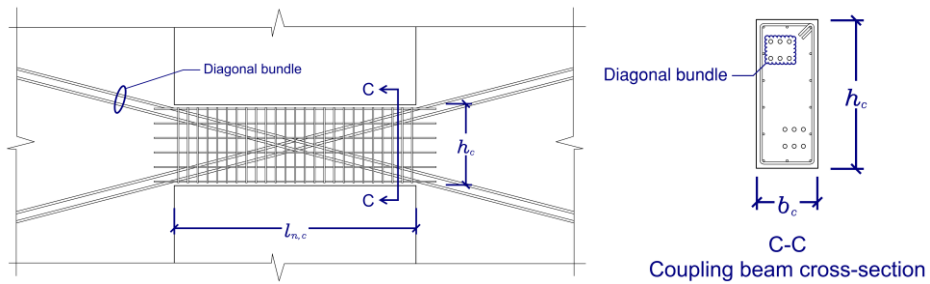


Figure 6.11: Coupling beams elevation and cross-section details.

6.8.1. 9-Story archetypes

This section provides a summary of all archetype designs.

6.8.1.1. ACI 318-14

Table 6.2: Summary of 9-story core-wall design according to ACI 318-14.

Story	f'_c (ksi)	f_y (ksi)	$L_{w,c}$ (ft)	$L_{w,s}$ (ft)	$t_{w,c}$ (in.)	$t_{w,s}$ (in.)	Shear Reinforcement		Flexural Reinforcement		
							Coupled dir. (@in.)	Solid dir. (@in.)	Interior Boundary	Exterior Boundary	Web
7-9	8	60	5	16	12	12	2 #6 @9	2 #5 @12	9 #7	36 #7	2 #5 @12
4-6	8	60	5	16	13	12	2 #6 @5.5	2 #6 @12	15 #8	60 #8	2 #5 @12
1-3	8	60	5	16	16	12	2 #6 @4.5	2 #6 @7.5	15 #11	60 #11	2 #5 @12

Table 6.3: Summary of 9-story coupling beam design; archetype designed per to ACI 318-14.

Level	f'_c (ksi)	f_y (ksi)	b (in.)	d (in.)	Diagonal bars
8-Roof	8	60	12	48	9 #11
5-7	8	60	13	48	14 #11
2-4	8	60	16	48	17 #11

6.8.1.2. ACI 318-19

Table 6.4: Summary of 9-story core-wall design according to ACI 318-19.

Story	f'_c (ksi)	f_y (ksi)	$L_{w,c}$ (ft)	$L_{w,s}$ (ft)	$t_{w,c}$ (in.)	$t_{w,s}$ (in.)	Shear Reinforcement		Flexural Reinforcement		
							Coupled dir. (@in.)	Solid dir. (@in.)	Interior Boundary	Exterior Boundary	Web
7-9	8	60	5	16	26	16	2 #6 @4	3 #6 @7	9 #7	36 #7	2 #6 @12
4-6	8	60	5	16	30	18	3 #6 @4	3 #6 @6.5	15 #8	60 #8	2 #6 @12
1-3	8	60	5	16	36	23	4 #6 @4	3 #6 @5	15 #11	60 #11	3 #6 @12

Table 6.5: Summary of 9-story coupling beam design; archetype designed per to ACI 318-19.

Level	f'_c (ksi)	f_y (ksi)	b (in.)	d (in.)	Diagonal bars
8-Roof	8	60	26	48	7 #11
5-7	8	60	30	48	10 #11
2-4	8	60	36	48	12 #11

6.8.1.3. ACI 318-25

Table 6.6: Summary of 9-story core-wall design according to ACI 318-25.

Story	f'_c (ksi)	f_y (ksi)	$L_{w,c}$ (ft)	$L_{w,s}$ (ft)	$t_{w,c}$ (in.)	$t_{w,s}$ (in.)	Shear Reinforcement		Flexural Reinforcement		
							Coupled dir. (@in.)	Solid dir. (@in.)	Interior Boundary	Exterior Boundary	Web
7-9	8	60	5	16	13	12	2 #6 @6	2 #6 @8	9 #7	36 #7	2 #5 @12
4-6	8	60	5	16	18	14	3 #6 @6	2 #6 @5.5	15 #8	60 #8	2 #6 @12
1-3	8	60	5	16	23	18	3 #6 @5	2 #6 @4	15 #11	60 #11	2 #6 @12

Table 6.7: Summary of 9-story coupling beam design; archetype designed per to ACI 318-25.

Level	f'_c (ksi)	f_y (ksi)	b (in.)	d (in.)	Diagonal bars
8-Roof	8	60	26	48	7 #11
5-7	8	60	30	48	10 #11
2-4	8	60	36	48	12 #11

6.8.1.4. ACI 318-25 and Rojas-Wallace shear equation

Table 6.8: Summary of 9-story core-wall design according to ACI 318-25 and the Rojas-Wallace 2022 shear equation.

Story	f'_c (ksi)	f_y (ksi)	$L_{w,c}$ (ft)	$L_{w,s}$ (ft)	$t_{w,c}$ (in.)	$t_{w,s}$ (in.)	Shear Reinforcement		Flexural Reinforcement		
							Coupled dir. (@in.)	Solid dir. (@in.)	Interior Boundary	Exterior Boundary	Web
7-9	8	60	5	16	13	12	2 #6 @4	2 #6 @6	9 #7	36 #7	2 #5 @12
4-6	8	60	5	16	18	12	3 #6 @4	3 #6 @4.5	15 #8	60 #8	2 #6 @12
1-3	8	60	5	16	23	12	2 #5 @10	3 #6 @4.5	15 #11	60 #11	2 #6 @12

Table 6.9: Summary of 9-story coupling beam design; archetype designed per to ACI 318-25 and the Rojas-Wallace 2022 shear equation.

Level	f'_c (ksi)	f_y (ksi)	b (in.)	d (in.)	Diagonal bars
8-Roof	8	60	26	48	7 #11
5-7	8	60	30	48	10 #11
2-4	8	60	36	48	12 #11

6.8.1.5. ACI 318-25 and Rojas-Wallace shear equation – redistributed shear demand

Table 6.10: Summary of 9-story core-wall design according to ACI 318-25 and the Rojas-Wallace 2022 shear equation and redistributed shear demand.

Story	f'_c (ksi)	f_y (ksi)	$L_{w,c}$ (ft)	$L_{w,s}$ (ft)	$t_{w,c}$ (in.)	$t_{w,s}$ (in.)	Shear Reinforcement		Flexural Reinforcement		
							Coupled dir. (@in.)	Solid dir. (@in.)	Interior Boundary	Exterior Boundary	Web
7-9	8	60	5	16	12	12	2 #5 @12	2 #6 @6	15 #7	30 #7	2 #5 @12
4-6	8	60	5	16	16	12	2 #5 @12	3 #6 @4.5	25 #8	50 #8	2 #5 @12
1-3	8	60	5	16	19	12	2 #5 @12	3 #6 @4.5	25 #11	50 #11	2 #5 @12

Table 6.11: Summary of 9-story coupling beam design; archetype designed per to ACI 318-25 and the Rojas-Wallace 2022 shear equation and redistributed shear demand.

Level	f'_c (ksi)	f_y (ksi)	b (in.)	d (in.)	Diagonal bars
8-Roof	8	60	26	48	7 #11
5-7	8	60	30	48	10 #11
2-4	8	60	36	48	12 #11

6.8.2. 12-Story archetypes

6.8.2.1. ACI 318-14

Table 6.12: Summary of 12-story core-wall design according to ACI 318-14.

Story	f'_c (ksi)	f_y (ksi)	$L_{w,c}$ (ft)	$L_{w,s}$ (ft)	$t_{w,c}$ (in.)	$t_{w,s}$ (in.)	Shear Reinforcement		Flexural Reinforcement		
							Coupled dir. (@in.)	Solid dir. (@in.)	Interior Boundary	Exterior Boundary	Web
10-12	8	60	7	20	12	12	2 #5 @12	2 #5 @12	9 #7	36 #7	2 #5 @12
7-9	8	60	7	20	12	12	2 #6 @11	2 #5 @12	15 #7	60 #7	2 #5 @12
4-6	8	60	7	20	12	12	2 #6 @7.5	2 #5 @9	15 #9	60 #9	2 #5 @12
1-3	8	60	7	20	14	12	2 #6 @6	2 #6 @9.5	15 #11	60 #11	2 #5 @12

Table 6.13: Summary of 12-story coupling beam design; archetype designed per to ACI 318-14.

Level	f'_c (ksi)	f_y (ksi)	b (in.)	d (in.)	Diagonal bars
11-Roof	8	60	12	48	7 #11
8-10	8	60	12	48	10 #11
5-7	8	60	13	48	12 #11
2-4	8	60	16	48	15 #11

6.8.2.2. ACI 318-19

Table 6.14: Summary of 12-story core-wall design according to ACI 318-19.

Story	f'_c (ksi)	f_y (ksi)	$L_{w,c}$ (ft)	$L_{w,s}$ (ft)	$t_{w,c}$ (in.)	$t_{w,s}$ (in.)	Shear Reinforcement		Flexural Reinforcement		
							Coupled dir. (@in.)	Solid dir. (@in.)	Interior Boundary	Exterior Boundary	Web
10-12	8	60	7	20	14	12	3 #6 @8	2 #6 @6	9 #7	36 #7	2 #5 @12
7-9	8	60	7	20	17	14	3 #6 @6.5	3 #6 @8	15 #7	60 #7	2 #5 @12
4-6	8	60	7	20	23	19	3 #6 @4.5	3 #6 @6	15 #9	60 #9	2 #6 @12
1-3	8	60	7	20	28	21	3 #6 @4	3 #6 @5	15 #11	60 #11	2 #6 @12

Table 6.15: Summary of 12-story coupling beam design; archetype designed per to ACI 318-19.

Level	f'_c (ksi)	f_y (ksi)	b (in.)	d (in.)	Diagonal bars
11-Roof	8	60	12	48	5 #11
8-10	8	60	12	48	7 #11
5-7	8	60	13	48	10 #11
2-4	8	60	16	48	11 #11

6.8.2.3. ACI 318-25

Table 6.16: Summary of 12-story core-wall design according to ACI 318-25.

Story	f'_c (ksi)	f_y (ksi)	$L_{w,c}$ (ft)	$L_{w,s}$ (ft)	$t_{w,c}$ (in.)	$t_{w,s}$ (in.)	Shear Reinforcement		Flexural Reinforcement		
							Coupled dir. (@in.)	Solid dir. (@in.)	Interior Boundary	Exterior Boundary	Web
10-12	8	60	7	20	12	12	2 #6 @9.5	2 #6 @7.5	9 #7	36 #7	2 #5 @12
7-9	8	60	7	20	12	12	2 #6 @7	2 #6 @7.5	15 #7	60 #7	2 #5 @12
4-6	8	60	7	20	15	14	2 #6 @5	2 #6 @5	15 #9	60 #9	2 #5 @12
1-3	8	60	7	20	18	16	2 #6 @4	2 #6 @4.5	15 #11	60 #11	2 #5 @12

Table 6.17: Summary of 12-story coupling beam design; archetype designed per to ACI 318-25.

Level	f'_c (ksi)	f_y (ksi)	b (in.)	d (in.)	Diagonal bars
11-Roof	8	60	12	48	5 #11
8-10	8	60	12	48	7 #11
5-7	8	60	13	48	10 #11
2-4	8	60	16	48	11 #11

6.8.2.4. ACI 318-25 – Rojas-Wallace shear equation

Table 6.18: Summary of 12-story core-wall design according to ACI 318-25 and the Rojas-Wallace 2022 shear equation.

Story	f'_c (ksi)	f_y (ksi)	$L_{w,c}$ (ft)	$L_{w,s}$ (ft)	$t_{w,c}$ (in.)	$t_{w,s}$ (in.)	Shear Reinforcement		Flexural Reinforcement		
							Coupled dir. (@in.)	Solid dir. (@in.)	Interior Boundary	Exterior Boundary	Web
10-12	8	60	7	20	12	12	2 #5 @12	2 #5 @12	9 #7	36 #7	2 #5 @12
7-9	8	60	7	20	12	12	2 #5 @12	2 #6 @7	15 #7	60 #7	2 #5 @12
4-6	8	60	7	20	15	12	2 #5 @12	3 #6 @6.5	15 #9	60 #9	2 #5 @12
1-3	8	60	7	20	18	12	2 #5 @12	3 #6 @6.5	15 #11	60 #11	2 #5 @12

Table 6.19: Summary of 12-story coupling beam design; archetype designed per to ACI 318-25 and the Rojas-Wallace 2022 shear equation.

Level	f'_c (ksi)	f_y (ksi)	b (in.)	d (in.)	Diagonal bars
11-Roof	8	60	12	48	5 #11
8-10	8	60	12	48	7 #11
5-7	8	60	13	48	10 #11
2-4	8	60	16	48	11 #11

6.8.2.5. ACI 318-25 – Rojas-Wallace shear equation – redistributed shear demand

Table 6.20: Summary of 12-story core-wall design according to ACI 318-25 and the Rojas-Wallace 2022 shear equation and redistributed shear demand.

Story	f'_c (ksi)	f_y (ksi)	$L_{w,c}$ (ft)	$L_{w,s}$ (ft)	$t_{w,c}$ (in.)	$t_{w,s}$ (in.)	Shear Reinforcement		Flexural Reinforcement		
							Coupled dir. (@in.)	Solid dir. (@in.)	Interior Boundary	Exterior Boundary	Web
10-12	8	60	7	20	12	12	2 #5 @12	2 #5 @12	15 #7	30 #7	2 #5 @12
7-9	8	60	7	20	12	12	2 #5 @12	2 #6 @7	25 #7	50 #7	2 #5 @12
4-6	8	60	7	20	12	12	2 #5 @12	3 #6 @6.5	25 #9	50 #9	2 #5 @12
1-3	8	60	7	20	15	12	2 #5 @12	3 #6 @6.5	25 #11	50 #11	2 #5 @12

Table 6.21: Summary of 12-story coupling beam design; archetype designed per to ACI 318-25 and the Rojas-Wallace 2022 shear equation and redistributed shear demand.

Level	f'_c (ksi)	f_y (ksi)	b (in.)	d (in.)	Diagonal bars
11-Roof	8	60	12	48	5 #11
8-10	8	60	12	48	7 #11
5-7	8	60	13	48	10 #11
2-4	8	60	16	48	11 #11

6.8.3. 15-Story archetypes

6.8.3.1. ACI 318-14

Table 6.22: Summary of 15-story core-wall design according to ACI 318-14.

Story	f'_c (ksi)	f_y (ksi)	$L_{w,c}$ (ft)	$L_{w,s}$ (ft)	$t_{w,c}$ (in.)	$t_{w,s}$ (in.)	Shear Reinforcement		Flexural Reinforcement		
							Coupled dir. (@in.)	Solid dir. (@in.)	Interior Boundary	Exterior Boundary	Web
13-15	8	60	9	23	12	12	2 #5 @12	2 #5 @12	6 #7	32 #7	2 #5 @12
10-12	8	60	9	23	12	12	2 #5 @12	2 #5 @12	9 #7	48 #7	2 #5 @12
7-9	8	60	9	23	12	12	2 #5 @10	2 #5 @12	9 #8	48 #8	2 #5 @12
4-6	8	60	9	23	12	12	2 #6 @9.5	2 #5 @9.5	9 #9	48 #9	2 #5 @12
1-3	8	60	9	23	12	12	2 #6 @7.5	2 #5 @7.5	9 #11	48 #11	2 #5 @12

Table 6.23: Summary of 15-story coupling beam design; archetype designed per to ACI 318-14.

Level	f'_c (ksi)	f_y (ksi)	b (in.)	d (in.)	Diagonal bars
14-Roof	8	60	12	48	6 #11
11-13	8	60	12	48	7 #11
8-10	8	60	12	48	9 #11
5-7	8	60	13	48	12 #11
2-4	8	60	16	48	14 #11

6.8.3.2. ACI 318-19

Table 6.24: Summary of 15-story core-wall design according to ACI 318-19.

Story	f'_c (ksi)	f_y (ksi)	$L_{w,c}$ (ft)	$L_{w,s}$ (ft)	$t_{w,c}$ (in.)	$t_{w,s}$ (in.)	Shear Reinforcement		Flexural Reinforcement		
							Coupled dir. (@in.)	Solid dir. (@in.)	Interior Boundary	Exterior Boundary	Web
13-15	8	60	9	23	12	12	3 #6 @11	2 #6 @9	6 #7	32 #7	2 #5 @12
10-12	8	60	9	23	12	12	3 #6 @9	2 #6 @8	9 #7	48 #7	2 #5 @12
7-9	8	60	9	23	15	12	3 #6 @7.5	3 #6 @9	9 #8	48 #8	2 #5 @12
4-6	8	60	9	23	20	13	3 #6 @5.5	3 #6 @6	9 #9	48 #9	2 #5 @12
1-3	8	60	9	23	23	15	3 #6 @4.5	3 #6 @5.5	9 #11	48 #11	2 #5 @12

Table 6.25: Summary of 15-story coupling beam design; archetype designed per to ACI 318-19.

Level	f'_c (ksi)	f_y (ksi)	b (in.)	d (in.)	Diagonal bars
14-Roof	8	60	12	48	6 #9
11-13	8	60	12	48	5 #11
8-10	8	60	15	48	7 #11
5-7	8	60	20	48	9 #11
2-4	8	60	23	48	10 #11

6.8.3.3. ACI 318-25

Table 6.26: Summary of 15-story core-wall design according to ACI 318-25.

Story	f'_c (ksi)	f_y (ksi)	$L_{w,c}$ (ft)	$L_{w,s}$ (ft)	$t_{w,c}$ (in.)	$t_{w,s}$ (in.)	Shear Reinforcement		Flexural Reinforcement		
							Coupled dir. (@in.)	Solid dir. (@in.)	Interior Boundary	Exterior Boundary	Web
13-15	8	60	9	23	12	12	2 #6 @12	2 #6 @12	6 #7	32 #7	2 #5 @12
10-12	8	60	9	23	12	12	2 #6 @11	2 #6 @12	9 #7	48 #7	2 #5 @12
7-9	8	60	9	23	12	12	3 #6 @8.5	2 #6 @9	9 #8	48 #8	2 #5 @12
4-6	8	60	9	23	13	13	3 #6 @8.5	2 #6 @5.5	9 #9	48 #9	2 #5 @12
1-3	8	60	9	23	15	15	3 #6 @7.5	2 #6 @5.5	9 #11	48 #11	2 #5 @12

Table 6.27: Summary of 15-story coupling beam design; archetype designed per to ACI 318-25.

Level	f'_c (ksi)	f_y (ksi)	b (in.)	d (in.)	Diagonal bars
14-Roof	8	60	12	48	6 #9
11-13	8	60	12	48	5 #11
8-10	8	60	12	48	7 #11
5-7	8	60	13	48	9 #11
2-4	8	60	15	48	10 #11

6.8.3.4. ACI 318-25 and Rojas-Wallace shear equation

Table 6.28: Summary of 15-story core-wall design according to ACI 318-25 and the Rojas-Wallace 2022 shear equation.

Story	f'_c (ksi)	f_y (ksi)	$L_{w,c}$ (ft)	$L_{w,s}$ (ft)	$t_{w,c}$ (in.)	$t_{w,s}$ (in.)	Shear Reinforcement		Flexural Reinforcement		
							Coupled dir. (@in.)	Solid dir. (@in.)	Interior Boundary	Exterior Boundary	Web
13-15	8	60	9	23	12	12	2 #5 @12	2 #6 @12	6 #7	32 #7	2 #5 @12
10-12	8	60	9	23	12	12	2 #5 @12	2 #6 @7.5	9 #7	48 #7	2 #5 @12
7-9	8	60	9	23	12	12	2 #5 @12	2 #6 @6.5	9 #8	48 #8	2 #5 @12
4-6	8	60	9	23	13	12	2 #5 @12	3 #6 @6.5	9 #9	48 #9	2 #5 @12
1-3	8	60	9	23	15	12	2 #5 @12	3 #6 @5.5	9 #11	48 #11	2 #5 @12

Table 6.29: Summary of 15-story coupling beam design; archetype designed per to ACI 318-25 and the Rojas-Wallace 2022 shear equation.

Level	f'_c (ksi)	f_y (ksi)	b (in.)	d (in.)	Diagonal bars
14-Roof	8	60	12	48	6 #9
11-13	8	60	12	48	5 #11
8-10	8	60	12	48	7 #11
5-7	8	60	13	48	9 #11
2-4	8	60	15	48	10 #11

6.8.3.5. ACI 318-25 and Rojas-Wallace shear equation – redistributed shear demand

Table 6.30: Summary of 15-story core-wall design according to ACI 318-25 and the Rojas-Wallace 2022 shear equation and redistributed shear demand.

Story	f'_c (ksi)	f_y (ksi)	$L_{w,c}$ (ft)	$L_{w,s}$ (ft)	$t_{w,c}$ (in.)	$t_{w,s}$ (in.)	Shear Reinforcement		Flexural Reinforcement		
							Coupled dir. (@in.)	Solid dir. (@in.)	Interior Boundary	Exterior Boundary	Web
13-15	8	60	9	23	12	12	2 #5 @12	2 #6 @12	10 #7	28 #7	2 #5 @12
10-12	8	60	9	23	12	12	2 #5 @12	2 #6 @7.5	15 #7	42 #7	2 #5 @12
7-9	8	60	9	23	12	12	2 #5 @12	2 #6 @6.5	15 #8	42 #8	2 #5 @12
4-6	8	60	9	23	12	12	2 #5 @12	3 #6 @6.5	15 #9	42 #9	2 #5 @12
1-3	8	60	9	23	12	12	2 #5 @12	3 #6 @5.5	15 #11	42 #11	2 #5 @12

Table 6.31: Summary of 15-story coupling beam design; archetype designed per to ACI 318-25 and the Rojas-Wallace 2022 shear equation and redistributed shear demand.

Level	f'_c (ksi)	f_y (ksi)	b (in.)	d (in.)	Diagonal bars
14-Roof	8	60	12	48	6 #9
11-13	8	60	12	48	5 #11
8-10	8	60	12	48	7 #11
5-7	8	60	12	48	9 #11
2-4	8	60	12	48	10 #11

6.8.4. 18-Story archetypes

6.8.4.1. ACI 318-14

Table 6.32: Summary of 18-story core-wall design according to ACI 318-14.

Story	f'_c (ksi)	f_y (ksi)	$L_{w,c}$ (ft)	$L_{w,s}$ (ft)	$t_{w,c}$ (in.)	$t_{w,s}$ (in.)	Shear Reinforcement		Flexural Reinforcement		
							Coupled dir. (@in.)	Solid dir. (@in.)	Interior Boundary	Exterior Boundary	Web
16-18	8	60	12	26	12	12	2 #5 @12	2 #5 @12	-	-	2 #5 @12
13-15	8	60	12	26	12	12	2 #5 @12	2 #5 @12	9 #7	33 #7	2 #5 @12
10-12	8	60	12	26	12	12	2 #5 @12	2 #5 @12	12 #8	33 #8	2 #5 @12
7-9	8	60	12	26	12	12	2 #5 @12	2 #5 @12	24 #8	60 #8	2 #5 @12
4-6	8	60	12	26	12	12	2 #5 @8.5	2 #5 @9.5	24 #10	60 #10	2 #5 @12
1-3	8	60	12	26	12	12	2 #5 @7.5	2 #5 @8	24 #11	60 #11	2 #5 @12

Table 6.33: Summary of 18-story coupling beam design; archetype designed per to ACI 318-14.

Level	f'_c (ksi)	f_y (ksi)	b (in.)	d (in.)	Diagonal bars
17-Roof	8	60	12	48	6 #11
14-16	8	60	12	48	7 #11
11-13	8	60	12	48	9 #11
8-10	8	60	12	48	13 #11
5-7	8	60	12	48	14 #11
2-4	8	60	12	48	12 #11

6.8.4.2. ACI 318-19

Table 6.34: Summary of 18-story core-wall design according to ACI 318-19.

Story	f'_c (ksi)	f_y (ksi)	$L_{w,c}$ (ft)	$L_{w,s}$ (ft)	$t_{w,c}$ (in.)	$t_{w,s}$ (in.)	Shear Reinforcement		Flexural Reinforcement		
							Coupled dir. (@in.)	Solid dir. (@in.)	Interior Boundary	Exterior Boundary	Web
16-18	8	60	12	26	12	12	2 #6 @11	2 #6 @8	-	-	2 #5 @12
13-15	8	60	12	26	12	12	2 #6 @9	2 #6 @7.5	9 #7	33 #7	2 #5 @12
10-12	8	60	12	26	12	12	2 #6 @8	2 #6 @7.5	12 #8	33 #8	2 #5 @12
7-9	8	60	12	26	13	15	2 #6 @6	2 #6 @5	24 #8	60 #8	2 #5 @12
4-6	8	60	12	26	17	20	2 #6 @4.5	3 #6 @5.5	24 #10	60 #10	2 #5 @12
1-3	8	60	12	26	18	20	2 #6 @4	3 #6 @5.5	24 #11	60 #11	2 #5 @12

Table 6.35: Summary of 18-story coupling beam design; archetype designed per to ACI 318-19.

Level	f'_c (ksi)	f_y (ksi)	b (in.)	d (in.)	Diagonal bars
17-Roof	8	60	12	48	5 #9
14-16	8	60	12	48	5 #11
11-13	8	60	12	48	6 #11
8-10	8	60	13	48	7 #11
5-7	8	60	17	48	9 #11
2-4	8	60	18	48	9 #11

6.8.4.3. ACI 318-25

Table 6.36: Summary of 18-story core-wall design according to ACI 318-25.

Story	f'_c (ksi)	f_y (ksi)	$L_{w,c}$ (ft)	$L_{w,s}$ (ft)	$t_{w,c}$ (in.)	$t_{w,s}$ (in.)	Shear Reinforcement		Flexural Reinforcement		
							Coupled dir. (@in.)	Solid dir. (@in.)	Interior Boundary	Exterior Boundary	Web
16-18	8	60	12	26	12	12	2 #5 @12	2 #5 @10.5	-	-	2 #5 @12
13-15	8	60	12	26	12	12	2 #5 @11	2 #5 @8	9 #7	33 #7	2 #5 @12
10-12	8	60	12	26	12	12	2 #5 @10	2 #5 @8	12 #8	33 #8	2 #5 @12
7-9	8	60	12	26	12	12	2 #6 @9.5	2 #6 @7	24 #8	60 #8	2 #5 @12
4-6	8	60	12	26	12	15	2 #6 @6.5	2 #6 @5	24 #10	60 #10	2 #5 @12
1-3	8	60	12	26	13	15	2 #6 @6	2 #6 @5	24 #11	60 #11	2 #5 @12

Table 6.37: Summary of 18-story coupling beam design; archetype designed per to ACI 318-25.

Level	f'_c (ksi)	f_y (ksi)	b (in.)	d (in.)	Diagonal bars
17-Roof	8	60	12	48	5 #9
14-16	8	60	12	48	5 #11
11-13	8	60	12	48	6 #11
8-10	8	60	12	48	7 #11
5-7	8	60	12	48	9 #11
2-4	8	60	13	48	9 #11

6.8.4.4. ACI 318-25 and Rojas-Wallace shear equation

Table 6.38: Summary of 18-story core-wall design according to ACI 318-25 and the Rojas-Wallace 2022 shear equation.

Story	f'_c (ksi)	f_y (ksi)	$L_{w,c}$ (ft)	$L_{w,s}$ (ft)	$t_{w,c}$ (in.)	$t_{w,s}$ (in.)	Shear Reinforcement		Flexural Reinforcement		
							Coupled dir. (@in.)	Solid dir. (@in.)	Interior Boundary	Exterior Boundary	Web
16-18	8	60	12	26	12	12	2 #5 @12	2 #5 @12	-	-	2 #5 @12
13-15	8	60	12	26	12	12	2 #5 @12	2 #5 @10	9 #7	33 #7	2 #5 @12
10-12	8	60	12	26	12	12	2 #5 @12	2 #7 @6	12 #8	33 #8	2 #5 @12
7-9	8	60	12	26	12	12	2 #5 @12	2 #6 @6	24 #8	60 #8	2 #5 @12
4-6	8	60	12	26	12	12	2 #5 @12	2 #6 @6	24 #10	60 #10	2 #5 @12
1-3	8	60	12	26	13	12	2 #5 @12	2 #6 @5	24 #11	60 #11	2 #5 @12

Table 6.39: Summary of 18-story coupling beam design; archetype designed per to ACI 318-25 and the Rojas-Wallace 2022 shear equation.

Level	f'_c (ksi)	f_y (ksi)	b (in.)	d (in.)	Diagonal bars
17-Roof	8	60	12	48	5 #9
14-16	8	60	12	48	5 #11
11-13	8	60	12	48	6 #11
8-10	8	60	12	48	7 #11
5-7	8	60	12	48	9 #11
2-4	8	60	13	48	9 #11

6.8.4.5. ACI 318-25 and Rojas-Wallace shear equation – redistributed shear demand

Table 6.40: Summary of 18-story core-wall design according to ACI 318-25 and the Rojas-Wallace 2022 shear equation and redistributed shear demand.

Story	f'_c (ksi)	f_y (ksi)	$L_{w,c}$ (ft)	$L_{w,s}$ (ft)	$t_{w,c}$ (in.)	$t_{w,s}$ (in.)	Shear Reinforcement		Flexural Reinforcement		
							Coupled dir. (@in.)	Solid dir. (@in.)	Interior Boundary	Exterior Boundary	Web
16-18	8	60	12	26	12	12	2 #5 @12	2 #5 @12	-	-	2 #5 @12
13-15	8	60	12	26	12	12	2 #5 @12	2 #5 @10	9 #7	33 #7	2 #5 @12
10-12	8	60	12	26	12	12	2 #5 @12	2 #7 @6	12 #8	33 #8	2 #5 @12
7-9	8	60	12	26	12	12	2 #5 @12	2 #6 @6	24 #8	60 #8	2 #5 @12
4-6	8	60	12	26	12	12	2 #5 @12	2 #6 @6	24 #10	60 #10	2 #5 @12
1-3	8	60	12	26	12	12	2 #5 @12	2 #6 @5	24 #11	60 #11	2 #5 @12

Table 6.41: Summary of 18-story coupling beam design; archetype designed per to ACI 318-25 and the Rojas-Wallace 2022 shear equation and redistributed shear demand.

Level	f'_c (ksi)	f_y (ksi)	b (in.)	d (in.)	Diagonal bars
17-Roof	8	60	12	48	5 #9
14-16	8	60	12	48	5 #11
11-13	8	60	12	48	6 #11
8-10	8	60	12	48	7 #11
5-7	8	60	12	48	9 #11
2-4	8	60	12	48	9 #11

7. ARCHETYPE CORE WALL ANALYTICAL MODELING

The nonlinear models used to analyze the archetypes are presented in this chapter. The three-dimensional version of the OpenSees Multi-Vertical-Line-Element-Model (MVLEM-3D) for reinforced concrete (RC) walls is used (Kalbasi, 2019; Kolozvari et al. 2021). Coupling beams are modeled with the proposed "CBeam" model.

7.1. System Modeling

The lateral-force-resisting system for each archetype is modeled using the structural analysis software OpenSees (McKenna et al., 2000). This modeling approach involves specifying the building geometry, member cross-sectional dimensions, and design (or expected) material properties of the structural walls and coupling beams, as summarized in Chapter 6. The models account for the wall layout (positioning) of the lateral system (coupled walls) and the gravity system (slab-column frame) in the building plan and over the height of the building, and the distribution of mass and the gravity loads.

A conceptual view of the model is depicted in Figure 7.1. At each story level, tributary mass is allocated to the element nodes, with gravitational loads (dead and live) assigned at these nodes based on their respective tributary areas, as illustrated in Figure 7.1. To adequately capture P-Delta effects, and to ensure that the two C-shaped wall piers are connected solely by coupling beams, two P-Delta columns are placed at the centroid of the core wall. One-half of the gravity loads are applied to each P-Delta column. The P-Delta columns are axially rigid and provide negligible flexural stiffness (conceptually pinned at each end). The location and connectivity of the P-Delta columns is depicted in Figure 7.1. The wall piers, with their specific material force-deformation relationships (Figure 7.2), are connected by CBeam elements. The shear response of the wall is simulated using a linear elastic spring with an effective shear stiffness of $0.5G$ (Figure 7.2).

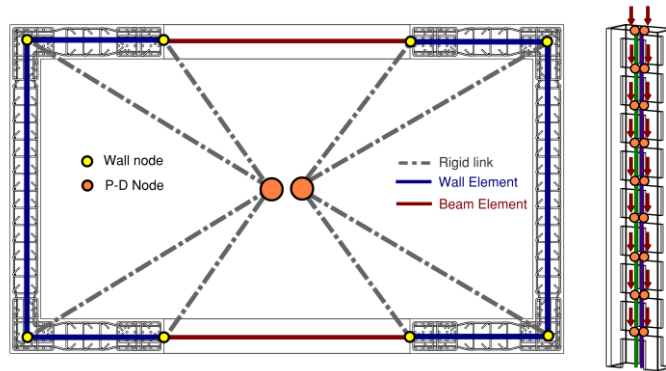


Figure 7.1: Implementation of leaning column in the analytical model. Left) plan view; right) 3-D view.

The modeling of wall piers in this study is accomplished using the three-dimensional, four-node variant of the Multiple-Vertical-Line-Element-Model (MVLEM-3D) within OpenSees. This model, an advanced version of the original MVLEM, was formulated, implemented, and validated by Kalbasi (2019), builds upon the work by Orakcal et al. (2004), Orakcal and Wallace (2006), and Kolozvari et al. (2015), as depicted in Figure 7.2. The axial and flexural responses of the model element are represented by an array of uniaxial elements (macro-fibers) distributed across the wall cross-section, linked to rigid beams at the top and bottom of the element to maintain the plane-section assumption, as illustrated in Figure 7.2.

Differing from a conventional displacement-based beam-column element model, the MVLEM-3D calculates the deformations and forces in the element fibers using averaged strains and stresses in each macro-fiber, aiming to reduce convergence issues and enhance numerical stability. The stiffness characteristics and force-deformation relationships of the uniaxial elements are derived from the hysteretic stress-strain relations for concrete and reinforcing steel (Figure 7.2), in conjunction with the tributary area assigned to each element. Notably, the model distinctly separates element flexure and shear responses, as shown in Figure 5.2b.

Despite the three-dimensional simulation environment for the archetypes, the impact of the wall's out-of-plane deformation on its in-plane force and deformation capacities is omitted, due to the absence of suitable analytical models and a scarcity of experimental data to validate these models. The in-plane behavior of walls is simulated through fibers, while the out-of-plane behavior employs a Kirchhoff elastic plate model. Although these modeling assumptions are prevalent in nonlinear analyses of RC walls, they underscore significant gaps that require further analytical and experimental exploration.

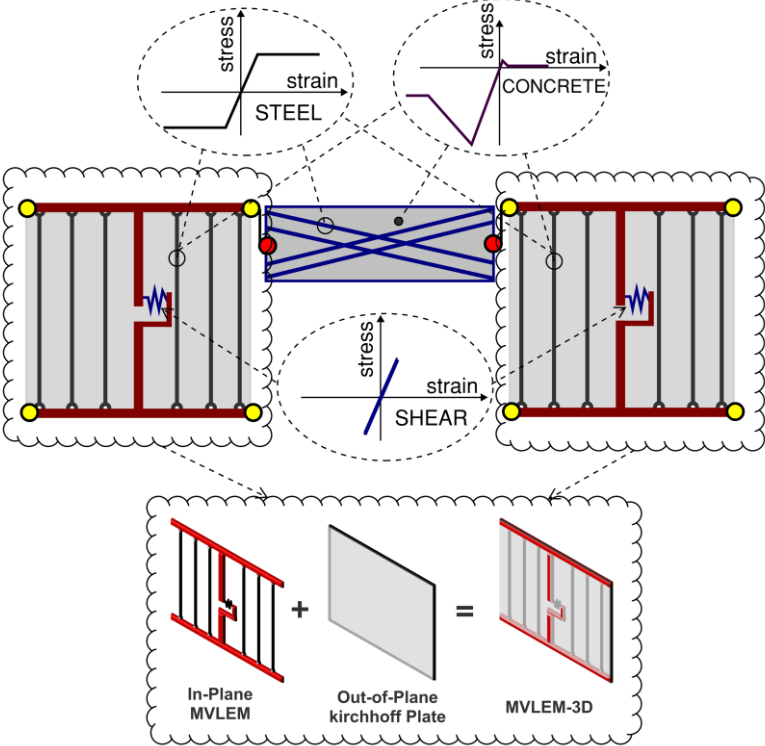


Figure 7.2: Coupling beam and shear wall elements connection.

In the MVLEM-3D element, the internal force vector is deduced from the axial stresses arising in concrete and reinforcing steel within each macro-fiber, coupled with the shear force generated by the horizontal spring, to accurately simulate the element responses. The relative rotational between the top and bottom boundaries of the element is lumped at the center of rotation, which

is coincident with the shear spring. A transformation matrix is used to determine nodal deformations from the rotation at the center of rotation. The curvature distribution is presumed constant along the element height; therefore, an adequate number of elements across the anticipated plastic hinge region must be used to reliably forecast local deformation responses. For the horizontal wall discretization, a sufficient number of fibers, typically around 6 inches in width, are employed to effectively represent the wall cross-section and the reinforcement layout in both the boundaries and the web of the wall. Vertically, the discretization incorporates two wall elements per story height in the plastic zone area (first three stories), as recommended by LATBSDC-2020. The discretization of the core-wall cross-section and its extension along the height of the structure is depicted in Figure 7.3.

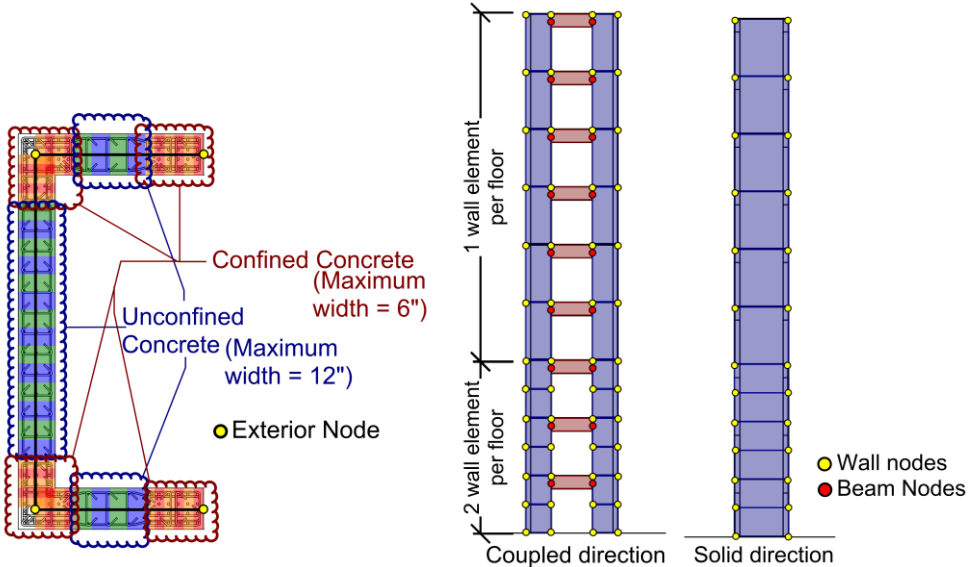


Figure 7.3: left) Wall cross-section discretization; right) Coupling beam discretization and its connection to adjacent walls.

The shear response of the model element is replicated using a horizontal spring connected to the top and bottom rigid beams using a vertical rigid strut. The shear behavior is commonly characterized by various ad-hoc force-deformation models (e.g., linear-elastic, bi-linear, origin-

oriented hysteresis models). In line with current design and evaluation standards (e.g., ASCE 41-17; LATBSDC, 2020), an elastic spring with a cracked effective shear stiffness of $0.5GA_w$ is utilized to represent the shear behavior; this modeling approach common in current engineering practice. The axial/flexural and shear responses in the MVLEM-3D element are described independently, resulting in no interplay between these responses, as shown in Figure 7.2.

In the structural assembly depicted in Figure 7.4, the coupling beams are affixed to the wall piers through the use of rigid beam elements. These elements are positioned such that the centerline of the longitudinal axis of the coupling beams are offset from the floor level by a distance equal to one-half the depth of the coupling beam elements, so that the tops of the beams align precisely with the floor levels. The cross-section of the coupling beams includes an effective slab width according to ACI 318-19 at the top of the beam (i.e., the beam cross section is an inverted L-shape). This modeling approach includes two significant benefits: the incorporation of a slab atop the coupling beams substantially increases the beam shear strength (Naish et al., 2013) and it enables the analytical model to accurately account for the axial restraint exerted by both the slab and the adjacent wall piers.

As elucidated in Chapter 4, the sensitivity analysis pertaining to the number of subsegments in the CBeam elements indicated the optimal use of 11 segments along the length of the coupling beams. In addition, the cross-sectional composition of these elements includes fibers measuring 0.5 inches by 0.5 inches, which allows for an accurate representation of the concrete material behavior.

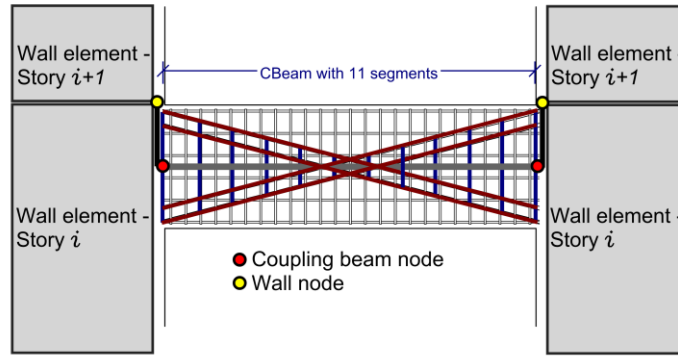


Figure 7.4: Coupling beam discretization and its connection to adjacent walls.

7.2. Damping

In accordance with Section 4.2.7 of the PEER TBI (2017) guidelines for Maximum Considered Earthquake Risk (MCE_R), the nonlinear model employs Rayleigh damping. The critical damping ratio, $\zeta_{critical}$, is determined as a function of the building height (H), formulated as $\zeta_{critical} = \frac{0.36}{\sqrt{H}}$. This relationship suggests a decrease in damping as building height increases, as depicted in Figure 7.5. The Rayleigh damping coefficients, which depend on mass and stiffness, are computed for periods of $0.2T_1$ and $1.5T_1$, where T_1 is the building fundamental period identified through modal analysis, using the current stiffness.

To reduce the effect of varying damping ratios across archetypes with an identical number of stories, the viscous damping ratio was assigned based on the average of the first modal periods from each of the five archetypes with the same story count.

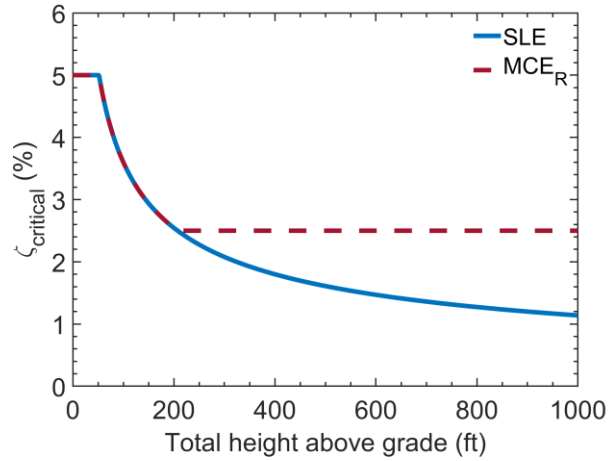


Figure 7.5: Recommended viscous damping based on building height per PEER TBI, 2017 provision.

7.2.1. Modal Analysis

As part of the model verification, modal analysis was conducted on all archetypes and summary of the analysis (mode shapes and modal periods) are provided in figure 7.6 through 7.9.

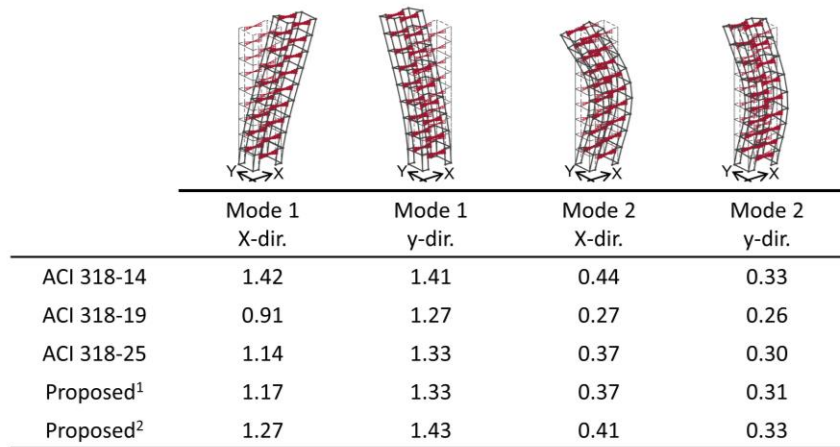


Figure 7.6: 9-story archetypes mode shapes and their associated modal periods.

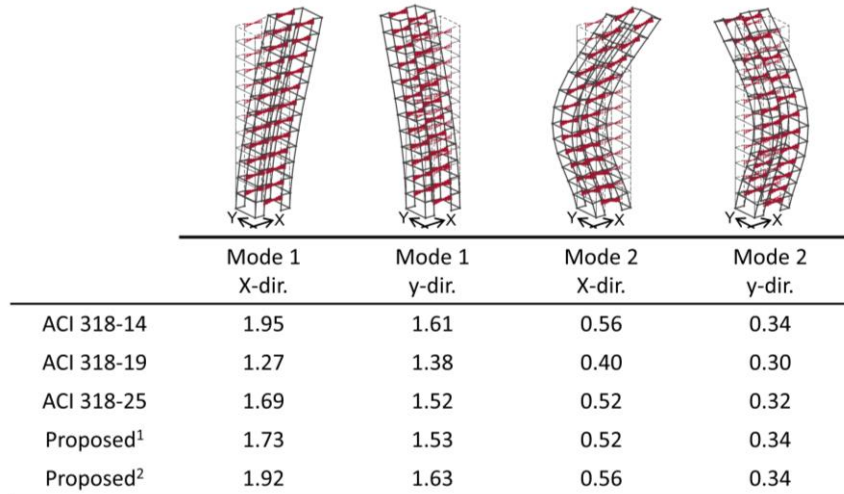


Figure 7.7: 12-story archetypes mode shapes and their associated modal periods.

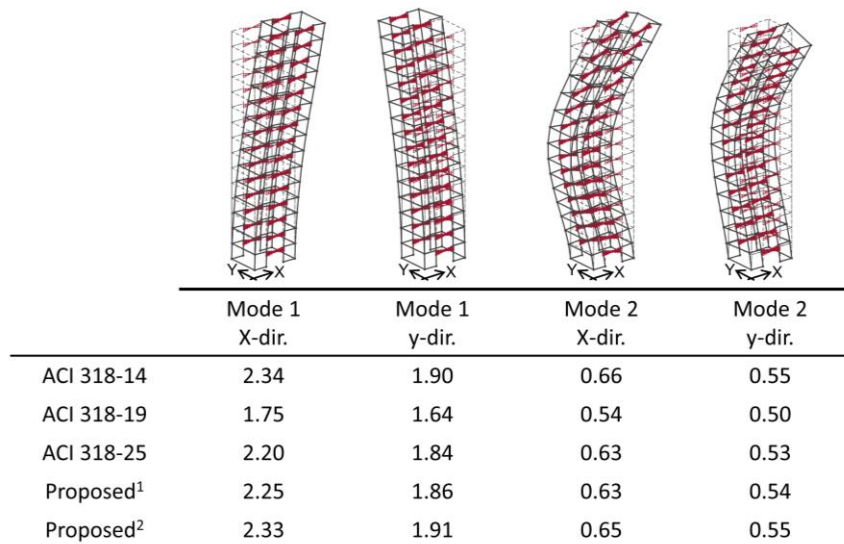


Figure 7.8: 15-story archetypes mode shapes and their associated modal periods.

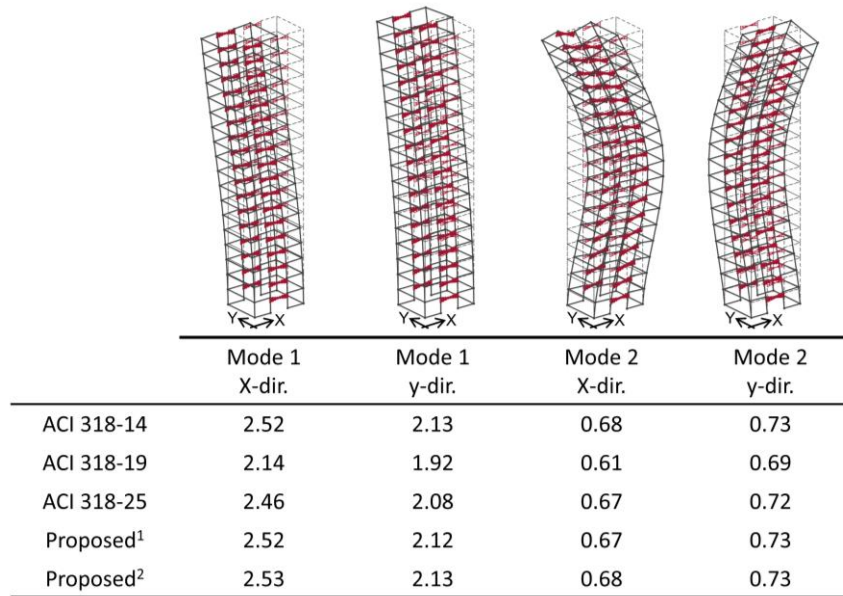


Figure 7.9: 18-story archetypes mode shapes and their associated modal periods.

8. NONLINEAR ANALYSIS

The objective of this chapter is to evaluate and compare the shear behavior for the various approaches used to design the core wall archetypes under seismic loading. To achieve this goal, a nonlinear static analysis, commonly referred to as pushover analysis, was initially conducted on all structural archetypes to ensure that analytical models were implemented correctly. This analysis employed a lateral load pattern for the first mode shape in each orthogonal direction. The gravity load combination applied in this analysis was based on $D+0.25L$, which consists of the dead load (D) plus 25% of the live load (L). Finally, a nonlinear dynamic analysis was conducted utilizing two suites of ground motions for archetypes with the same number of stories. These suites were selected and scaled using the Conditional Mean Spectrum (CMS) approach, conditioned to the first and second mode periods of the archetypes.

8.1. Failure Assessment

In general, three main failure modes could be considered and assessed through post-processing of results (non-simulated): 1) flexural, 2) axial, and 3) shear failure. Details of the failure modes considered are presented in the following subsections. However, due to the nature of this project, shear failure is the only mode of failure that is used to compare behavior of various archetype designs.

8.1.1. Flexural Failure via Drift Capacity Model

Flexural failure can be characterized using the drift (rotation) capacity model, as proposed by Abdullah and Wallace (2019). This approach was formulated based on an extensive analysis of a database comprising over 1000 tests on concrete shear walls. The database includes comprehensive data, e.g., details of the wall cross-sectional details, construction material information, configuration of the provided transverse reinforcement, and primary experimental

results. The summary of tests includes the observed failure mode, including concrete crushing, buckling of reinforcement bars, reinforcement fracture, or instability at the wall boundary due to flexural compression.

The drift capacity is identified as the total displacement or rotation where the strength of the test specimen drops to 80% of its maximum strength. By examining the influence of various design elements on these data, two distinct formulas were derived to calculate the lateral drift capacity of walls at points of substantial strength reduction. This analysis utilized a subset of the larger database, which included 164 tests on walls generally satisfying ACI 318-14 requirements for detailing of special structural shear walls. A notable feature of the models is the low coefficient of variation (COV values of 0.15 and 0.16).

Furthermore, the drift capacity model is employed to develop comprehensive models for the total rotation and curvature of plastic hinges, a critical aspect for nonlinear modeling of taller structures.

The length of these plastic hinges, assumed to be half the wall length ($l_w/2$), which is commonly used in engineering practice based on studies reported by Wallace and Moehle (2012) and Segura and Wallace (2018).

The following figures illustrate the compilation of the 164 tests within the drift capacity model and juxtapose the predicted drift capacities against those observed experimentally. The formulas for calculating drift capacity are adjusted based on the configuration of the reinforcement, specifically the arrangement of overlapping hoops and crossties.

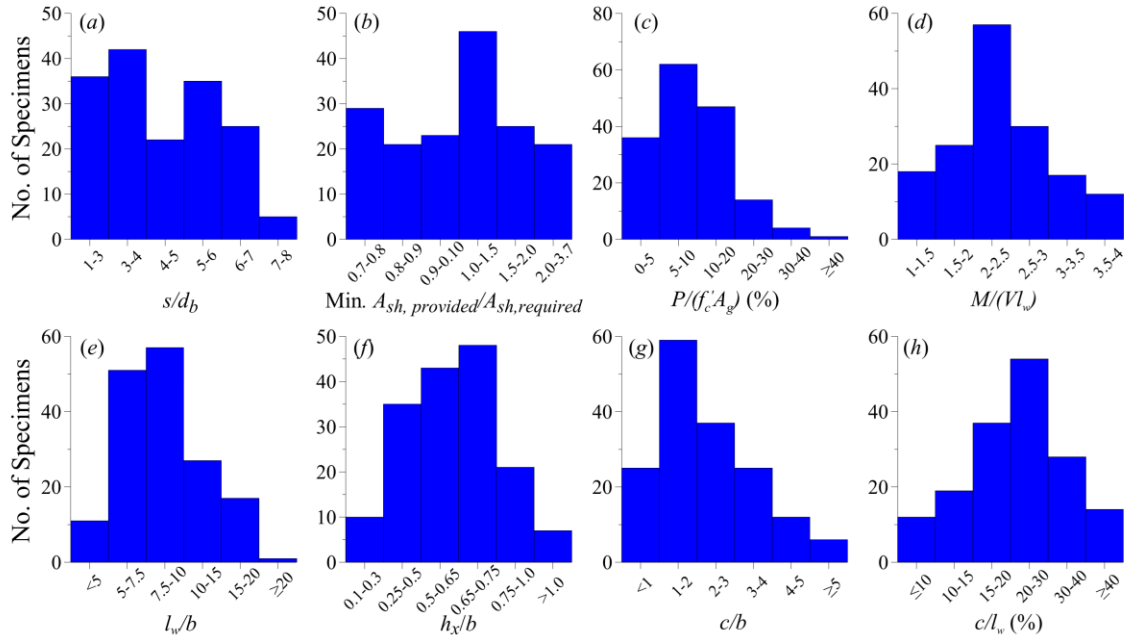


Figure 8.1: Histogram of 164 Tests in the Drift capacity model (Abdullah, 2019).

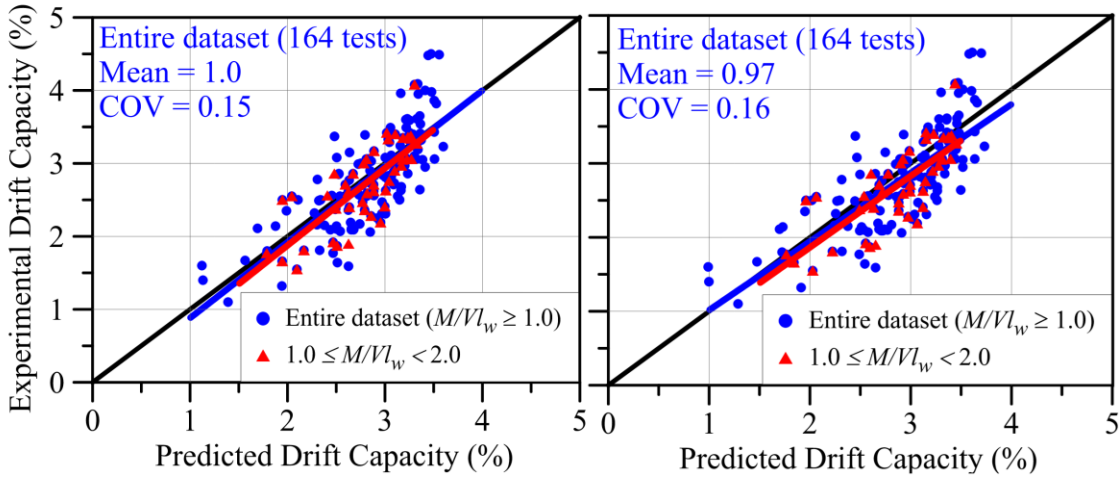


Figure 8.2: Comparison of predicted drift capacity with experimental drift capacity (Abdullah, 2019). Left) predicted drift capacity with equation 8.1; right) predicted drift capacity with equation 8.2.

$$\frac{\delta_c}{h_w} (\%) = 3.85 - \frac{l_w c}{\alpha b^2} - \frac{v_{max}}{10 \sqrt{f'_c}} \quad \text{Eq. 8.1}$$

that $\alpha = 60$ for boundaries utilize overlapping hoops and 45 where a combination of a single perimeter hoop with supplemental cross ties is used.

$$\frac{\delta_c}{h_w} (\%) = 4.0 - \frac{l_w c}{\alpha b^2} - \frac{v_{max}}{10\sqrt{f'_c}} \quad \text{Eq. 8.2}$$

that $\alpha = 50$ for boundaries utilize overlapping hoops and 40 where a combination of a single perimeter hoop with supplemental crossties is used.

8.1.2. Axial Failure

The concept of axial failure in walls is explained using a model created by Wallace et al. (2008). This model determines the drift capacity at which a wall can no longer support the gravity load assigned to a wall based on a critical diagonal crack orientation and the slip resistance along the crack. This model is based on an earlier (similar) model developed for columns, modified to account for differences in the behavior of columns and walls. The primary difference in the column and wall versions of the model is the assumed crack orientation, which is constant for columns and assumed to form along the longest diagonal distance over the single-story height of the wall. In Figure 8.3b, the correlation between the anticipated drift ratio at the point of axial failure and the ratio of axial stress is illustrated, considering standard geometries, materials, and reinforcement configurations. These relations are then compared against various experimental results conducted by Wallace et al. (2008), specifically those with axial load ratios of 5% and 10%. The illustration includes two blue dashed lines indicating possible variations in lateral drift at the point of axial failure, based on different assumed shear friction relationships. Additionally, a red broken line depicts a modified prediction of the model to align with specific test conditions, notably the absence of hooks in horizontal web reinforcement. The model aligns reasonably well with test outcomes, particularly noting the relative consistency of results with axial load ratios above approximately 3%, despite some observable sensitivity to the chosen shear friction relationship. These observations underscore the need for further comprehensive investigations to evaluate the lateral drift capacity of walls or piers, especially considering enhanced detailing, increased axial loads, and varying amounts of longitudinal reinforcement.

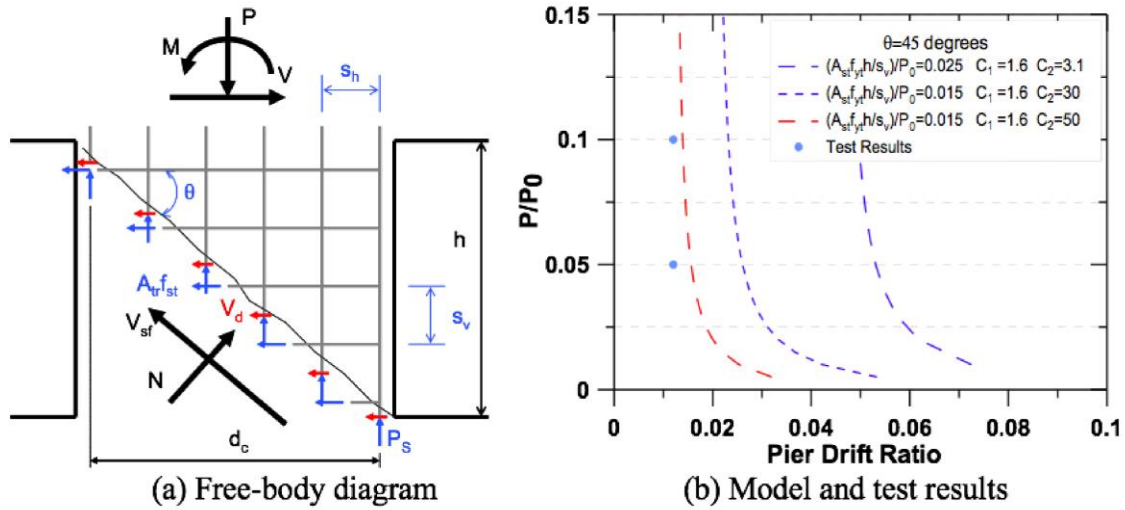


Figure 8.3: Axial load capacity model for a shear wall pier after diagonal cracking.

In 2021, Abdullah and Wallace conducted a study using linear regression to analyze data from 85 special walls and 65 ordinary walls. They used the variables $\frac{l_w c}{b^2}$ and $\frac{P}{A_g f'_c}$ as predictors to develop equations predicting the average drift capacity at axial failure ($\frac{\Delta_a}{h_w}$) for these walls. The minimum values for these equations were determined based on engineering expertise, suggesting displacement-ductility values around two for special walls and one for ordinary walls at axial failure. This was in line with previous findings that the yield drift for special walls controlled by flexure is generally between 0.6% and 0.8%.

$$\left\{ \begin{array}{l} \text{special walls} \\ \text{ordinary walls} \end{array} \right. \rightarrow \begin{array}{l} \frac{\Delta_a}{h_w} (\%) = 4.1 - \left(\frac{l_w c}{40 b^2} \right) - \left(2.5 \frac{P}{A_g f'_c} \right) \geq 1.5\% \\ \frac{\Delta_a}{h_w} (\%) = 3.65 - \left(\frac{l_w c}{30 b^2} \right) - \left(3.5 \frac{P}{A_g f'_c} \right) \geq 0.8\% \end{array} \quad \text{Eq. 8.3}$$

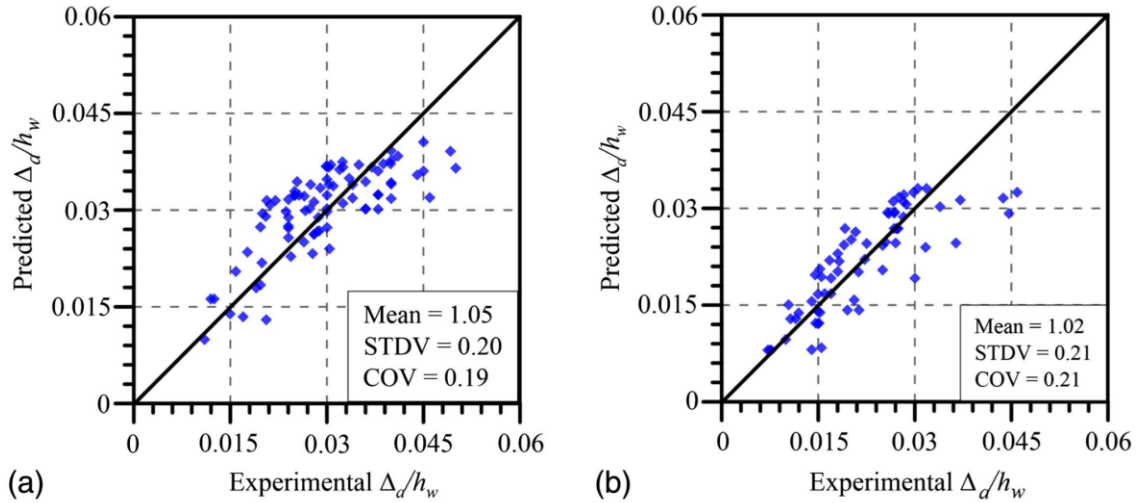


Figure 8.4: Comparison of predicted drift capacities with experimental drift capacities: a) special walls; and b) ordinary walls.

These predictive equations were then compared to actual experimental data in Figure 8.4, showing the drift capacities of both wall types. For special walls, the comparison yielded an average ratio of predicted to experimental values of 1.05, with a standard deviation (STDV) of 0.20 and a coefficient of variation (COV) of 0.19 across drift values ranging from about 1.5% to 4.5%. For ordinary walls, the mean ratio was 1.02, with a STDV of 0.21 and a COV of 0.21.

8.1.3. Shear Failure

Since the shear wall analytical model (MVLEM-3D) does not account for the interaction between shear and flexure, exceedance from the shear limit is evaluated by post-processing of the analysis results. Two shear strength equations are considered in these assessments: 1) the ACI 318 shear strength equation, and 2) the shear strength equation proposed by Rojas and Wallace in 2022. The ACI 318 shear strength equation (Eq. 6.10) provides a shear strength that is independent of the axial load history; however, it does consider variables of f_{yt} , f'_c , and h_w/l_w . On the other hand, the shear strength equation proposed by Rojas and Wallace considers the effect of axial load history on the walls, as well as the contribution of longitudinal rebars in the tension boundary elements. As the axial load and ratio of M_u/V_u during the load history, the wall shear strength is

updated (calculated) and compared with the instantaneous shear demand to assess if the limit is exceeded. This process is depicted in Figure 8.5, where the red square denotes shear demand reached the limit for the ACI 318-19 shear strength equation, and the black square denotes shear demand reached the limit for the Rojas-Wallace (2022) shear strength equation (Eq. 6.10).

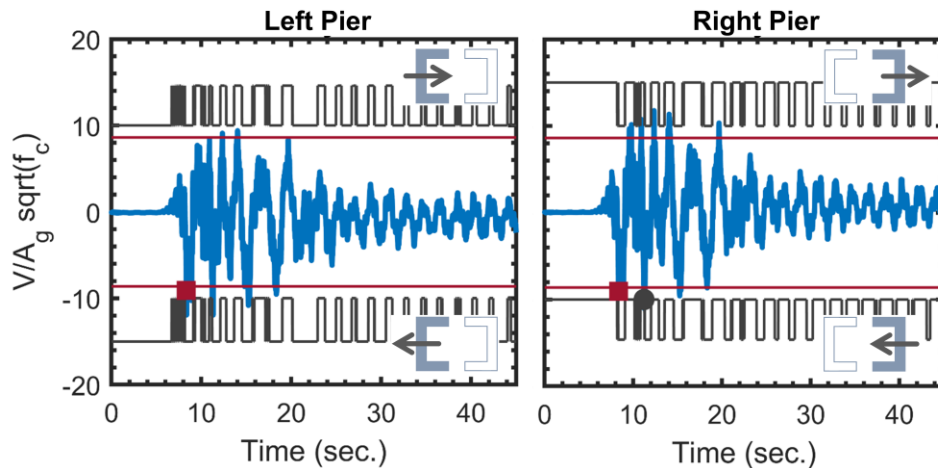


Figure 8.5: Assessment of shear limit exceedance. The red line represents the ACI 318 shear strength, and the black line represents the Rojas-Wallace 2022 shear strength history.

8.2. Nonlinear Static Analysis Results

Results from the nonlinear static analyses are presented in Figures 8.6 through 8.17 for the archetypes considered in this study. The analysis results confirm that archetypes designed based on ACI 318-14 provide higher strength in the coupled direction, as the R-factor designed for is lower than in the subsequent provisions ($R = 6$ versus $R = 8$). Whereas, in the solid wall direction, the archetypes show approximately the same strength, as the R-factor is the same for all archetypes and is equal to 6. Table 8.1 summarizes the yield strength of each archetype. Nonetheless, since the wall thickness varies between the archetypes, the normalized shear strength of the models to the web area of the walls (A_g) in the direction of loading is not consistent in the pushover plots.

Table 8.1: Base shear strength capacity of archetypes.

Design Code	9-Story		12-Story		15-Story		18-Story	
	V_x (kips)	V_y (kips)	V_x (kips)	V_y (kips)	V_x (kips)	V_y (kips)	V_x (kips)	V_y (kips)
ACI 318-14	4457	3157	4325	3157	3246	2387	4662	3321
ACI 318-19	3810	3069	3780	3240	2770	2005	4090	3335
ACI 318-25	3806	3052	3950	3195	2768	2006	4232	3318
R-W	3812	3051	3890	3190	2767	2003	4228	3317
R-W w/ Redist.	3795	3043	3780	3176	2765	2003	4221	3315

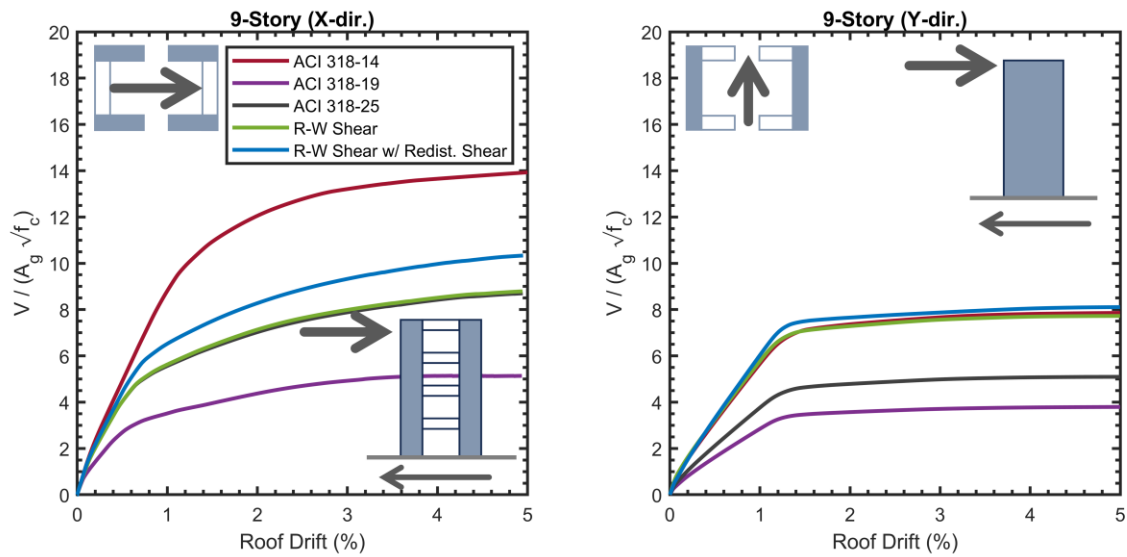


Figure 8.6: 9-story archetypes pushover analysis results (roof drift vs. total base shear).

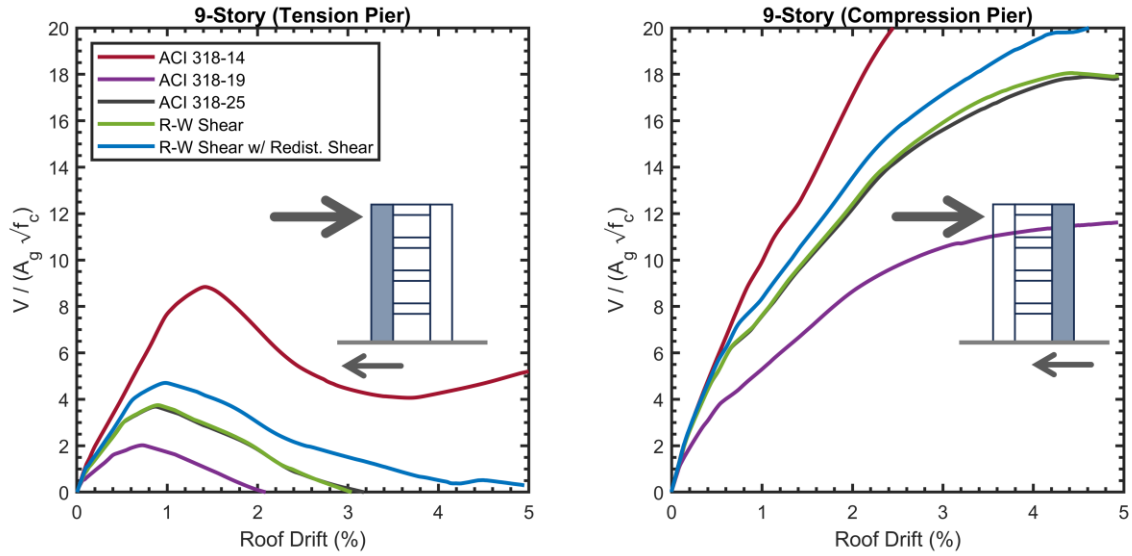


Figure 8.7: 9-story archetypes pushover analysis results (roof drift vs. each base shear in the coupled direction).

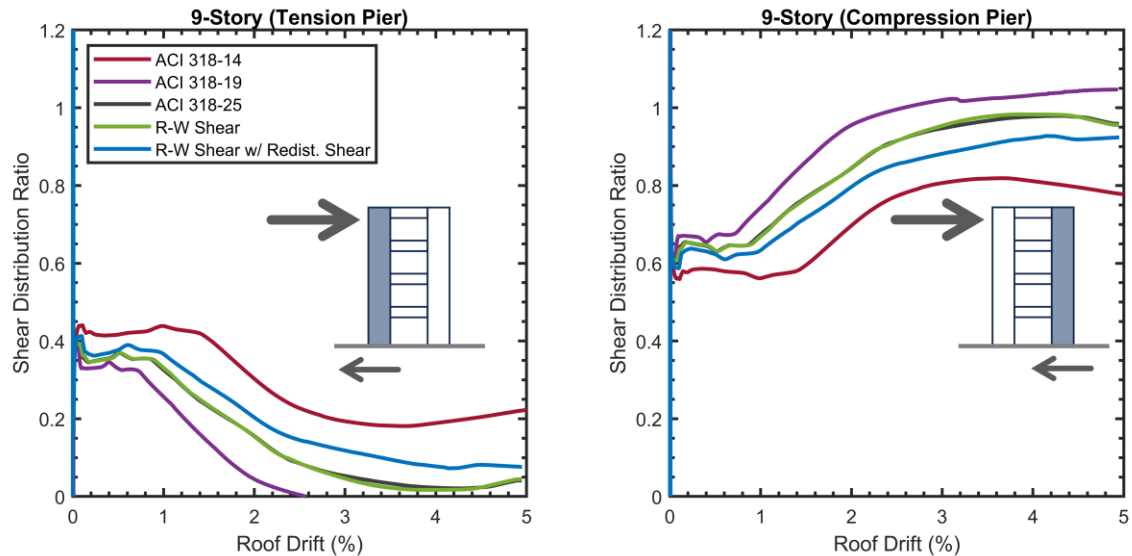


Figure 8.8: 9-story archetypes shear distribution ratio between the wall piers.

As shown in Figures 8.6 and 8.7, 9-story archetypes yield at around 1% roof drift. Up to this roof drift, the shear force distribution between the wall piers is about 40%-60% (40% of the total base shear is resisted by the tension pier and 60% by the compression pier). This distribution of shear force between the piers mainly depends on the moment strength of wall piers in the direction of

loading. Note that this ratio is quite close to the ratio calculated during the design process of the redistributed shear archetype (refer to Appendix B for detailed calculations).

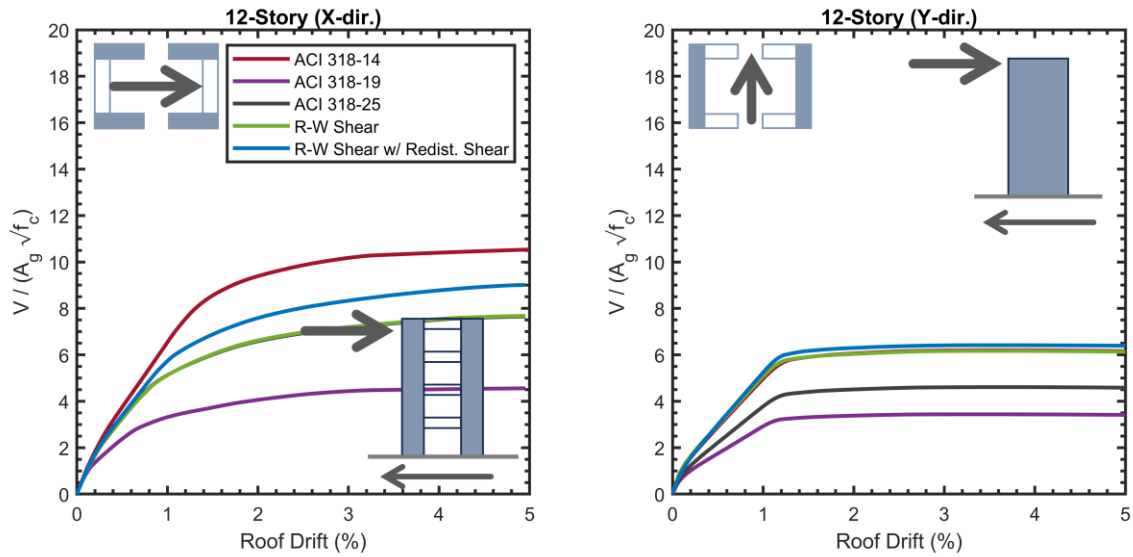


Figure 8.9: 12-story archetypes pushover analysis results (roof drift vs. total base shear).

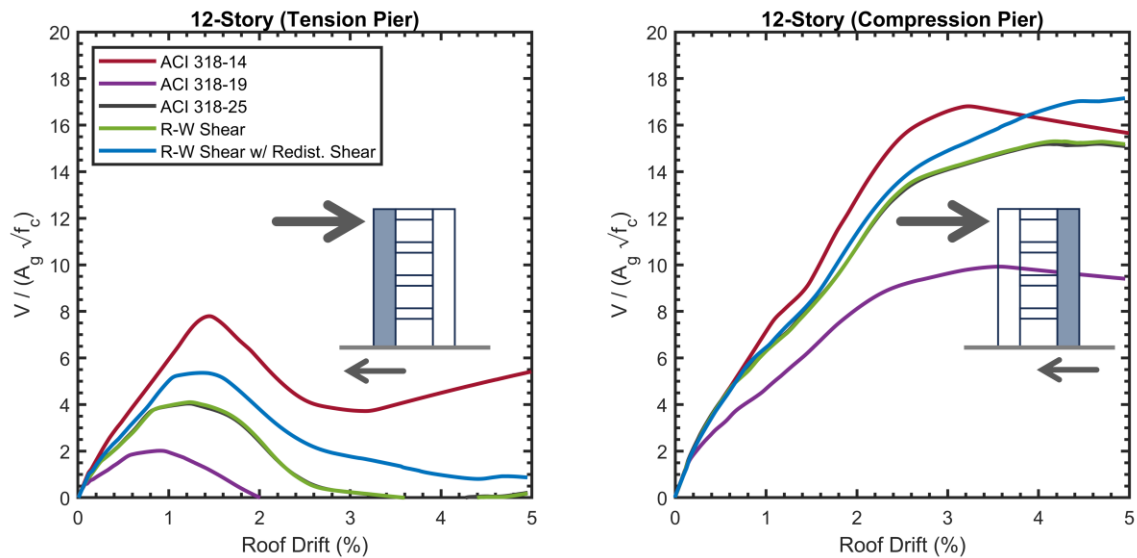


Figure 8.10: 12-story archetypes pushover analysis results (roof drift vs. each base shear in the coupled direction).

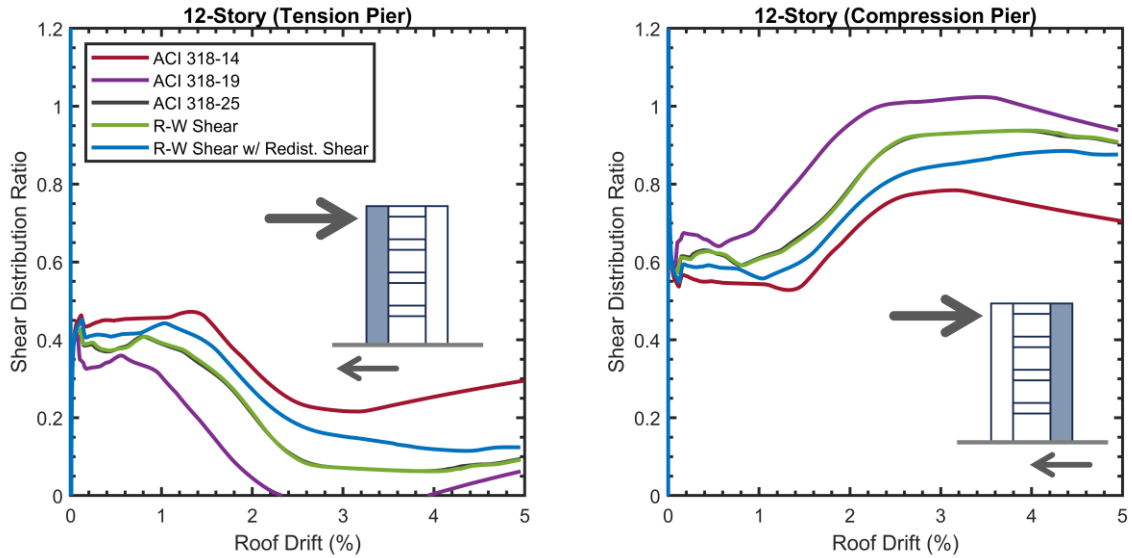


Figure 8.11: 12-story archetypes shear distribution ratio between the wall piers.

Figures 8.9 and 8.10 indicate that 12-story archetypes begin to yield at approximately 1.2% roof drift. Until this point of roof drift, the distribution of shear force between the wall piers is about 40%-60% ratio (with 40% of the total base shear being resisted by the tension pier and 60% by the compression pier). It's noteworthy that this ratio closely aligns with the ratio determined during the design phase of the redistributed shear archetype (see Appendix B for in-depth calculations).

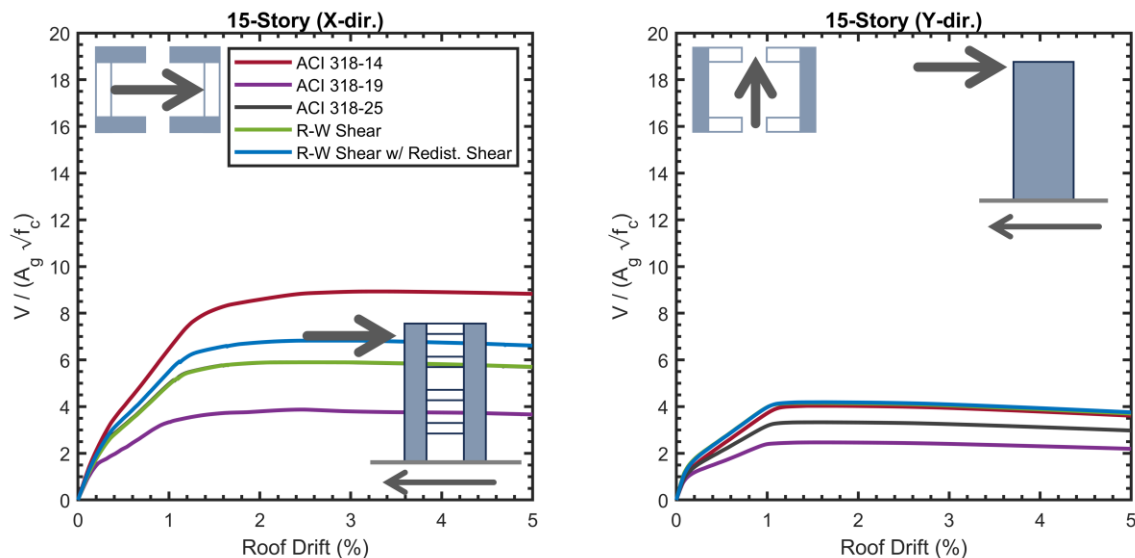


Figure 8.12: 15-story archetypes pushover analysis results (roof drift vs. total base shear).

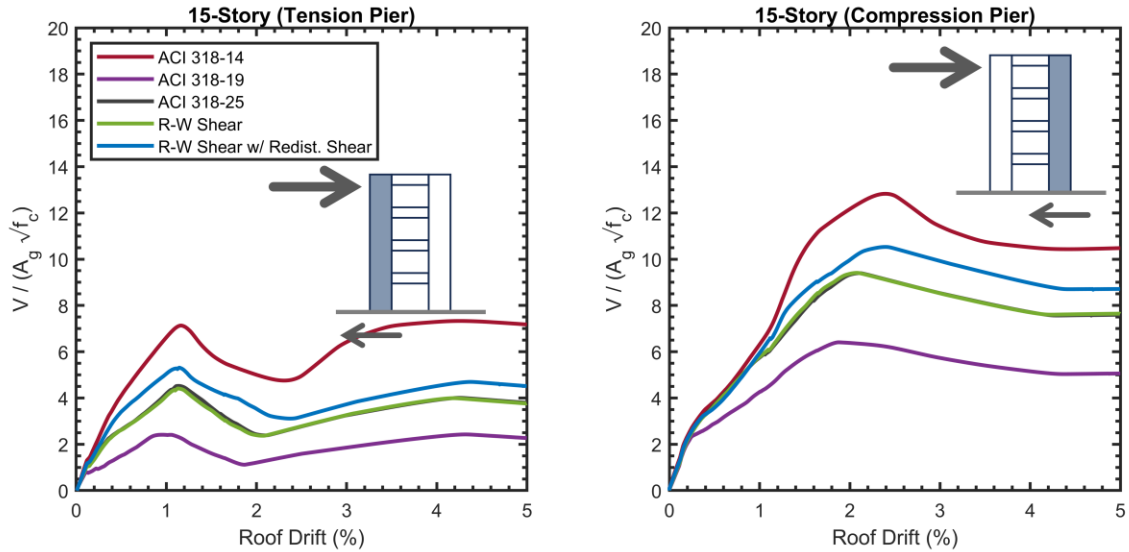


Figure 8.13: 15-story archetypes pushover analysis results (roof drift vs. each base shear in the coupled direction).

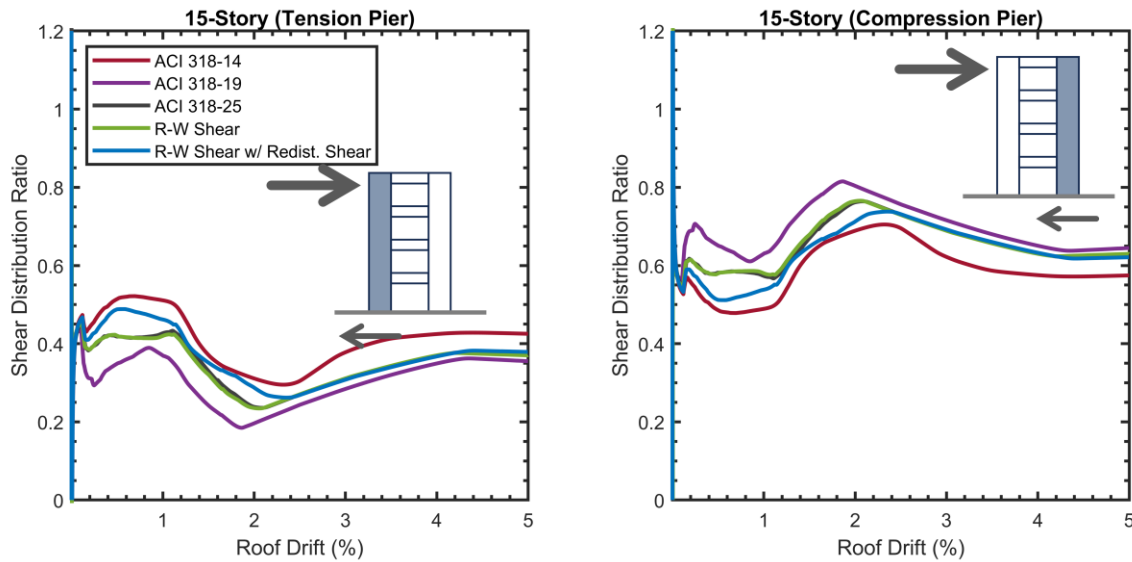


Figure 8.14: 15-story archetypes shear distribution ratio between the wall piers.

Figures 8.12 and 8.13 illustrate that 15-story archetypes begin to yield at a roof drift of approximately 1.4%. Until reaching this roof drift level, the shear force distribution between wall piers ranges from 35%-45% in the tension pier and 55%-65% in the compression pier. The highest shear force ratio in the compression pier, 65%, is observed in the model designed based on ACI 318-19, while the lowest ratio, 55%, is found in the model designed based on ACI 318-14. This

variation is primarily because the thicker C-shaped walls result in nearly equal capacity in both loading directions compared to the thinner C-shaped walls. Notably, this shear force distribution is consistent with the ratio identified in the initial design stage for the redistributed shear archetype, as extensively outlined in Appendix B.

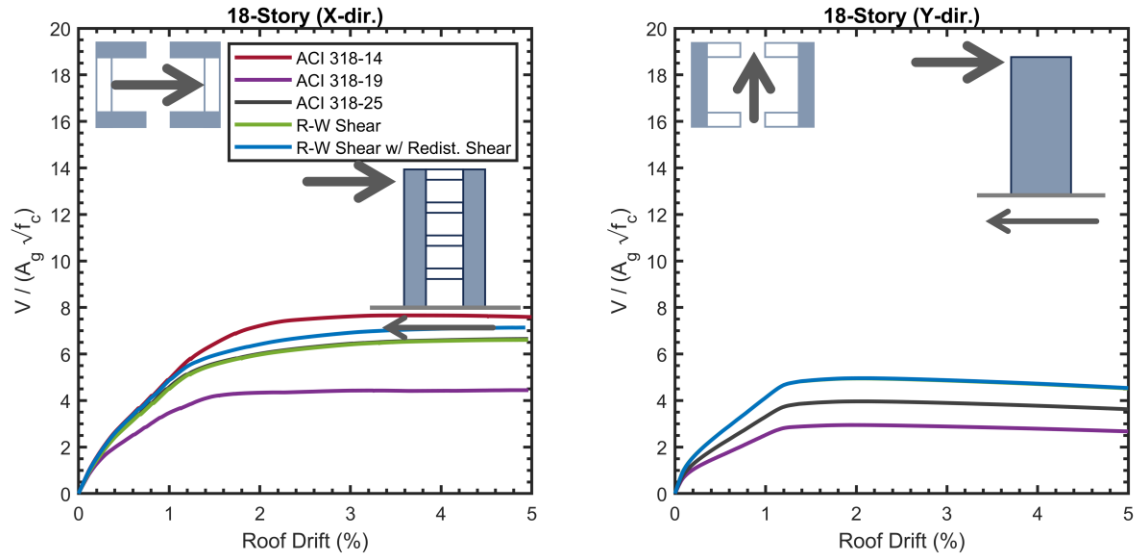


Figure 8.15: 18-story archetypes pushover analysis results (roof drift vs. total base shear).

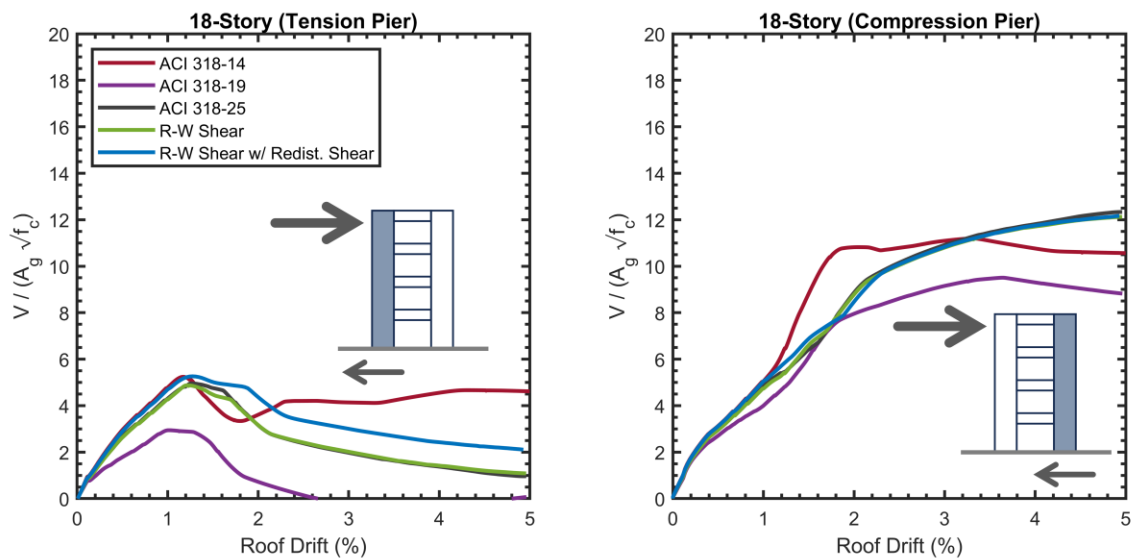


Figure 8.16: 18-story archetypes pushover analysis results (roof drift vs. each base shear in the coupled direction).

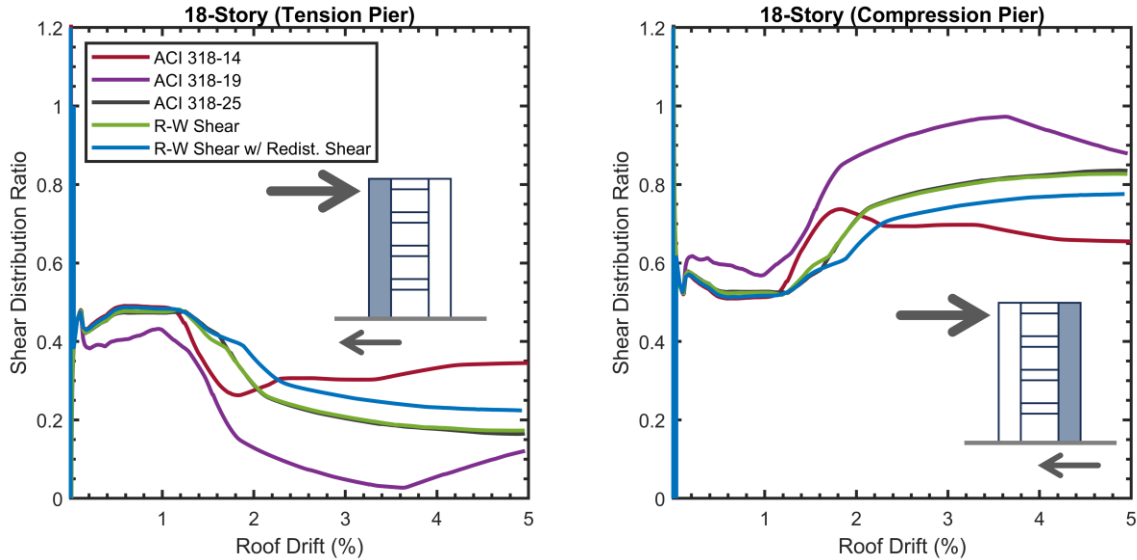


Figure 8.17: 18-story archetypes shear distribution ratio between the wall piers.

Figures 8.15 and 8.16 show that 18-story archetypes start to yield at a roof drift of approximately 1.7%. Up to this level of roof drift, the distribution of shear force between the wall piers varies from 40% to 50% in the tension pier and 50% to 60% in the compression pier. The highest shear force ratio in the compression pier, 60%, is observed in the model designed based on ACI 318-19, while the lowest ratio, 50%, is noted in the other models. This difference is mainly because the thicker C-shaped walls provide nearly equal capacity in both loading directions compared to thinner C-shaped walls. Importantly, this shear force distribution aligns with the ratio identified in the initial design phase for the redistributed shear archetype, as detailed in Appendix B.

8.3. Ground motion selection

To evaluate the seismic behavior of archetypes under dynamic seismic loading, for archetypes with the same number of stories, two suites of ground motions (13 GM in each suite) is selected to appropriately represent the spectral shape at the risk-targeted maximum considered earthquake (MCE_R) performance level at a site located in Los Angeles, California (latitude 34.155, longitude -118.466). This location (same considered for the design) has site spectral acceleration

values of $S_s = 1.961g$ and $S_1 = 0.699g$. The Uniform Hazard Response Spectrum for this site is shown in Figure 8.18.

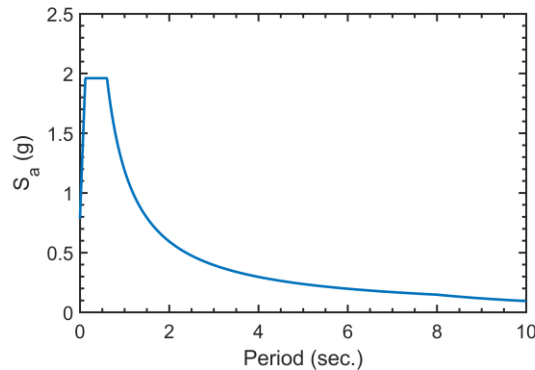


Figure 8.18: Site specific uniform Hazard Spectrum (UHS).

The spectral acceleration associated with the considered period of each archetype was extracted from the Uniform Hazard Response Spectrum (Figure 8.18) and then used to generate a Conditional Mean Spectrum (CMS) (Baker, 2011). The period used to match the spectrum is the average of 1st and 2nd modal periods obtained from the Eigen Analysis performed on the OpenSees archetype analytical models with the same number of stories with expected gravity load applied ($D+0.25L$). Table 8.2 represents the considered modal periods to condition the mean of each suite of ground motions. Figure 8.19 illustrates the 9-story archetypes selected suites of ground motions. Detailed information on the process, selected ground motions, and their associated scale factors for all archetypes are provided in appendix C.

Table 8.2: Period and spectral accelerations used to condition the suites of ground motions.

No. Stories	Mode 1		Mode 2	
	Period (sec.)	$S_a(g)$	Period (sec.)	$S_a(g)$
9	1.27	0.9357	0.34	1.9610
12	1.62	0.7335	0.42	1.9610
15	2.00	0.5942	0.58	1.9610
18	2.26	0.5258	0.69	1.7222

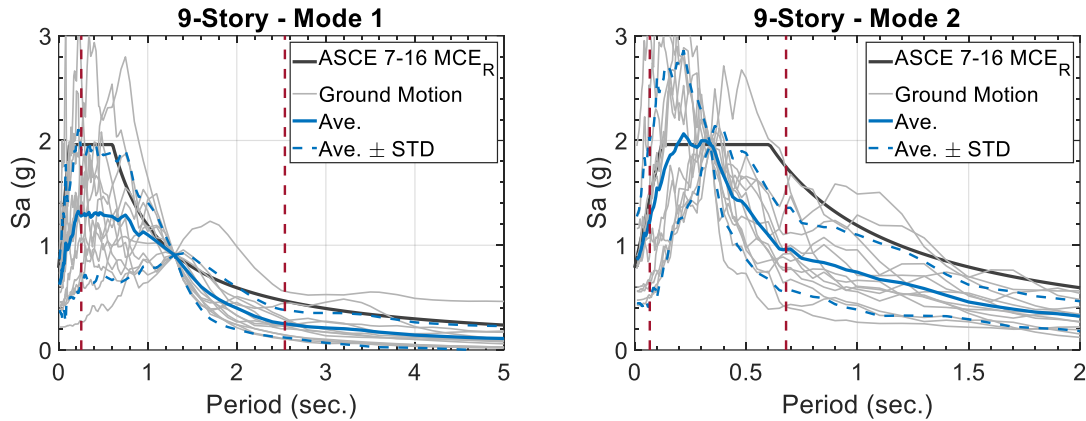


Figure 8.19: Response spectra of selected suites of ground motions conditioned to first and second modes of 9-story archetypes.

8.4. Analysis Procedure

A Krylov-Newton solution algorithm (implemented using the OpenSees command 'algorithm KrylovNewton') is employed to conduct the nonlinear analysis. Convergence is achieved if the norm of the displacement increment, defined by the OpenSees command 'test NormDisplncr', is less than the adopted error tolerance of 10^{-6} . In cases where a convergence error occurred, the structure was examined for shear limit. If shear demand exceeded the limit in the model, the analysis terminated. Otherwise, convergence is first pursued using the updated (current) tangent stiffness matrix corresponding to the beginning of each analysis step by increasing the number of iterations to 100 (command algorithm KrylovNewton -MaxDim 100, default value is 3). If convergence is still not achieved at a given time step, iterations are performed using the initial stiffness matrix of the model, by using the OpenSees command algorithm KrylovNewton-initial'. In cases where convergence errors persisted, the analysis was terminated, and a convergence failure reported. However, during the dynamic analysis in this study, none of the archetypes were flagged as having a convergence failure.

8.5. Nonlinear Dynamic Analysis Results

Following the pushover analyses, Response History Analyses (RHA) were conducted for each archetype. Figures 8.20 through 8.35 demonstrate the maximum shear demand-to-reduced shear strength ratio ($DCR = V_e/V_n$), where V_e represents the demand obtained from the nonlinear dynamic analysis and V_n is the capacity according to ACI 318 or R-W 2022, as specified for each case. These figures show profiles for each archetype under both suites of ground motions, conditioned to modes 1 and 2. According to ACI 318-19, the ϕ -factor for shear action in RC structural walls is equal to 0.75. For interpreting the shear behavior of various design of archetypes, it is presumed that a DCR less than 0.7 indicates an overly conservative design.

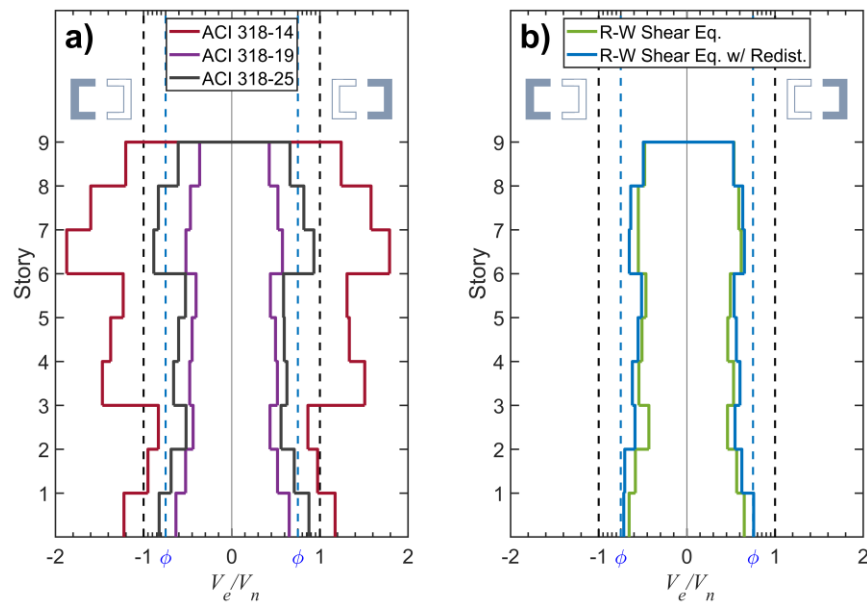


Figure 8.20: 9-story archetypes V_e/V_n ratio profile using suites of ground motions conditioned to mode 1; a) ACI 318 shear strength, b) R-W shear strength equation.

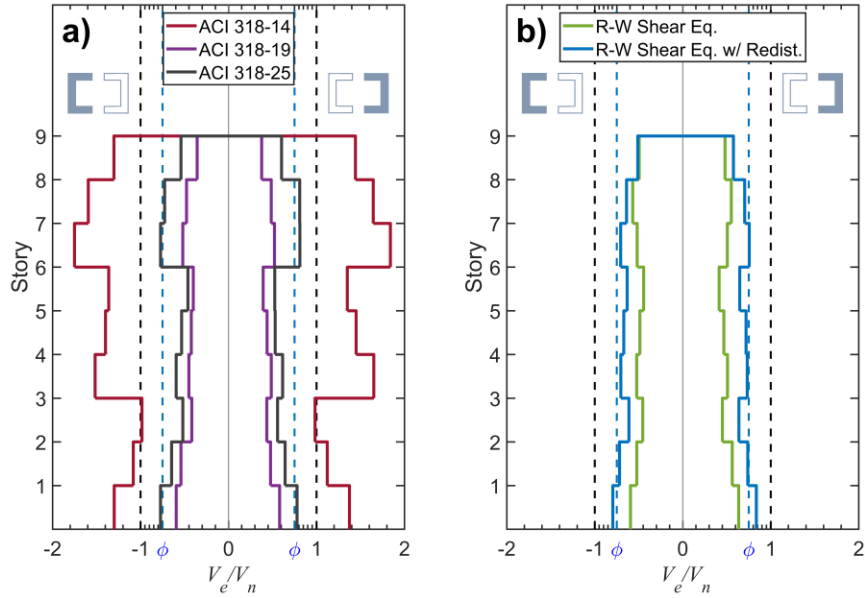


Figure 8.21: 9-story archetypes V_e/V_n ratio profile using suites of ground motions conditioned to mode 2; a) ACI 318 shear strength, b) R-W shear strength equation.

Figures 8.20.a and 8.21.a clearly show that the DCRs of the archetype designed based on ACI 318-14, obtained using the ACI shear strength equation is over 1.31. However, for the archetype designed based on ACI 318-19, this ratio is about 0.56. For the archetype designed based on ACI 318-25, the DCR is 0.75 for the ACI shear strength equation. It can be concluded that while the ACI 318-14 (no shear amplification) underdesigns the wall piers, ACI 318-19 (with shear amplification of up to 3) overdesigns them in a coupled wall system. However, as the ACI 318-25 decreases the shear amplification from its preceding code cycle, it provides the right amount of shear strength based on ACI 318 shear strength equation.

Additionally, comparison between the two 9-story archetypes designed based on the R-W shear strength equation, with and without redistribution of shear demand between the piers, show that distributing the shear can lead to a more efficient design, as indicated by the DCR ratio of 0.73. In contrast, neglecting the proper distribution of shear between the piers results in a thicker wall design in the coupled direction (19-inch versus 23-inch), with a DCR ratio of about 0.6. It can also be noted that although both ACI 318-25 and R-W 2022 with shear distribution archetype provides

a DCR of 0.75, the R-W 2022 with shear distribution archetype is the thinner one, but it compensates the loss of thickness with adjustments to the longitudinal rebars in the interior and exterior boundary elements. It is also noteworthy that the same trend is observed in the DCR obtained from averaging the shear DCR over the height of the structure as shown in Figures 22 and 23.

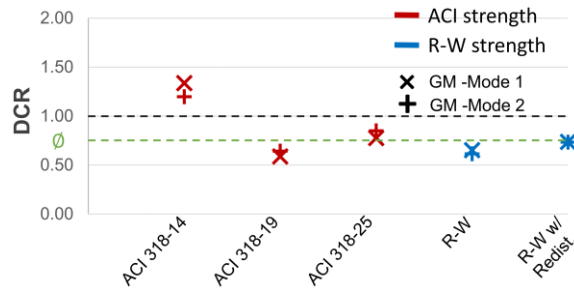


Figure 8.22: comparison between the V_e/V_n (base shear) ratio of 9-story archetypes.

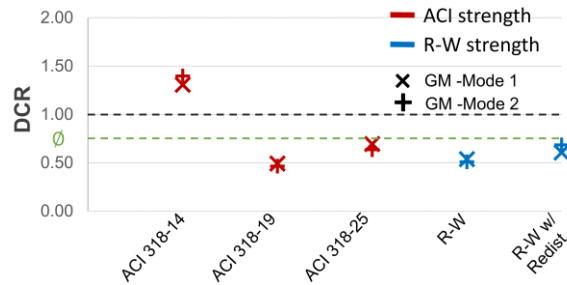


Figure 8.23: comparison between the V_e/V_n (average shear) ratio over the height of 9-story archetypes.

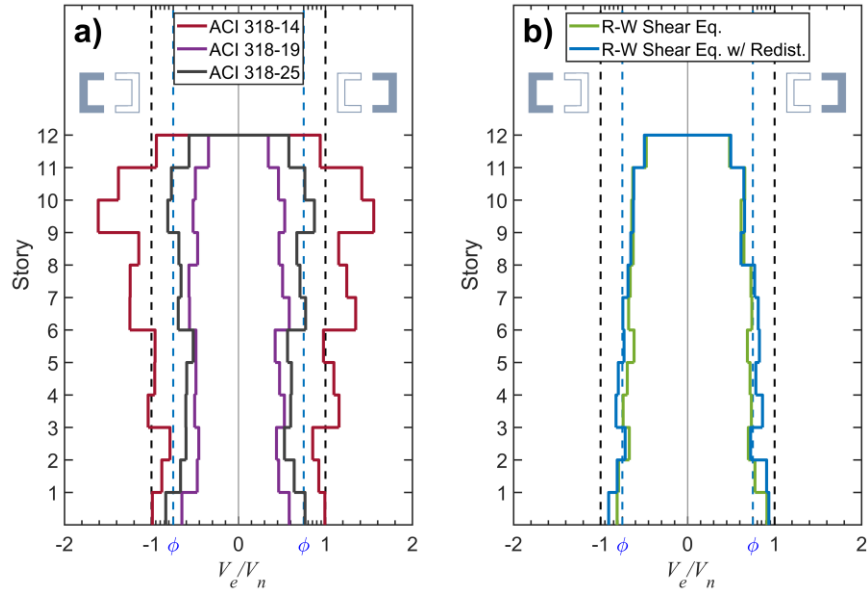


Figure 8.24: 12-story archetypes V_e/V_n ratio profile using suites of ground motions conditioned to mode 1; a) ACI 318 shear strength, b) R-W shear strength equation.

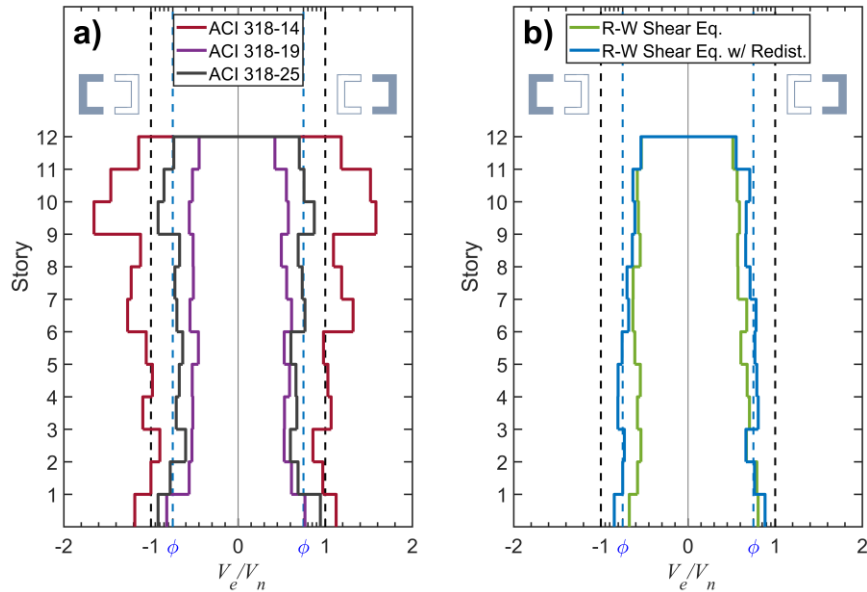


Figure 8.25: 12-story archetypes V_e/V_n ratio profile using suites of ground motions conditioned to mode 2; a) ACI 318 shear strength, b) R-W shear strength equation.

As demonstrated in Figures 8.24.a and 8.25a, the 12-story archetype designed per ACI 318-14 shows a DCR of 1.2. However, for the archetype designed according to ACI 318-19, the DCR is approximately 0.75. Regarding the archetype aligned with ACI 318-25, the DCR is 0.9 based on

ACI shear strength equation. Similar to observations from the 9-story archetype. ACI 318-25 appears to provide a more reasonable design compared to the underdesigned ACI 318-14 and oversized ACI 318-19.

Furthermore, analyzing two 12-story archetypes designed based on the R-W shear strength equation, with and without shear demand redistribution, shows that effective shear distribution can lead to a more economical structure. The archetype with shear distribution has a DCR of 0.79, while ignoring proper shear distribution, results in a higher DCR of about 0.83 and thicker wall piers (15-inch versus 18-inch walls).

Additionally, while both ACI 318-25 and R-W 2022 with shear distribution archetypes yield similar DCRs of 0.75, the latter is thinner (15-inch versus 18-inch walls). However, it compensates for reduced thickness with adjustments to the longitudinal rebars in the interior and exterior boundary elements. Specifically, the ACI 318-25 uses 15 #11 bars for the interior boundary and 60 #11 for the exterior, whereas the R-W with distribution uses 25 #11 and 50 #11 bars for the interior and exterior boundaries, respectively.

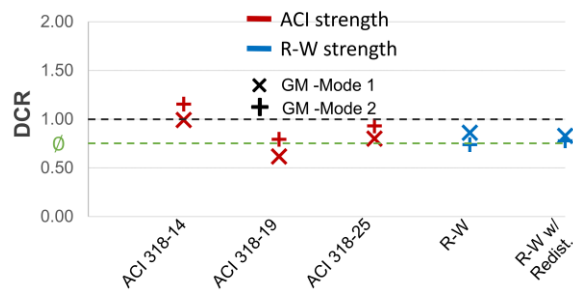


Figure 8.26: comparison between the V_e/V_n (base shear) ratio of 12-story archetypes.

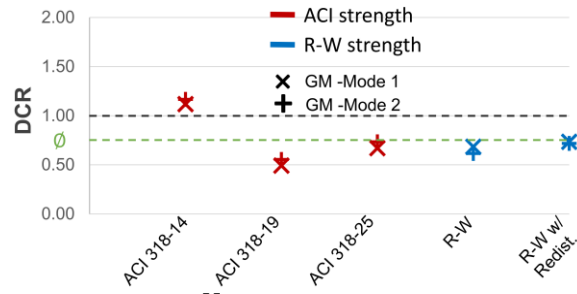


Figure 8.27: comparison between the V_e/V_n (average shear) ratio over the height of 12-story archetypes.

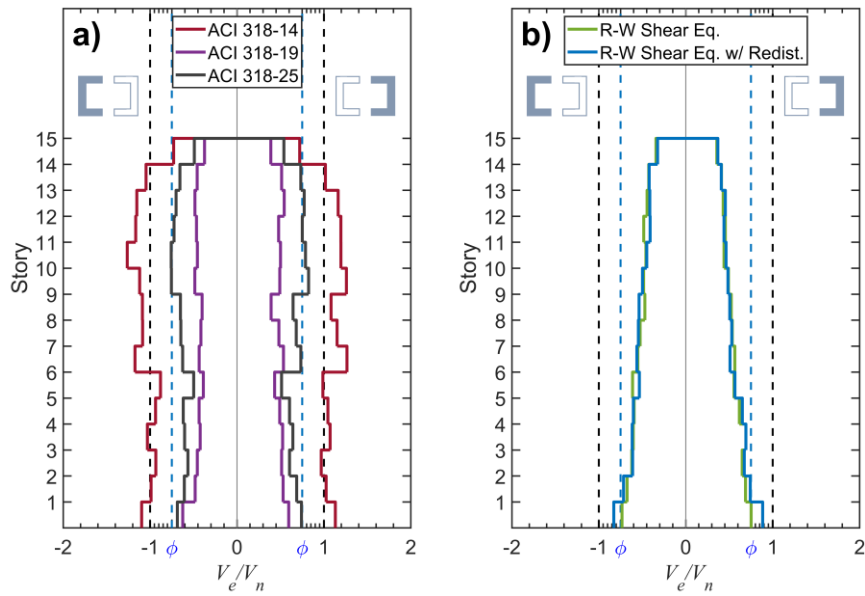


Figure 8.28: 15-story archetypes V_e/V_n ratio profile using suites of ground motions conditioned to mode 1; a) ACI 318 shear strength, b) R-W shear strength equation.

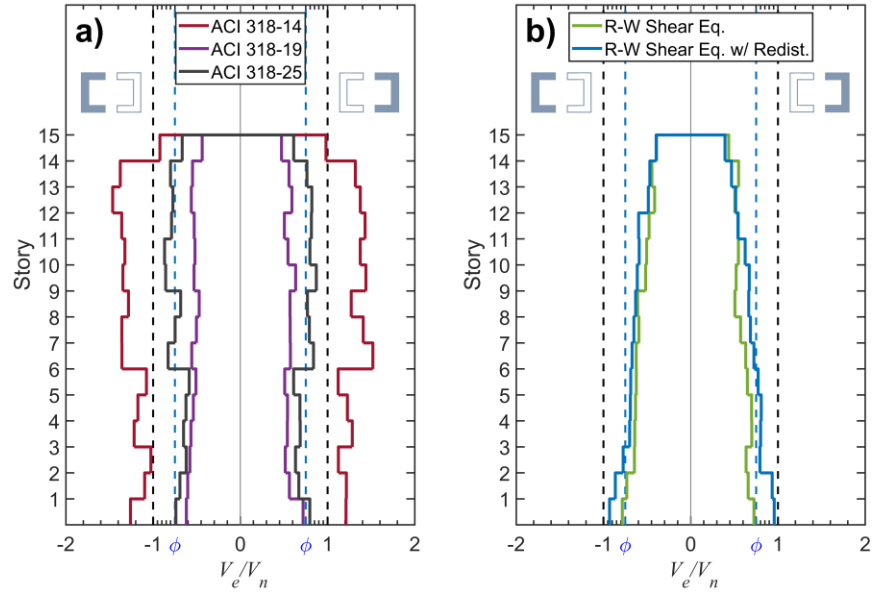


Figure 8.29: 15-story archetypes V_e/V_n ratio profile using suites of ground motions conditioned to mode 2; a) ACI 318 shear strength, b) R-W shear strength equation.

Figures 8.28 and 8.29 indicates that for the 15-story archetype based on ACI 318-14, the DCR calculated using the ACI shear equation under both ground motion suites is approximately 1.2. On the other hand, the archetype designed according to ACI 318-19 exhibits a DCR of about 0.65 depicting an overdesigned archetype. For the archetype adhering to ACI 318-25 provisions, the DCR is 0.75 from the ACI shear strength equation.

Moreover, the analysis of two 15-story archetypes, designed based on the R-W shear strength equation and considering both with and without the redistribution of shear demands, as the same as 9 and 12 story structures, indicate that effectively distribution of shear can result in a more efficient design (12-inch versus 15-inch wall) with similar shear demand to capacity ratio (DCR of 0.75 ($=\phi$) obtained from both archetypes).

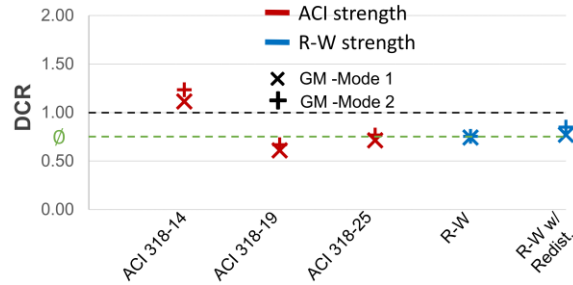


Figure 8.30: comparison between the V_e/V_n (base shear) ratio of 15-story archetypes.

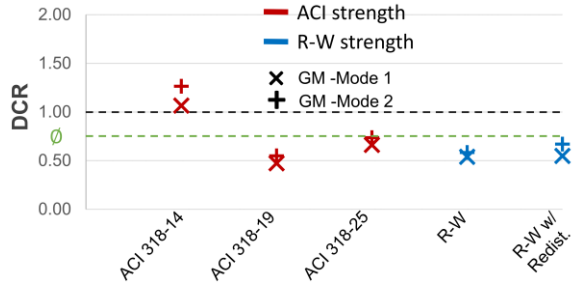


Figure 8.31: comparison between the V_e/V_n (average shear) ratio over the height of 15-story archetypes.

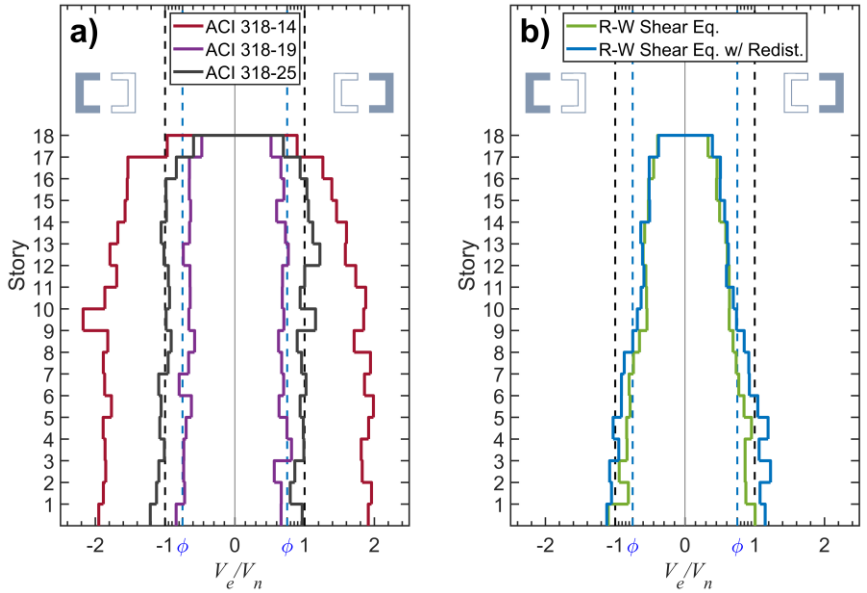


Figure 8.32: 18-story archetypes V_e/V_n ratio profile using suites of ground motions conditioned to mode 1; a) ACI 318 shear strength, b) R-W shear strength equation.

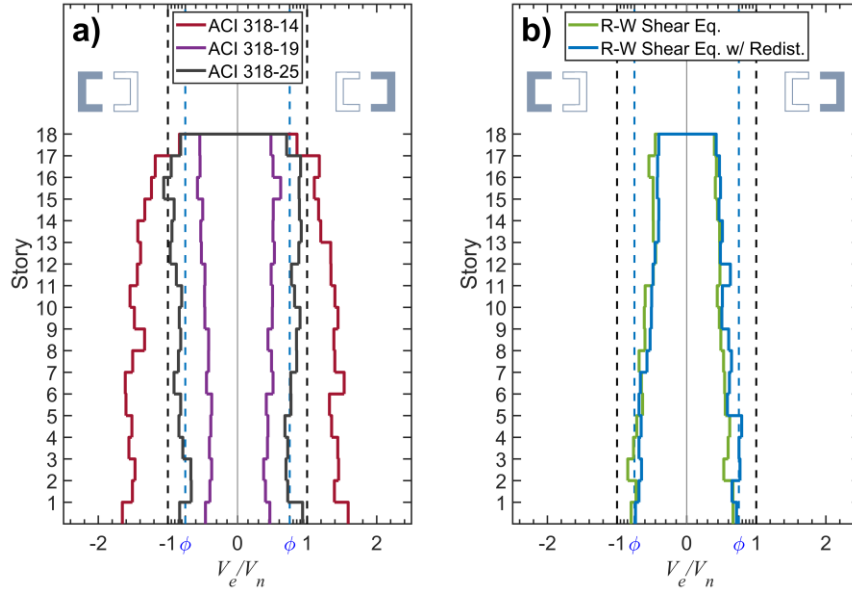


Figure 8.33: 18-story archetypes V_e/V_n ratio profile using suites of ground motions conditioned to mode 2; a) ACI 318 shear strength, b) R-W shear strength equation.

Figures 8.32 and 8.33 distinctly illustrate that for the 18-story archetype based on ACI 318-14, the Demand-to-Capacity Ratio (DCR) calculated using the R-W shear equation under both suites of ground motion is approximately 1.88 for the suite of ground motion conditioned to mode 1 and 1.6 for the suite of ground motion conditioned to mode 2. Meanwhile, the archetype designed according to ACI 318-19 exhibits DCRs of about 0.75 and 0.6 for the suites of ground motions conditioned to mode 1 and 2, respectively. For the archetype adhering to ACI 318-25 provisions, DCRs are 1.2 and 0.8 for the suites of ground motions conditioned to mode 1 and 2, respectively. Additionally, the analysis of two 18-story archetypes, designed based on the R-W shear strength equation and considering both with and without the redistribution of shear demand between the piers, indicates that effective shear distribution can lead to a more efficient design. This is particularly evident in the archetype utilizing redistribution of shear, which has thinner wall piers in the coupling direction and achieves a DCR ratio of 0.75 under the suite of ground motion conditioned to mode 2. For the suite of ground motions conditioned to mode 1, the DCRs are 1.05 versus 0.9.

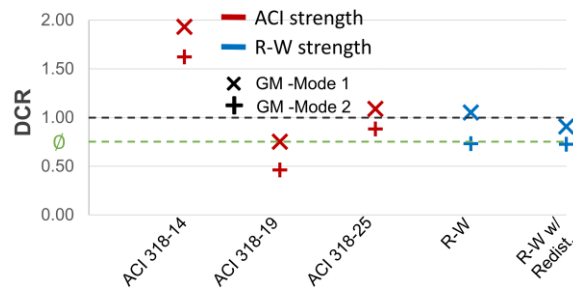


Figure 8.34: comparison between the V_e/V_n (base shear) ratio of 18-story archetypes.

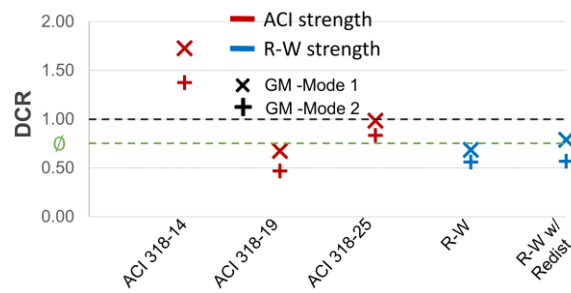


Figure 8.35: comparison between the V_e/V_n (average shear) ratio over the height of 18-story archetypes.

8.6. Summary of Results

Table 8.3 summarizes the base shear DCR results for all archetypes, with Figures 8.36 and 8.37 graphically presenting these findings. The ACI shear strength equation reveals that nearly all archetypes, except those designed per ACI 318-19, are prone to exceed shear limit, as their base shear DCR suggests. Notably, the DCRs derived from the R-W equation show a decreasing efficacy of the proposed design approach as structure height increases, as the shear demand between the wall piers becomes more even. This trend is supported by nonlinear static analysis results and shear distribution ratio plots. Moreover, archetypes adhering to ACI 318-19 provisions exhibit significantly lower DCRs, indicating potential overdesign in wall cross-sections. There is a similar pattern in the average shear DCR across the height of the archetypes, albeit with a lower demand-to-capacity ratio. Comprehensive nonlinear static and dynamic analyses reveal that the

shear distribution between wall piers varies, being more pronounced in structures influenced by shear behavior (9 and 12 stories) compared to those dominated by flexural behavior (15 and 18 stories). This variance in shear distribution impacts the efficiency of the design procedure. However, even in 18-story archetypes, effective shear distribution can reduce wall thickness and significantly lower the need for shear reinforcements in shear wall webs.

Table 8.3. Summary of shear DCR.

	Provision	DCR			Provision	DCR	
		Mode 1	Mode 2			Mode 1	Mode 2
9-Story	ACI 318-14	1.20	1.34	12-Story	ACI 318-14	1.11	1.24
	ACI 318-19	0.64	0.59		ACI 318-19	0.61	0.67
	ACI 318-25	0.85	0.78		ACI 318-25	0.71	0.77
	R-W ¹	0.65	0.61		R-W ¹	0.74	0.75
	R-W ²	0.74	0.73		R-W ²	0.77	0.85
15-Story	ACI 318-14	0.99	1.15	18-Story	ACI 318-14	1.93	1.62
	ACI 318-19	0.62	0.79		ACI 318-19	0.75	0.46
	ACI 318-25	0.80	0.93		ACI 318-25	1.09	0.88
	R-W ¹	0.86	0.74		R-W ¹	1.05	0.73
	R-W ²	0.83	0.78		R-W ²	0.83	0.73

¹ Archetype designed based on R-W 2022 shear strength equation without considering shear distribution.

² Archetype designed based on R-W 2022 shear strength equation considering shear distribution.

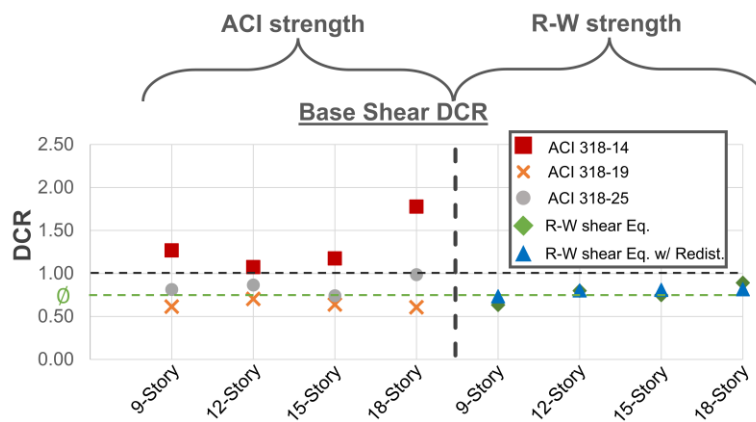


Figure 8.36: Comparison between the story height on the based shear V_e/V_n ratio.

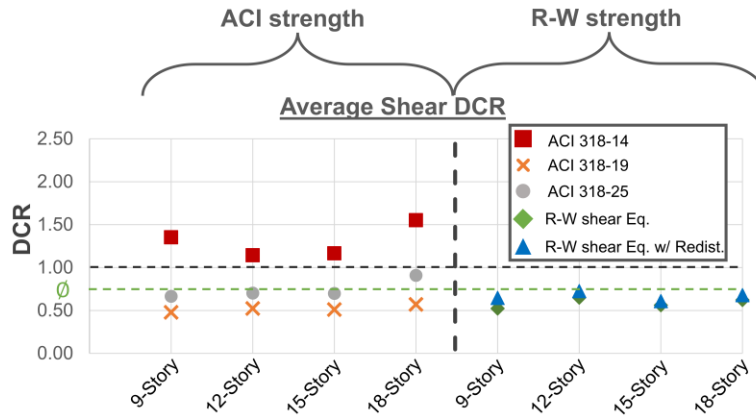


Figure 8.37: Comparison between the story height on the average of V_e/V_n ratio over the height of archetypes.

Furthermore, while many studies validate the realism of shear amplification in ACI 318-19 and 318-25, recent research indicates that ACI 318's shear strength for structural walls is overly conservative. The adoption of the latest R-W 2022 shear strength equation suggests that a more reasonable design approach could result in substantially thinner structural walls than currently practiced. The study shows that these optimized core walls can perform comparably to those designed according to ACI 318-19 standards.

9. SUMMARY AND CONCLUSION

9.1. Summary

The objective of this study was to develop, calibrate, and verify, using experimental results, a coupling beam modeling approach that integrates axial and lateral interactions under cyclic loading condition to reliably predict the elastic and inelastic responses. The proposed analytical model incorporates a fiber-based reinforced concrete cross-section and represents diagonal reinforcement as truss members to account for interaction along the beam span. This feature allows the model to capture changes in axial force, which affect lateral stiffness, strength and deformation capacity of the beam. Additionally, the model includes slip-extension behavior between the coupling beam and the supporting wall through zero-length sections at both ends of the element.

Detailed studies were conducted to calibrate the model by comparing analytically predicted responses with experimentally measured or derived responses from six isolated coupling beam test specimens. These test specimens represented a range of variables, including different quantities of diagonal and longitudinal reinforcement and different boundary conditions. Two test specimens were included to evaluate the effect of a slab on coupling beam behavior and one test was used to assess the ability of the model to simulate hybrid reinforcing configurations. The influence of axial restraint was assessed using two identical coupling beams, one with axial restraint provided using a post-tensioned bar and one without axial restraint. A 12-story coupled wall specimen was also used to validate the model in conjunction with wall elements.

Furthermore, the creation of large databases and new tools such as machine learning have led to the development of new empirical shear strength equations for RC structural walls. An important feature of some of the new models is the inclusion of axial load as a feature in the wall shear strength equation. Prior experimental studies have highlighted the large difference in the shear force demands between wall piers in coupled/core wall systems, with the compression pier

typically resisting as much as 90% of the total shear. The proposed numerical model is able to effectively capture the redistribution of the shear force (and moment) demands in a couple wall. Using the proposed model, various design approaches for coupled walls were evaluated to propose a new design approach that accounts for demand redistribution. The various approaches were evaluated using nonlinear models of archetype buildings with 9, 12, 15, and 18 stories subjected to MCE_R suites of ground motions. The results of the study indicated that structures designed considering the redistribution of shear forces between wall piers and new wall shear strength equations that account for axial load to demonstrate more reliable shear performance and more efficient material usage. Specific conclusions related to the overall study are summarized in the next section.

9.2. Conclusions

The following conclusions were established through analytical studies conducted using the proposed analytical model:

- The predicted coupling beam behavior is affected by the hysteretic behavior of the constitutive materials, particularly steel strain hardening, material strength degradation, and buckling of reinforcement.
- The proposed analytical model can predict, with significant precision, the observed shear strength of coupling beams from various test programs. However, determining the axial load behavior of the coupling beams is sensitive to various factors, such as slip-extension behavior between diagonal reinforcing bars and concrete, the behavior of adjacent wall piers.
- The proposed coupling beam analytical model was capable of accurately predicting both axial and lateral behavior of the beam. Additionally, the model was able to capture the effect of axial restraint on the beam, resulting in an increase in lateral (shear) strength and

a decrease in deformation capacity, with reasonable accuracy, typically with less than 5% discrepancy from the experimentally measured values.

- Analytical studies revealed that employing nine or more segments along the length of all specimens was sufficient to limit variability of model results due to mesh dependency. However, it should be noted that adopting a high number of segments may result in numerical localization of the stress and strain, leading to artificially large strain predictions. Use a material regularization might address this issue.
- The model is both computationally efficient (in terms of runtime) and stable (regarding convergence stability). The analysis duration for the investigated coupled wall specimen was approximately 12 minutes, with convergence achieved using the Krylov-Newton method and by leveraging the current tangent stiffness during the analysis.
- In combination with the MVLEM-3D wall model, the CBeam model predicts the overall load-displacement behavior of the coupled wall specimen subjected to unidirectional loading with a reasonable degree of accuracy (typically in the range of 0 to 15% for initial and unloading/reloading stiffness). The estimated lateral yield strength of the system was within 5% of the experimentally determined values for loading cycles applied in the direction of the coupled wall.
- Due to the limitations of the plane-sections-remain-plane assumption incorporated within the MVLEM-3D element, effective widths associated with wall flanges are over-estimated and the unloading/reloading lateral stiffness of the coupled wall system was overestimated by 10%.
- To obtain an efficient design for core wall systems, use of more sophisticated wall shear strength expressions that account for the influence of axial force on shear strength and redistribution of shear demands between the tension and compression wall piers is required. Results showed that considering these factors using the proposed design

approach resulted in Demand-to-Capacity Ratios (DCR) close to $\phi=0.75$ regardless of the number of stories.

- The shear amplification factor, such as introduced in ACI 318-19, was observed in the analytical results; however, considering the redistribution of wall shear forces and incorporation the new shear equation resulted in wall designs that thickness values similar to those for designs based on ACI 318-14, which did not include shear amplification, with similar or less shear reinforcements.

9.3. Future Studies and Possible Model Improvements

Based on the studies presented, the following topics are suggested for future research:

- This study demonstrated that analytical predictions using the proposed CBeam model successfully captured the behavior of diagonally reinforced coupling beams. However, the model could be extended to consider composite coupling beams with steel I-sections embedded in concrete.
- Evaluate coupled/core wall behavior under seismic loading emphasizing on vertical component of ground motions.
- Conduct a P-695 study to obtain coupled/core walls fragility functions and evaluate R (response modification factor) and C_d (deformation amplification factor) for these structural systems compare to the current ASCE 7-22 prescribed values ($R = 8$, $C_d = 8$).
- As the demands and capacity of wall piers in a coupled/core walls are changed, it is recommended to evaluate the required ϕ -factor for shear design of RC walls.

APPENDIX A - CBeam ELEMENT USER MANUAL

The proposed coupling beam model is developed and implemented in the nonlinear analysis platform OpenSees as a new element category called CBeam. The model is implemented in a two-dimensional domain with three DOFs per node. Table A.1 illustrates input parameters in OpenSees. Input parameters include: 1) an element tag which is unique for the element (eleTag), 2) two external nodes defined ends of the element (iNode, jNode), 3) predefined reinforced concrete section tag (ConcSecTag), 4) the array of length of n segments along the axis of the element (nLengthSegments), 5) diagonal steel material tag (steelTag), 6) number of diagonal bar layers in each bundle (m), 7) the array of covers from axis of the diagonal bar layers at the end face of coupling beam from outer concrete layer (c), 8) slip–extension section tag (seTag).

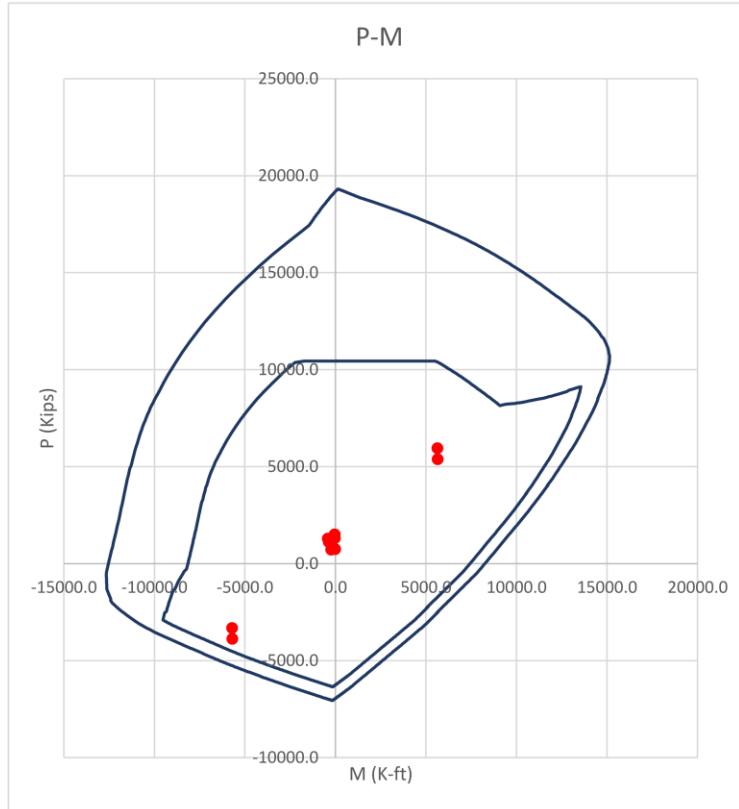
Table A.1. OpenSees user input for CBeam element.

User input format	element CBeam \$eleTag \$iNode \$jNode \$ConcSecTag -nLengthSegments {\$nLengthSegments} \$steelTag \$m -cover {\$c} \$seTag
Description of input parameters	eleTag Unique element tag
	iNode, jNode External node tags
	ConcSecTag Tag of pre-defined fiber-based reinforced concrete section
	nLengthSegments Array of n segment length along the axis of the beam
	steelTag Pre-defined uniaxial steel material tag
	m Number of diagonal bar layers in each bundle of steel
	cover Array of spacing between diagonal bar layers to the most outer layer of concrete
	seTag Pre-defined fiber-based slip–extension section tag

APPENDIX B – ARCHETYPES DESIGN (9-Stories)

B.1. 9-Story ACI 318-14

Coupled-Direction						
Wall Pier	Story		1			
<u>Comp. Pier</u>			<u>Tension Pier</u>			
M_u	5632 k-ft		M_u	5688 k-ft		
C_u	5944 kips		T_u	-3880 kips		
l_w	5 ft		l_w	5 ft		
l_f	16 ft		l_f	16 ft		
t_w	16 in		t_w	16 in		
t_f	12 in		t_f	12 in		
ϕ	0.65		ϕ	0.90		
f_y	60.0 ksi					
f_c	8.0 ksi					
<u>Interior Bnd</u>		in # Layer	Spacing	# Layer	BE L	
A_s	26.1 in ²	4	3	5.00	5.0	22
Use	15	#11	Provided A_s	23.4 in²		Check P-M to Verify
<u>Exterior Bnd</u>		in # Layer	Spacing	# Layer	BE L	
A_s	62.3 in ²	4	3	5.00	20.0	82
Use	60	#11	Provided A_s	93.6 in²		Check P-M to Verify
Shear						
<u>Comp. Pier</u>			<u>Tension Pier</u>			
h_w	117 ft		h_w	117 ft		
f_y	60.0 ksi		f_y	60.0 ksi		
V_u	643.9 kips		V_u	643.9 kips		
ω_v	1.0		ω_v	1.0		
n_{story}	9		n_{story}	9		
n_s	9.0		n_s	9.0		
Ω_v	1.0		Ω_v	1		
V_e	644 kips		V_e	644 kips		
ϕ	0.75		ϕ	0.75		
ϕV_c	128.8 kips		ϕV_c	128.8 kips		
ρ_t	0.0119		ρ_t	0.0119		
Need	2 curtain of #6		Need	2 curtain of #6		
@	4.6 in		@	4.6 in		
Use	2 curtain of #6		Use	2 curtain of #6		
@	4.5 in		@	4.5 in		
ϕV_n	644 kips	OK	ϕV_n	644 kips	OK	
<u>Vertical Web Bar</u>						
$\rho_{l,min}$	0.0025		$\rho_{l,min}$	0.0025		
Need min of	2 curtain of #5		Need min of	2 curtain of #5		
	@ 15.5 in			@ 15.5 in		
Use	2 curtain of #5		Use	2 curtain of #5		
@	12 in		@	12 in		



Check Minimum Reinforcement

Compression Pier

Outer Bound

SBE Required?	YES
C_{critic}	3.4 in
c	13.3 in
l_w	5 ft
t_w	16 in
l_{be}	7.3 in
f_y	60.0 ksi
f_c	8.0 ksi
ρ_{min}	0.00894
n Bar	60
bar Size	#11
$\rho_{provided}$	0.806 OK

Inner Bound

SBE Required?	NO
C_{critic}	3.4 in
c	0.0 in
l_w	5 ft
t_w	16 in
l_{be}	9.0 in
f_y	60.0 ksi
f_c	8.0 ksi
ρ_{min}	0.00894
n Bar	15
bar Size	#11
$\rho_{provided}$	0.163 OK

Tension Pier

Outer Bound

SBE Required?	YES
C_{critic}	3.4 in
c	13.3 in
l_w	5 ft
t_w	16 in
l_{be}	7.3 in
f_y	60.0 ksi
f_c	8.0 ksi
ρ_{min}	0.00894
n Bar	60
bar Size	#11
$\rho_{provided}$	0.806 OK

Inner Bound

SBE Required?	NO
C_{critic}	3.4 in
c	0.0 in
l_w	5 ft
t_w	16 in
l_{be}	9.0 in
f_y	60.0 ksi
f_c	8.0 ksi
ρ_{min}	0.00894
n Bar	15
bar Size	#11
$\rho_{provided}$	0.163 OK

Drift Check

C_d	5.0			
All. Drift	2.00%			
h_{wcs}	117 ft			
δ_x	5.51 in			
δ_x / h_{wcs}	0.39%			
$C_d \delta_x / h_{wcs}$	1.96%	<	$(\delta / h_{wcs})_{all.}$	2.00% Drift OK

SBE vs OBE

Compression Pier

h_w 117 ft

l_w 5 ft

t_w 16 in

c 13.3 in

C_d 5.0

disp. X 5.51 in

$1.5 \delta_u / h_{wCS}$ 0.0294

M_u 5632 k-ft

V_u 643.87 kips

C_{critic} 3.4 in < c 13.3 in **SBE Required**
OBE Required above 5 ft

Tension Pier

h_w 117 ft

l_w 5 ft

t_w 16 in

c 16.7 in

C_d 5.0

disp. X 5.51 in

$1.5 \delta_u / h_{wCS}$ 0.0294

M_u 5688 k-ft

V_u 643.87 kips

C_{critic} 3.4 in < c 16.7 in **SBE Required**
OBE Required above 5 ft

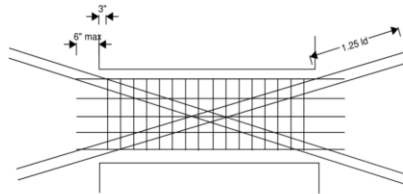
Boundary Element Shear Reinforcement

Clear Cover	2.5 in	Clear C	2.5 in	
Axial Rebar Size	#11	Axial Re	#11	
f_y	60.0 ksi	f_y	60.0 ksi	
f_c	8.0 ksi	f_c	8.0 ksi	
b	16.0 in	b	16.0 in	
d	82.0 in	d	22.0 in	
Shear bar size	#6	Shear b	#6	
A_g	1312 in ²	A_g	352 in ²	
n tie leg,b	4	n tie leg	3	
n tie leg,d	20	n tie leg	5	
$b_{c,b}$	8.1 in	$b_{c,b}$	8.1 in	
$b_{c,d}$	74.1 in	$b_{c,d}$	14.1 in	
A_{ch}	599.4 in ²	A_{ch}	114.0 in ²	
$h_{x,b}$	2.7 in OK	$h_{x,b}$	4.0 in OK	
$h_{x,d}$	3.9 in OK	$h_{x,d}$	3.5 in OK	
$A_{sh,b}$	1.76 in ²	$A_{sh,b}$	1.32 in ²	
$A_{sh,d}$	8.8 in ²	$A_{sh,d}$	2.2 in ²	
$h_{x,limit}$	14.0 in	$h_{x,limit}$	14.0 in	
$s_{0,b}$	7.8 in	$s_{0,b}$	7.3 in	
$s_{0,d}$	7.4 in	$s_{0,d}$	7.5 in	
$s_{1,b}$	4.6 in	$s_{1,b}$	4.0 in	
$s_{1,b}$	4.5 in	$s_{1,b}$	4.1 in	
$s_{2,b}$	18.1 in	$s_{2,b}$	13.6 in	
$s_{2,d}$	9.9 in	$s_{2,d}$	13.0 in	
s_3	5.3 in	s_3	5.3 in	
	Use #6 @ 4.5 in		Use #6 @ 4.0 in	

Coupling Beam**Story 2**

V_u 684.1 kips
 b 16 in
 d 48 in
 l 12 ft
 f'_c 8 ksi
 f_y 60 ksi
 ϕ 0.85
 bundle d 4 in
 diag. cover 3 in
 α 0.26 rad

$$V_u / (A_g \sqrt{f'_c}) = 10.0 < 10$$



$$A_{vd} \geq 26.3 \text{ in}^2$$

USE 17 #11 $A_{vd} 26.5 \text{ in}^2$
 nX 4
 nY 3

Clear Cover 1.5 in

b_{cx} 13 in

b_{cy} 45 in

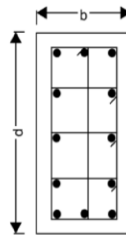
Conf. Bar #6 d 0.75 in

nX_{skin} 3

nY_{skin} 7

h_x 5.4 in < 8 in

h_y 6.6 in < 8 in

X-Direction

s1 8.5 in

s2 8.1 in

s3 6.0 in

s4 9.4 in

Use s 6.0 in

Y-Direction

s1 5.7 in

s2 5.5 in

s3 6.0 in

s4 9.4 in

Use s 5.5 in

Anchorage

K_{tr} 2.5

all ψ 1.3

l_d 36.9 in

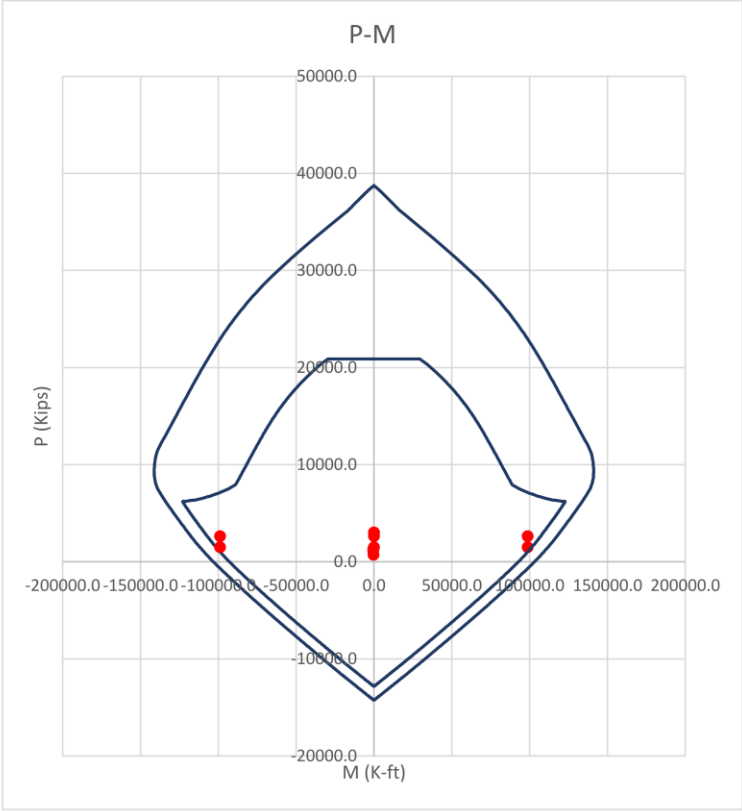
1.25 l_d 46.1 in

if using headed bars

l_{dt} 15.1 in

1.25 l_{dt} 18.9 in

Solid-Direction									
Wall Pier		Story		1					
<u>Comp. Pier</u>					<u>Tension Pier</u>				
M_u	98813	k-ft	M_u	98813	k-ft				
C_u	2625	kips	T_u	2625	kips				
l_w	16	ft	29 l_w	16	ft				
l_f	5	ft	l_f	5	ft				
t_w	12	in	t_w	12	in				
t_f	16	in	t_f	16	in				
ϕ	0.90		ϕ	0.90					
f_y	60.0	ksi							
f_c	8.0	ksi							
<u>Interior Bnd</u>		in	# Layer	Spacing	# Layer	BE L			
A_s	118.7	in ²	4	5	1.50	15.0	62		
Use	75	#11	Provided A_s		117 in²	Check P-M to Verify			
<u>Exterior Bnd</u>		in	# Layer	Spacing	# Layer	BE L			
A_s	118.7	in ²	4	5	1.50	15.0	62		
Use	75	#11	Provided A_s		117 in²	Check P-M to Verify			
Shear									
<u>Comp. Pier</u>					<u>Tension Pier</u>				
h_w	117	ft	h_w	117	ft				
f_y	60.0	ksi	f_y	60.0	ksi				
V_u	1272.0	kips	V_u	1272.0	kips				
ω_v	1.0		ω_v	1.0					
n_{story}	9		n_{story}	9					
n_s	9.0		n_s	9.0					
Ω_v	1.0		Ω_v	1					
V_e	1272	kips	V_e	1272	kips				
ϕ	0.75		ϕ	0.75					
ϕV_c	309.1	kips	ϕV_c	309.1	kips				
ρ_t	0.0093		ρ_t	0.0093					
Need	2	curtain of #6	Need	2	curtain of #6				
@	7.9	in	@	7.9	in				
Use	2	curtain of #6	Use	2	curtain of #6				
@	7.5	in	@	7.5	in				
ϕV_n	1323	kips	OK	ϕV_n	1323	kips	OK		
<u>Vertical Web Bar</u>									
$\rho_{l,min}$	0.0025		$\rho_{l,min}$	0.0025					
Need min of	2	curtain of #5	Need min of	2	curtain of #5				
@	20.7	in	@	20.7	in				
Use	2	curtain of #5	Use	2	curtain of #5				
@	12	in	@	12	in				



SBE vs OBE

Compression Pier

h_w 117 ft

l_w 16 ft

t_w 12 in

c 31.6 in

C_d 5.0

disp. X 5.51 in

$1.5 \delta_u / h_{wCS}$ 0.0294

M_u 98813 k-ft

V_u 1272 kips

C_{critic} 10.9 in < c 31.6 in **SBE Required**
OBE Required above 25.9 ft

Tension Pier

h_w 117 ft

l_w 16 ft

t_w 12 in

c 31.6 in

C_d 5.0

disp. X 5.51 in

$1.5 \delta_u / h_{wCS}$ 0.0294

M_u 98813 k-ft

V_u 1272 kips

C_{critic} 10.9 in < c 31.6 in **SBE Required**
OBE Required above 25.9 ft

Check Minimum Reinforcement

Compression Pier

Outer Bound

SBE Required?	YES
C_{critic}	10.9 in
c	31.6 in
l_w	16 ft
t_w	12 in
l_{be}	12.4 in
f_y	60.0 ksi
f_c	8.0 ksi
ρ_{min}	0.00894
n Bar	75
bar Size	#11
$\rho_{provided}$	0.784 OK

Inner Bound

SBE Required?	NO
C_{critic}	10.9 in
c	0.0 in
l_w	16 ft
t_w	12 in
l_{be}	28.8 in
f_y	60.0 ksi
f_c	8.0 ksi
ρ_{min}	0.00894
n Bar	75
bar Size	#11
$\rho_{provided}$	0.339 OK

Tension Pier

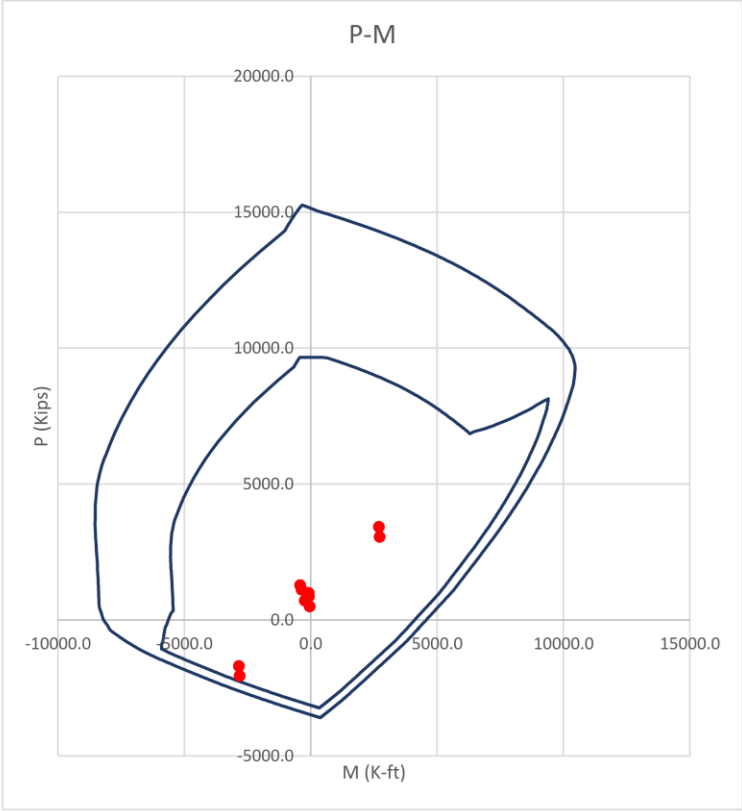
Outer Bound

SBE Required?	YES
C_{critic}	10.9 in
c	31.6 in
l_w	16 ft
t_w	12 in
l_{be}	12.4 in
f_y	60.0 ksi
f_c	8.0 ksi
ρ_{min}	0.00894
n Bar	75
bar Size	#11
$\rho_{provided}$	0.784 OK

Inner Bound

SBE Required?	NO
C_{critic}	10.9 in
c	0.0 in
l_w	16 ft
t_w	12 in
l_{be}	28.8 in
f_y	60.0 ksi
f_c	8.0 ksi
ρ_{min}	0.00894
n Bar	75
bar Size	#11
$\rho_{provided}$	0.339 OK

Coupled-Direction									
Wall Pier		Story		4					
<u>Comp. Pier</u>					<u>Tension Pier</u>				
M_u	2695	k-ft	M_u	2812	k-ft				
C_u	3426	kips	T_u	-2057	kips				
l_w	5	ft	l_w	5	ft				
l_f	16	ft	l_f	16	ft				
t_w	13	in	t_w	13	in				
t_f	12	in	t_f	12	in				
ϕ	0.65		ϕ	0.90					
f_y	60.0	ksi	b	0.000001					
f_c	8.0	ksi	f'_{cc}	11	ksi				
<u>Interior Bnd</u>			in	# Layer	Spacing	# Layer	BE L		
A_s	12.5	in ²	4	3	3.50	5.0	22		
Use	15	#8	Provided A_s		11.85	in ²	Check P-M to Verify		
<u>Exterior Bnd</u>			in	# Layer	Spacing	# Layer	BE L		
A_s	32.1	in ²	4	3	3.50	20.0	82		
Use	60	#8	Provided A_s		47.4	in ²	Check P-M to Verify		
Shear	9	8	L-in Fln'g		34	L-in Web	34.00		
<u>Comp. Pier</u>					<u>Tension Pier</u>				
h_w	117	ft	h_w	117	ft				
f_y	60.0	ksi	f_y	60.0	ksi				
V_u	506.3	kips	V_u	506.3	kips				
ω_v	1.0		ω_v	1.0					
n_{story}	9		n_{story}	9					
n_s	9.0		n_s	9.0					
Ω_v	1.0		Ω_v	1					
V_e	506	kips	V_e	506	kips				
ϕ	0.75		ϕ	0.75					
ϕV_c	104.6	kips	ϕV_c	104.6	kips				
ρ_t	0.0114		ρ_t	0.0114					
Need	2	curtain of #6	Need	2	curtain of #6				
@	5.9	in	@	5.9	in				
Use	2	curtain of #6	Use	2	curtain of #6				
@	5.5	in	@	5.5	in				
ϕV_n	523	kips	OK	ϕV_n	523	kips	OK		
<u>Vertical Web Bar</u>									
$\rho_{l,min}$	0.0025		$\rho_{l,min}$	0.0025					
Need min of	2	curtain of #5	Need min of	2	curtain of #5				
@	19.1	in	@	19.1	in				
Use	2	curtain of #5	Use	2	curtain of #5				
@	12	in	@	12	in				



Check Minimum Reinforcement

Compression Pier

Outer Bound

SBE Required?	YES
C_{critic}	3.4 in
c	9.4 in
l_w	5 ft
t_w	13 in
l_{be}	3.4 in
f_y	60.0 ksi
f_c	8.0 ksi
ρ_{min}	0.00894
n Bar	60
bar Size	#8
$\rho_{provided}$	1.082 OK

Inner Bound

SBE Required?	NO
C_{critic}	3.4 in
c	0.0 in
l_w	5 ft
t_w	13 in
l_{be}	9.0 in
f_y	60.0 ksi
f_c	8.0 ksi
ρ_{min}	0.00894
n Bar	15
bar Size	#8
$\rho_{provided}$	0.101 OK

Tension Pier

Outer Bound

SBE Required?	YES
C_{critic}	3.4 in
c	9.4 in
l_w	5 ft
t_w	13
l_{be}	3.4 in
f_y	60.0 ksi
f_c	8.0 ksi
ρ_{min}	0.00894
n Bar	60
bar Size	#8
$\rho_{provided}$	1.082 OK

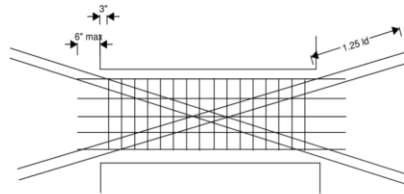
Inner Bound

SBE Required?	NO
C_{critic}	3.4 in
c	0.0 in
l_w	5 ft
t_w	13 in
l_{be}	9.0 in
f_y	60.0 ksi
f_c	8.0 ksi
ρ_{min}	0.00894
n Bar	15
bar Size	#8
$\rho_{provided}$	0.101 OK

Coupling Beam**Story 4**

V_u 565.6 kips
 b 13 in
 d 48 in
 l 12 ft
 f'_c 8 ksi
 f_y 60 ksi
 ϕ 0.85
 bundle d 4 in
 diag. cover 3 in
 α 0.26 rad

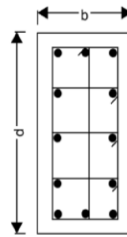
$$V_u / (A_g \sqrt{f'_c}) = 10.1 > 10$$



$$A_{vd} \geq 21.7 \text{ in}^2$$

USE 14 #11 $A_{vd} = 21.8 \text{ in}^2$
 $nX = 4$
 $nY = 3$

Clear Cover 1.5 in
 $b_{cx} = 10$ in
 $b_{cy} = 45$ in
 Conf. Bar #6 $d = 0.75$ in
 $nX_{skin} = 3$
 $nY_{skin} = 7$
 $h_x = 3.9$ in < 8 in
 $h_y = 6.6$ in < 8 in

X-Direction

$s1 = 11.0$ in
 $s2 = 8.5$ in
 $s3 = 6.0$ in
 $s4 = 9.4$ in
Use $s = 6.0$ in

Y-Direction

$s1 = 5.7$ in
 $s2 = 4.4$ in
 $s3 = 6.0$ in
 $s4 = 9.4$ in
Use $s = 4.4$ in

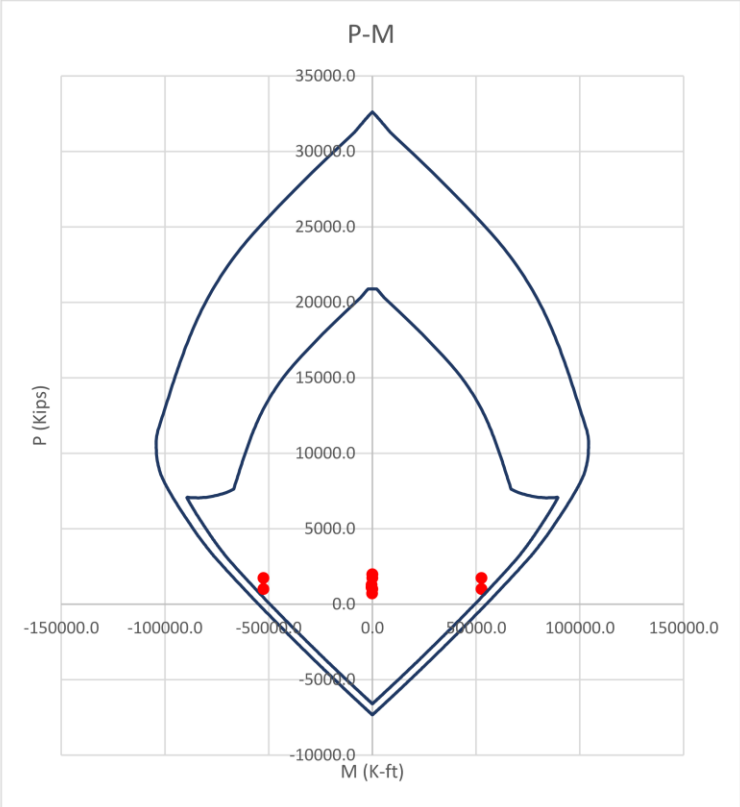
Anchorage

$K_{tr} = 2.5$
 all $\psi = 1.3$
 $l_d = 36.9$ in
 $1.25 l_d = 46.1$ in

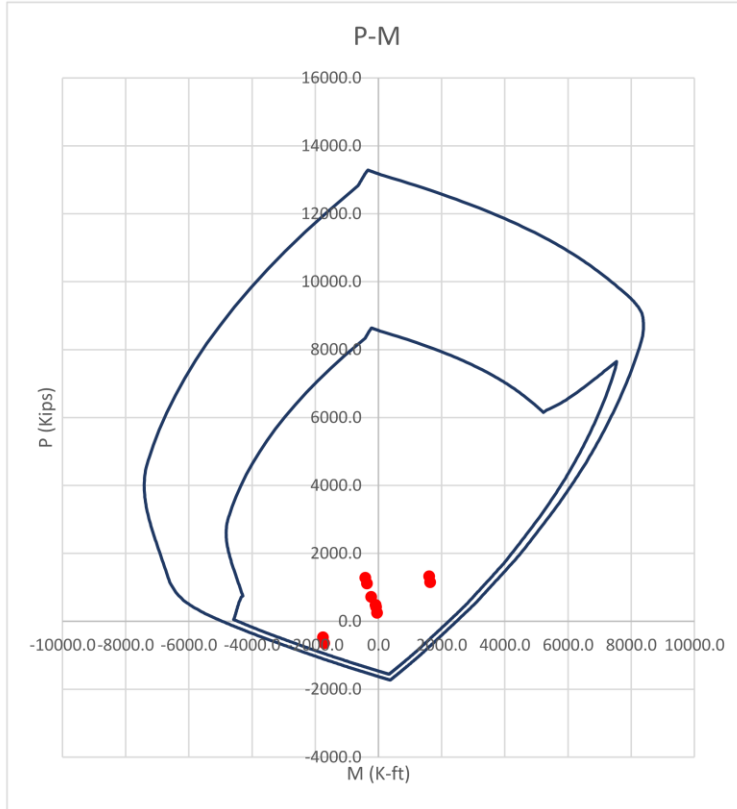
if using headed bars

$l_{dt} = 15.1$ in
 $1.25 l_{dt} = 18.9$ in

Solid-Direction									
Wall Pier		Story		4					
<u>Comp. Pier</u>					<u>Tension Pier</u>				
M_u	52577	k-ft	M_u	52577	k-ft				
C_u	1735	kips	T_u	1735	kips				
l_w	16	ft	29 l_w	16	ft				
l_f	5	ft	l_f	5	ft				
t_w	12	in	t_w	12	in				
t_f	16	in	t_f	16	in				
ϕ	0.90		ϕ	0.90					
f_y	60.0	ksi							
f_c	8.0	ksi							
<u>Interior Bnd</u>			in	# Layer	Spacing	# Layer	BE L		
A_s	60.0	in ²		4	5	1.50	15.0	62	
Use	75	#8	Provided A_s	59.25	in²	Check P-M to Verify			
<u>Exterior Bnd</u>			in	# Layer	Spacing	# Layer	BE L		
A_s	60.0	in ²		4	5	1.50	15.0	62	
Use	75	#8	Provided A_s	59.25	in²	Check P-M to Verify			
Shear									
<u>Comp. Pier</u>					<u>Tension Pier</u>				
h_w	117	ft	h_w	117	ft				
f_y	60.0	ksi	f_y	60.0	ksi				
V_u	923.4	kips	V_u	923.4	kips				
ω_v	1.0		ω_v	1.0					
n_{story}	9		n_{story}	9					
n_s	9.0		n_s	9.0					
Ω_v	1.0		Ω_v	1					
V_e	923	kips	V_e	923	kips				
ϕ	0.75		ϕ	0.75					
ϕV_c	309.1	kips	ϕV_c	309.1	kips				
ρ_t	0.0059		ρ_t	0.0059					
Need	2	curtain of #6	Need	2	curtain of #6				
@	12.4	in	@	12.4	in				
Use	2	curtain of #6	Use	2	curtain of #6				
@	12	in	@	12	in				
ϕV_n	943	kips	OK	ϕV_n	943	kips	OK		
<u>Vertical Web Bar</u>									
$\rho_{l,min}$	0.0025		$\rho_{l,min}$	0.0025					
Need min of	2	curtain of #5	Need min of	2	curtain of #5				
@	20.7	in	@	20.7	in				
Use	2	curtain of #5	Use	2	curtain of #5				
@	12	in	@	12	in				



Coupled-Direction										
Wall Pier		Story		7						
<u>Comp. Pier</u>					<u>Tension Pier</u>					
M_u	1600	k-ft	M_u	1722	k-ft					
C_u	1320	kips	T_u	-647	kips					
l_w	5	ft	l_w	5	ft					
l_f	16	ft	l_f	16	ft					
t_w	12	in	t_w	12	in					
t_f	12	in	t_f	12	in					
ϕ	0.90		ϕ	0.90						
f_y	60.0	ksi								
f_c	8.0	ksi								
<u>Interior Bnd</u>		in	# Layer	Spacing	# Layer	BE L				
A_s	7.4	in ²	4	3	3.00	3.0	14			
Use	9	#7	Provided A_s	5.4	in²	Check P-M to Verify				
<u>Exterior Bnd</u>		in	# Layer	Spacing	# Layer	BE L				
A_s	14.0	in ²	4	3	3.00	12.0	50			
Use	36	#7	Provided A_s	21.6	in²	Check P-M to Verify				
Shear		9	8	L-in Fl'n'g	30	L-in Web	34.00			
<u>Comp. Pier</u>					<u>Tension Pier</u>					
h_w	117	ft	h_w	117	ft					
f_y	60.0	ksi	f_y	60.0	ksi					
V_u	359.5	kips	V_u	359.5	kips					
ω_v	1.0		ω_v	1.0						
n_{story}	9		n_{story}	9						
n_s	9.0		n_s	9.0						
Ω_v	1.0		Ω_v	1						
V_e	360	kips	V_e	360	kips					
ϕ	0.75		ϕ	0.75						
ϕV_c	96.6	kips	ϕV_c	96.6	kips					
ρ_t	0.0081		ρ_t	0.0081						
Need	2	curtain of #6	Need	2	curtain of #6					
@	9.0	in	@	9.0	in					
Use	2	curtain of #6	Use	2	curtain of #6					
@	9	in	@	9	in					
ϕV_n	361	kips	OK	ϕV_n	361	kips	OK			
<u>Vertical Web Bar</u>										
$\rho_{l,min}$	0.0025		$\rho_{l,min}$	0.0025						
Need min of	2	curtain of #5	Need min of	2	curtain of #5					
@	20.7	in	@	20.7	in					
Use	2	curtain of #5	Use	2	curtain of #5					
@	12	in	@	12	in					



Check Minimum Reinforcement

Compression Pier

Outer Bound

SBE Required?	YES
C_{critic}	3.4 in
c	5.4 in
l_w	5 ft
t_w	12 in
l_{be}	1.7 in
f_y	60.0 ksi
f_c	8.0 ksi
ρ_{min}	0.00894
n Bar	36
bar Size	#7
$\rho_{provided}$	1.060 OK

Inner Bound

SBE Required?	NO
C_{critic}	3.4 in
c	0.0 in
l_w	5 ft
t_w	12 in
l_{be}	9.0 in
f_y	60.0 ksi
f_c	8.0 ksi
ρ_{min}	0.00894
n Bar	9
bar Size	#7
$\rho_{provided}$	0.050 OK

Tension Pier

Outer Bound

SBE Required?	YES
C_{critic}	3.4 in
c	5.4 in
l_w	5 ft
t_w	12 in
l_{be}	1.7 in
f_y	60.0 ksi
f_c	8.0 ksi
ρ_{min}	0.00894
n Bar	36
bar Size	#7
$\rho_{provided}$	1.060 OK

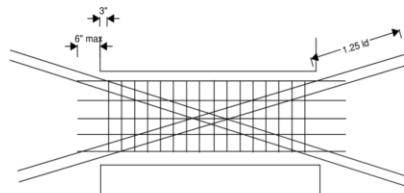
Inner Bound

SBE Required?	NO
C_{critic}	3.4 in
c	0.0 in
l_w	5 ft
t_w	12 in
l_{be}	9.0 in
f_y	60.0 ksi
f_c	8.0 ksi
ρ_{min}	0.00894
n Bar	9
bar Size	#7
$\rho_{provided}$	0.050 OK

Coupling Beam**Story****7**

V_u 368.5 kips
 b 12 in
 d 48 in
 l 12 ft
 f'_c 8 ksi
 f_y 60 ksi
 ϕ 0.85
 bundle d 4 in
 diag. cover 3 in
 α 0.26 rad

$V_u / (A_g \sqrt{f'_c})$ 7.2 < 10



$A_{vd} \geq$ 14.2 in²

USE 9 #11 A_{vd} 14 in²
 nX 4
 nY 3

Clear Cover 1.5 in

b_{cx} 9 in

b_{cy} 45 in

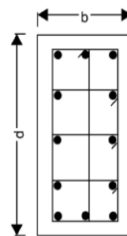
Conf. Bar #6 d 0.75 in

nX_{skin} 3

nY_{skin} 7

h_x 3.4 in < 8 in

h_y 6.6 in < 8 in

X-Direction

s1 12.2 in

s2 8.7 in

s3 6.0 in

s4 9.4 in

Use s 6.0 in

Y-Direction

s1 5.7 in

s2 4.1 in

s3 6.0 in

s4 9.4 in

Use s 4.1 in

Anchorage

K_{tr} 2.5

all ψ 1.3

l_d 36.9 in

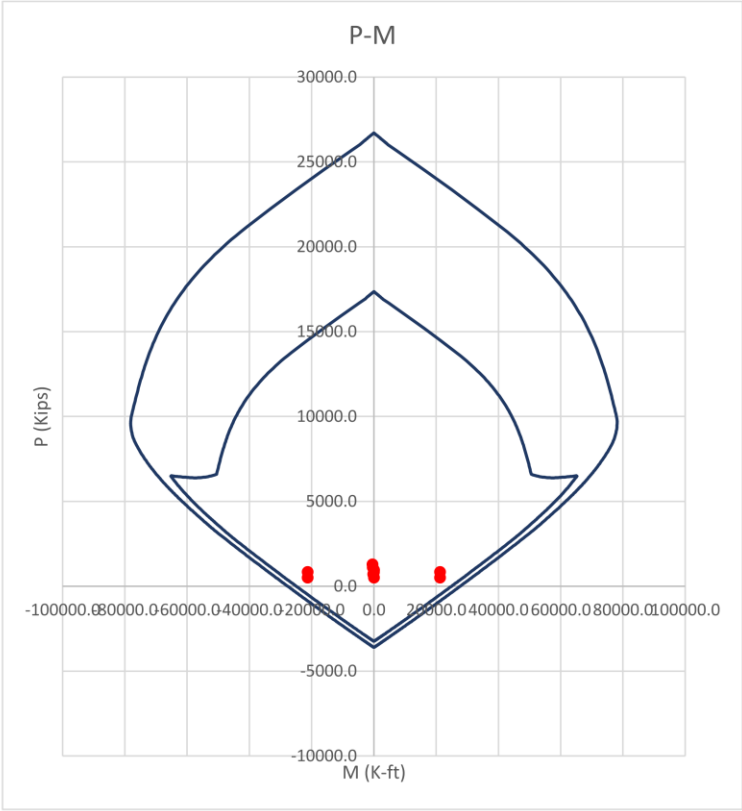
1.25 l_d 46.1 in

if using headed bars

l_{dt} 15.1 in

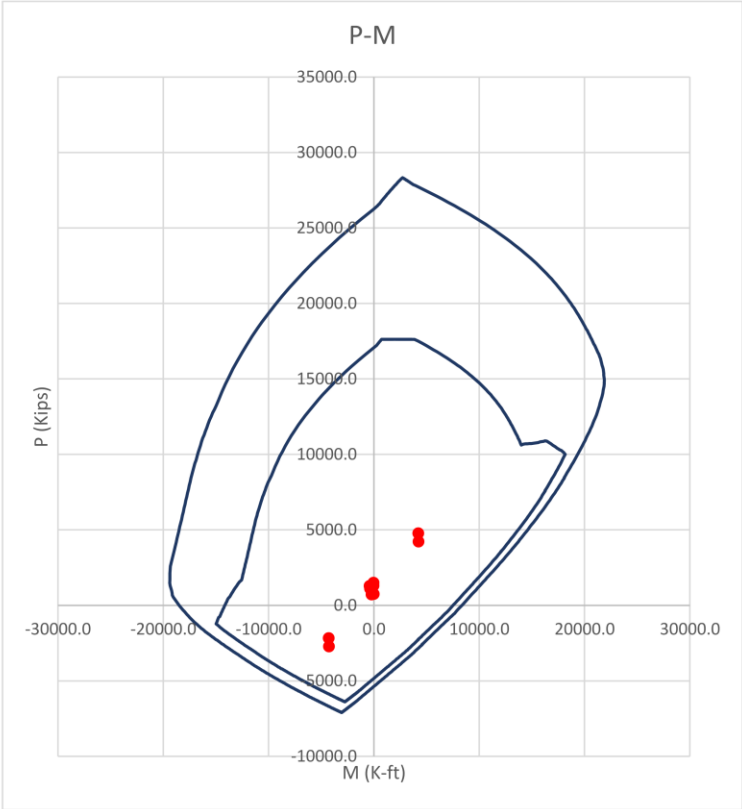
1.25 l_{dt} 18.9 in

Solid-Direction									
Wall Pier		Story		7					
<u>Comp. Pier</u>					<u>Tension Pier</u>				
M_u	21271	k-ft	M_u	21271	k-ft				
C_u	845	kips	T_u	845	kips				
l_w	16	ft	29 l_w	16	ft				
l_f	5	ft	l_f	5	ft				
t_w	12	in	t_w	12	in				
t_f	12	in	t_f	12	in				
ϕ	0.90		ϕ	0.90					
f_y	60.0	ksi							
f_c	8.0	ksi							
<u>Interior Bnd</u>		in	# Layer	Spacing	# Layer	BE L			
A_s	22.9	in ²	4	5	1.50	9.0	38		
Use	45	#7	Provided A_s		27 in²	Check P-M to Verify			
<u>Exterior Bnd</u>		in	# Layer	Spacing	# Layer	BE L			
A_s	22.9	in ²	4	5	1.50	9.0	38		
Use	45	#7	Provided A_s		27 in²	Check P-M to Verify			
Shear									
<u>Comp. Pier</u>					<u>Tension Pier</u>				
h_w	117	ft	h_w	117	ft				
f_y	60.0	ksi	f_y	60.0	ksi				
V_u	651.2	kips	V_u	651.2	kips				
ω_v	1.0		ω_v	1.0					
n_{story}	9		n_{story}	9					
n_s	9.0		n_s	9.0					
Ω_v	1.0		Ω_v	1					
V_e	651	kips	V_e	651	kips				
ϕ	0.75		ϕ	0.75					
ϕV_c	309.1	kips	ϕV_c	309.1	kips				
ρ_t	0.0033		ρ_t	0.0033					
Need	2	curtain of #5	Need	2	curtain of #5				
@	15.7	in	@	15.7	in				
Use	2	curtain of #5	Use	2	curtain of #5				
@	12	in	@	12	in				
ϕV_n	756	kips	OK	ϕV_n	756	kips	OK		
<u>Vertical Web Bar</u>									
$\rho_{l,min}$	0.0025		$\rho_{l,min}$	0.0025					
Need min of	2	curtain of #5	Need min of	2	curtain of #5				
@	20.7	in	@	20.7	in				
Use	2	curtain of #5	Use	2	curtain of #5				
@	12	in	@	12	in				



B.2. 9-Story ACI 318-19

Coupled-Direction						
Wall Pier		Story	1			Ω_0
						3.0
<u>Comp. Pier</u>			<u>Tension Pier</u>			
M_u	4215 k-ft			M_u	4271 k-ft	
C_u	4786 kips			T_u	-2722 kips	
l_w	5 ft			l_w	5 ft	
l_f	16 ft			l_f	16 ft	
t_w	36 in			t_w	36 in	
t_f	18 in			t_f	18 in	
ϕ	0.65			ϕ	0.90	
f_y	60.0 ksi					
f_c	8.0 ksi					
<u>Interior Bnd</u>			in	# Layer	Spacing	# Layer BE L
A_s	19.5 in ²		4	3	15.00	5.0 22
Use	15	#11		Provided A_s	23.4 in²	Check P-M to Verify
<u>Exterior Bnd</u>			in	# Layer	Spacing	# Layer BE L
A_s	45.0 in ²		4	3	15.00	20.0 82
Use	60	#11		Provided A_s	93.6 in²	Check P-M to Verify
Shear		9	8	L-in Fln'g	126 L-in Web	34.00
<u>Comp. Pier</u>			<u>Tension Pier</u>			
h_w	117 ft			h_w	117 ft	
f_y	60.0 ksi			f_y	60.0 ksi	
V_u	482.9 kips			V_u	482.9 kips	
ω_v	1.24			ω_v	1.24	
n_{story}	9			n_{story}	9	
n_s	9.0			n_s	9.0	
Ω_v	3.71			Ω_v	3.87	3.26
V_e	1449 kips			V_e	1449 kips	
ϕ	0.75			ϕ	0.75	
ϕV_c	289.8 kips			ϕV_c	289.8 kips	
ρ_t	0.0119			ρ_t	0.0119	
	Need	4 curtain of #6		Need	4 curtain of #6	
	@	4.1 in		@	4.1 in	
	Use	4 curtain of #6		Use	4 curtain of #6	
	@	4 in		@	4 in	
ϕV_n	1449 kips	OK		ϕV_n	1449 kips	OK
<u>Vertical Web Bar</u>						
$\rho_{l,min}$	0.0025			$\rho_{l,min}$	0.0025	
Need min of	3 curtain of #6			Need min of	3 curtain of #6	
	@	14.7 in		@	14.7 in	
Use	3 curtain of #6			Use	3 curtain of #6	
@	12 in			@	12 in	



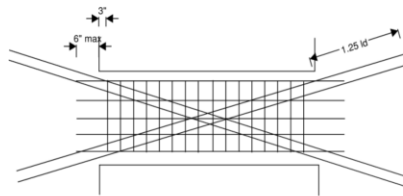
Drift Check

C_d	5.0			
All. Drift	2.00%			
h_{wcs}	117 ft			
δ_x	5.51 in			
δ_x / h_{wcs}	0.39%			
$C_d \delta_x / h_{wcs}$	1.96%	<	$(\delta / h_{wcs})_{all.}$	2.00% <u>Drift OK</u>

Coupling Beam**Story 2**

V_u 502.4 kips
 b 36 in
 d 48 in
 l 12 ft
 f'_c 8 ksi
 f_y 60 ksi
 ϕ 0.85
 bundle d 4 in
 diag. cover 3 in
 α 0.26 rad

$V_u / (A_g \sqrt{f'_c})$ 3.3 < 10



$A_{vd} \geq$ 19.3 in²

USE 12 #11 A_{vd} 18.7 in²
 n_X 4
 n_Y 3

Clear Cover 1.5 in

b_{cx} 33 in

b_{cy} 45 in

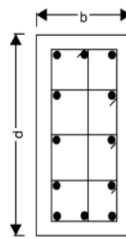
Conf. Bar #6 d 0.75 in

n_{X_skin} 3

n_{Y_skin} 7

h_x 15.4 in < 8 in

h_y 6.6 in < 8 in

X-Direction

s1 3.3 in

s2 6.1 in

s3 6.0 in

s4 9.4 in

Use s 3.3 in

Y-Direction

s1 5.7 in

s2 10.5 in

s3 6.0 in

s4 9.4 in

Use s 5.7 in

Anchorage

K_{tr} 2.5

all ψ 1.3

l_d 36.9 in

1.25 l_d 46.1 in

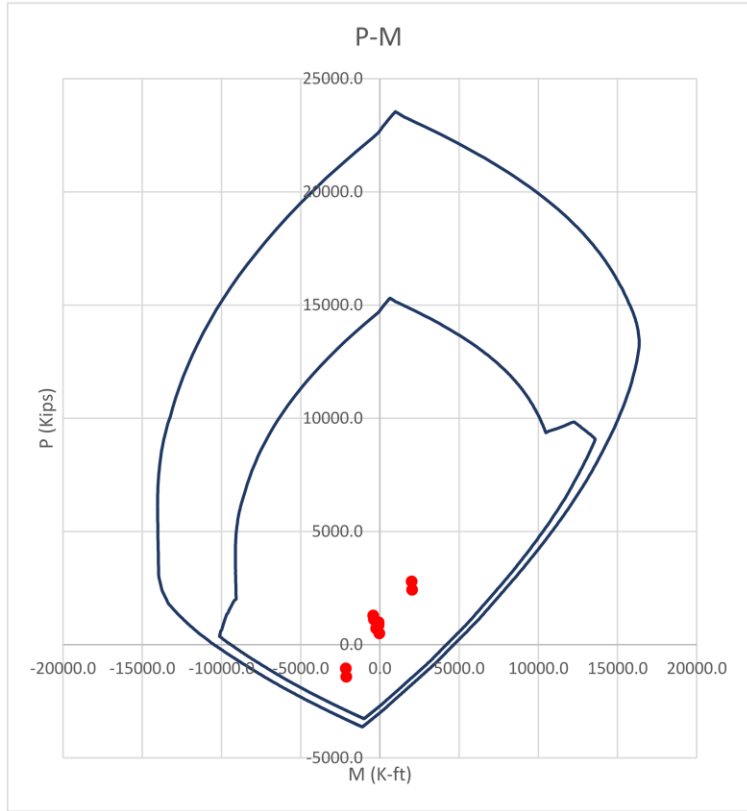
if using headed bars

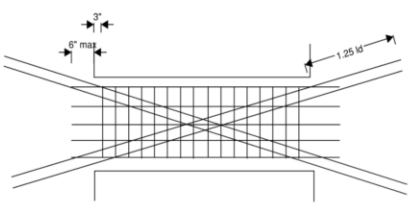
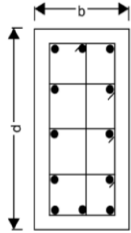
l_{dt} 15.1 in

1.25 l_{dt} 18.9 in

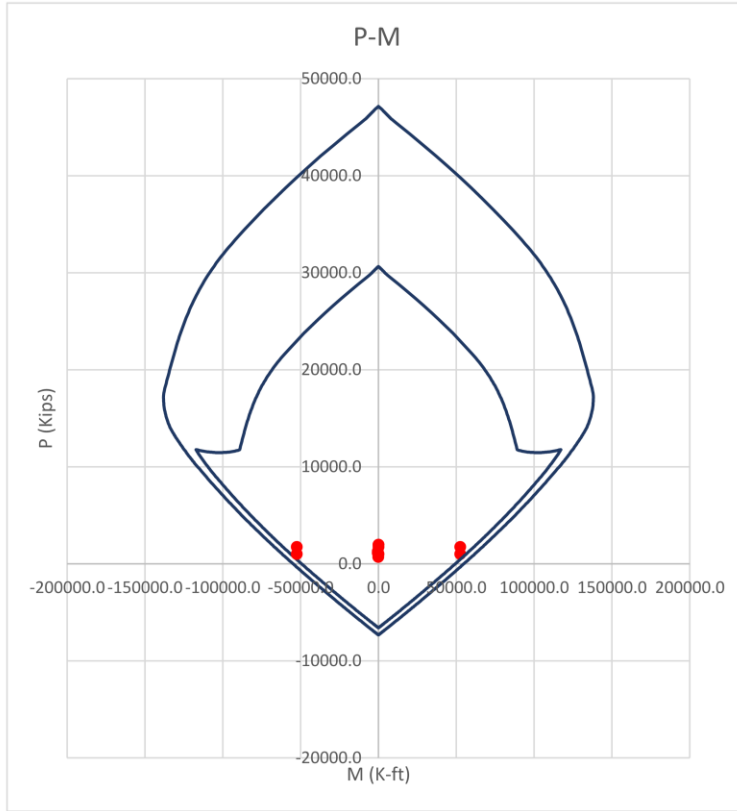
Solid-Direction						
Wall Pier		Story		1		Ω_0
						3.0
<u>Comp. Pier</u>			<u>Tension Pier</u>			
M_u	98813 k-ft		M_u	98813 k-ft		
C_u	2625 kips		T_u	2625 kips		
l_w	16 ft	29	l_w	16 ft		
l_f	5 ft		l_f	5 ft		
t_w	23 in		t_w	23 in		
t_f	36 in		t_f	36 in		
ϕ	0.90		ϕ	0.90		
f_y	60.0 ksi					
f_c	8.0 ksi					
<u>Interior Bnd</u>		in	# Layer	Spacing	# Layer	BE L
A_s	118.7 in ²		4	5	4.25	15.0 62
Use	75	#11	Provided A_s		117 in²	Check P-M to Verify
<u>Exterior Bnd</u>		in	# Layer	Spacing	# Layer	BE L
A_s	118.7 in ²		4	5	4.25	15.0 62
Use	75	#11	Provided A_s		117 in²	Check P-M to Verify
Shear						
<u>Comp. Pier</u>			<u>Tension Pier</u>			
h_w	117 ft		h_w	117 ft		
f_y	60.0 ksi		f_y	60.0 ksi		
V_u	1272.0 kips		V_u	1272.0 kips		
ω_v	1.60		ω_v	1.60		
n_{story}	9		n_{story}	9		
n_s	9.0		n_s	9.0		
Ω_v	1.41		Ω_v	1.41		
V_e	2870 kips		V_e	2870 kips		
ϕ	0.75		ϕ	0.75		
ϕV_c	592.5 kips		ϕV_c	592.5 kips		
ρ_t	0.0115		ρ_t	0.0115		
Need	3	curtain of #6	Need	3	curtain of #6	
@	5.0 in		@	5.0 in		
Use	3	curtain of #6	Use	3	curtain of #6	
@	5 in		@	5 in		
ϕV_n	2873 kips	OK	ϕV_n	2873 kips	OK	
<u>Vertical Web Bar</u>						
$\rho_{l,min}$	0.0025		$\rho_{l,min}$	0.0025		
Need min of	2	curtain of #6	Need min of	2	curtain of #6	
	@	15.3 in		@	15.3 in	
Use	2	curtain of #6	Use	2	curtain of #6	
@	12 in		@	12 in		

Coupled-Direction									
Wall Pier		Story		4		Ω_0		3.0	
<u>Comp. Pier</u>					<u>Tension Pier</u>				
M_u	2003	k-ft	M_u	2119	k-ft	T_u	-1418	kips	
C_u	2786	kips	T_u	-1418	kips				
l_w	5	ft	l_w	5	ft				
l_f	16	ft	l_f	16	ft				
t_w	30	in	t_w	30	in				
t_f	18	in	t_f	18	in				
ϕ	0.65		ϕ	0.90					
f_y	60.0	ksi							
f_c	8.0	ksi							
<u>Interior Bnd</u>									
A_s	9.3	in ²	in	# Layer	3	Spacing	# Layer	5.0	BE L
Use	15		#11	Provided A_s	23.4	in²	Check P-M to Verify		
<u>Exterior Bnd</u>									
A_s	22.9	in ²	in	# Layer	3	Spacing	# Layer	20.0	BE L
Use	60		#11	Provided A_s	93.6	in²	Check P-M to Verify		
<u>Shear</u>									
	9		8	L-in Fl'n'g	102	L-in Web	34.00		
<u>Comp. Pier</u>					<u>Tension Pier</u>				
h_w	117	ft	h_w	117	ft				
f_y	60.0	ksi	f_y	60.0	ksi				
V_u	379.7	kips	V_u	379.7	kips				
ω_v	1.24		ω_v	1.24					
n_{story}	9		n_{story}	9					
n_s	9.0		n_s	9.0					
Ω_v	4.54		Ω_v	4.16		3.40			
V_e	1139	kips	V_e	1139	kips				
ϕ	0.75		ϕ	0.75					
ϕV_c	241.5	kips	ϕV_c	241.5	kips				
ρ_t	0.0111		ρ_t	0.0111					
Need	3	curtain of #6	Need	3	curtain of #6				
@	4.0	in	@	4.0	in				
Use	3	curtain of #6	Use	3	curtain of #6				
@	4	in	@	4	in				
ϕV_n	1132	kips	N.G.	ϕV_n	1132	kips	N.G.		
<u>Vertical Web Bar</u>									
$\rho_{l,min}$	0.0025		$\rho_{l,min}$	0.0025					
Need min of	2	curtain of #6	Need min of	2	curtain of #6				
@	11.7	in	@	11.7	in				
Use	2	curtain of #6	Use	2	curtain of #6				
@	12	in	@	12	in				

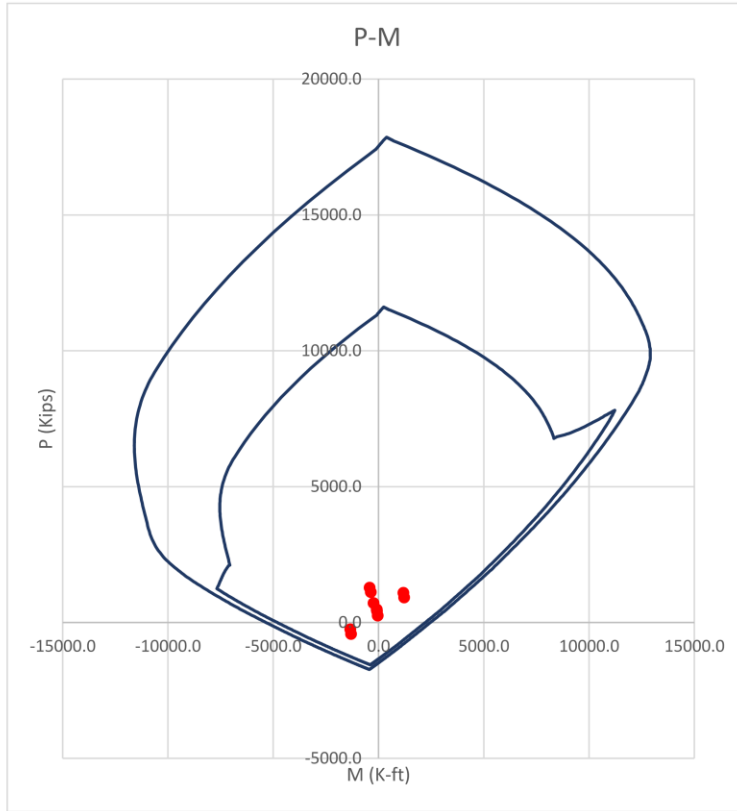


Coupling Beam		Story	4
V_u	413.5 kips	$V_u/(A_g \sqrt{f'_c})$	3.2 < 10
b	30 in		
d	48 in		
l	12 ft		
f'_c	8 ksi		
f_y	60 ksi		
ϕ	0.85		
bundle d	4 in		
diag. cover	3 in		
α	0.26 rad		
			
$A_{vd} \geq$	15.9 in ²	USE	10 #11 A_{vd} 15.6 in ²
		nX	4
		nY	3
Clear Cover	1.5 in		
b_{cx}	27 in		
b_{cy}	45 in		
Conf. Bar	#6	d	0.75 in
nX_skin	3		
nY_skin	7		
h_x	12.4 in	< 8 in	
h_y	6.6 in	< 8 in	
			
<u>X-Direction</u>		<u>Y-Direction</u>	
s1	4.1 in	s1	5.7 in
s2	6.6 in	s2	9.2 in
s3	6.0 in	s3	6.0 in
s4	9.4 in	s4	9.4 in
Use s	4.1 in	Use s	5.7 in
Anchorage			
K_{tr}	2.5		
all ψ	1.3		
l_d	36.9 in		
1.25 l_d	46.1 in		
if using headed bars			
l_{dt}	15.1 in		
1.25 l_{dt}	18.9 in		

Solid-Direction						
Wall Pier		Story	4			Ω_0
						3.0
<u>Comp. Pier</u>			<u>Tension Pier</u>			
M_u	52577 k-ft		M_u	52577 k-ft		
C_u	1735 kips		T_u	1735 kips		
l_w	16 ft	29	l_w	16 ft		
l_f	5 ft		l_f	5 ft		
t_w	18 in		t_w	18 in		
t_f	30 in		t_f	30 in		
ϕ	0.90		ϕ	0.90		
f_y	60.0 ksi					
f_c	8.0 ksi					
<u>Interior Bnd</u>		in	# Layer	Spacing	# Layer	BE L
A_s	60.0 in ²		4	5	3.00	15.0 62
Use	75	#8	Provided A_s	59.25 in²	Check P-M to Verify	
<u>Exterior Bnd</u>		in	# Layer	Spacing	# Layer	BE L
A_s	60.0 in ²		4	5	3.00	15.0 62
Use	75	#8	Provided A_s	59.25 in²	Check P-M to Verify	
Shear						
<u>Comp. Pier</u>			<u>Tension Pier</u>			
h_w	117 ft		h_w	117 ft		
f_y	60.0 ksi		f_y	60.0 ksi		
V_u	923.4 kips		V_u	923.4 kips		
ω_v	1.60		ω_v	1.60		
n_{story}	9		n_{story}	9		
n_s	9.0		n_s	9.0		
Ω_v	1.50		Ω_v	1.50		
V_e	2216 kips		V_e	2216 kips		
ϕ	0.75		ϕ	0.75		
ϕV_c	463.7 kips		ϕV_c	463.7 kips		
ρ_t	0.0113		ρ_t	0.0113		
Need	3 curtain of #6		Need	3 curtain of #6		
@	6.5 in		@	6.5 in		
Use	3 curtain of #6		Use	3 curtain of #6		
@	6.5 in		@	6.5 in		
ϕV_n	2218 kips	OK	ϕV_n	2218 kips	OK	
<u>Vertical Web Bar</u>						
$\rho_{l,min}$	0.0025		$\rho_{l,min}$	0.0025		
Need min of	2 curtain of #6		Need min of	2 curtain of #6		
	@ 19.6 in			@ 19.6 in		
Use	2 curtain of #6		Use	2 curtain of #6		
@	12 in		@	12 in		

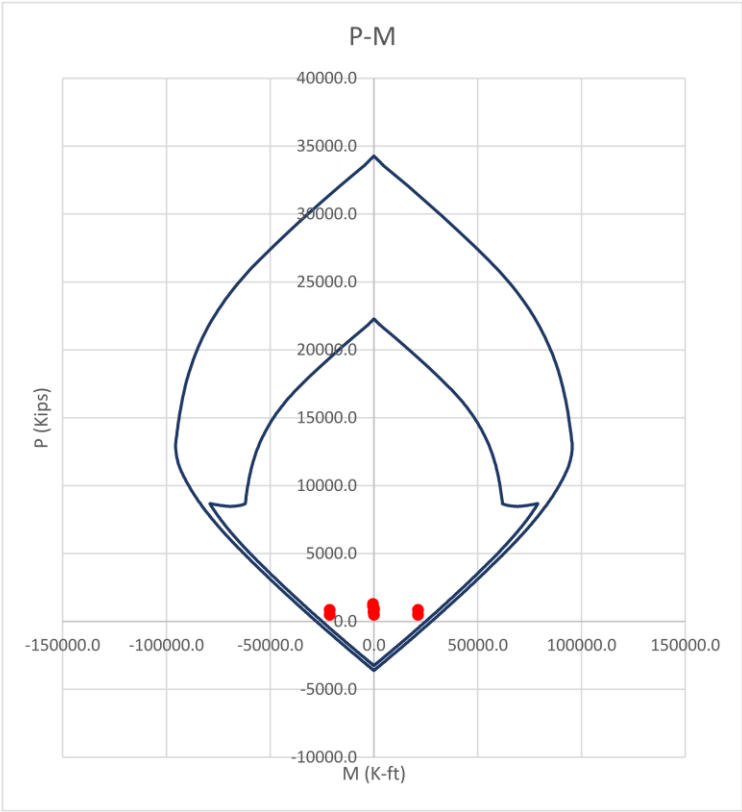


Coupled-Direction									
Wall Pier		Story		7		Ω_0		3.0	
<u>Comp. Pier</u>					<u>Tension Pier</u>				
M_u	1180	k-ft	M_u	1303	k-ft				
C_u	1096	kips	T_u	-423	kips				
l_w	5	ft	l_w	5	ft				
l_f	16	ft	l_f	16	ft				
t_w	26	in	t_w	26	in				
t_f	12	in	t_f	12	in				
ϕ	0.90		ϕ	0.90					
f_y	60.0	ksi							
f_c	8.0	ksi							
<u>Interior Bnd</u>			in	# Layer	Spacing	# Layer	BE L		
A_s	5.5	in ²	4	3	10.00	3.0	14		
Use	9		#7	Provided A_s	5.4 in²		Check P-M to Verify		
<u>Exterior Bnd</u>			in	# Layer	Spacing	# Layer	BE L		
A_s	9.9	in ²	4	3	10.00	12.0	50		
Use	36		#7	Provided A_s	21.6 in²		Check P-M to Verify		
Shear		9	8	L-in Fl'n'g	86	L-in Web	34.00		
<u>Comp. Pier</u>					<u>Tension Pier</u>				
h_w	117	ft	h_w	117	ft				
f_y	60.0	ksi	f_y	60.0	ksi				
V_u	269.7	kips	V_u	269.7	kips				
ω_v	1.24		ω_v	1.24					
n_{story}	9		n_{story}	9					
n_s	9.0		n_s	9.0					
Ω_v	4.12		Ω_v	4.24					
V_e	809	kips	V_e	809	kips				
ϕ	0.75		ϕ	0.75					
ϕV_c	209.3	kips	ϕV_c	209.3	kips				
ρ_t	0.0085		ρ_t	0.0085					
Need	2	curtain of #6	Need	2	curtain of #6				
@	4.0	in	@	4.0	in				
Use	2	curtain of #6	Use	2	curtain of #6				
@	4	in	@	4	in				
ϕV_n	803	kips	N.G.	ϕV_n	803	kips	N.G.		
<u>Vertical Web Bar</u>					<u>Vertical Web Bar</u>				
$\rho_{l,min}$	0.0025		$\rho_{l,min}$	0.0025					
Need min of	2	curtain of #5	Need min of	2	curtain of #5				
@	9.5	in	@	9.5	in				
Use	2	curtain of #5	Use	2	curtain of #5				
@	12	in	@	12	in				



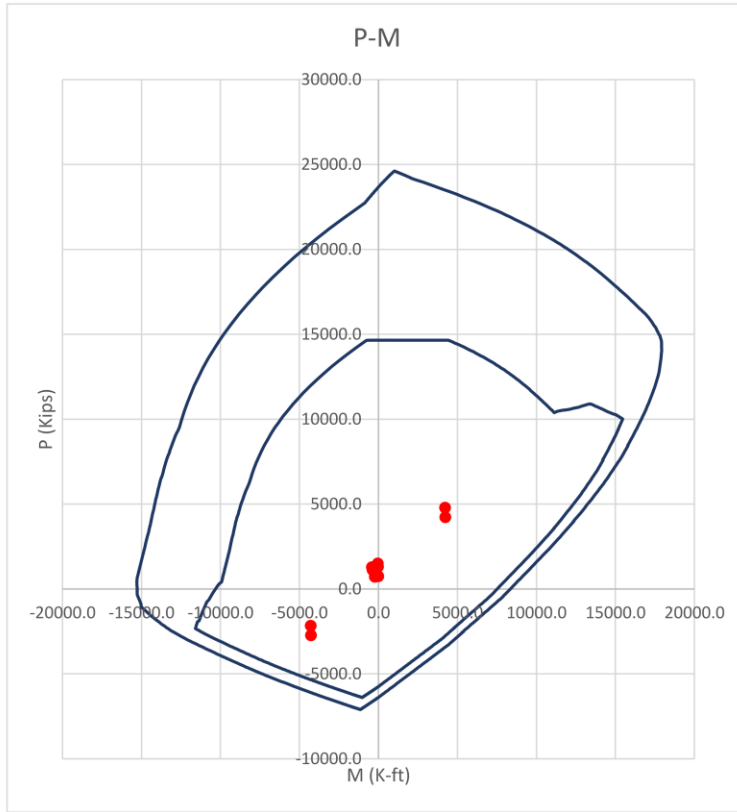
Coupling Beam		Story	7
V_u	265.6 kips	$V_u / (A_g \sqrt{f'_c})$	2.4 < 10
b	26 in		
d	48 in		
l	12 ft		
f'_c	8 ksi		
f_y	60 ksi		
ϕ	0.85		
bundle d	4 in		
diag. cover	3 in		
α	0.26 rad		
$A_{vd} \geq$	10.2 in ²	USE	6 #11 A_{vd} 9.36 in ²
		nX	4
		nY	3
Clear Cover	1.5 in		
b_{cx}	23 in		
b_{cy}	45 in		
Conf. Bar	#6	d	0.75 in
nX_skin	3		
nY_skin	7		
h_x	10.4 in	< 8 in	
h_y	6.6 in	< 8 in	
<u>X-Direction</u>		<u>Y-Direction</u>	
s1	4.8 in	s1	5.7 in
s2	7.0 in	s2	8.3 in
s3	6.0 in	s3	6.0 in
s4	9.4 in	s4	9.4 in
Use s	4.8 in	Use s	5.7 in
Anchorage			
K_{tr}	2.5		
all ψ	1.3		
l_d	36.9 in		
1.25 l_d	46.1 in		
if using headed bars			
l_{dt}	15.1 in		
1.25 l_{dt}	18.9 in		

Solid-Direction						
Wall Pier		Story		7		Ω_0
						3.0
<u>Comp. Pier</u>			<u>Tension Pier</u>			
M_u	21271 k-ft	M_u	21271 k-ft			
C_u	845 kips	T_u	845 kips			
l_w	16 ft	l_w	16 ft			
l_f	5 ft	l_f	5 ft			
t_w	16 in	t_w	16 in			
t_f	17 in	t_f	17 in			
ϕ	0.90	ϕ	0.90			
f_y	60.0 ksi					
f_c	8.0 ksi					
<u>Interior Bnd</u>		in	# Layer	Spacing	# Layer	BE L
A_s	22.9 in ²	4	5	2.50	9.0	38
Use	45	#7	Provided A_s	27 in²	Check P-M to Verify	
<u>Exterior Bnd</u>		in	# Layer	Spacing	# Layer	BE L
A_s	22.9 in ²	4	5	2.50	9.0	38
Use	45	#7	Provided A_s	27 in²	Check P-M to Verify	
Shear						
<u>Comp. Pier</u>			<u>Tension Pier</u>			
h_w	117 ft	h_w	117 ft			
f_y	60.0 ksi	f_y	60.0 ksi			
V_u	651.2 kips	V_u	651.2 kips			
ω_v	1.60	ω_v	1.60			
n_{story}	9	n_{story}	9			
n_s	9.0	n_s	9.0			
Ω_v	1.90	Ω_v	1.90			
V_e	1954 kips	V_e	1954 kips			
ϕ	0.75	ϕ	0.75			
ϕV_c	412.2 kips	ϕV_c	412.2 kips			
ρ_t	0.0112	ρ_t	0.0112			
Need	3 curtain of #6	Need	3 curtain of #6			
@	7.4 in	@	7.4 in			
Use	3 curtain of #6	Use	3 curtain of #6			
@	7 in	@	7 in			
ϕV_n	2041 kips	ϕV_n	2041 kips	OK		
<u>Vertical Web Bar</u>						
$\rho_{l,min}$	0.0025	$\rho_{l,min}$	0.0025			
Need min of	2 curtain of #5	Need min of	2 curtain of #5			
	@ 15.5 in		@ 15.5 in			
Use	2 curtain of #5	Use	2 curtain of #5			
@	12 in	@	12 in			



B.3. 9-Story ACI 318-25

Coupled-Direction									
Wall Pier		Story		1		Ω_0		2.5	
<u>Comp. Pier</u>					<u>Tension Pier</u>				
M_u	4215 k-ft			M_u	4271 k-ft				
C_u	4786 kips			T_u	-2722 kips				
l_w	5 ft			l_w	5 ft				
l_f	16 ft			l_f	16 ft				
t_w	23 in			t_w	23 in				
t_f	18 in			t_f	18 in				
ϕ	0.65			ϕ	0.90				
f_y	60.0 ksi								
f_c	8.0 ksi								
<u>Interior Bnd</u>					<u>Exterior Bnd</u>				
A_s	19.5 in ²		in # Layer	4 3	Spacing	# Layer	BE L		
					8.50	5.0	22		
Use	15	#11	Provided A_s	23.4 in²	Check P-M to Verify				
A_s	45.0 in ²		in # Layer	4 3	Spacing	# Layer	BE L		
					8.50	20.0	82		
Use	60	#11	Provided A_s	93.6 in²	Check P-M to Verify				
Shear					Shear				
	9	8	L-in Fln'g	74 L-in Web	34.00				
<u>Comp. Pier</u>					<u>Tension Pier</u>				
h_w	117 ft			h_w	117 ft				
f_y	60.0 ksi			f_y	60.0 ksi				
V_u	482.9 kips			V_u	482.9 kips				
ω_v	1.24			ω_v	1.24				
n_{story}	9			n_{story}	9				
n_s	9.0			n_s	9.0				
Ω_v	1.50			Ω_v	1.50				
V_e	898 kips			V_e	898 kips				
ϕ	0.75			ϕ	0.75				
ϕV_c	185.1 kips			ϕV_c	185.1 kips				
ρ_t	0.0115			ρ_t	0.0115				
	Need	3 curtain of #6			Need	3 curtain of #6			
	@	5.0 in			@	5.0 in			
	Use	3 curtain of #6			Use	3 curtain of #6			
	@	5 in			@	5 in			
ϕV_n	898 kips	OK		ϕV_n	898 kips	OK			
<u>Vertical Web Bar</u>					<u>Vertical Web Bar</u>				
$\rho_{l,min}$	0.0025			$\rho_{l,min}$	0.0025				
Need min of	2 curtain of #6			Need min of	2 curtain of #6				
	@	15.3 in			@	15.3 in			
Use	2 curtain of #6			Use	2 curtain of #6				
@	12 in			@	12 in				



Drift Check

C_d	5.0			
All. Drift	2.00%			
h_{wcs}	117 ft			
δ_x	5.51 in			
δ_x / h_{wcs}	0.39%			
$C_d \delta_x / h_{wcs}$	1.96%	<	$(\delta / h_{wcs})_{all.}$	2.00% Drift OK

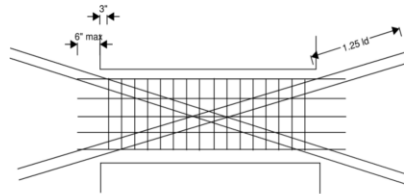
OK

OK

Coupling Beam

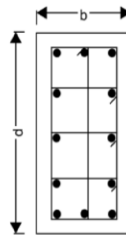
V_u 475.6 kips
 b 23 in
 d 48 in
 l 12 ft
 f'_c 8 ksi
 f_y 60 ksi
 ϕ 0.85
 bundle d 4 in
 diag. cover 3 in
 α 0.26 rad

$V_u / (A_g \sqrt{f'_c}) \quad 4.8 < 10$



$A_{vd} \geq$ 18.3 in² **USE 12 #11** A_{vd} 18.7 in²
 n_x 4
 n_y 3

Clear Cover 1.5 in
 b_{cx} 20 in
 b_{cy} 45 in
 Conf. Bar #6 d 0.75 in
 n_{x_skin} 3
 n_{y_skin} 7
 h_x 8.9 in < 8 in
 h_y 6.6 in < 8 in

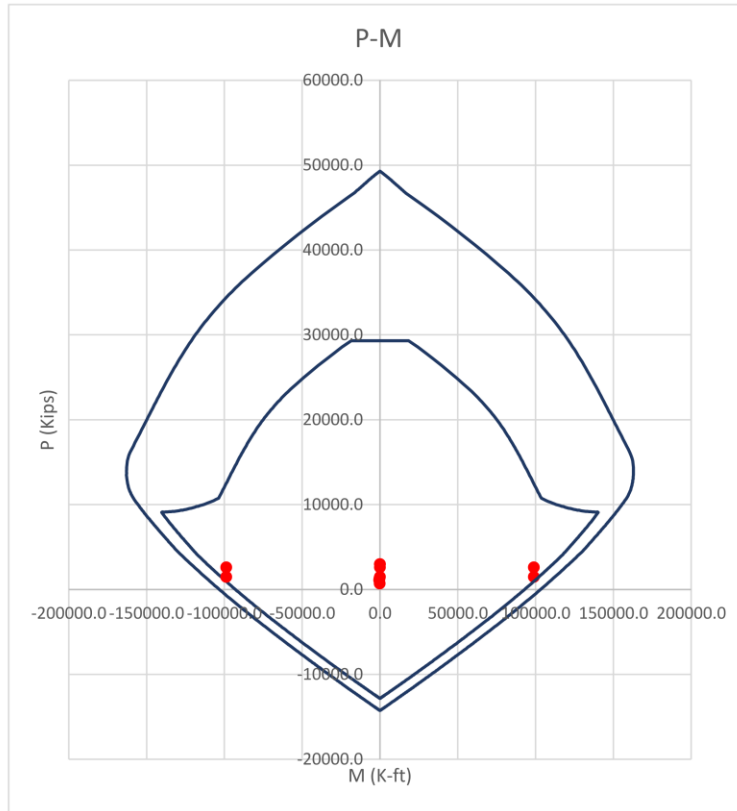


<u>X-Direction</u>		<u>Y-Direction</u>	
s1	5.5 in	s1	5.7 in
s2	7.3 in	s2	7.5 in
s3	6.0 in	s3	6.0 in
s4	9.4 in	s4	9.4 in
Use s	5.5 in	Use s	5.7 in

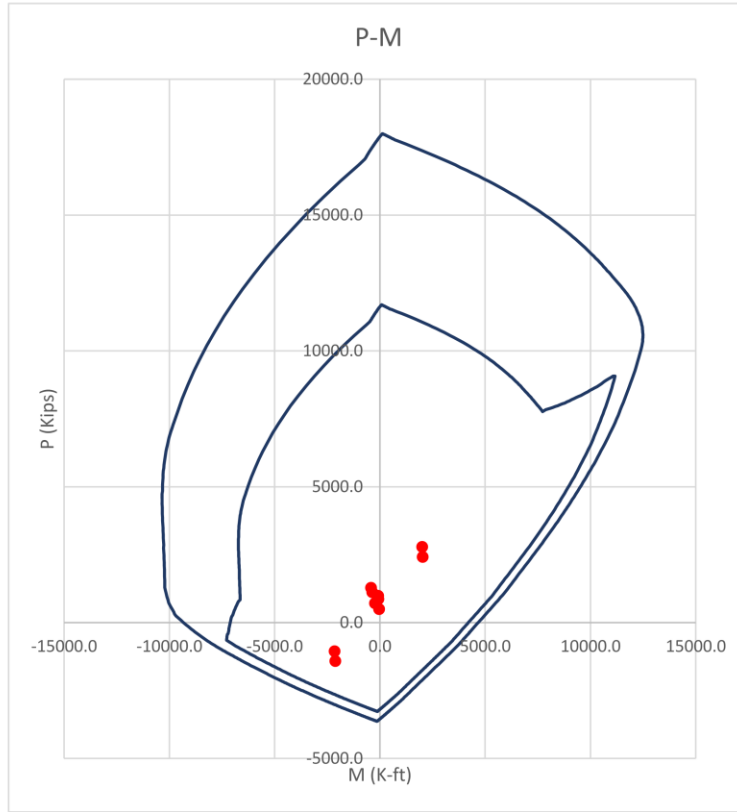
Anchorage
 K_{tr} 2.5 N.G. #VALUE!
 all ψ 1.3
 l_d 36.9 in
1.25 l_d **46.1 in**

if using headed bars
 l_{dt} 15.1 in
1.25 l_{dt} **18.9 in**

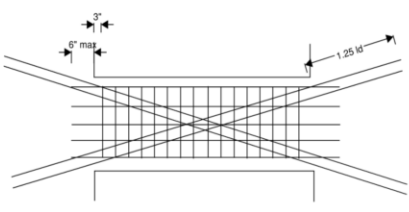
Solid-Direction						
Wall Pier		Story		1		Ω_0
						2.5
<u>Comp. Pier</u>			<u>Tension Pier</u>			
M_u	98813	k-ft	M_u	98813	k-ft	
C_u	2625	kips	T_u	2625	kips	
l_w	16	ft	l_w	16	ft	
l_f	5	ft	l_f	5	ft	
t_w	18	in	t_w	18	in	
t_f	23	in	t_f	23	in	
ϕ	0.90		ϕ	0.90		
f_y	60.0	ksi				
f_c	8.0	ksi				
<u>Interior Bnd</u>		in	# Layer	Spacing	# Layer	BE L
A_s	118.7	in ²	4	5	3.00	15.0 62
Use	75	#11	Provided A_s		117 in²	Check P-M to Verify
<u>Exterior Bnd</u>		in	# Layer	Spacing	# Layer	BE L
A_s	118.7	in ²	4	5	3.00	15.0 62
Use	75	#11	Provided A_s		117 in²	Check P-M to Verify
Shear						
<u>Comp. Pier</u>			<u>Tension Pier</u>			
h_w	117	ft	h_w	117	ft	
f_y	60.0	ksi	f_y	60.0	ksi	
V_u	1272.0	kips	V_u	1272.0	kips	
ω_v	1.24		ω_v	1.24		
n_{story}	9		n_{story}	9		
n_s	9.0		n_s	9.0		
Ω_v	1.41		Ω_v	1.41		
V_e	2224	kips	V_e	2224	kips	
ϕ	0.75		ϕ	0.75		
ϕV_c	463.7	kips	ϕV_c	463.7	kips	
ρ_t	0.0113		ρ_t	0.0113		
Need	2	curtain of #6	Need	2	curtain of #6	
@	4.3	in	@	4.3	in	
Use	2	curtain of #6	Use	2	curtain of #6	
@	4	in	@	4	in	
ϕV_n	2318	kips	ϕV_n	2318	kips	OK
<u>Vertical Web Bar</u>						
$\rho_{l,min}$	0.0025		$\rho_{l,min}$	0.0025		
Need min of	2	curtain of #6	Need min of	2	curtain of #6	
@	19.6	in	@	19.6	in	
Use	2	curtain of #6	Use	2	curtain of #6	
@	12	in	@	12	in	



Coupled-Direction						
Wall Pier	Story 4			Ω_0	2.5	
<u>Comp. Pier</u>			<u>Tension Pier</u>			
M_u	2003 k-ft		M_u	2119 k-ft		
C_u	2786 kips		T_u	-1418 kips		
l_w	5 ft		l_w	5 ft		
l_f	16 ft		l_f	16 ft		
t_w	18 in		t_w	18 in		
t_f	14 in		t_f	14 in		
ϕ	0.65		ϕ	0.90		
f_y	60.0 ksi					
f_c	8.0 ksi					
<u>Interior Bnd</u>		in	# Layer	Spacing	# Layer	BE L
A_s	9.3 in ²	4	3	6.00	5.0	22
Use	15	#11	Provided A_s	23.4 in²	Check P-M to Verify	
<u>Exterior Bnd</u>		in	# Layer	Spacing	# Layer	BE L
A_s	22.9 in ²	4	3	6.00	20.0	82
Use	60	#11	Provided A_s	93.6 in²	Check P-M to Verify	
Shear	9	8	L-in Fl'n'g	54 L-in Web	34.00	
<u>Comp. Pier</u>			<u>Tension Pier</u>			
h_w	117 ft		h_w	117 ft		
f_y	60.0 ksi		f_y	60.0 ksi		
V_u	379.7 kips		V_u	379.7 kips		
ω_v	1.24		ω_v	1.24		
n_{story}	9		n_{story}	9		
n_s	9.0		n_s	9.0		
Ω_v	1.50		Ω_v	1.50		
V_e	706 kips		V_e	706 kips		
ϕ	0.75		ϕ	0.75		
ϕV_c	144.9 kips		ϕV_c	144.9 kips		
ρ_t	0.0116		ρ_t	0.0116		
Need	3 curtain of #6		Need	3 curtain of #6		
@	6.3 in		@	6.3 in		
Use	3 curtain of #6		Use	3 curtain of #6		
@	6 in		@	6 in		
ϕV_n	724 kips	OK	ϕV_n	724 kips	OK	
<u>Vertical Web Bar</u>						
$\rho_{l,min}$	0.0025		$\rho_{l,min}$	0.0025		
Need min of	2 curtain of #5		Need min of	2 curtain of #5		
	@ 13.8 in			@ 13.8 in		
Use	2 curtain of #5		Use	2 curtain of #5		
@	12 in		@	12 in		

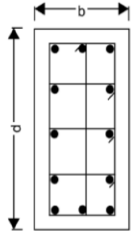


Coupling Beam		Story	4
V_u	413.5 kips	$V_u/(A_g \sqrt{f'_c})$	5.4 < 10
b	18 in		
d	48 in		
l	12 ft		
f'_c	8 ksi		
f_y	60 ksi		
ϕ	0.85		
bundle d	4 in		
diag. cover	3 in		
α	0.26 rad		



$A_{vd} \geq$	15.9 in ²	USE	10 #11	A_{vd}	15.6 in ²
		n_X	4		
		n_Y	3		

Clear Cover	1.5 in		
b_{cx}	15 in		
b_{cy}	45 in		
Conf. Bar	#6	d	0.75 in
n_{X_skin}	3		
n_{Y_skin}	7		
h_x	6.4 in	< 8 in	
h_y	6.6 in	< 8 in	

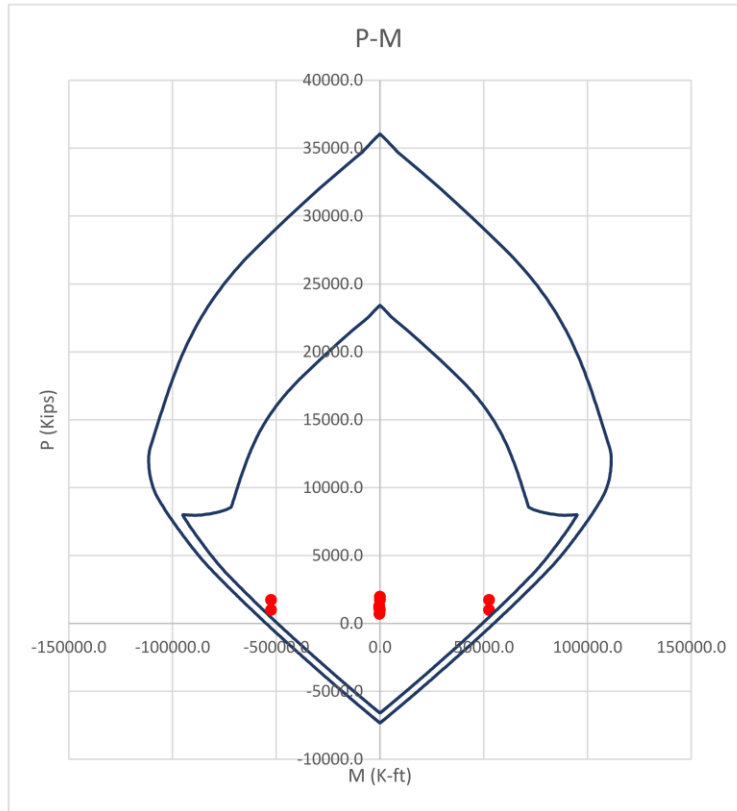


<u>X-Direction</u>		<u>Y-Direction</u>	
s1	7.3 in	s1	5.7 in
s2	7.9 in	s2	6.1 in
s3	6.0 in	s3	6.0 in
s4	9.4 in	s4	9.4 in
Use s	6.0 in	Use s	5.7 in

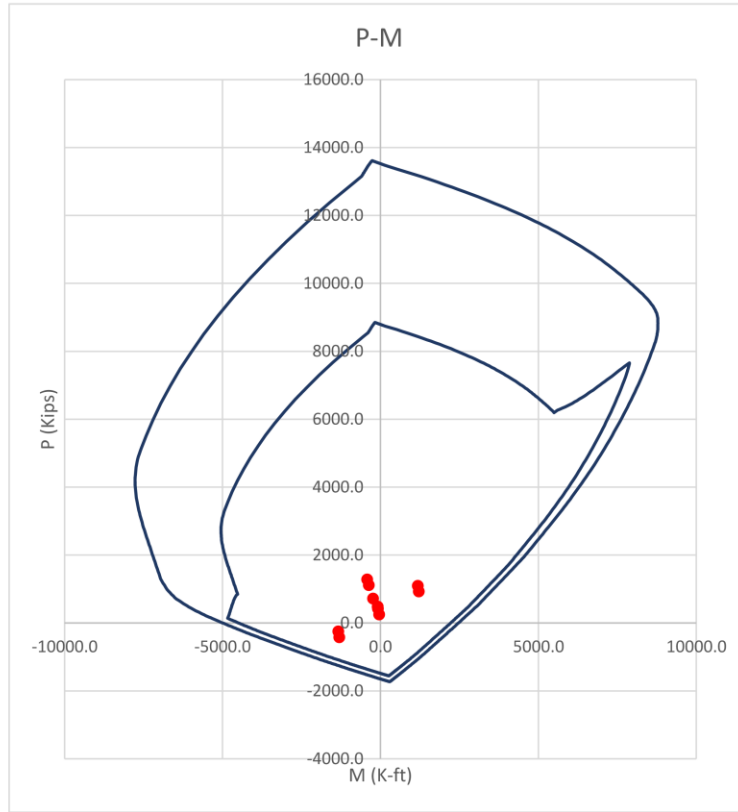
Anchorage	
K_{tr}	2.5
all ψ	1.3
l_d	36.9 in
1.25 l_d	46.1 in

if using headed bars	
l_{dt}	15.1 in
1.25 l_{dt}	18.9 in

Solid-Direction						
Wall Pier		Story	4			Ω_0
						2.5
<u>Comp. Pier</u>			<u>Tension Pier</u>			
M_u	52577 k-ft		M_u	52577 k-ft		
C_u	1735 kips		T_u	1735 kips		
l_w	16 ft		l_w	16 ft		
l_f	5 ft		l_f	5 ft		
t_w	14 in		t_w	14 in		
t_f	18 in		t_f	18 in		
ϕ	0.90		ϕ	0.90		
f_y	60.0 ksi					
f_c	8.0 ksi					
<u>Interior Bnd</u>		in	# Layer	Spacing	# Layer	BE L
A_s	60.0 in ²		4	5	2.00	15.0 62
Use	75	#8	Provided A_s	59.25 in²	Check P-M to Verify	
<u>Exterior Bnd</u>		in	# Layer	Spacing	# Layer	BE L
A_s	60.0 in ²		4	5	2.00	15.0 62
Use	75	#8	Provided A_s	59.25 in²	Check P-M to Verify	
Shear						
<u>Comp. Pier</u>			<u>Tension Pier</u>			
h_w	117 ft		h_w	117 ft		
f_y	60.0 ksi		f_y	60.0 ksi		
V_u	923.4 kips		V_u	923.4 kips		
ω_v	1.24		ω_v	1.24		
n_{story}	9		n_{story}	9		
n_s	9.0		n_s	9.0		
Ω_v	1.50		Ω_v	1.50		
V_e	1718 kips		V_e	1718 kips		
ϕ	0.75		ϕ	0.75		
ϕV_c	360.6 kips		ϕV_c	360.6 kips		
ρ_t	0.0112		ρ_t	0.0112		
Need	2 curtain of #6		Need	2 curtain of #6		
@	5.6 in		@	5.6 in		
Use	2 curtain of #6		Use	2 curtain of #6		
@	5.5 in		@	5.5 in		
ϕV_n	1743 kips	OK	ϕV_n	1743 kips	OK	
<u>Vertical Web Bar</u>						
$\rho_{l,min}$	0.0025		$\rho_{l,min}$	0.0025		
Need min of	2 curtain of #5		Need min of	2 curtain of #5		
	@ 17.7 in			@ 17.7 in		
Use	2 curtain of #5		Use	2 curtain of #5		
@	12 in		@	12 in		

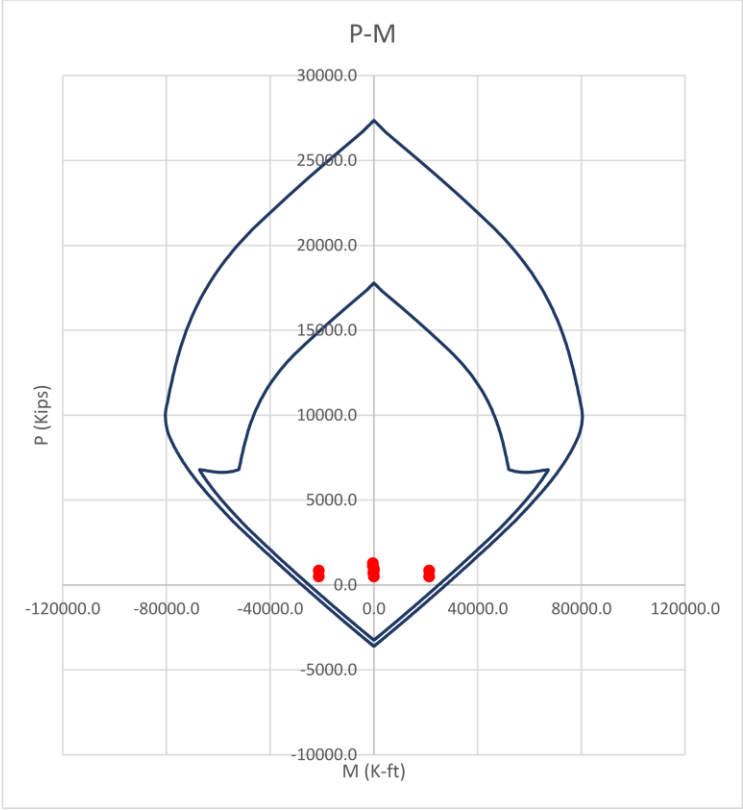


Coupled-Direction									
Wall Pier		Story		7		Ω_0		2.5	
<u>Comp. Pier</u>					<u>Tension Pier</u>				
M_u	1180	k-ft	M_u	1303	k-ft				
C_u	1096	kips	T_u	-423	kips				
l_w	5	ft	l_w	5	ft				
l_f	16	ft	l_f	16	ft				
t_w	13	in	t_w	13	in				
t_f	12	in	t_f	12	in				
ϕ	0.90		ϕ	0.90					
f_y	60.0	ksi							
f_c	8.0	ksi							
<u>Interior Bnd</u>			in	# Layer	Spacing	# Layer	BE L		
A_s	5.5	in ²	4	3	3.50	3.0	14		
Use	9		#7	Provided A_s	5.4 in²		Check P-M to Verify		
<u>Exterior Bnd</u>			in	# Layer	Spacing	# Layer	BE L		
A_s	9.9	in ²	4	3	3.50	12.0	50		
Use	36		#7	Provided A_s	21.6 in²		Check P-M to Verify		
Shear		9	8	L-in Fl'n'g	34	L-in Web	34.00		
<u>Comp. Pier</u>					<u>Tension Pier</u>				
h_w	117	ft	h_w	117	ft				
f_y	60.0	ksi	f_y	60.0	ksi				
V_u	269.7	kips	V_u	269.7	kips				
ω_v	1.24		ω_v	1.24					
n_{story}	9		n_{story}	9					
n_s	9.0		n_s	9.0					
Ω_v	1.50		Ω_v	1.50					
V_e	502	kips	V_e	502	kips				
ϕ	0.75		ϕ	0.75					
ϕV_c	104.6	kips	ϕV_c	104.6	kips				
ρ_t	0.0113		ρ_t	0.0113					
Need	2	curtain of #6	Need	2	curtain of #6				
@	6.0	in	@	6.0	in				
Use	2	curtain of #6	Use	2	curtain of #6				
@	6	in	@	6	in				
ϕV_n	501	kips	OK	ϕV_n	501	kips	OK		
<u>Vertical Web Bar</u>					<u>Vertical Web Bar</u>				
$\rho_{l,min}$	0.0025		$\rho_{l,min}$	0.0025					
Need min of	2	curtain of #5	Need min of	2	curtain of #5				
@	19.1	in	@	19.1	in				
Use	2	curtain of #5	Use	2	curtain of #5				
@	12	in	@	12	in				



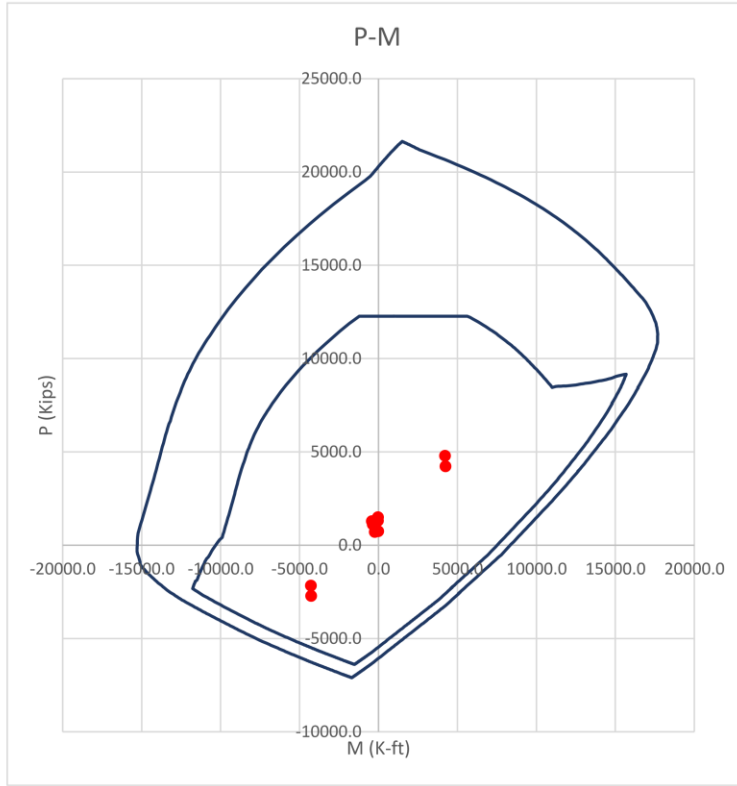
Coupling Beam		Story	7
V_u	265.6 kips	$V_u / (A_g \sqrt{f'_c})$	4.8 < 10
b	13 in		
d	48 in		
l	12 ft		
f'_c	8 ksi		
f_y	60 ksi		
ϕ	0.85		
bundle d	4 in		
diag. cover	3 in		
α	0.26 rad		
$A_{vd} \geq$	10.2 in ²	USE	7 #11 A_{vd} 10.9 in ²
		nX	4
		nY	3
Clear Cover	1.5 in		
b_{cx}	10 in		
b_{cy}	45 in		
Conf. Bar	#6	d	0.75 in
nX_skin	3		
nY_skin	7		
h_x	3.9 in	< 8 in	
h_y	6.6 in	< 8 in	
<u>X-Direction</u>		<u>Y-Direction</u>	
s1	11.0 in	s1	5.7 in
s2	8.5 in	s2	4.4 in
s3	6.0 in	s3	6.0 in
s4	9.4 in	s4	9.4 in
Use s	6.0 in	Use s	4.4 in
Anchorage			
K_{tr}	2.5		
all ψ	1.3		
l_d	36.9 in		
1.25 l_d	46.1 in		
if using headed bars			
l_{dt}	15.1 in		
1.25 l_{dt}	18.9 in		

Solid-Direction						
Wall Pier		Story	7			Ω_0
						2.5
<u>Comp. Pier</u>			<u>Tension Pier</u>			
M_u	21271 k-ft		M_u	21271 k-ft		
C_u	845 kips		T_u	845 kips		
l_w	16 ft		l_w	16 ft		
l_f	5 ft		l_f	5 ft		
t_w	12 in		t_w	12 in		
t_f	13 in		t_f	13 in		
ϕ	0.90		ϕ	0.90		
f_y	60.0 ksi					
f_c	8.0 ksi					
<u>Interior Bnd</u>		in	# Layer	Spacing	# Layer	BE L
A_s	22.9 in ²		4	5	1.50	9.0 38
Use	45	#7	Provided A_s		27 in²	Check P-M to Verify
<u>Exterior Bnd</u>		in	# Layer	Spacing	# Layer	BE L
A_s	22.9 in ²		4	5	1.50	9.0 38
Use	45	#7	Provided A_s		27 in²	Check P-M to Verify
Shear						
<u>Comp. Pier</u>			<u>Tension Pier</u>			
h_w	117 ft		h_w	117 ft		
f_y	60.0 ksi		f_y	60.0 ksi		
V_u	651.2 kips		V_u	651.2 kips		
ω_v	1.24		ω_v	1.24		
n_{story}	9		n_{story}	9		
n_s	9.0		n_s	9.0		
Ω_v	1.50		Ω_v	1.50		
V_e	1211 kips		V_e	1211 kips		
ϕ	0.75		ϕ	0.75		
ϕV_c	309.1 kips		ϕV_c	309.1 kips		
ρ_t	0.0087		ρ_t	0.0087		
Need	2 curtain of #6		Need	2 curtain of #6		
@	8.4 in		@	8.4 in		
Use	2 curtain of #6		Use	2 curtain of #6		
@	8 in		@	8 in		
ϕV_n	1260 kips	OK	ϕV_n	1260 kips	OK	
<u>Vertical Web Bar</u>						
$\rho_{l,min}$	0.0025		$\rho_{l,min}$	0.0025		
Need min of	2 curtain of #5		Need min of	2 curtain of #5		
	@ 20.7 in			@ 20.7 in		
Use	2 curtain of #5		Use	2 curtain of #5		
@	12 in		@	12 in		



B.4. 9-Story ACI 318-25 and Rojas and Wallace 2022 Shear Equation

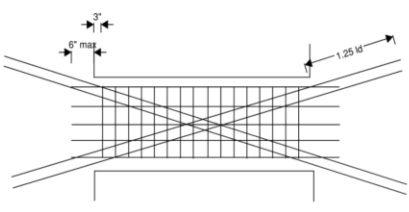
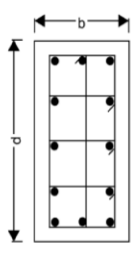
Coupled-Direction									
Wall Pier		Story		1		Ω_0		2.5	
<u>Comp. Pier</u>			<u>Tension Pier</u>						
M_u	4215 k-ft		M_u	4271 k-ft					
C_u	4786 kips		T_u	-2722 kips					
l_w	5 ft		l_w	5 ft					
l_f	16 ft		l_f	16 ft					
t_w	23 in		t_w	23 in					
t_f	12 in		t_f	12 in					
ϕ	0.65		ϕ	0.90					
f_y	60.0 ksi								
f_c	8.0 ksi								
<u>Interior Bnd</u>			in	# Layer	Spacing	# Layer	BE L		
A_s	19.5 in ²		4	3	8.50	5.0	22		
Use	15	#11	Provided A_s		23.4 in²	Check P-M to Verify			
<u>Exterior Bnd</u>			in	# Layer	Spacing	# Layer	BE L		
A_s	45.0 in ²		4	3	8.50	20.0	82		
Use	60	#11	Provided A_s		93.6 in²	Check P-M to Verify			
	9	8	L-in Fln'g		74 L-in Web	34.00			
<u>Vertical Web Bar</u>									
$\rho_{l,min}$	0.0025		$\rho_{l,min}$	0.0025					
Need min of	2	curtain of #6	Need min of	2	curtain of #6				
	@	15.3 in		@	15.3 in				
Use	2	curtain of #6	Use	2	curtain of #6				
	@	12 in		@	12 in				



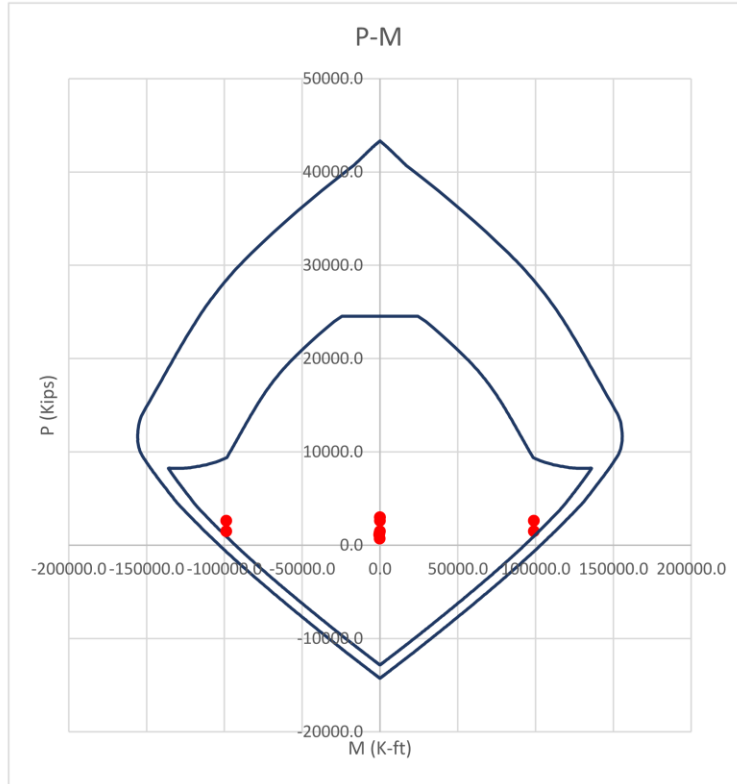
Wall Pier - Shear

Comp. Pier		Tension Pier	
f_y	60.0 ksi	f_y	60.0 ksi
f_c	8.0 ksi	f_c	8.0 ksi
n_{story}	9	n_{story}	9
h_w	117 ft	h_w	117 ft
t_w	23 in	t_w	23 in
l_w	5 ft	l_w	5 ft
t_{fl}	12 in	t_{fl}	12 in
b_{fl}	8 ft	b_{fl}	0 ft
P_U	4786 kips		kips
V_U	483 kips		kips
M_U	4215 k-ft	M_U	4271 k-ft
Ω_v	1.50	Ω_v	1.50
n_s	9.0	n_s	9.0
ω_v	1.24	ω_v	1.24
V_e	898 kips	V_e	898 kips
ϕ	0.75	ϕ	0.75
ρ_{sb}	1.70%	ρ_{sb}	6.78%
α_{shape}	1.50	α_{shape}	1.00
$V_{n,lim}$	1851 kips	$V_{n,lim}$	1234 kips
$\alpha_{c,p}$	0.177	$\alpha_{c,p}$	0.020
$\alpha_{s,p}$	0.357	$\alpha_{s,p}$	0.355
ϕV_c	1462 kips	ϕV_c	165 kips
ρ_{wh}	0.25%	ρ_{wh}	0.25%
	Need 2 curtain of #5	Need 2 curtain of #5	
	@ 10.8 in	@ 10.8 in	
	Use 2 curtain of #5	Use 2 curtain of #5	
	@ 10 in	@ 10 in	
ϕV_n	1389 kips	ϕV_n	926 kips
$V_e/\phi V_n$	0.647	$V_e/\phi V_n$	0.970
	OK		OK

* no flange in compression

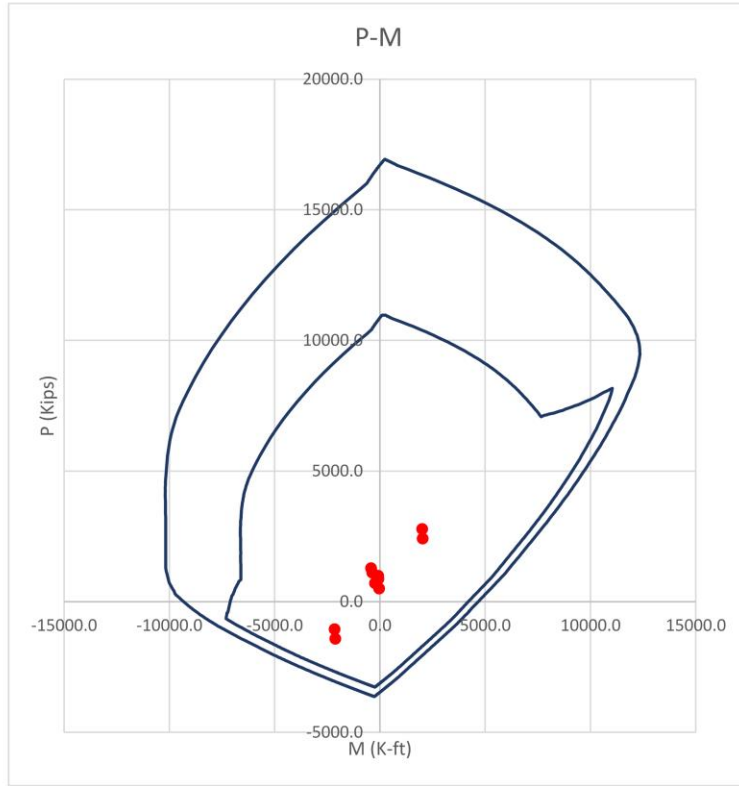
Coupling Beam		Story	2
V_u	502.4 kips	$V_u/(A_g \sqrt{f'_c})$	5.1 < 10
b	23 in		
d	48 in		
l	12 ft		
f'_c	8 ksi		
f_y	60 ksi		
ϕ	0.85		
bundle d	4 in		
diag. cover	3 in		
α	0.26 rad		
			
$A_{vd} \geq$	19.3 in ²	USE	12 #11 A_{vd} 18.7 in ²
		nX	4
		nY	3
Clear Cover	1.5 in		
b_{cx}	20 in		
b_{cy}	45 in		
Conf. Bar	#6	d	0.75 in
nX_skin	3		
nY_skin	7		
h_x	8.9 in	< 8 in	
h_y	6.6 in	< 8 in	
			
<u>X-Direction</u>		<u>Y-Direction</u>	
s1	5.5 in	s1	5.7 in
s2	7.3 in	s2	7.5 in
s3	6.0 in	s3	6.0 in
s4	9.4 in	s4	9.4 in
Use s	5.5 in	Use s	5.7 in
Anchorage			
K_{tr}	2.5		
all ψ	1.3		
l_d	36.9 in		
1.25 l_d	46.1 in		
if using headed bars			
l_{dt}	15.1 in		
1.25 l_{dt}	18.9 in		

Solid-Direction						
Wall Pier	Story 1			Ω_0	2.5	
<u>Comp. Pier</u>			<u>Tension Pier</u>			
M_u	98813	k-ft	M_u	98813	k-ft	
C_u	2625	kips	T_u	2625	kips	
l_w	16	ft	29 l_w	16	ft	
l_f	5	ft	l_f	5	ft	
t_w	12	in	t_w	12	in	
t_f	23	in	t_f	23	in	
ϕ	0.90		ϕ	0.90		
f_y	60.0	ksi				
f_c	8.0	ksi				
<u>Interior Bnd</u>						
A_s	118.7	in ²	in # Layer	Spacing	# Layer	BE L
			4 5	1.50	15.0	62
Use	75	#11	Provided A_s	117 in²	Check P-M to Verify	
<u>Exterior Bnd</u>						
A_s	118.7	in ²	in # Layer	Spacing	# Layer	BE L
			4 5	1.50	15.0	62
Use	75	#11	Provided A_s	117 in²	Check P-M to Verify	
<u>Vertical Web Bar</u>						
$\rho_{l,min}$	0.0025		$\rho_{l,min}$	0.0025		
Need min of	2	curtain of #5	Need min of	2	curtain of #5	
	@	20.7 in		@	20.7 in	
Use	2	curtain of #5	Use	2	curtain of #5	
@	12 in		@	12 in		



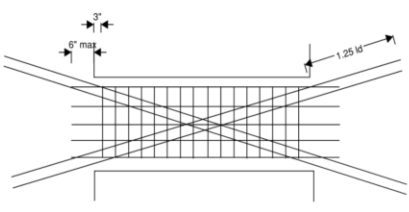
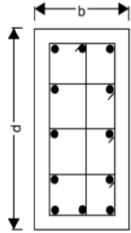
Wall Pier - Shear			
<u>Comp. Pier</u>		<u>Tension Pier</u>	
f_y	60.0 ksi	f_y	60.0 ksi
f_c	8.0 ksi	f_c	8.0 ksi
n_{story}	9	n_{story}	9
h_w	117 ft	h_w	117 ft
t_w	12 in	t_w	12 in
l_w	16 ft	l_w	16 ft
t_{fl}	23 in	t_{fl}	23 in
b_{fl}	5 ft	b_{fl}	5 ft
P_U	2625 kips	P_U	2625 kips
V_u	1272 kips	V_u	1272 kips
M_u	98813 k-ft	M_u	98813 k-ft
Ω_v	1.40	Ω_v	1.40
n_s	9.0	n_s	9.0
ω_v	1.24	ω_v	1.24
V_e	2209 kips	V_e	2209 kips
ϕ	0.75	ϕ	0.75
ρ_{sb}	5.08%	ρ_{sb}	5.08%
α_{shape}	1.50	α_{shape}	1.50
$V_{n,lim}$	3091 kips	$V_{n,lim}$	3091 kips
$\alpha_{c,p}$	0.025	$\alpha_{c,p}$	0.025
$\alpha_{s,p}$	0.254	$\alpha_{s,p}$	0.254
ϕV_c	348 kips	ϕV_c	348 kips
ρ_{wh}	1.99%	ρ_{wh}	1.99%
	Need 3 curtain of #6		Need 3 curtain of #6
	@ 5.5 in		@ 5.5 in
	Use 3 curtain of #6		Use 3 curtain of #6
	@ 5.5 in		@ 5.5 in
ϕV_n	2210 kips	ϕV_n	2210 kips
$V_e/\phi V_n$	0.999	OK $V_e/\phi V_n$	0.999 OK

Coupled-Direction									
Wall Pier		Story		4		Ω_0		2.5	
<u>Comp. Pier</u>					<u>Tension Pier</u>				
M_u	2003	k-ft	M_u	2119	k-ft	T_u	-1418	kips	
C_u	2786	kips	T_u	-1418	kips	l_w	5	ft	
l_w	5	ft	l_w	5	ft	l_f	16	ft	
l_f	16	ft	l_f	16	ft	t_w	18	in	
t_w	18	in	t_w	18	in	t_f	12	in	
t_f	12	in	t_f	12	in	ϕ	0.90		
ϕ	0.65		ϕ	0.90		f_y	60.0	ksi	
f_y	60.0	ksi	f_c	8.0	ksi				
f_c	8.0	ksi							
<u>Interior Bnd</u>									
A_s	9.3	in ²	in	# Layer	3	Spacing	# Layer	BE L	
				4	3	6.00	5.0	22	
Use	15	#8	Provided A_s	11.85	in²	Check P-M to Verify			
<u>Exterior Bnd</u>									
A_s	22.9	in ²	in	# Layer	3	Spacing	# Layer	BE L	
				4	3	6.00	20.0	82	
Use	60	#8	Provided A_s	47.4	in²	Check P-M to Verify			
	9	8	L-in Fl'n'g	54	L-in Web	34.00			
<u>Vertical Web Bar</u>									
$P_{l,min}$	0.0025		$P_{l,min}$	0.0025					
Need min of	2	curtain of #5	Need min of	2	curtain of #5				
	@	13.8 in		@	13.8 in				
Use	2	curtain of #5	Use	2	curtain of #5				
@	12 in		@	12 in					

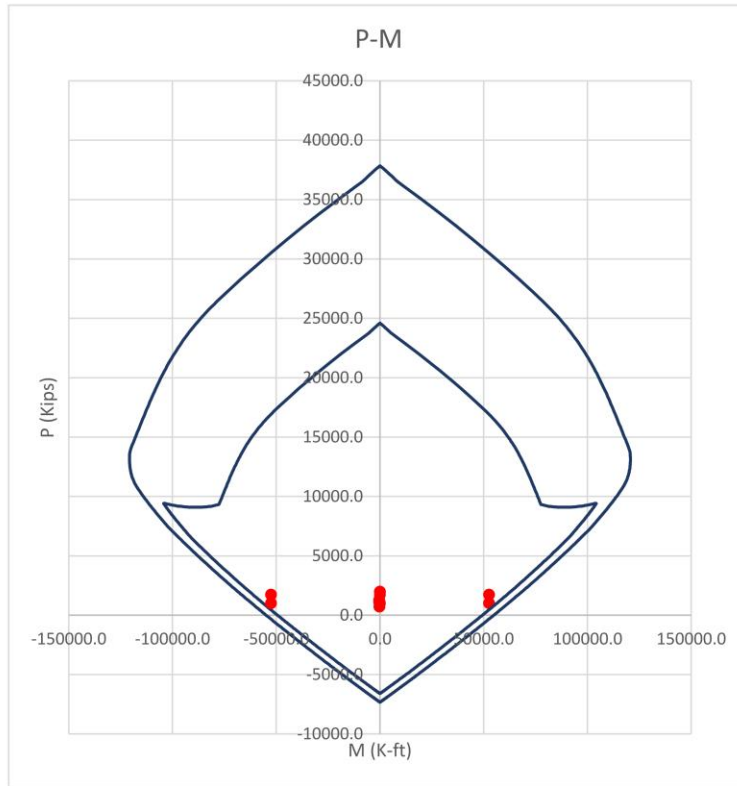


Wall Pier - Shear			
<u>Comp. Pier</u>		<u>Tension Pier</u>	
f_y	60.0 ksi	f_y	60.0 ksi
f_c	8.0 ksi	f_c	8.0 ksi
n_{story}	9	n_{story}	9
h_w	117 ft	h_w	117 ft
t_w	18 in	t_w	18 in
l_w	5 ft	l_w	5 ft
t_{fl}	12 in	t_{fl}	12 in
b_{fl}	8 ft	b_{fl}	0 ft
P_U	2786 kips	P_U	0 kips
V_U	380 kips	V_U	380 kips
M_U	2003 k-ft	M_U	2119 k-ft
Ω_v	1.50	Ω_v	1.50
n_s	9.0	n_s	9.0
ω_v	1.24	ω_v	1.24
V_e	706 kips	V_e	706 kips
ϕ	0.75	ϕ	0.75
ρ_{sb}	1.10%	ρ_{sb}	4.39%
α_{shape}	1.50	α_{shape}	1.00
$V_{n,lim}$	1449 kips	$V_{n,lim}$	966 kips
$\alpha_{c,p}$	0.160	$\alpha_{c,p}$	0.033
$\alpha_{s,p}$	0.422	$\alpha_{s,p}$	0.414
ϕV_c	1035 kips	ϕV_c	215 kips
ρ_{wh}	0.25%	ρ_{wh}	0.25%
	Need 2 curtain of #5	Need 2 curtain of #5	
	@ 13.8 in	@ 13.8 in	
	Use 2 curtain of #5	Use 2 curtain of #5	
	@ 12 in	@ 12 in	
ϕV_n	1087 kips	ϕV_n	724 kips
$V_e/\phi V_n$	0.650	$V_e/\phi V_n$	0.975
	OK		OK

* no flange in compression

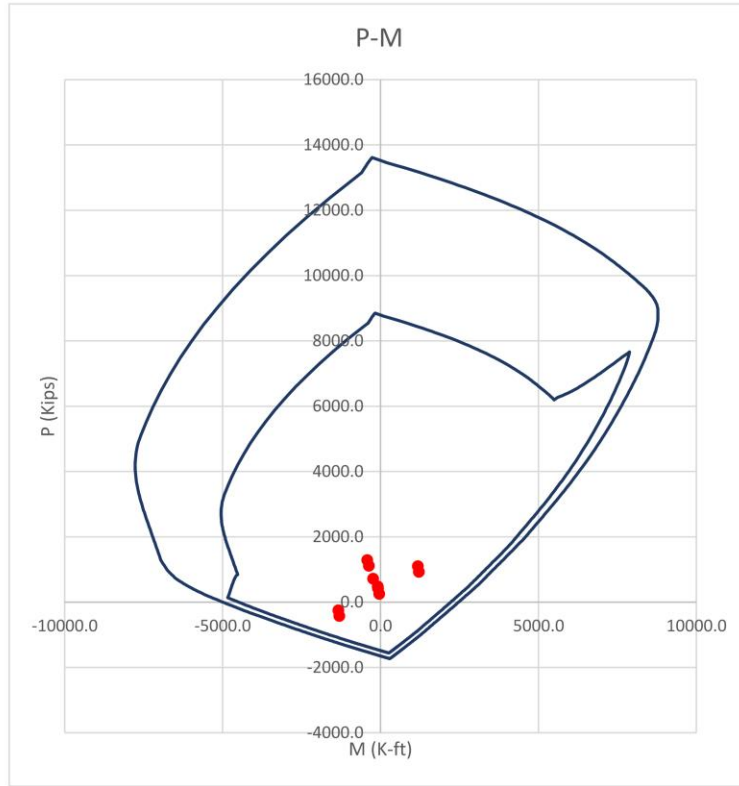
Coupling Beam		Story	4
V_u	413.5 kips	$V_u/(A_g \sqrt{f'_c})$	5.4 < 10
b	18 in		
d	48 in		
l	12 ft		
f'_c	8 ksi		
f_y	60 ksi		
ϕ	0.85		
bundle d	4 in		
diag. cover	3 in		
α	0.26 rad		
			
$A_{vd} \geq$	15.9 in ²	USE	10 #11 A_{vd} 15.6 in ²
		nX	4
		nY	3
Clear Cover	1.5 in		
b_{cx}	15 in		
b_{cy}	45 in		
Conf. Bar	#6	d	0.75 in
nX_skin	3		
nY_skin	7		
h_x	6.4 in	< 8 in	
h_y	6.6 in	< 8 in	
			
<u>X-Direction</u>		<u>Y-Direction</u>	
s1	7.3 in	s1	5.7 in
s2	7.9 in	s2	6.1 in
s3	6.0 in	s3	6.0 in
s4	9.4 in	s4	9.4 in
Use s	6.0 in	Use s	5.7 in
Anchorage			
K_{tr}	2.5		
all ψ	1.3		
l_d	36.9 in		
1.25 l_d	46.1 in		
if using headed bars			
l_{dt}	15.1 in		
1.25 l_{dt}	18.9 in		

Solid-Direction						
Wall Pier	Story			4	Ω_0	2.5
<u>Comp. Pier</u>			<u>Tension Pier</u>			
M_u	52577	k-ft	M_u	52577	k-ft	
C_u	1735	kips	T_u	1735	kips	
l_w	16	ft	29 l_w	16	ft	
l_f	5	ft	l_f	5	ft	
t_w	12	in	t_w	12	in	
t_f	24	in	t_f	24	in	
ϕ	0.90		ϕ	0.90		
f_y	60.0	ksi				
f_c	8.0	ksi				
<u>Interior Bnd</u>						
A_s	60.0	in ²	in # Layer	5	Spacing	# Layer BE L
			4		1.50	15.0 62
Use	75	#8	Provided A_s	59.25	in²	Check P-M to Verify
<u>Exterior Bnd</u>						
A_s	60.0	in ²	in # Layer	5	Spacing	# Layer BE L
			4		1.50	15.0 62
Use	75	#8	Provided A_s	59.25	in²	Check P-M to Verify
<u>Vertical Web Bar</u>						
$\rho_{l,min}$	0.0025		$\rho_{l,min}$	0.0025		
Need min of	2	curtain of #5	Need min of	2	curtain of #5	
	@	20.7 in		@	20.7 in	
Use	2	curtain of #5	Use	2	curtain of #5	
@	12 in		@	12 in		



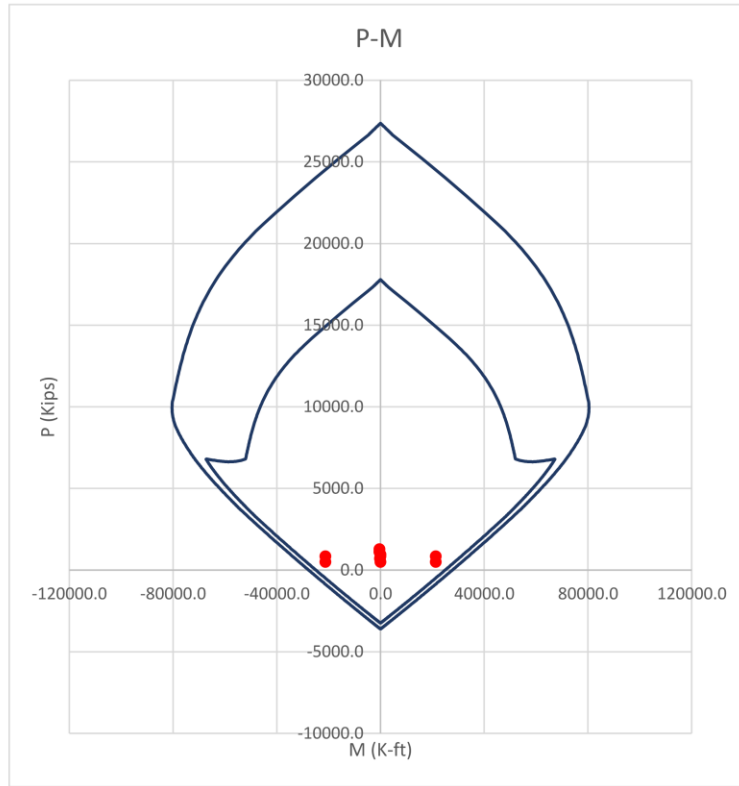
Wall Pier - Shear			
<u>Comp. Pier</u>		<u>Tension Pier</u>	
f_y	60.0 ksi	f_y	60.0 ksi
f_c	8.0 ksi	f_c	8.0 ksi
n_{story}	9	n_{story}	9
h_w	117 ft	h_w	117 ft
t_w	12 in	t_w	12 in
l_w	16 ft	l_w	16 ft
t_{fl}	24 in	t_{fl}	24 in
b_{fl}	5 ft	b_{fl}	5 ft
P_U	1735 kips	P_U	1735 kips
V_u	923 kips	V_u	923 kips
M_u	52577 k-ft	M_u	52577 k-ft
Ω_v	1.50	Ω_v	1.48
n_s	9.0	n_s	9.0
ω_v	1.24	ω_v	1.24
V_e	1718 kips	V_e	1695 kips
ϕ	0.75	ϕ	0.75
ρ_{sb}	2.57%	ρ_{sb}	2.57%
α_{shape}	1.50	α_{shape}	1.50
$V_{n,lim}$	3091 kips	$V_{n,lim}$	3091 kips
$\alpha_{c,p}$	0.023	$\alpha_{c,p}$	0.023
$\alpha_{s,p}$	0.281	$\alpha_{s,p}$	0.281
ϕV_c	317 kips	ϕV_c	317 kips
ρ_{wh}	2.23%	ρ_{wh}	2.15%
	Need 3 curtain of #6		Need 3 curtain of #6
	@ 4.9 in		@ 5.1 in
	Use 3 curtain of #6		Use 3 curtain of #6
	@ 4.5 in		@ 4.5 in
ϕV_n	1781 kips	ϕV_n	1781 kips
$V_e/\phi V_n$	0.964	OK $V_e/\phi V_n$	0.951 OK

Coupled-Direction									
Wall Pier		Story		7		Ω_0		2.5	
<u>Comp. Pier</u>					<u>Tension Pier</u>				
M_u	1180	k-ft	M_u	1303	k-ft				
C_u	1096	kips	T_u	-423	kips				
l_w	5	ft	l_w	5	ft				
l_f	16	ft	l_f	16	ft				
t_w	13	in	t_w	13	in				
t_f	12	in	t_f	12	in				
ϕ	0.90		ϕ	0.90					
f_y	60.0	ksi							
f_c	8.0	ksi							
<u>Interior Bnd</u>									
A_s	5.5	in ²	in	# Layer	Spacing	# Layer	BE	L	
			4	3	3.50	3.0	14		
Use	9		#7	Provided A_s	5.4 in²				Check P-M to Verify
<u>Exterior Bnd</u>									
A_s	9.9	in ²	in	# Layer	Spacing	# Layer	BE	L	
			4	3	3.50	14.0	58		
Use	42		#7	Provided A_s	25.2 in²				Check P-M to Verify
	9		8	L-in Fl'n'g	34 L-in Web		34.00		
<u>Vertical Web Bar</u>									
$\rho_{l,min}$	0.0025								$\rho_{l,min}$ 0.0025
Need min of	2	curtain of	#6						Need min of 2 curtain of #6
		@	27.1 in						@ 27.1 in
Use	2	curtain of	#6						Use 2 curtain of #6
@	12 in								@ 12 in



Wall Pier - Shear					
Comp. Pier			Tension Pier		
f_y	60.0 ksi		f_y	60.0 ksi	
f_c	8.0 ksi		f_c	8.0 ksi	
n_{story}	9		n_{story}	9	
h_w	117 ft		h_w	117 ft	
t_w	13 in		t_w	13 in	
l_w	5 ft		l_w	5 ft	
t_{fl}	12 in		t_{fl}	12 in	
b_{fl}	8 ft		b_{fl}	0 ft	* no flange in compression
P_U	1096 kips		P_U	0 kips	
V_U	270 kips		V_U	270 kips	
M_U	1180 k-ft		M_U	1303 k-ft	
Ω_v	1.50	3.12	Ω_v	1.50	2.92
n_s	9.0		n_s	9.0	
ω_v	1.24		ω_v	1.24	
V_e	502 kips		V_e	502 kips	
ϕ	0.75		ϕ	0.75	
ρ_{sb}	0.69%		ρ_{sb}	3.23%	
α_{shape}	1.50		α_{shape}	1.00	
$V_{n,lim}$	1046 kips		$V_{n,lim}$	698 kips	
$\alpha_{c,p}$	0.104		$\alpha_{c,p}$	0.038	
$\alpha_{s,p}$	0.449		$\alpha_{s,p}$	0.435	
ϕV_c	488 kips		ϕV_c	177 kips	
ρ_{wh}	0.25%		ρ_{wh}	0.25%	rho_prov.
	Need 2 curtain of #5		Need 2 curtain of #5	0.0040	
	@ 19.1 in		@ 19.1 in		
	Use 2 curtain of #5		Use 2 curtain of #5		
	@ 12 in		@ 12 in		
ϕV_n	660 kips		ϕV_n	523 kips	
$V_e/\phi V_n$	0.760	OK	$V_e/\phi V_n$	0.959	OK

Solid-Direction						
Wall Pier	Story 7			Ω_0 2.5		
<u>Comp. Pier</u>			<u>Tension Pier</u>			
M_u	21271	k-ft	M_u	21271	k-ft	
C_u	845	kips	T_u	845	kips	
l_w	16	ft	29 l_w	16	ft	
l_f	5	ft	l_f	5	ft	
t_w	12	in	t_w	12	in	
t_f	13	in	t_f	13	in	
ϕ	0.90		ϕ	0.90		
f_y	60.0	ksi				
f_c	8.0	ksi				
<u>Interior Bnd</u>						
A_s	22.9		in # Layer	5	Spacing	# Layer BE L
			4	1.50		2
Use	45	#7	Provided A_s	27 in²	Check P-M to Verify	
<u>Exterior Bnd</u>						
A_s	22.9 in ²		in # Layer	5	Spacing	# Layer BE L
			4	1.50	9.0	38
Use	45	#7	Provided A_s	27 in²	Check P-M to Verify	
<u>Vertical Web Bar</u>						
$\rho_{l,min}$	0.0025		$\rho_{l,min}$	0.0025		
Need min of	2	curtain of #5	Need min of	2	curtain of #5	
	@	20.7 in		@	20.7 in	
Use	2	curtain of #5	Use	2	curtain of #5	
@	12 in		@	12 in		

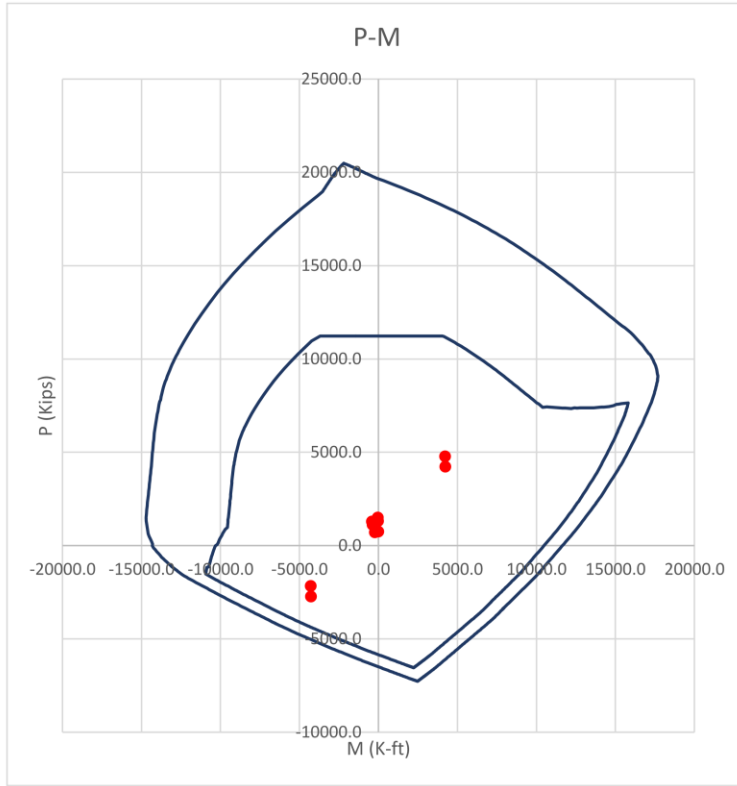


Wall Pier - Shear			
<u>Comp. Pier</u>		<u>Tension Pier</u>	
f_y	60.0 ksi	f_y	60.0 ksi
f_c	8.0 ksi	f_c	8.0 ksi
n_{story}	9	n_{story}	9
h_w	117 ft	h_w	117 ft
t_w	12 in	t_w	12 in
l_w	16 ft	l_w	16 ft
t_{fl}	13 in	t_{fl}	13 in
b_{fl}	5 ft	b_{fl}	5 ft
P_U	845 kips	P_U	845 kips
V_u	651 kips	V_u	651 kips
M_u	21271 k-ft	M_u	21271 k-ft
Ω_v	1.50	Ω_v	1.50
n_s	9.0	n_s	9.0
ω_v	1.24	ω_v	1.24
V_e	1211 kips	V_e	1211 kips
ϕ	0.75	ϕ	0.75
ρ_{sb}	1.17%	ρ_{sb}	1.17%
α_{shape}	1.25	α_{shape}	1.25
$V_{n,lim}$	2585 kips	$V_{n,lim}$	2585 kips
$\alpha_{c,p}$	0.027	$\alpha_{c,p}$	0.027
$\alpha_{s,p}$	0.339	$\alpha_{s,p}$	0.339
ϕV_c	376 kips	ϕV_c	376 kips
ρ_{wh}	1.21%	ρ_{wh}	1.21%
	Need 2 curtain of #6		Need 2 curtain of #6
	@ 6.1 in		@ 6.1 in
	Use 2 curtain of #6		Use 2 curtain of #6
	@ 6 in		@ 6 in
ϕV_n	1217 kips	ϕV_n	1217 kips
$V_e/\phi V_n$	0.995	OK	$V_e/\phi V_n$ 0.995 OK

Coupling Beam		Story	7
V_u	265.6 kips	$V_u / (A_g \sqrt{f'_c})$	4.8 < 10
b	13 in		
d	48 in		
l	12 ft		
f'_c	8 ksi		
f_y	60 ksi		
ϕ	0.85		
bundle d	4 in		
diag. cover	3 in		
α	0.26 rad		
$A_{vd} \geq$	10.2 in ²	USE	6 #11 A_{vd} 9.36 in ²
		nX	4
		nY	3
Clear Cover	1.5 in		
b_{cx}	10 in		
b_{cy}	45 in		
Conf. Bar	#6	d	0.75 in
nX_skin	3		
nY_skin	7		
h_x	3.9 in	< 8 in	
h_y	6.6 in	< 8 in	
<u>X-Direction</u>		<u>Y-Direction</u>	
s1	11.0 in	s1	5.7 in
s2	8.5 in	s2	4.4 in
s3	6.0 in	s3	6.0 in
s4	9.4 in	s4	9.4 in
Use s	6.0 in	Use s	4.4 in
Anchorage			
K_{tr}	2.5		
all ψ	1.3		
l_d	36.9 in		
1.25 l_d	46.1 in		
if using headed bars			
l_{dt}	15.1 in		
1.25 l_{dt}	18.9 in		

B.5. 9-Story ACI 318-25 and Rojas and Wallace 2022 Shear Equation – Considering Shear Distribution

Coupled-Direction										
Wall Pier	Story			1				Ω_0	2.5	
<u>Comp. Pier</u>					<u>Tension Pier</u>					
M_u	4215	k-ft			M_u	4271	k-ft			
C_u	4786	kips			T_u	-2722	kips			
l_w	5	ft			l_w	5	ft			
l_f	16	ft			l_f	16	ft			
t_w	19	in			t_w	19	in			
t_f	12	in			t_f	12	in			
ϕ	0.65				ϕ	0.90				
f_y	60.0	ksi								
f_c	8.0	ksi								
<u>Interior Bnd</u>										
A_s	19.5	in ²	4	# Layer	5	Spacing	3.25	# Layer	5.0	BE L
Use	25		#11	Provided A_s	39 in²					Check P-M to Verify
<u>Exterior Bnd</u>										
A_s	45.0	in ²	4	# Layer	3	Spacing	6.50	# Layer	16.7	BE L
Use	50		#11	Provided A_s	78 in²					Check P-M to Verify
	9		8	L-in Fln'g			58 L-in Web			34.00
<u>Vertical Web Bar</u>										
$\rho_{l,min}$	0.0025				$\rho_{l,min}$	0.0025				
Need min of	2	curtain of	#6		Need min of	2	curtain of	#6		
	@	18.5	in			@	18.5	in		
Use	2	curtain of	#6		Use	2	curtain of	#6		
	@	12	in			@	12	in		



Wall Pier - Shear

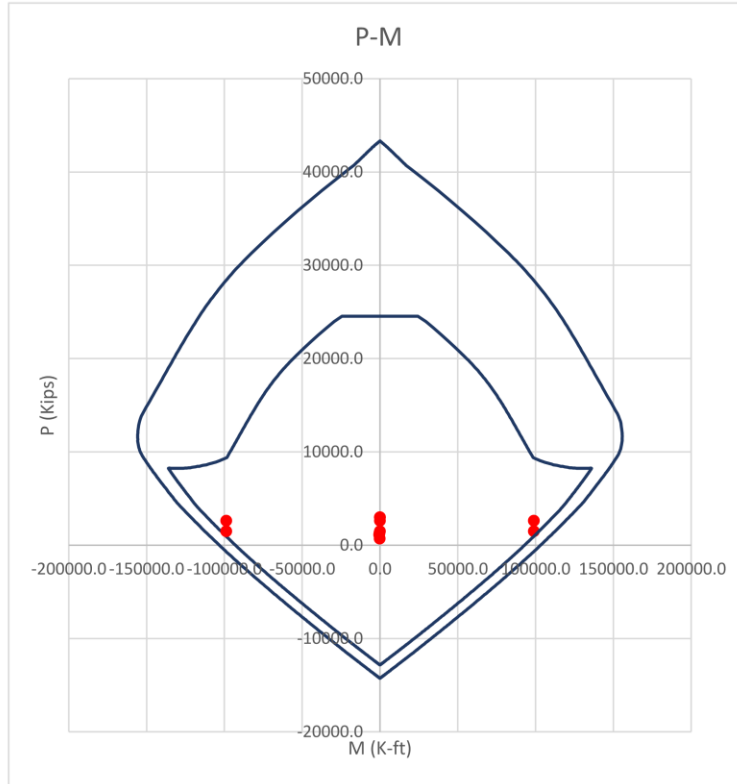
Comp. Pier		Tension Pier		
f_y	60.0 ksi	f_y	60.0 ksi	
f_c	8.0 ksi	f_c	8.0 ksi	
n_{story}	9	n_{story}	9	
h_w	117 ft	h_w	117 ft	
t_w	19 in	t_w	19 in	
l_w	5 ft	l_w	5 ft	
t_{fl}	12 in	t_{fl}	12 in	
b_{fl}	8 ft	b_{fl}	0 ft	* no flange in compression
P_U	4786 kips		kips	
V_U	595 kips		kips	
M_U	4215 k-ft	M_U	4271 k-ft	
Ω_v	1.50	Ω_v	1.50	
n_s	9.0	n_s	9.0	
ω_v	1.24	ω_v	1.24	
V_e	1106 kips	V_e	690 kips	
ϕ	0.75	ϕ	0.75	
ρ_{sb}	3.42%	ρ_{sb}	6.84%	
α_{shape}	1.50	α_{shape}	1.00	
$V_{n,lim}$	1529 kips	$V_{n,lim}$	1020 kips	
$\alpha_{c,p}$	0.245	$\alpha_{c,p}$	0.013	
$\alpha_{s,p}$	0.383	$\alpha_{s,p}$	0.326	
ϕV_c	1677 kips	ϕV_c	91 kips	
ρ_{wh}	0.25%	ρ_{wh}	0.25%	
Need	2 curtain of #5	Need	2 curtain of #5	
@	13.1 in	@	13.1 in	
Use	2 curtain of #5	Use	2 curtain of #5	
@	12 in	@	12 in	
ϕV_n	1147 kips	ϕV_n	765 kips	
$V_e/\phi V_n$	0.964	OK $V_e/\phi V_n$	0.903	OK

Wall Pier - Shear Distribution

M_{TP}	-9773 k-ft
M_{CP}	15657 k-ft
Comp. Pier Shear Ratio	0.62
Tens. Pier Shear Ratio	0.38

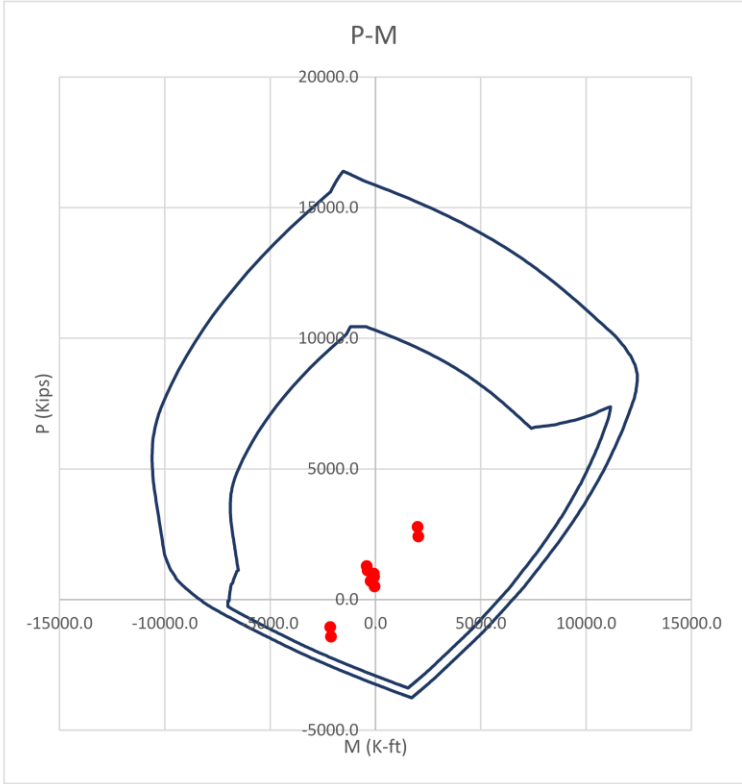
Coupling Beam		Story	2
V_u	502.4 kips	$V_u/(A_g \sqrt{f'_c})$	6.2 < 10
b	19 in		
d	48 in		
l	12 ft		
f'_c	8 ksi		
f_y	60 ksi		
ϕ	0.85		
bundle d	4 in		
diag. cover	3 in		
α	0.26 rad		
$A_{vd} \geq$	19.3 in ²	USE	12 #11 A_{vd} 18.7 in ²
		nX	4
		nY	3
Clear Cover	1.5 in		
b_{cx}	16 in		
b_{cy}	45 in		
Conf. Bar	#6	d	0.75 in
nX_skin	3		
nY_skin	7		
h_x	6.9 in	< 8 in	
h_y	6.6 in	< 8 in	
<u>X-Direction</u>		<u>Y-Direction</u>	
s1	6.9 in	s1	5.7 in
s2	7.7 in	s2	6.4 in
s3	6.0 in	s3	6.0 in
s4	9.4 in	s4	9.4 in
Use s	6.0 in	Use s	5.7 in
Anchorage			
K_{tr}	2.5		
all ψ	1.3		
M_{TP}	36.9 in		
M_{CP}	46.1 in		
if using headed bars			
l_{dt}	15.1 in		

Solid-Direction									
Wall Pier		Story		1		Ω_0		2.5	
<u>Comp. Pier</u>					<u>Tension Pier</u>				
M_u	98813	k-ft	M_u	98813	k-ft				
C_u	2625	kips	T_u	2625	kips				
l_w	16	ft	l_w	16	ft				
l_f	5	ft	l_f	5	ft				
t_w	12	in	t_w	12	in				
t_f	19	in	t_f	19	in				
ϕ	0.90		ϕ	0.90					
f_y	69.0	ksi							
f_c	10.4	ksi							
<u>Interior Bnd</u>			in	# Layer	Spacing	# Layer	BE L		rho
A_s	103.2	in ²		4	5	1.50	15.0	62	0.1573
Use	75	#11		Provided A_s		117 in²		Check P-M to Verify	
<u>Exterior Bnd</u>			in	# Layer	Spacing	# Layer	BE L		rho
A_s	103.2	in ²		4	5	1.50	15.0	62	0.1573
Use	75	#11		Provided A_s		117 in²		Check P-M to Verify	
<u>Vertical Web Bar</u>									
$\rho_{l,min}$	0.0025		$\rho_{l,min}$	0.0025					rho_prov.
Need min of	2	curtain of #5	Need min of	2	curtain of #5				0.0043
	@	20.7 in		@	20.7 in				
Use	2	curtain of #5	Use	2	curtain of #5				
@	12 in		@	12 in					



Wall Pier - Shear			
<u>Comp. Pier</u>		<u>Tension Pier</u>	
f_y	60.0 ksi	f_y	60.0 ksi
f_c	8.0 ksi	f_c	8.0 ksi
n_{story}	9	n_{story}	9
h_w	117 ft	h_w	117 ft
t_w	12 in	t_w	12 in
l_w	16 ft	l_w	16 ft
t_{fl}	23 in	t_{fl}	23 in
b_{fl}	5 ft	b_{fl}	5 ft
P_U	2625 kips	P_U	2625 kips
V_u	1272 kips	V_u	1272 kips
M_u	98813 k-ft	M_u	98813 k-ft
Ω_v	1.40	Ω_v	1.40
n_s	9.0	n_s	9.0
ω_v	1.24	ω_v	1.24
V_e	2209 kips	V_e	2209 kips
ϕ	0.75	ϕ	0.75
ρ_{sb}	5.08%	ρ_{sb}	5.08%
α_{shape}	1.50	α_{shape}	1.50
$V_{n,lim}$	3091 kips	$V_{n,lim}$	3091 kips
$\alpha_{c,p}$	0.025	$\alpha_{c,p}$	0.025
$\alpha_{s,p}$	0.254	$\alpha_{s,p}$	0.254
ϕV_c	348 kips	ϕV_c	348 kips
ρ_{wh}	1.99%	ρ_{wh}	1.99%
	Need 3 curtain of #6		Need 3 curtain of #6
	@ 5.5 in		@ 5.5 in
	Use 3 curtain of #6		Use 3 curtain of #6
	@ 5.5 in		@ 5.5 in
ϕV_n	2210 kips	ϕV_n	2210 kips
$V_e/\phi V_n$	0.999	OK	$V_e/\phi V_n$ 0.999 OK

Coupled-Direction									
Wall Pier		Story		4		Ω_0		2.5	
<u>Comp. Pier</u>					<u>Tension Pier</u>				
M_u	2003	k-ft	M_u	2119	k-ft	T_u	-1418	kips	
C_u	2786	kips	T_u	-1418	kips	I_w	5	ft	
I_w	5	ft	I_w	5	ft	I_f	16	ft	
I_f	16	ft	I_f	16	ft	t_w	16	in	
t_w	16	in	t_w	16	in	t_f	12	in	
t_f	12	in	t_f	12	in	ϕ	0.90		
ϕ	0.65		ϕ	0.90		f_y	60.0	ksi	
f_y	60.0	ksi	f_c	8.0	ksi				
f_c	8.0	ksi							
<u>Interior Bnd</u>									
A_s	9.3	in ²	in	# Layer	5	Spacing	# Layer	5.0	BE L
Use	25	#8	Provided A_s	19.75	in²	Check P-M to Verify			
<u>Exterior Bnd</u>									
A_s	22.9	in ²	in	# Layer	3	Spacing	# Layer	16.7	BE L
Use	50	#8	Provided A_s	39.5	in²	Check P-M to Verify			
	9	8	L-in Fl'n'g	46	L-in Web	34.00			
<u>Vertical Web Bar</u>									
$\rho_{l,min}$	0.0025		$\rho_{l,min}$	0.0025					
Need min of	2	curtain of #5	Need min of	2	curtain of #5				
	@	15.5 in		@	15.5 in				
Use	2	curtain of #5	Use	2	curtain of #5				
@	12 in		@	12 in					

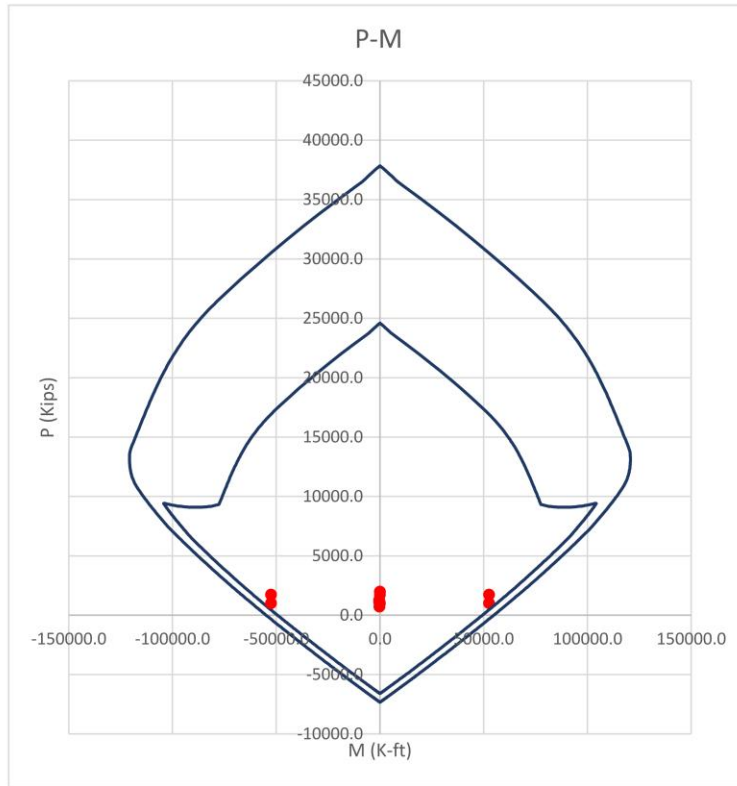


Wall Pier - Shear

Comp. Pier		Tension Pier	
f_y	60.0 ksi	f_y	60.0 ksi
f_c	8.0 ksi	f_c	8.0 ksi
n_{story}	9	n_{story}	9
h_w	117 ft	h_w	117 ft
t_w	16 in	t_w	16 in
l_w	5 ft	l_w	5 ft
t_{fl}	12 in	t_{fl}	12 in
b_{fl}	8 ft	b_{fl}	0 ft
P_U	2786 kips	P_U	0 kips
V_U	490 kips	V_U	270 kips
M_U	2003 k-ft	M_U	2119 k-ft
Ω_v	1.50	Ω_v	1.50
n_s	9.0	n_s	9.0
ω_v	1.24	ω_v	1.24
V_e	911 kips	V_e	501 kips
ϕ	0.75	ϕ	0.75
ρ_{sb}	2.06%	ρ_{sb}	4.11%
α_{shape}	1.50	α_{shape}	1.00
$V_{n,lim}$	1288 kips	$V_{n,lim}$	859 kips
$\alpha_{c,p}$	0.202	$\alpha_{c,p}$	0.023
$\alpha_{s,p}$	0.460	$\alpha_{s,p}$	0.370
ϕV_c	1162 kips	ϕV_c	133 kips
ρ_{wh}	0.25%	ρ_{wh}	0.25%
	Need 2 curtain of #5		Need 2 curtain of #5
	@ 15.5 in		@ 15.5 in
	Use 2 curtain of #5		Use 2 curtain of #5
	@ 12 in		@ 12 in
ϕV_n	966 kips	ϕV_n	644 kips
$V_e/\phi V_n$	0.943	$V_e/\phi V_n$	0.779
	OK		OK

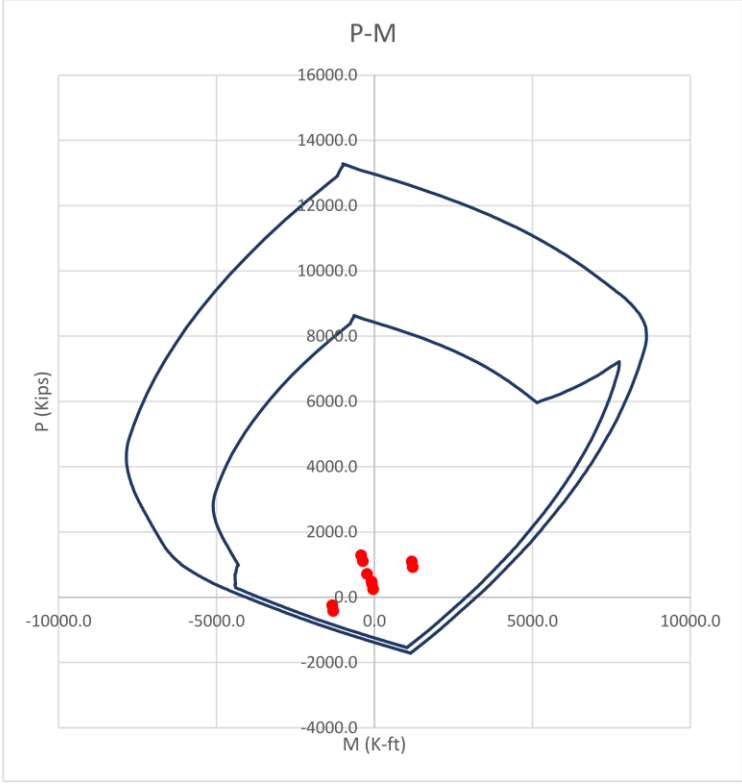
* no flange in compression

Solid-Direction									
Wall Pier		Story		4		Ω_0		2.5	
<u>Comp. Pier</u>					<u>Tension Pier</u>				
M_u	52577	k-ft	M_u	52577	k-ft				
C_u	1735	kips	T_u	1735	kips				
l_w	16	ft	l_w	16	ft				
l_f	5	ft	l_f	5	ft				
t_w	12	in	t_w	12	in				
t_f	20	in	t_f	20	in				
ϕ	0.90		ϕ	0.90					
f_y	60.0	ksi							
f_c	8.0	ksi							
<u>Interior Bnd</u>			in	# Layer	Spacing	# Layer	BE L		rho
A_s	60.0	in ²		4	5	1.50	15.0	62	0.0796
Use	75	#8		Provided A_s	59.25	in²		Check P-M to Verify	
<u>Exterior Bnd</u>			in	# Layer	Spacing	# Layer	BE L		rho
A_s	60.0	in ²		4	5	1.50	15.0	62	0.0796
Use	75	#8		Provided A_s	59.25	in²		Check P-M to Verify	
<u>Vertical Web Bar</u>									
$\rho_{l,min}$	0.0025		$\rho_{l,min}$	0.0025					rho_prov.
Need min of	2	curtain of #5	Need min of	2	curtain of #5				0.0043
	@	20.7 in		@	20.7 in				
Use	2	curtain of #5	Use	2	curtain of #5				
@	12 in		@	12 in					



Wall Pier - Shear					
<u>Comp. Pier</u>			<u>Tension Pier</u>		
f_y	60.0 ksi		f_y	60.0 ksi	
f_c	8.0 ksi		f_c	8.0 ksi	
n_{story}	9		n_{story}	9	
h_w	117 ft		h_w	117 ft	
t_w	12 in		t_w	12 in	
l_w	16 ft		l_w	16 ft	
t_{fl}	24 in		t_{fl}	24 in	
b_{fl}	5 ft		b_{fl}	5 ft	
P_U	1735 kips		P_U	1735 kips	
V_u	923 kips		V_u	923 kips	
M_u	52577 k-ft		M_u	52577 k-ft	
Ω_v	1.50		Ω_v	1.48	
n_s	9.0		n_s	9.0	
ω_v	1.24		ω_v	1.24	
V_e	1718 kips		V_e	1695 kips	
ϕ	0.75		ϕ	0.75	
ρ_{sb}	2.57%		ρ_{sb}	2.57%	
α_{shape}	1.50		α_{shape}	1.50	
$V_{n,lim}$	3091 kips		$V_{n,lim}$	3091 kips	
$\alpha_{c,p}$	0.023		$\alpha_{c,p}$	0.023	
$\alpha_{s,p}$	0.281		$\alpha_{s,p}$	0.281	
ϕV_c	317 kips		ϕV_c	317 kips	
ρ_{wh}	2.23%		ρ_{wh}	2.15%	
	Need 3 curtain of #6		Need 3 curtain of #6		
	@ 4.9 in		@ 5.1 in		
	Use 3 curtain of #6		Use 3 curtain of #6		
	@ 4.5 in		@ 4.5 in		
ϕV_n	1781 kips		ϕV_n	1781 kips	
$V_e/\phi V_n$	0.964	OK	$V_e/\phi V_n$	0.951	OK

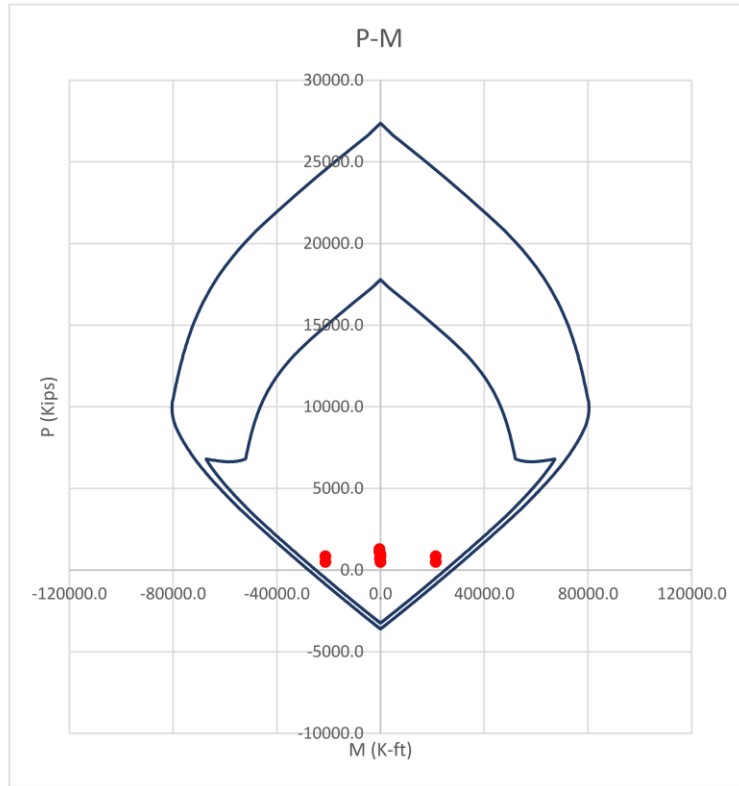
Coupled-Direction									
Wall Pier		Story		7		Ω_0		2.5	
<u>Comp. Pier</u>					<u>Tension Pier</u>				
M_u	1180	k-ft	M_u	1303	k-ft				
C_u	1096	kips	T_u	-423	kips				
l_w	5	ft	l_w	5	ft				
l_f	16	ft	l_f	16	ft				
t_w	12	in	t_w	12	in				
t_f	12	in	t_f	12	in				
ϕ	0.90		ϕ	0.90					
f_y	60.0	ksi							
f_c	8.0	ksi							
<u>Interior Bnd</u>									
A_s	5.5	in ²	in	# Layer	5	Spacing	# Layer	BE L	
				4		1.50	5.0	22	
Use	25		#7	Provided A_s		15 in²		Check P-M to Verify	
<u>Exterior Bnd</u>									
A_s	9.9	in ²	in	# Layer	3	Spacing	# Layer	BE L	
				4		3.00	16.7	68.66667	
Use	50		#7	Provided A_s		30 in²		Check P-M to Verify	
	9		8	L-in Fl'n'g		30 L-in Web		34.00	
<u>Vertical Web Bar</u>									
$\rho_{l,min}$	0.0025		$\rho_{l,min}$	0.0025					
Need min of	2	curtain of #5	Need min of	2	curtain of #5				
	@	20.7 in		@	20.7 in				
Use	2	curtain of #5	Use	2	curtain of #5				
@	12 in		@	12 in					



Wall Pier - Shear			
<u>Comp. Pier</u>		<u>Tension Pier</u>	
f_y	60.0 ksi	f_y	60.0 ksi
f_c	8.0 ksi	f_c	8.0 ksi
n_{story}	9	n_{story}	9
h_w	117 ft	h_w	117 ft
t_w	12 in	t_w	12 in
l_w	5 ft	l_w	5 ft
t_{fl}	12 in	t_{fl}	12 in
b_{fl}	8 ft	b_{fl}	0 ft
P_U	1096 kips	P_U	0 kips
V_U	325 kips	V_U	214 kips
M_U	1180 k-ft	M_U	1303 k-ft
Ω_v	1.50	Ω_v	1.50
n_s	9.0	n_s	9.0
ω_v	1.24	ω_v	1.24
V_e	604 kips	V_e	399 kips
ϕ	0.75	ϕ	0.75
ρ_{sb}	2.08%	ρ_{sb}	4.17%
α_{shape}	1.50	α_{shape}	1.00
$V_{n,lim}$	966 kips	$V_{n,lim}$	644 kips
$\alpha_{c,p}$	0.121	$\alpha_{c,p}$	0.031
$\alpha_{s,p}$	0.478	$\alpha_{s,p}$	0.403
ϕV_c	524 kips	ϕV_c	132 kips
ρ_{wh}	0.25%	ρ_{wh}	0.25%
	Need 2 curtain of #5	Need 2 curtain of #5	
	@ 20.7 in	@ 20.7 in	
	Use 2 curtain of #5	Use 2 curtain of #5	
	@ 12 in	@ 12 in	
ϕV_n	724 kips	ϕV_n	483 kips
$V_e/\phi V_n$	0.834	$V_e/\phi V_n$	0.826
	OK		OK

* no flange in compression

Solid-Direction									
Wall Pier		Story		7		Ω_0		2.5	
<u>Comp. Pier</u>					<u>Tension Pier</u>				
M_u	21271	k-ft	M_u	21271	k-ft				
C_u	845	kips	T_u	845	kips				
l_w	16	ft	l_w	16	ft				
l_f	5	ft	l_f	5	ft				
t_w	12	in	t_w	12	in				
t_f	12	in	t_f	12	in				
ϕ	0.90		ϕ	0.90					
f_y	60.0	ksi							
f_c	8.0	ksi							
<u>Interior Bnd</u>			in	# Layer	Spacing	# Layer	BE L		rho
A_s	22.9	in ²		4	5	1.50	15.0	62	0.0605
Use	75		#7	Provided A_s		45 in²		Check P-M to Verify	
<u>Exterior Bnd</u>			in	# Layer	Spacing	# Layer	BE L		rho
A_s	22.9	in ²		4	5	1.50	15.0	62	0.0605
Use	75		#7	Provided A_s		45 in²		Check P-M to Verify	
<u>Vertical Web Bar</u>									
$\rho_{l,min}$	0.0025		$\rho_{l,min}$	0.0025					rho_prov.
Need min of	2	curtain of #5	Need min of	2	curtain of #5				0.0043
	@	20.7 in		@	20.7 in				
Use	2	curtain of #5	Use	2	curtain of #5				
@	12 in		@	12 in					



Wall Pier - Shear			
<u>Comp. Pier</u>		<u>Tension Pier</u>	
f_y	60.0 ksi	f_y	60.0 ksi
f_c	8.0 ksi	f_c	8.0 ksi
n_{story}	9	n_{story}	9
h_w	117 ft	h_w	117 ft
t_w	12 in	t_w	12 in
l_w	16 ft	l_w	16 ft
t_{fl}	13 in	t_{fl}	13 in
b_{fl}	5 ft	b_{fl}	5 ft
P_U	845 kips	P_U	845 kips
V_u	651 kips	V_u	651 kips
M_u	21271 k-ft	M_u	21271 k-ft
Ω_v	1.50	Ω_v	1.50
n_s	9.0	n_s	9.0
ω_v	1.24	ω_v	1.24
V_e	1211 kips	V_e	1211 kips
ϕ	0.75	ϕ	0.75
ρ_{sb}	1.17%	ρ_{sb}	1.17%
α_{shape}	1.25	α_{shape}	1.25
$V_{n,lim}$	2585 kips	$V_{n,lim}$	2585 kips
$\alpha_{c,p}$	0.027	$\alpha_{c,p}$	0.027
$\alpha_{s,p}$	0.339	$\alpha_{s,p}$	0.339
ϕV_c	376 kips	ϕV_c	376 kips
ρ_{wh}	1.21%	ρ_{wh}	1.21%
	Need 2 curtain of #6		Need 2 curtain of #6
	@ 6.1 in		@ 6.1 in
	Use 2 curtain of #6		Use 2 curtain of #6
	@ 6 in		@ 6 in
ϕV_n	1217 kips	ϕV_n	1217 kips
$V_e/\phi V_n$	0.995	OK	$V_e/\phi V_n$ 0.995 OK

APPENDIX C - GROUND MOTION SELECTION

To evaluate different core wall design approaches and assess the effectiveness of the proposed method, this study employs nonlinear dynamic analysis on detailed numerical models subjected to carefully chosen and appropriately scaled ground motions. This appendix provides an in-depth exploration of the ground motion selection process.

In the domain of dynamic structural analysis, the primary goal is to anticipate how a structure responds when exposed to ground motions characterized by a specified spectral acceleration (S_a) at a particular period. These S_a values often represent significant levels, typically associated with a relatively low probability of occurrence, such as 10% or 2% over a 50-year span for the structure in question. Focusing exclusively on S_a at a single period proves advantageous due to its direct connection to a ground motion hazard curve, a product of the probabilistic seismic hazard analysis (PSHA) framework. Noteworthy contributions to this field include the studies of Bazzurro and Cornell (1994), Cornell et al. (2002), and Cornell and Krawinkler (2000). Prediction of structural responses primarily involves selecting ground motions that align with a predetermined target response spectrum, which subsequently serves as input for dynamic analysis.

In the pursuit of estimating structural responses by matching ground motions with a target response spectrum, it is important to identify the "representative" response spectrum corresponding to the specified site S_a value at a single period. The resulting target spectrum, derived through this approach referred to as the Conditional Mean Spectrum (CMS); This procedure, initially proposed by Baker and Cornell in 2006, forms the basis of the content in this appendix.

Moreover, this appendix presents a comprehensive listing of the selected ground motions and details the scale factors used in the dynamic analysis.

C.1. Procedure for Computing CMS

The central parameter in this procedure is the conditional mean parameter (ε), which represents the normalized residual derived from a ground motion model (attenuation model) prediction, defined as:

$$\varepsilon(T) = \frac{\ln(S_a(T)) - \mu_{\ln(S_a)}(M, R, T)}{\sigma_{\ln(S_a)}(T)}$$

To simplify this approach for easy replication, a systematic calculation procedure is presented in this section:

1. Identify the Target S_a at a Given Period and the Associated M , R , and ε :

To initiate the calculation, determine a target S_a value at a period of interest, denoted as T^* . Typically, T^* corresponds to the first-mode period of the structure under consideration but can be any period of interest. Additionally, identify the magnitude (M), distance (R), and $\varepsilon(T^*)$ values associated with the target $S_a(T^*)$. If the target $S_a(T^*)$ is obtained from Probabilistic Seismic Hazard Analysis (PSHA), the mean (M), distance (R), and $\varepsilon(T^*)$ values can be taken from the mean values obtained through deaggregation, as provided by the U.S. Geological Survey. If this calculation is for a scenario with specific M , R , and S_a , ε would be the number of standard deviations by which the target S_a exceeds the median prediction for the given M and R (often $\varepsilon = 1$ in deterministic evaluations of this kind, corresponding to "*median* + $1\sigma S_a$ ").

2. Compute the Mean and Standard Deviation of the Response Spectrum, Given M and

R :

Next, calculate the mean ($\mu_{\ln(S_a)}(M, R, T)$) and standard deviation ($\sigma_{\ln(S_a)}(T)$) of the natural logarithm of spectral acceleration values at all periods for the target M , R , etc., using existing ground-motion models or online calculation tools. (e.g., <http://www.opensha.org> or http://peer.berkeley.edu/products/rep_nga_models.html).

3. Compute ε at Other Periods, Given $\varepsilon(T^*)$:

Calculate the "conditional mean" ε for multiple periods but for various periods.

$$\mu_{\varepsilon(T_i)|\varepsilon(T^*)} = \rho(T_i, T^*)\varepsilon(T^*)$$

where, $\mu_{\varepsilon(T_i)|\varepsilon(T^*)}$, is the mean value of $\varepsilon(T_i)$, given $\varepsilon(T^*)$. Additionally, $\rho(T_{min}, T_{max})$, can be obtained from previous studies as below:

$$\rho(T_{min}, T_{max}) = 1 - \cos\left(\frac{\pi}{2} - \left[0.359 + 0.163I_{(T_{min} < 0.189)} \ln\left(\frac{T_{min}}{0.189}\right)\right] \ln\left(\frac{T_{max}}{T_{min}}\right)\right)$$

using the notation $I_{(T_{min} < 0.189)}$, we denote an indicator that is 1 when $T_{min} < 0.189s$ and 0 in other cases. In this context, T_{min} represents the shorter period, while T_{max} signifies the longer period of the two under consideration (Baker and Cornell 2006).

4. Compute Conditional Mean Spectrum (CMS):

Utilizing the mean and standard deviation from step 2 and the conditional mean ε values from step 3, compute the CMS. Substituting the mean value of $\varepsilon(T_i)$ from step 3 into the equation for $\ln(S_a(T))$ produces the corresponding conditional mean value of $\ln(S_a(T_i))$, given $\ln(S_a(T^*))$.

Ground-Motion Selection:

Once the CMS is computed, it can be employed to select ground motions for dynamic structural analysis. The CMS provides information about the mean spectral shape associated with the target $S_a(T^*)$. Ground motions that closely match this target spectral shape can be considered representative of ground motions with the target $S_a(T^*)$ value.

To identify ground motions that match a target CMS, one must first determine the period range over which the CMS should be matched. This range should ideally encompass all periods that significantly affect structural responses. It may include higher mode periods of vibration as well as longer periods that influence nonlinear structures with extended first-mode periods. A recommended period range is from $0.2T_1$ to $2.0T_1$, following ASCE 7-16.

To measure the similarity between ground motions and the target CMS, one effective criterion is the sum of squared errors (SSE) between the logarithms of the ground motion's spectrum and the target spectrum:

$$SSE = \sum_{j=1}^n \left(\ln \left(S_a(T_j) \right) - \ln \left(S_{a_{CMS}}(T_j) \right) \right)^2$$

Where $\ln \left(S_a(T_j) \right)$ represents the log spectral acceleration of the ground motion at period T_j , and $\ln \left(S_{a_{CMS}}(T_j) \right)$ is the log CMS value at period T_j . This equation should cover the period range determined earlier, as Baker and Cornell 2006 suggests, 50 values per order-of-magnitude of periods are sufficient for assessing ground motion similarity.

Ground motions matching the target CMS can be selected by evaluating the SSE equation for each ground motion under consideration, choosing those with the smallest SSE values. This approach is enhanced when ground motion scaling is considered. Scaling can be used to align ground motion spectral amplitudes with the target amplitude, facilitating the identification of ground motions that closely match the target. The scale factor for a ground motion can be determined in several ways. One method scales each ground motion so that its $S_a(T^*)$ matches the target $S_a(T^*)$ from the CMS, with the scale factor calculated as the ratio between the target and unscaled ground motion's $S_a(T^*)$.

This scaling approach is straightforward, ensures that ground motions match the target $S_a(T^*)$ precisely, and has minimal impact on the match to the target spectrum at other periods. It is the recommended scaling method for use with this procedure.

In addition to the CMS process of selecting and scaling the suites of ground motion, all motions undergo post-processing to ensure that the filter frequencies applied to the raw ground motions are appropriate. In the low-frequency range, this means the filter frequency is at least smaller than $1/1.25$ times the lowest considered frequency of the structure $\left(\frac{1}{1.25 \times 2T} \right)$, and in the high-frequency range, it is at least larger than $1.25/0.2T$ (see Figure C.1).

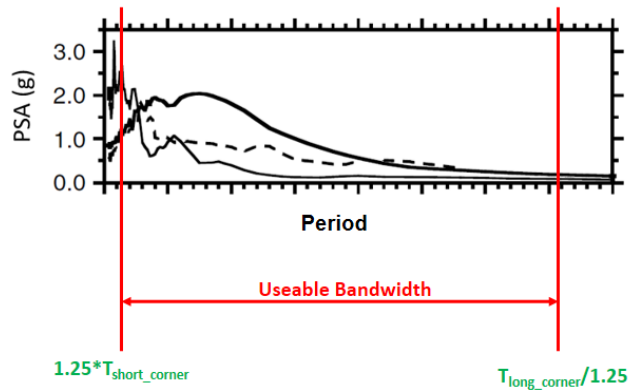


Figure C.1: Usable frequency (period) of ground motions (figure from Bozorgnia class notes).

C.2. Archetypes Mode Shapes and Modal Periods

To evaluate the seismic behavior of the archetypes, two suites of 13 ground motions have been defined. Each suite is conditioned on the average of the first and second modal periods of each archetype with the same number of stories. Figures C.2 through C.5 depict the mode shapes under consideration and their associated modal periods.

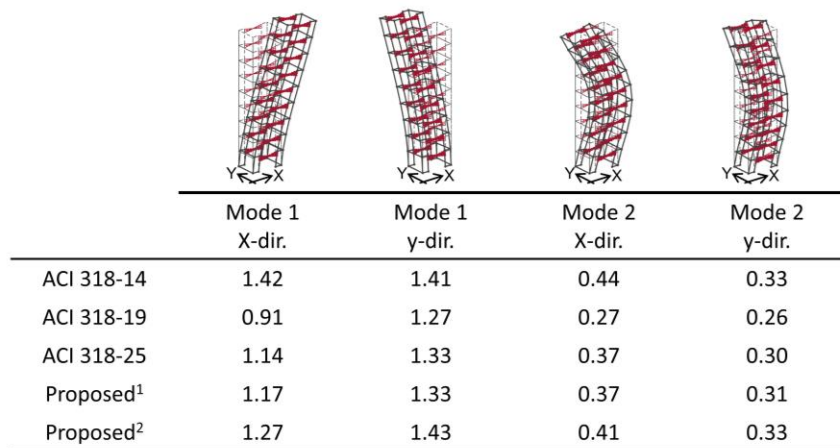


Figure C.2: 9-story archetypes mode shapes and their associated modal periods.

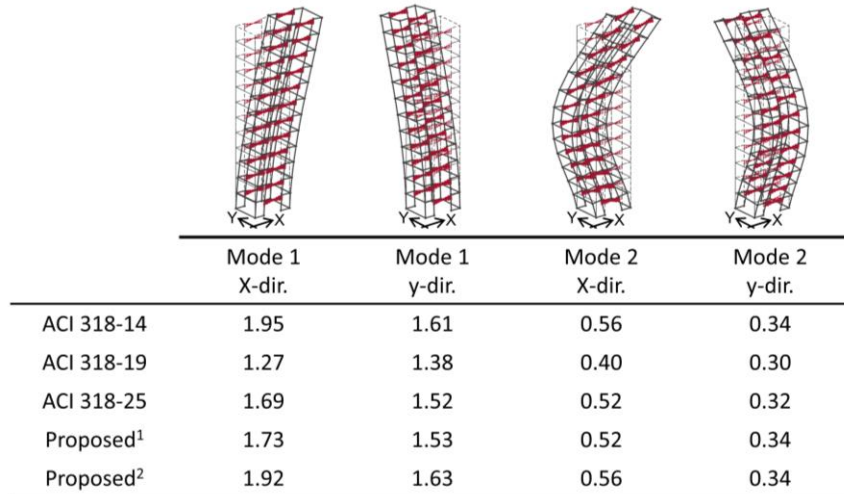


Figure C.3: 12-story archetypes mode shapes and their associated modal periods.

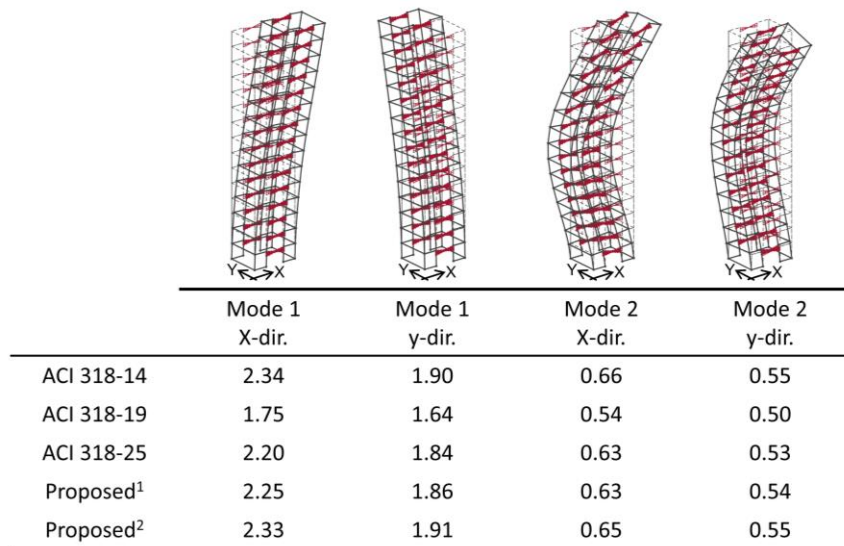


Figure C.4: 15-story archetypes mode shapes and their associated modal periods.

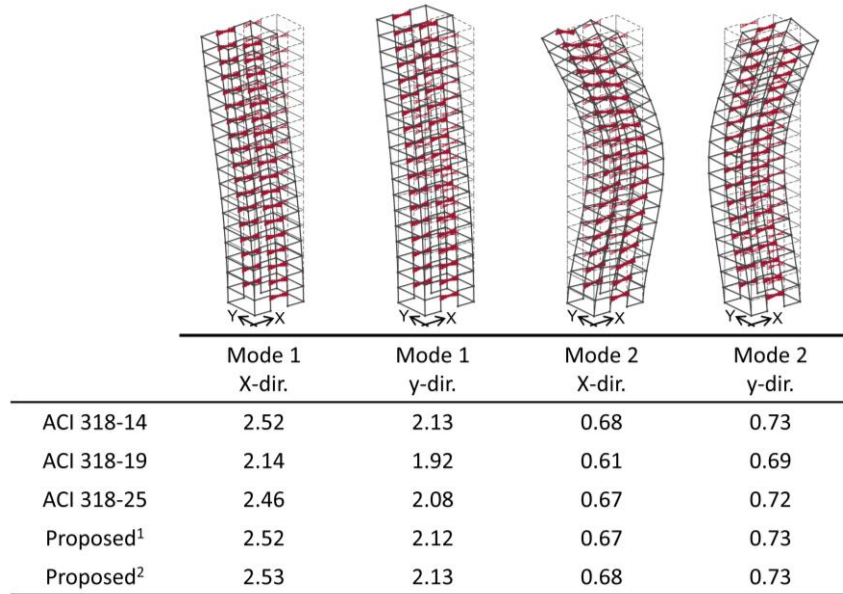


Figure C.5: 18-story archetypes mode shapes and their associated modal periods.

Table C.1. Considered modal periods and the period range in the ground motion selection procedure.

# Story	Mode 1			Mode 2		
	T	0.2T	2.0T	T	0.2T	2.0T
9-Story	1.27	0.25	2.54	0.34	0.07	0.67
12-Story	1.62	0.32	3.24	0.42	0.08	0.84
15-Story	2.00	0.40	4.01	0.58	0.12	1.15
18-Story	2.26	0.45	4.51	0.69	0.14	1.38

C.3. Selected ground motions

Figures C.6 through C.9 represent the response spectra of selected suites of ground motions conditioned to the first and second modes.

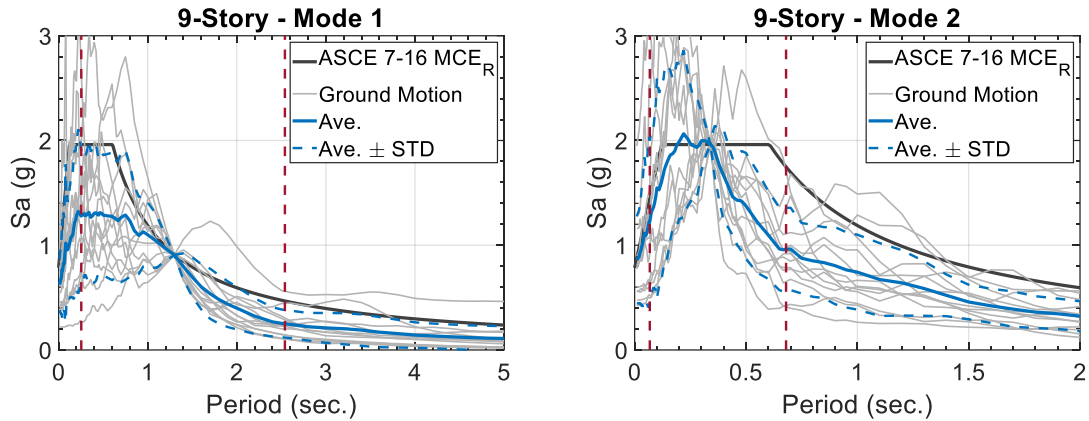


Figure C.6: RotD50 response spectra of selected suites of ground motions conditioned to first and second modes of 9-story archetypes.

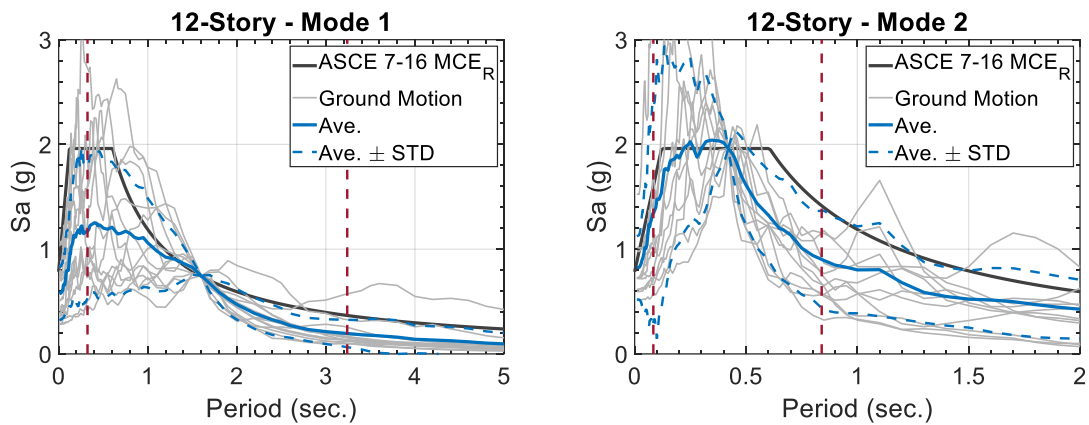


Figure C.7: RotD50 response spectra of selected suites of ground motions conditioned to first and second modes of 12-story archetypes.

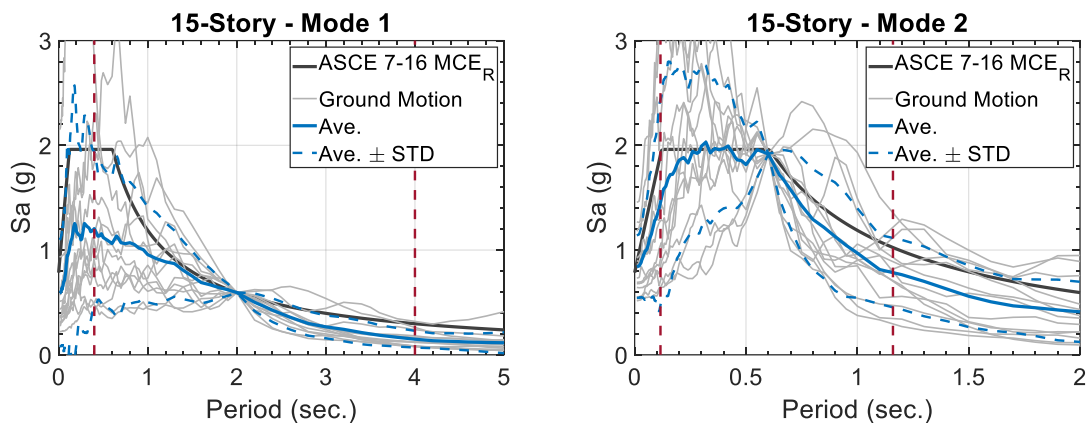


Figure C.8: RotD50 response spectra of selected suites of ground motions conditioned to first and second modes of 15-story archetypes.

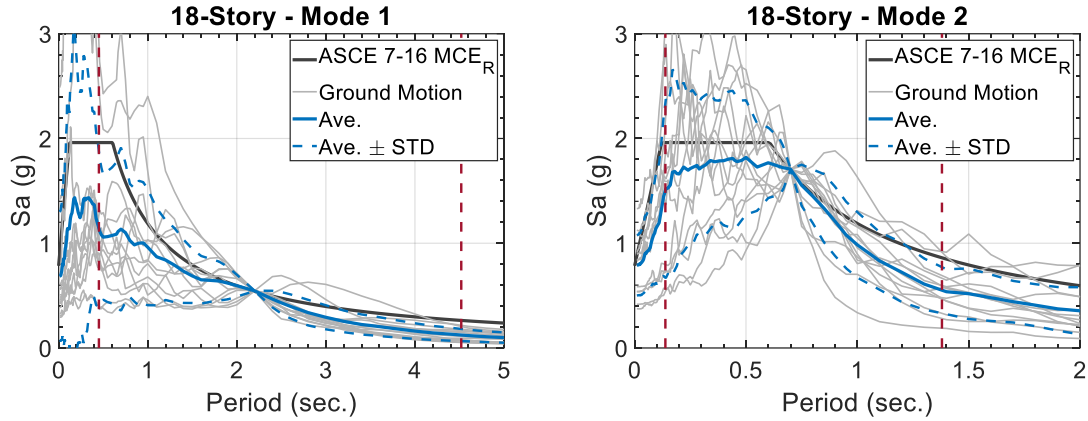


Figure C.9: RotD50 response spectra of selected suites of ground motions conditioned to first and second modes of 18-story archetypes.

Table C.2. Selected ground motions and the scaling factors used.

	9-Story		12-Story		15-Story		18-Story									
	Mode 1	Mode 2	Mode 1	Mode 2	Mode 1	Mode 2	Mode 1	Mode 2								
	RSN	Scale Factor	RSN	Scale Factor	RSN	Scale Factor	RSN	Scale Factor								
1	4884	2.04	1614	3.59	1536	1.56	6927	2.88	4856	0.53	4031	2.71	4856	0.51	4868	1.10
2	4863	1.96	265	3.11	4884	3.13	2457	3.81	1517	0.69	1283	3.76	5800	3.55	1246	2.66
3	8090	3.55	6960	2.88	5814	3.10	998	2.04	1496	3.90	6966	3.87	1120	0.64	1003	2.51
4	459	2.89	1141	1.68	5816	2.11	1107	3.49	1628	1.65	4223	1.83	5264	0.49	1489	3.58
5	1054	0.87	1077	1.82	3265	2.87	4223	1.57	4857	3.64	987	3.84	527	1.95	3968	0.64
6	5778	3.33	5657	0.94	764	2.71	786	3.04	759	3.30	1201	1.84	1504	1.32	125	2.44
7	8063	1.60	4870	3.87	1119	1.07	8118	3.06	1048	1.64	1605	2.13	5784	3.11	995	3.23
8	900	2.05	1602	1.11	4040	0.93	6897	2.92	1204	3.11	721	3.29	5618	2.49	5778	2.12
9	1048	1.41	1078	3.06	4850	2.30	1039	2.97	285	3.78	4850	2.50	20	3.27	3745	3.95
10	4864	2.98	517	2.52	963	2.02	5657	1.10	529	3.12	322	2.37	529	3.61	1602	1.69
11	338	1.63	967	3.79	1054	1.19	1479	2.69	1166	3.33	727	1.95	4866	3.91	755	2.60
12	8064	0.96	1489	3.52	527	1.77	1007	2.07	527	1.66	3754	2.31	4849	2.22	1495	3.83
13	4040	0.94	848	1.60	8064	0.99	5267	3.88	1545	1.88	4889	2.78	6888	1.60	1004	1.12

REFERENCES

1. Abdullah S. A. (2019). Reinforced Concrete Structural Walls: Test Database and Modeling Parameters. Ph.D. Dissertation, Dept. of Civil and Environmental Engineering, Univ. of California.
2. Abdullah S., Wallace, J.W. (2019). Drift Capacity of Structural Walls with Special Boundary Elements. *ACI Structural Journal*, Vol. 116, No. 1, pp.183-194.
3. Abdullah, S. A., Wallace, J. W. (2021). Drift Capacity at Axial Failure of RC Structural Walls and Wall Piers. *J. Struct. Eng., ASCE*, 147(6): 04021062.
4. ACI. (2008). ACI 318 Committee. Building Code Requirements for Structural Concrete. Farmington Hills, Michigan: American Concrete Institute.
5. ACI. (2014). ACI 318 Committee. Building Code Requirements for Structural Concrete. Farmington Hills, Michigan: American Concrete Institute.
6. ACI. (2019). ACI 318 Committee. Building Code Requirements for Structural Concrete. Farmington Hills, Michigan: American Concrete Institute.
7. ACI. (2025). ACI 318 Committee Approved Change Proposal. Special Structural Walls – Wall shear amplification clarification and simplification.
8. ACI Committee 374, “Acceptance Criteria for Moment Frames Based on Structural Testing (ACI 374.1-05) and Commentary,” American Concrete Institute, Farmington Hills, MI, 2005, 9 pp.
9. Adebar P., Hindi R., Gonzalez E. (2001). Seismic Behavior of a Full-Scale Diagonally Reinforced Slender Coupling Beam. Technical Report, Dept. of Civil Engineering, The University of British Columbia, Vancouver, Canada.
10. Aktan A., Bertero V. (1984). Seismic Response of R/C Frame-Wall Structures. *Journal of Structural Engineering*, 110 (8), 1803-1821.

11. Alsiwat J., Saatcioglu M. (1992). Reinforcement Anchorage Slip under Monotonic Loading. *Journal of Structural Engineering*, 118 (9), 2421-2438.
12. Ameen S. (2018). "Diagonally Reinforced Coupling Beams with High Strength Steel", Ph.D. Dissertation, University of Kansas.
13. ASCE/SEI. (2016). "Minimum design loads for buildings and other structures." ASCE/SEI 7-16, Reston, VA.
14. ASCE/SEI. (2022). "Minimum design loads for buildings and other structures." ASCE/SEI 7-22, Reston, VA.
15. ASCE/SEI 41-06. (2006). "Seismic Evaluation and Retrofit of Existing Buildings." American Society of Civil Engineers. Reston, Virginia.
16. ASCE/SEI 41-13. (2013). "Seismic Evaluation and Retrofit of Existing Buildings." American Society of Civil Engineers. Reston, Virginia.
17. ASCE/SEI 41-17. (2017). "Seismic Evaluation and Retrofit of Existing Buildings." American Society of Civil Engineers. Reston, Virginia.
18. ATC Online Hazard Tool: <https://hazards.atcouncil.org>
19. Baker J. W. (2011). Conditional Mean Spectrum: Tool for Ground-Motion Selection. *J. Struct. Eng.*, ASCE, 137(3): 322-331. DOI: 10.1061/(ASCE)ST.1943-541X.0000215.
20. Baker J. W., Cornell C. A. (2006). Spectral Shape, Epsilon and Record Selection. *Earthquake Eng. Struct. Dyn.*, 35(9), 1077–1095.
21. Barney K., Rabbat B., Fiorato A. E., Russell H. G., Corley W. G. (1980). Behavior of Coupling Beams under Load Reversals. Portland Cement Association.
22. Bazzurro P., Cornell C. A. (1994). Seismic Hazard Analysis of Non-Linear Structures I: Methodology. *J. Struct. Eng.*, 120(11), 3320–3344.
23. Belarbi A., Hsu T.C. (1994). "Constitutive Laws of Concrete in Tension and Reinforcing Bars Stiffened by Concrete", *ACI Structural Journal*, Vol. 91, No. 4, pp. 465-474.

24. Binney J. (1972). Diagonally Reinforced Coupling Beams. MS Thesis, University of Canterbury, Christchurch, New Zealand.
25. Bower O. (2008). Analytical Investigation into the Effect of Axial Restraint on the Stiffness and Ductility of Diagonally Reinforced Concrete Coupling Beams. MS Thesis, University of Cincinnati.
26. Bozorgnia Y. (2020), University of California, Los Angeles CEE 245 (Earthquake Ground Motion Characterization) Course Note (Academic year 2019-2020).
27. Brena S., Ihtiyar O. (2011). Performance of conventionally reinforced coupling beams subjected to cyclic loading. *Journal of Structural Engineering*, 137, 665-676.
28. Chang G.A., Mander J.B., (1994) "Seismic Energy Based Fatigue Damage Analysis of Bridge Columns: Part 1 – Evaluation of Seismic Capacity," NCEER Technical Report No. NCEER-94-0006, Dept. of Civ. Engng., State Univ. of New York at Buffalo, N.Y.
29. Ciampi V., Eligehausen R., Bertero V. V., Popov E. P. (1982). Analytical Model for Concrete Anchorages of Reinforcing Bars Under Generalized Excitations: College of Engineering, University of California Berkeley, CA, USA.
30. Coleman, Spacone. (2001). Localization Issues in Force-Based Frame Elements. *Journal of Structural Engineering*, 127 (11), 1257-1265.
31. Cornell C. A., Jalayer F., Hamburger R. O., and Foutch D. A. (2002). Probabilistic Basis for 2000 SAC Federal Emergency Management Agency Steel Moment Frame Guidelines. *J. Struct. Eng.*, 128(4), 526–533.
32. Cornell C.A., Krawinkler H. (2000). Progress and Challenges in Seismic Performance Assessment. *PEER Center News*, 3(2), 1–2.
33. Dhakal P. R., Maekawa K., (2002). Path-dependent cyclic stress–strain relationship of reinforcing bar including buckling. *Engineering Structures*, Vol. 24, No. 11, pp. 1383-1396. DOI: 10.1016/S0141-0296(02)00080-9.

34. Du X., Hajjar J. (2021). Three-dimensional nonlinear displacement-based beam element for members with angle and tee sections. *Engineering Structures*, Vol. 239, <https://doi.org/10.1016/j.engstruct.2021.112239>.
35. Elgehausen R., Popov, E. P., Bertoro, V. V., (1983). Local bond stress-slip relationships of deformed bars under generalized excitations. Report 82/23, Earthquake Engineering Research Centre, University of California, Berkely, pp. 169.
36. Elwood J. K., Eberhard O. M., (2009). Effective Stiffness of Reinforced Concrete Columns. *Structural Journal*, Vol. 106, Is. 4, pp. 476-484. DOI: 10.14359/56613.
37. ETABS, Structural Analysis and Design Software, Computers and Structures Inc.
38. FEMA. (2007). "Interim Testing Protocols for Determining the Seismic Performance Characteristics of Structural and Nonstructural Components." FEMA 461, Washington, DC.
39. Filippou F. C., Popov E. G., Bertero V. V., (1983). "Effects of Bond Deterioration on Hysteretic Behavior of Reinforced Concrete Joints", EERC Report No. UCB/EERC-83/19, Earthquake Engineering Research Center, University of California, Berkeley.
40. Fortney P. (2005). The Next Generation of Coupling Beams. PhD Thesis, University of Cincinnati.
41. Fortney P., Rassati G., Shahrooz B. (2008). Investigation on the effect of transverse reinforcement on performance of diagonally reinforced coupling beams. *ACI Structural Journal*, 105, 781-788.
42. Galano L., Vignoli A. (2000). Seismic behavior of short coupling beams with different reinforcement layouts. *ACI Structural Journal*, 97, 876-885.
43. Gomes A., Appleton J., (1998). Nonlinear cyclic stress-strain relationship of reinforcing bars including buckling. *Engineering Structures*, Vol. 19, Is. 10, pp. 822-826, [https://doi.org/10.1016/S0141-0296\(97\)00166-1](https://doi.org/10.1016/S0141-0296(97)00166-1).
44. Hellesland J., Scordelis A. C. (1981). Analysis of RC Bridge Columns Under Imposed Deformations, ETH Zürich, Rämistrasse 101, 8092 Zürich, Schweiz, www.library.ethz.ch

45. Ji X., Wang Y., Ma Q., and Okazaki T. (2017). Cyclic Behavior of Replaceable Steel Coupling Beams. ASCE J. of Struct. Eng., [https://doi.org/10.1061/\(ASCE\)ST.1943-541X.0001661](https://doi.org/10.1061/(ASCE)ST.1943-541X.0001661).
46. Kalbasi Anaraki K. (2019). Three-Dimensional Four-Node Macroscopic Models Nonlinear Analysis of Reinforced Concrete Walls. Master of Science Thesis, CSUF. <https://www.proquest.com/openview/188a09eacf39f79466ecda4b8f03154e/1?pq-origsite=gscholar&cbl=18750&diss=y>
47. Kent D. C., Park R. (1971). Flexural Members with Confined Concrete. Journal of the Structural Division, ASCE, V. 97, No. ST7, pp. 1969-1990.
48. Kolozvari K., Kalbasi K., Orakcal K., Wallace J.W. (2021). Three-dimensional model for nonlinear analysis of slender flanged reinforced concrete walls. Journal of Engineering Structures. 236 (2021) 112105.
49. Kolozvari K., Kalbasi K., Orakcal K., Wallace J.W. (2021). Three-dimensional shear-flexure interaction model for analysis of non-planar reinforced concrete walls. Journal of Building Engineering. 44 (2021) 102946.
50. Kolozvari K., Orakcal K., and Wallace, J. W. (2015). Modeling of cyclic shear-flexure interaction in reinforced concrete structural walls. Part I: Theory. ASCE J. of Struct. Eng., 141(5) 04014135.
51. Kolozvari K. (2013). Analytical Modeling of Cyclic Shear - Flexure Interaction in Reinforced Concrete Structural Walls, Ph.D. Dissertation, UCLA.
52. Kolozvari K, Orakcal K, Wallace JW (2015c). "Shear-Flexure Interaction Modeling for Reinforced Concrete Structural Walls and Columns under Reversed Cyclic Loading," Pacific Earthquake Engineering Research Center, PEER Report No. 12/2015.
53. Kolozvari K, Tran T, Orakcal K., and Wallace JW (2015b). "Modeling of cyclic shear-flexure interaction in reinforced concrete structural walls - Part II: Experimental validation." ASCE Journal of Structural Engineering, 141 (5) 04014136.

54. Kwan A., Zhao Z. (2002). Cyclic behavior of deep reinforced concrete coupling beams. Proc Inst Civil Eng: Struct Build, 152, 283-293.
55. Kwan A., Zhao Z. (2002). Testing of coupling beams with equal end rotations maintained and local joint deformation allowed. Proc Inst Civil Eng: Struct Build, 152, 67-78.
56. Lehman D., Turgeon J., Birely A., Hart C., Marley K., Kuchma D., Lowe L. (2013). Seismic Behavior of a Modern Concrete Coupled Wall. Journal of Structural Engineering ASCE, 139, 1371-1381. DOI: 10.1061/(ASCE)ST.1943-541X.0000853.
57. Lim E., Hwang S. J., Cheng C.-H., Lin P. Y. (2016). Cyclic Tests of Reinforced Concrete Coupling Beam with Intermediate Span-Depth Ratio. ACI Structural Journal, 113 (03), 515-524.
58. Los Angeles Tall Buildings Structural Design Council (LATBSDC) (2017). "An Alternative Procedure for Seismic Analysis and Design of Tall Buildings Located in the Los Angeles Region."
59. Los Angeles Tall Buildings Structural Design Council (LATBSDC) (2020). "An Alternative Procedure for Seismic Analysis and Design of Tall Buildings Located in the Los Angeles Region."
60. Los Angeles Tall Buildings Structural Design Council (LATBSDC) (2023). "An Alternative Procedure for Seismic Analysis and Design of Tall Buildings."
61. Lu Y., Panagiotou M., (2016). Three-Dimensional Beam–Truss Model for Reinforced Concrete Walls and Slabs – Part 2: Modeling Approach and Validation for Slabs and Coupled Walls. Earthquake Engng Struct. Dyn. 2016; 45:1707–1724, DOI: 10.1002/eqe.2720.
62. Malcom R. C., (2015). "Seismic Performance of Reinforced Concrete Coupled Walls" M.Sc. Thesis, University of Auckland.
63. Mander, Priestley, & Park. (1988). Observed Stress-Strain Behavior of Confined Concrete. Journal of Structural Engineering, 114 (8), 1827-1849.

64. Mander, Priestley, & Park. (1988). Theoretical Stress-Strain Model for Confined Concrete. *Journal of Structural Engineering*, 114 (8), 1804-1826.
65. Mari A. (1984). Nonlinear Geometric, Material and Time Dependent Analysis of Three Dimensional Reinforced and Prestressed Concrete Frames. Division of Structural Engineering and Structural Mechanics, University of California, Berkeley, UC -SESM Report No. 84-10, June 1984.
66. McKenna F., Fenves G. L., Scott M. H., Jeremic B. Open System for Earthquake Engineering Simulation (OpenSees). Pacific Earthquake Engineering Research Center, University of California, Berkeley.
67. Moehle J. (2014). *Seismic Design of Reinforced Concrete Buildings*. McGraw Hill.
68. Naish D., Fry, A., Klemencic, R., Wallace, J. (2013). Reinforced Concrete Coupling Beams – Part II: Modeling. *ACI Structural Journal*. 110:6, 1067-1075.
69. Naish D, Wallace J. W., Fry J. A., Klemencic R. (2009). Reinforced concrete link beams: alternative details for improved construction, SGEL Report, University of California, Los Angeles CA, 2009.
70. Naish D. A. (2010). Testing and Modeling of Reinforced Concrete Coupling Beams. PhD Thesis, University of California, Los Angeles.
71. Neuenhofer A., Filippou F. C. (1997). Evaluation of Nonlinear Frame Finite-Element Models. *Journal of Structural Engineering*, Volume 123, Issue 7, [https://doi.org/10.1061/\(ASCE\)0733-9445\(1997\)123:7\(958\)](https://doi.org/10.1061/(ASCE)0733-9445(1997)123:7(958)).
72. NZS 3101 (2006). *Concrete Structures Standard, Part 1: The Design of Concrete Structures: Part 2: Commentary on the Design of Concrete Structures*, Standards New Zealand, Wellington, New Zealand. ISBN 1-86975-043-8.
73. Orakcal K., Wallace J. W. (2006). Flexural Modeling of Reinforced Concrete Walls - Experimental Verification. *ACI Structural Journal*, 103 2 196-206.

74. Orakcal K., Conte J. P., Wallace J. W. (2004). Flexural Modeling of Reinforced Concrete Structural Walls - Model Attributes. *ACI Structural Journal*, 101 (5) 688-698.
75. Ozselcuk A. (1990). *Experimental and Analytical Studies of Coupled Wall Structures*. Berkeley: University of California, Berkeley.
76. Panagiotou M. (2008). *Seismic Design, Testing and Analysis of Reinforced Concrete Wall Buildings*, Ph.D. Dissertation, UC San Diego.
77. Panthaki F. D. (1991). "Low cycle fatigue behavior of high strength and ordinary reinforcing steels," MS thesis, Dept. of Civ. Engrg., State Univ. of New York at Buffalo, N.Y.
78. Paulay T. (1969). "The Coupling of Shear Walls." PhD Thesis, University of Canterbury, Christchurch, New Zealand.
79. Paulay T. (1971). Coupling Beams of Reinforced Concrete Shear Walls. *Journal of the Structural Division, American Society of Civil Engineers*, 97 (3), 843-862.
80. Paulay T., Binney J. R. (1974). "Diagonally Reinforced Coupling Beams of Shear Walls", *Shear in Reinforced Concrete*, SP-42, American Concrete Institute, Detroit, MI, 2, 579-598.
81. Paulay T., Priestley M. J. N. (1992). *Seismic Design of Reinforced Concrete and Masonry Buildings*, John Wiley & Sons Inc., New York.
82. PEER/ATC-72-1. (2010). *Modeling and Acceptance Criteria for Seismic Design and Analysis of Tall Buildings*. Redwood City, California: Applied Technology Council.
83. PEER Report 2014/18. (2014). *Three-Dimensional Beam-Truss Model for Reinforced-Concrete Walls and Slabs Subjected to Cyclic Static or Dynamic Loading*. Lu, Y.; Panagiotou, M.; Koutromanos, I. Berkeley, CA: Pacific Earthquake Engineering Research Center.
84. PEER Report (2017). "Guidelines for Performance-Based Seismic Design of Tall Buildings." Berkeley, CA.
85. Perform 3D, 3D Performance Based Design Software, Computers and Structures Inc.

86. Poudel, A., Lequesne, R., and Lepage, A. (2018). "Diagonally Reinforced Concrete Coupling Beams: Effects of Axial Restraint". SL Report No. 18-3 2018-09, University of Kansas Center for Research, Inc., 39pp.
87. Rojas L. M. (2022). Framework to Define Performance Requirements for Structural Component Models and Application to Reinforced Concrete Wall Shear Strength. Ph.D. Dissertation, University of California, Los Angeles.
88. Rojas L. M., Wallace W., Abdullah S., Kolozvari K., (2023). Seismic Shear Design of RC Structural Walls, Building for the Future: Durable, Sustainable, Resilient. DOI: 10.1007/978-3-031-32511-3_114.
89. Saatcioglu M., Razvi S. R. (1992). Strength and Ductility of Confined Concrete. Journal of Structural Engineering, American Society of Civil Engineers, 118 (6), 1590-1607.
90. Saatcioglu M., Razvi S. R. (1992). Strength and Ductility of Confined Concrete. ASCE Journal of Structural Engineering, 1186, 1590-1607.
91. Santhakumar A. R. (1974). The Ductility of Coupled Shear Walls. PhD Thesis, University of Canterbury, Christchurch, New Zealand.
92. Scott B. D., Park R., Priestley M. J. N. (1982). Stress-Strain Behavior of Concrete Confined by Overlapping Hoops at Low and High Strain Rates. Journal of the American Concrete Institute, V. 79, No. 1, pp. 13-27.
93. Scott, M. H., and G. L. Fenves. (2010). A Krylov Subspace Accelerated Newton Algorithm: Application to Dynamic Progressive Collapse Simulation of Frames. Journal of Structural Engineering, 136(5).
94. Segura C. L., Wallace W. J. (2018). Impact of Geometry and Detailing on Drift Capacity of Slender Walls. ACI Structural Journal, V. 115, No. 3, May, pp. 885-896. doi: 10.14359/51702046

95. Segura C. L., Wallace W. J. (2018). Seismic Performance Limitations and Detailing of Slender Reinforced Concrete Walls. *ACI Structural Journal*, V. 115, No. 3, May, pp. 849-860. doi: 10.14359/51701918
96. Shiu K. N., Aristizabal-Ochoa, J. D., Barney, G. B., Fiorato, A. E., Corley, W. G. (1981). Earthquake resistant structural walls: Coupled wall tests. NSF Report, Bibcode: 1981STIN.8221450S.
97. Spacone E., Filippou F. C., TAUCER F. F. (1996). Fibre beam-column model for non-linear analysis of R/C frames: Part II. Applications, *Earthquake Engineering & Structural Dynamics*, Vol. 25, Is. 7, pp. 727-742. [https://doi.org/10.1002/\(SICI\)1096-9845\(199607\)25:7<727::AID-EQE577>3.0.CO;2-O](https://doi.org/10.1002/(SICI)1096-9845(199607)25:7<727::AID-EQE577>3.0.CO;2-O).
98. Standards New Zealand - NZS 3101. (1995). Concrete Structures Standard. Wellington: Standards New Zealand.
99. Sugaya K. (2003). Experimental Study on Variation Mechanism of Carrying shear force at the time of the earthquake of Coupling Beams with T-shaped Continuous Layer Coupled Wall. PhD Thesis, Japan.
100. Sugaya K., Teshigawara, Kato. (2000). Experimental Study on Carrying Shear Force Ratio of 12 Story Coupled Shear Wall. 12WCEEE 2000. -: 12WCEE.
101. Tall Buildings Initiative: "Guidelines for Performance-Based Seismic Design of Tall Buildings", PEER Report 2017/06.
102. Tassios T., Moretti M., Bezas A. (1996). On the behavior and ductility of reinforced concrete coupling beams of shear walls. *ACI Structural Journal*, 93, 711-720.
103. Taucer F. F., Spacone E., Filippou F. C. (1991). "A fiber beam-column element for seismic response analysis of reinforced concrete structures." Rep. No. UCB/EERC-91/17, Earthquake Engineering Research Center, College of Engineering, University of California, Berkeley, CA.
104. Tegos I. A., Penelis G. (1988). Seismic Resistance of Short Columns and Coupling Beams Reinforced with Inclined Bars. *ACI Structural Journal*, 85-S10, 82-88.

105. Uriz P., Mahin S. A. (2008). Toward Earthquake-Resistant Design of Concentrically Braced Steel-Frame Structures, PEER Report 2008-08. Pacific Earthquake Engineering Research Center, University of California, Berkeley, CA.
106. Wallace J. W. (1994). A New Methodology for Seismic Design of Reinforced Concrete Shear Walls. *Journal of Structural Engineering*, American Society of Civil Engineers, 120 (3), 863-884.
107. Wallace J. W. (2007). Modeling Issues for Tall Reinforced Concrete Core Wall Buildings. *The Structural Design of Tall and Special Buildings*, 16 (5), 615-632.
108. Wallace, J. W., (2012). Behavior, Design, and Modeling of Structural Walls and Coupling Beams – Lessons from Recent Laboratory Tests and Earthquakes,” *International Journal of Concrete Structures and Materials*, V. 6, No. 1, pp. 3-18. doi: 10.1007/s40069-012-0001-4.
109. Wallace, J. W., Elwood, K. J., Massone L. M. (2008). An Axial Load Capacity Model for Shear Critical RC Wall Piers. *J. Struct. Eng.*, ASCE, Vol. 134, No. 9, pp 1548-1557.
110. Wallace, J. W., Moehle, J. P., (1992). Ductility and Detailing Requirements of Bearing Wall Buildings,” *Journal of Structural Engineering*, ASCE, V. 118, No. 6, pp. 1625-1644. doi: 10.1061/(ASCE)0733-9445(1992)118:6(1625).
111. Yassin M. H. M. (1994). “Nonlinear Analysis of Prestressed Concrete Structures Under Monotonic and Cyclic Loads”, Dissertation, University of California, Berkeley.
112. Zhou J. (2003). “Effect of Inclined Reinforcement on Seismic Response of Coupling Beams”, Ph.D. Dissertation, McGill University, Montreal, Canada.
113. Zhao J., Sritharan S., (2007). Modeling of Strain Penetration Effects in Fiber-Based Analysis of Reinforced Concrete Structure. *Structural Journal*, Vol. 104, Is. 2, pp. 133-141. DOI: 10.14359/18525.
114. Zhu Y., Zhou F. L., Su R. K. L. (2008). Seismic Effects on Coupled Shear Wall Structure by Coupling Beams with Side Bolted Steel Plates. *Proceedings, 14th World Conference on Earthquake Engineering*, Beijing, China.